



City Research Online

City, University of London Institutional Repository

Citation: Montesano, G. (2023). Improving the structure function relationship in the macula. (Unpublished Doctoral thesis, City, University of London)

This is the accepted version of the paper.

This version of the publication may differ from the final published version.

Permanent repository link: <https://openaccess.city.ac.uk/id/eprint/31674/>

Link to published version:

Copyright: City Research Online aims to make research outputs of City, University of London available to a wider audience. Copyright and Moral Rights remain with the author(s) and/or copyright holders. URLs from City Research Online may be freely distributed and linked to.

Reuse: Copies of full items can be used for personal research or study, educational, or not-for-profit purposes without prior permission or charge. Provided that the authors, title and full bibliographic details are credited, a hyperlink and/or URL is given for the original metadata page and the content is not changed in any way.

Improving the structure function relationship in the macula

GIOVANNI MONTESANO

Submitted for the degree of
Doctor of Philosophy

City, University of London
Division of Optometry and Visual Science
July 2023

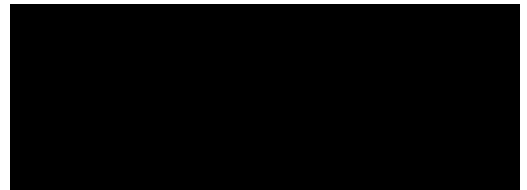




The work contained in this thesis was completed by the candidate, Giovanni Montesano, under the supervision of Professor David Crabb and Dr Deanna Taylor. It has not been submitted for any other degrees, either now or in the past. All the experimental work has been either published or has been submitted for publication in peer-reviewed academic journals, as required for the PhD programme by prospective publications. All sources of information have been acknowledged and references have been given. The University Librarian of City, University of London is permitted to allow the thesis to be copied in whole or in part without further reference to the author. This permission covers only single copies made for study purposes, subject to normal conditions of acknowledgement.

Signed

Giovanni Montesano



Abstract

The macula is the central part of the retina responsible for central vision and can suffer damage from many diseases, including diabetes, macular degeneration and glaucoma. Establishing a relationship between functional measurements, such as perimetry, and structural metrics, such as those obtained through imaging, has proven both clinically appealing and challenging, owing to specific features of this area of the retina. The programme of work presented in this thesis focuses on improving the accuracy of structure-function analyses of the macula as well as the mechanistic understanding of structure-function relationship in both healthy and diseased eyes.

The first study revisits and improves previous models quantifying the length of Henle's fibres. This directly relates to the radial displacement of Retinal Ganglion Cells (RGCs) from their photoreceptors and affects structure-function mapping. The study demonstrated the inaccuracy of previous methods used to displace perimetric stimuli, proposing a correct implementation of these calculations. These results were made available to other researchers in a user-friendly web application.

The second study explored how natural positioning of observers in front of imaging and perimetry devices, as well as their fixation and eye movements, affected the precision of macular structure-function mapping. The study analysed data from an eye-tracking perimeter used to test both healthy eyes and patients with glaucoma. An optimal strategy for structure-function mapping was developed and the mapping error introduced by fixation was quantified.

The third study used data from an eye-tracking perimeter and the framework of an established neural model of spatial summation to investigate the structure-function relationship in early neural loss in patients with diabetes without diabetic retinopathy, quantified with both imaging and functional tests, including Frequency Doubling Perimetry, standard visual acuity and contrast sensitivity.

The fourth study involved the prospective collection of data from healthy observers with perimetric stimuli of different sizes and durations, using custom software. The data were used to develop a computational model of perimetric sensitivity able to reproduce the interaction between spatial and temporal summation in the context of cortical integration and their link to the number of retinal ganglion cells being stimulated.

In the fifth study, the methodology and mechanistic framework developed in the previous studies were applied to test the computational model in glaucoma. The model was used to obtain functional estimates of retinal ganglion cell damage from standard automated perimetry data collected in glaucoma patients and healthy age-related controls. The results were correlated with imaging and histology data from previous literature.

Table of Contents

List of figures	6
List of tables	7
List of abbreviations.....	8
Acknowledgements.....	9
1. Background.....	10
1.1. Imaging of macular retinal structures	10
1.2. Perimetric testing of the macula	11
1.2.1. Spatial summation	13
1.2.2. Temporal summation	14
1.2.3. Interaction between stimulus duration and size	14
1.3. Macular structure-function relationship	14
1.4. Objectives of this research.....	16
1.5. References	16
2. Revisiting the Drasdo model: implications for structure-function analysis of the macular region	18
2.1. Introduction	18
2.2. Methods.....	20
2.2.1. Datasets	20
2.2.2. Histology map	21
2.2.3. Schematic eye.....	21
2.2.4. Scaling of eye structures and cell density.....	22
2.2.5. OCT data processing	23
2.2.6. Conversion of GCL thickness maps into estimated RGC counts	24
2.2.7. Displacement model	24
2.2.8. Displacement of perimetric stimuli	24
2.2.9. Development of the web App.....	25
2.3. Results	26
2.3.1. Scaling of eye structures with axial length	26
2.3.2. Variability of displacement with axial length.....	27
2.3.3. Displacement of perimetric stimuli	27
2.4. Discussion	30
2.5. Appendix.....	33
2.5.1. Appendix 1.....	33
2.5.2. Appendix 2.....	34
2.5.3. Appendix 3.....	35
2.6. Acknowledgments	36
2.7. References	37
3. Systematic and random mapping errors in structure – function analysis of the macula.....	39
3.1. Introduction	39

3.2. Methods	41
3.2.1. Data collection	41
3.2.2. Analysis of fixation and projection data	41
3.2.3. Structural mapping	42
3.2.4. Quantification of projection errors.....	43
3.2.5. Statistical analysis	44
3.3. Results	44
3.3.1. Mapping error introduced by grid rotation	45
3.3.2. Projection errors due to fixation movement	47
3.4. Discussion	50
3.4.1. Mapping error introduced by grid rotation	50
3.4.2. Projection errors due to fixation movement	50
3.4.3. Limitations	52
3.5. Appendix	53
3.5.1. Identification of evoked displacements.....	53
3.6. References	55
4. Evidence for structural and functional damage of the inner retina in diabetes with no diabetic retinopathy	57
4.1. Introduction	57
4.2. Methods	58
4.2.1. Data collection	58
4.2.2. Data analysis	61
4.3. Results	64
4.3.1. Sample description	64
4.3.2. Structural metrics	64
4.3.3. Functional metrics	65
4.3.4. Structure-function relationship	65
4.4. Discussion	68
4.4.1. Structural metrics	69
4.4.2. Functional metrics	69
4.4.3. Structure-function relationship	70
4.4.4. Effect of disease duration and HbA1C	71
4.4.5. Conclusions	71
4.5. Appendix	72
4.5.1. Flowchart of the selection steps.....	72
4.5.2. Spatial summation of perimetric stimuli	73
4.6. Acknowledgements	75
4.7. References	76
5. Spatiotemporal summation of perimetric stimuli in healthy observers	79
5.1. Introduction	79
5.2. Methods	80
5.2.1. Participants	80
5.2.2. Psychophysical experimental procedure	81
5.2.3. Imaging	83
5.2.4. Modelling of perimetric sensitivity	83
5.3. Results	89
5.3.1. Average response	89

5.3.2.	Results from the spatiotemporal model.....	90
5.3.3.	Frequency of seeing curves	93
5.4.	Discussion	95
5.5.	Conclusions	99
5.6.	Appendix.....	99
5.6.1.	MOCS fitting.....	99
5.6.2.	Mosaic arrangement for computation	100
5.6.3.	A multiscale filter hypothesis for spatiotemporal integration.....	100
5.7.	Supplementary material	105
5.7.1.	Spatial summation with midsize OFF retinal ganglion cells.....	105
5.7.2.	Effect of optical factor compensation	106
5.7.3.	Average parameters for the psychometric functions	108
5.7.4.	Results with an alternative temporal impulse response	109
5.8.	References	109
6.	<i>Spatial summation in the glaucomatous macula: a link with retinal ganglion cell damage</i>	<i>113</i>
6.1.	Introduction	114
6.2.	Methods.....	115
6.2.1.	Study population	115
6.2.2.	Study protocol	116
6.2.3.	Spatial summation model	118
6.3.	Results	121
6.3.1.	Study population	121
6.3.2.	Model calibration.....	121
6.3.3.	Template fitting	122
6.3.4.	Structure-function relationship	124
6.4.	Discussion	126
6.5.	Appendix.....	130
6.5.1.	Computational model.....	130
6.5.2.	Bayesian fitting	130
6.6.	Supplementary material	131
6.6.1.	Influence of low perimetric accuracy for advanced damage.....	133
6.7.	References	136
7.	<i>Conclusions and future directions.....</i>	<i>140</i>
7.1.	References	141

List of figures

Figure 1.1 Example of how Optical Coherence Tomography imaging can be used to characterise structural features of the macula.	10
Figure 1.2 Schematic of a psychometric function.	11
Figure 1.3 Relationship between 10-2 (red dots) and the 24-2 (black circles) for a right eye.	12
Figure 1.4 Schematic exemplifying Ricco’s law.	13
Figure 1.5 Schematic anatomy of the retina.	15
Figure 2.1 Rendering of the schematic eye, with a projection of a 10-2 grid	22
Figure 2.2 Representations of the two candidate methods to apply the displacement to perimetric stimuli.	25
Figure 2.3 Scaling of ocular structures with axial lengths.	26
Figure 2.4 Fitting results	27
Figure 2.5 Comparison of the results between the two displacement methods for perimetric stimuli.	28
Figure 2.6 Comparison of the results between the two displacement methods for perimetric stimuli for real structural data.	29
Figure 2.7 Screenshot of the second screen from the web App.	33
Figure 2.8 Raw averages and cubic interpolation of cell densities.	34
Figure 2.9 Example of how the displacement is computed along a specific meridian.	36
Figure 3.1 Examples of mapping errors.	42
Figure 3.2 Error introduced by grid rotation.	46
Figure 3.3 Examples from four different subjects of projection errors during a 10-2 VF test.	47
Figure 3.4 Fixation bias and mapping errors.	49
Figure 3.5 Projection error prediction.	50
Figure 3.6 Calculation of concordant displacements	54
Figure 3.7 Box-plots of the unbiased error for each subject.	54
Figure 4.1 Schematic of the stimulus displacement	63
Figure 4.2 Box-plots of the average thickness values recorded for each ETDRS sector.	65
Figure 4.3 Scatter plot and regression lines for the global structure-function relationship.	66
Figure 4.4 Scatter plot and regression lines for the topographic structure-function relationship for microperimetry.	67
Figure 4.5 Scatter plot and regression lines for the topographic structure-function relationship for FDT.	68
Figure 4.6 Flowchart of the selection steps detailed in the methods.	73
Figure 4.7 Observed structure-function relationship compared to the theoretical framework of spatial summation.	74
Figure 4.8 Example of how the microperimetric test could be modified to improve detection of neural damage.	75
Figure 5.1 Retinal Ganglion Cell (RGC) receptive field (RF) modelling.	85
Figure 5.2. Effect of optical blur for different pupil sizes.	86
Figure 5.3 Example of the interaction of stimulus size and duration in the proposed model.	88
Figure 5.4 Spatial summation curves.	90
Figure 5.5 Model fit results for spatial summation data.	91
Figure 5.6 Model fit results for spatiotemporal summation data.	93
Figure 5.7 Psychometric functions.	94
Figure 5.8. Change in psychometric slope.	94

Figure 5.9. Application to glaucoma.	99
Figure 5.10. Implementation of the mosaic.	100
Figure 5.11. Example of how a change in scale results in a horizontal translation of the spatial summation curve.	101
Figure 5.12. Spatiotemporal response surface.	102
Figure 5.13. Response envelope modelling.	103
Figure 5.14 Replication of the model in cortical filter model using a two-stage model.	104
Figure 5.15. Model fit results with midget RGCs.	106
Figure 5.16. Effect of optical factors on model fit results.	107
Figure 5.17. Effect of different impulse response functions.	109
Figure 6.1. Displacement of perimetric stimuli.	117
Figure 6.2. Schematic illustrating the hierarchical fitting process for the template.	120
Figure 6.3. Template calibration.	122
Figure 6.4. Template fitting results.	123
Figure 6.5. Effect of stimulus size.	124
Figure 6.6. Structure-function relationship.	125
Figure 6.7. Structure-function model fitting results.	126
Figure 6.8. Template fit for each location of the 10-2 grid.	131
Figure 6.9. Prediction error and test-retest variability.	132
Figure 6.10. Simulation of sharp-edged defects.	133
Figure 6.11. Template fitting on simulated full-threshold data.	134

List of tables

Table 2.1 Descriptive statistics for relevant variables in the two datasets.	21
Table 2.2 Density data at different eccentricities of the 10-2 grid.	30
Table 2.3 Data for the schematic eye used in this paper along with the original values from Drasdo and Fowler.	35
Table 3.1.	45
Table 3.2 Fixation metrics and projection errors.	48
Table 4.1 Descriptive statistics of the analysed sample.	64
Table 5.1 Characteristic of each eye in the sample.	89
Table 5.2 Model fit results for spatial summation data.	91
Table 5.3 Model fit results for spatiotemporal summation data.	92
Table 5.4. Model fit results with midget RGCs.	105
Table 5.5. Effect of optical factors on model fit results.	106
Table 5.6. Parameters for the psychometric functions.	108
Table 6.1. Descriptive statistics of the sample.	121
Table 6.2. Template fitting error.	123
Table 6.3. Structure-function model fitting error.	124
Table 6.4. Effect of censoring on fitting error.	135

List of abbreviations

AL = Axial Length	IPL = Inner Plexiform Layer
AMD = Age Related Macular Degeneration	MAE = Mean Absolute Error
AO = Adaptive Optics	MAR = Minimum Angle of Resolution
BCEA = Bivariate Contour Ellipse Area	MCMC = Markov Chain MonteCarlo
BCVA = Best Corrected Visual Acuity	MD = Mean Deviation
BM = Bruch's Membrane	MOCS = Method of Constant Stimuli
CD = Concordant Displacement	MS = Mean Sensitivity
CDF = Cumulative Distribution Function	MTF = Modulation Transfer Function
CI = Confidence Interval	NFL = Nerve Fibre Layer
cMD = central Mean Deviation	OCT = Optical Coherence Tomography
CMP = Compass perimeter	ONH = Optic Nerve Head
cp-RNFL = circumpapillary Retinal Nerve Fibre Layer	OPL = Outer Plexiform Layer
CS = Contrast Sensitivity	P-OFF-RGC = Parasol OFF Retinal Ganglion Cell
D = Diopters	PRL = Preferred Retinal Locus
DL = Diffraction Limited	qCSF = quick contrast sensitivity function
DLS = Differential Light Sensitivity	RF = Receptive Field
DM = Diabetes Mellitus	RGC = Retinal Ganglion Cells
DoG = Difference of Gaussian	RGC-RF = Retinal Ganglion Cells Receptive Field
DR = Diabetic Retinopathy	RGCL = Retinal Ganglion Cell Layer
ETDRS = Early Treatment Diabetic Retinopathy Study	RMSE = Root Mean Squared Error
FDT = Frequency Doubling Technology perimetry	RNFL = Retinal Nerve Fibre Layer
FoS = Frequency of Seeing	RPE = Retinal Pigment Epithelium
FT = Full Threshold	SAP = Standard Automated Perimetry
GCL = Ganglion Cell Layer	SD = Standard Deviation
GLM = Generalised Linear Model	SD-OCT = Spectral Domain Optical Coherence Tomography
HbA1C = glycated haemoglobin plasma concentration	SITA = Swedish Interactive Thresholding Algorithm
HFA = Humphrey Field Analyzer	TD = Total Deviation
HFA = Humphrey Field Analyzer	V1 = Primary Visual Cortex
ILM = Inner Limiting Membrane	VF = Visual Field
INL = Inner Limiting Membrane	W _c = Weber Contrast
IOP = Intraocular Pressure	ZEST = Zippy Estimation through Sequential Testing

Acknowledgements

I would like to greatly thank my supervisors, Prof. David Crabb and Dr Deanna Taylor, for their guidance and support during my PhD. I would also like to thank Prof. David Garway-Heath, Dr Pádraig Mulholland, Dr Tony Redmond and Prof. Ruth Hogg for their help and supervision in various steps of my project.

A great thank you goes to my colleagues in the CrabbLab and at Moorfields Eye Hospital, especially to Dr Giovanni Ometto and Dr Beth Higgins for being excellent collaborators and amazing friends.

I would also like to thank all my collaborators in Italy and in the UK, and Josephine Evans in particular, for their help with organising and performing the data collection.

Finally, I would like to thank my family, especially my mom, my dad, and my sister: distances grow bigger, but they remain an irreplaceable support in my career and every aspect of my life. A very special thank you is for Irene: she has been there for me through many academic endeavours before, and this yet another one. I could not imagine doing what I do without her, and I am grateful she is still putting up with this after so many years!

1. Background

The macula is the central part of the retina devoted to high resolution visual acuity and plays a crucial role in human vision. It covers an area of 5 to 6 mm around the fovea, the central depression of the retina containing the highest density of photoreceptors in a healthy eye¹. The macular region can become damaged by several diseases, including glaucoma, diabetes, and age-related macular degeneration (AMD).

1.1. Imaging of macular retinal structures

Many methods can be used to acquire structural data of the eye through imaging. However, Optical Coherence Tomography (OCT) has become increasingly popular as a simple, non-invasive tool to obtain detailed cross-sectional images of the retina. The introduction of Spectral Domain OCT devices (SD-OCT) has greatly improved image quality and scanning speed, allowing for automated segmentation of the different retinal layers (**Figure 1.1**). This, in turn, allows for the creation of detailed anatomical maps that can be used to investigate the effect of diseases individual layers. Very briefly, OCT uses laser interferometry to generate images by quantifying the reflectivity profile along one axis of a partially transparent tissue. This profile is called an *A-scan*. Many *A-scans* are acquired in a scanning motion to generate a two-dimensional section of the tissue, called a *B-scan*². These *B-scans* are then combined to form a volumetric reconstruction of the tissue under investigation, such as the retina. These volumes can finally be used to reconstruct detailed anatomical maps. The most common are thickness maps of the different layers, but reflectivity maps can also be used. OCT scans are used to observe and quantify changes to the retinal tissues and monitor their evolution over time.

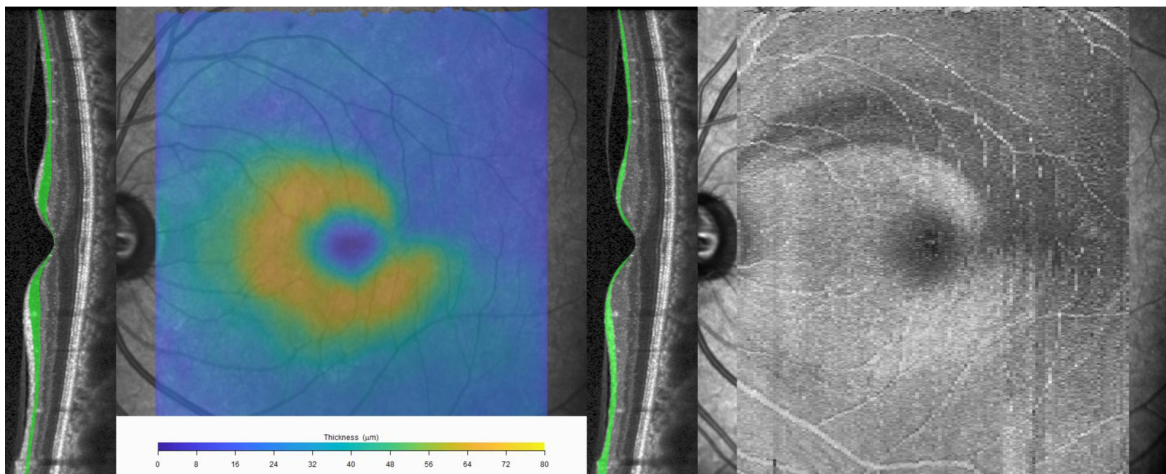


Figure 1.1 Example of how Optical Coherence Tomography imaging can be used to characterise structural features of the macula. The side vertical panels show a B-scan through the fovea. Many of these B-scans (121 in this example) can be segmented to build thickness maps (left, for the Ganglion Cell Layer, GCL) or reflectivity maps (right, for the Retinal Nerve Fibre Layer, RNFL). The corresponding layers in the B-scan are shaded in green. This example shows the macula of an eye with glaucoma, which demonstrates areas of thinning of the GCL and reduced reflectivity of the RNFL.

1.2. Perimetric testing of the macula

Standard Automated Perimetry (SAP) is one of the most widely used functional tests in clinical practice. It provides a topographical quantification of the Differential Light Sensitivity (DLS) to contrast for each tested retinal location^{3, 4}. In clinical SAP, visual function is often tested at multiple pre-defined locations of the visual field (VF) with simple circular stimuli of different intensities over a uniform background. A subject being tested is asked to respond, usually by pressing a button, every time a stimulus is perceived. A test strategy would then use responses to different stimulus intensities to define some quantities related to the sensitivity of the tested locations. In most applications, the quantity of interest is the 50%-threshold of the psychometric function. The psychometric function describes the probability of responding to a stimulus given its intensity (**Figure 1.2**). For clinical perimetry, especially for studying damage from glaucoma or neurological diseases, the test is often performed in photopic conditions, with a uniform background intensity ($I_b = 10 \text{ cd/m}^2$). However, the test can also be performed in mesopic or scotopic conditions, and this is more common in the clinical field of medical retina⁵. The strength of the stimulus is then defined in terms of Weber's contrast (W_c)

$$W_c = \frac{I - I_b}{I_b}$$

where I is the intensity of the stimulus. In this context, the 50%-threshold of the psychometric function is referred to as *contrast sensitivity* or *Differential Light Sensitivity* (DLS). Usual choices for stimulus size and duration are 0.43 *degrees* (diameter) and 200 *ms*. Different stimulus characteristics can greatly affect the response of the observer. For example, larger stimulus sizes are known to reduce the variability of the response yielding steeper psychometric functions⁶. Importantly, contrast sensitivity increases with larger stimuli and longer durations, meaning that a progressively lower contrast is needed to detect increasingly larger/longer stimuli.

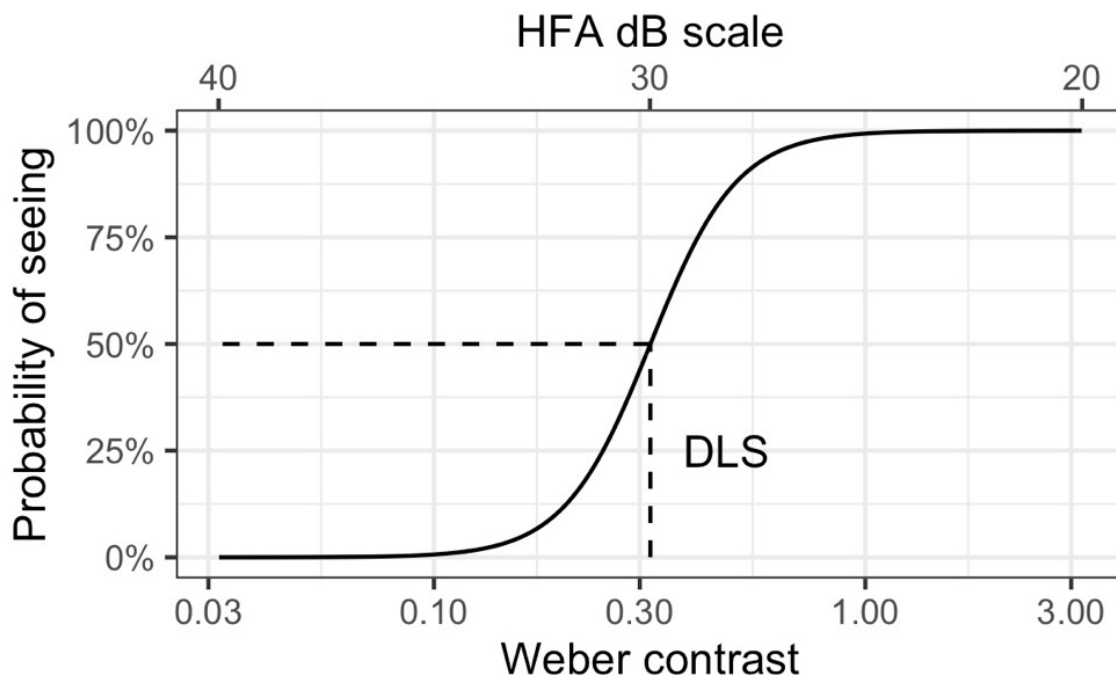


Figure 1.2 Schematic of a psychometric function. The dashed line indicates the 50%-threshold. HFA = Humphrey Field Analyzer; DLS = Differential Light Sensitivity.

In conventional perimetry, DLS is often expressed in a relative dB scale, reporting attenuation of the brightest stimulus available on the device instead of contrast. For the Humphrey Field Analyzer (HFA, Zeiss Meditec, Dublin, CA), the most commonly used SAP device, the brightest stimulus is 3185 cd/m². This, along with a background of 10 cd/m², has become the standard for the vast majority of projection-based perimeters. To convert HFA dB back to Weber contrast, the following formula can be used, keeping in mind that in projection systems any stimulus is already summed to its background

$$W_c = \frac{3185/10^{dB/10}}{10}$$

The most commonly used testing pattern for the macular region is the 10-2 grid. This grid spans the central 10 degrees of the VF with a spacing of 2 degrees between tested locations. This is much more spatially resolved than the more common 24-2 and 30-2 grids, where the spacing is 6 degrees. A schematic showing the relationship between the 10-2 and a 24-2 testing grids is shown in **Figure 1.3**.

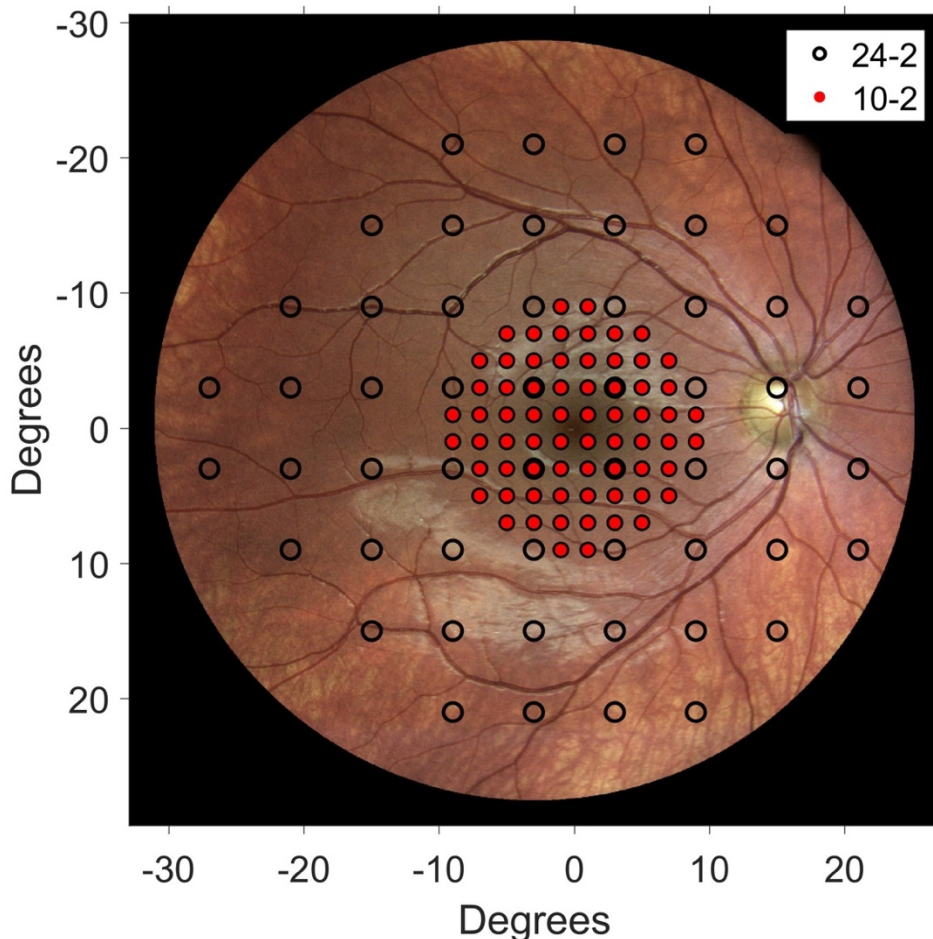


Figure 1.3 Relationship between 10-2 (red dots) and the 24-2 (black circles) for a right eye.

1.2.1. Spatial summation

The change in DLS with increasing stimulus area sizes has been widely used to characterise specific properties of the visual system. Often, the relationship is studied by evaluating the change in log-DLS according to the log-Area of circular stimuli. Such a log-log relationship is linear with a slope of 1 (*total or complete summation*) up to a certain critical size, after which the slope is generally shallower (*partial summation*, example in **Figure 1.4**). The total summation behaviour is usually referred to as *Ricco's law*, and the critical area size is often named *Ricco's area*.

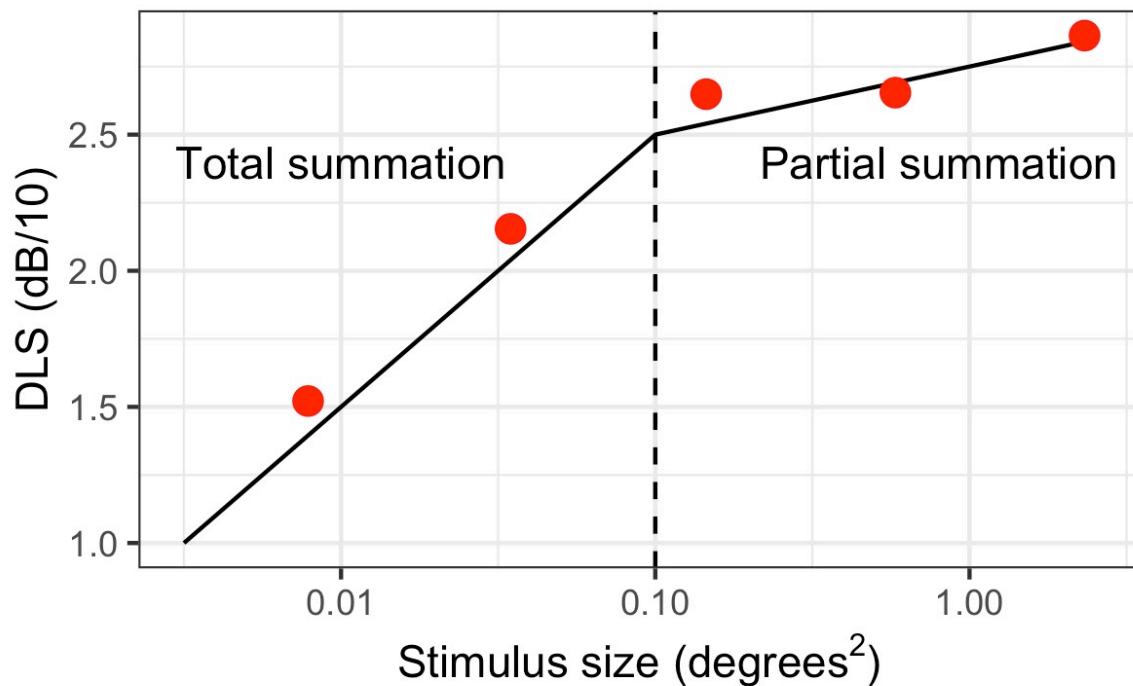


Figure 1.4 Schematic exemplifying Ricco's law. The vertical dashed line represents the critical stimulus size; DLS = Differential Light Sensitivity.

The critical size of the stimulus changes with eccentricity, being larger in the periphery than centrally. This is thought to reflect the change in density of the Retinal Ganglion Cell (RGC) receptive fields (RFs) across the retina. According to this view, the visual system is organised in such a way that the number of RGC-RFs within Ricco's area is constant across the VF. Therefore, the RGC-RF density would act as the scaling factor for Ricco's law at different eccentricities. This has been confirmed by experimental evidence with both simple circular and complex stimuli. Many authors also believe that the constant number of RGCs at critical size is reflective of how the RGCs are hierarchically connected to the primary visual cortex (V1)⁷⁻⁹. Although the estimates vary, the critical number of RGCs is reported to be between $\sim 14^9$ and $\sim 32^{7,8}$, also according to the specific RGC mosaic considered. This view seems also coherent with the observation that the Cortical Magnification Factor (CMF, i.e. the millimetres of V1 that receive input from one degree of VF) decreases with eccentricity, scaling approximately with the density of RGCs⁸⁻¹¹. Importantly, this scaling principle appears to hold even when the number of RGCs is reduced due to disease, for example in the case of glaucoma. Redmond et al.¹² demonstrated an increase in Ricco's area in patients with early glaucoma compared to age-matched controls at the same eccentricity. Swanson et al. also used the same scaling principle to model sensitivity loss in glaucoma with usual stimulus

parameters^{7, 8, 13}, although they highlighted that such a scaling could be obtained by different cortical filters independently of the underlying RGC density. However, most of these interpretations do not make an effort to incorporate the effect other stimulus properties, such as the background or duration of the stimulus, which have been shown to dynamically alter spatial summation¹⁴⁻¹⁶.

1.2.2. Temporal summation

Much of the reasoning regarding spatial summation can be applied to explain the effect of different stimulus durations on DLS. As for stimulus sizes, DLS also increases for longer stimuli. The relationship between log-Durations and log-DLS is similar to the one described for spatial summation: log-DLS increases linearly with a slope of 1 until a critical duration is reached. For supra-critical durations, the slope is < 1 . This is known as *Bloch's law*. Temporal summation for perimetric stimuli has been studied to a lesser extent than its spatial counterpart^{14, 15, 17-19}. Most of the studies involving temporal summation focussed either on complex stimuli or on motion detection^{17, 20-22}. However, much like Ricco's area, critical duration increases with eccentricity in healthy observers²³ and, importantly, in patients who experience loss of RGCs due to glaucoma²⁴. Mulholland et al.²⁴ showed that glaucoma patients with early damage had longer critical durations at the same eccentricity compared to age-matched controls when tested with a stimulus 0.48 degrees in diameter. Interestingly, the critical duration could be equated between the two groups by scaling the stimulus to match the individual Ricco's area, compensating for RGC loss in the glaucoma group.

1.2.3. Interaction between stimulus duration and size

One aspect that has not been explored in depth is the interaction between stimulus size and duration. Barlow¹⁵ and Owen¹⁴, similarly to Mulholland et al.²⁴, showed that critical duration is shorter with larger stimulus sizes. Importantly, they also showed that the converse is true, i.e. Ricco's area decreases with longer stimulus durations. This latter piece of evidence is particularly relevant to interpret the results of spatial summation experiments: changes to Ricco's areas would not be expected if the critical number of RGCs only depended on spatial 'hard-wiring' of the visual system, and specifically of retina-V1 connections. Simply put, given this evidence, it seems unreasonable to interpret the results of spatial summation experiments to make inference on RGC-V1 convergence, if the measured critical area changes with stimulus duration. Critically, most of the work on spatiotemporal integration focussed on the use of spatiotemporal receptive fields, which however treat temporal and spatial integration as completely separable and independent^{20, 25}.

1.3. Macular structure-function relationship

Imaging data, usually referred to as 'structural information', and functional data, such as visual acuity or VF sensitivity from SAP, are often acquired to diagnose eye diseases and monitor their progression. Therefore, linking structural and functional measurements is of paramount importance for both clinical and research applications. The macula offers a great opportunity to investigate localised structure-function relationship because of the high level of spatial detail offered by imaging techniques in this region of the retina (see **Figure 1.1**). In some cases, this link is straightforward. For example, in advanced AMD patients who develop geographic atrophy, areas with atrophic photoreceptors and damaged retinal pigmented epithelium show severe functional impairment. Notably, the topography of the

corresponding VF defect will match the atrophic area²⁶. This is often the case for many diseases involving the outer retina. On the other hand, such a close correspondence might be lacking in pathological changes of the inner retina, such as early damage in diabetic patients²⁷ and, most importantly, glaucoma. The reasons are several:

- The inner retina in the macular region has some peculiar anatomical features that make the structure-function link difficult. Mainly, bipolar cells and retinal ganglion cells (RGCs) are radially displaced from the fovea and connected to their corresponding photoreceptors by Henle's fibres (**Figure 1.5**). This implies that the RGCs will not co-localise with their corresponding photoreceptors on the retinal plane, creating a disagreement between the functional and structural mapping²⁸.
- The loss of neurons in diseases involving the inner retina is very often gradual. This highlights the disconnect between structural measurements, usually acquired in the linear scale, and functional measurements, such as perimetry, usually acquired in the logarithmic scale (decibels, dB) for intermediate stages of damage²⁹.
- The residual tissue measured with structural parameters might not contain functional neural units. This is the basis for the so called 'floor effect' in structural measurements²⁹, where a progression in functional damage is observed despite negligible changes in structural parameters.
- The complex elaborations of the visual input performed by the inner retina and along higher levels of the visual system can determine a non-linear relationship between structural and functional changes^{7, 8, 30}.

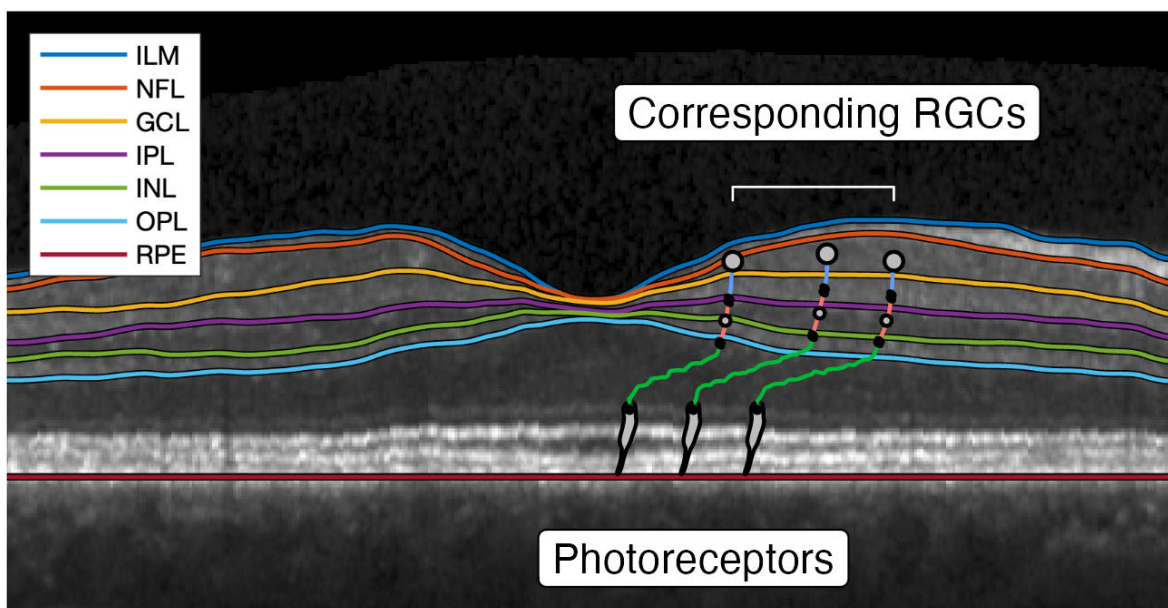


Figure 1.5 Schematic anatomy of the retina. The diagram shows the connections between the photoreceptors and the Retinal Ganglion Cells (RGCs) via Henle's fibres and bipolar cells (whose cell bodies are located in the INL). The B-scan is from a healthy retina. Except for the ILM, all the names refer to the layer above the corresponding line. ILM = Inner Limiting Membrane; NFL = Nerve Fibre Layer; GCL = Ganglion Cell Layer; IPL = Inner Plexiform Layer; INL = Inner Limiting Membrane; OPL = Outer Plexiform Layer; RPE = Retinal Pigment Epithelium.

A plethora of methods and techniques can be used to model the empirical structure-function relationship. These can range from simple linear regression, after accounting for the differences in scale (logarithmic for SAP, linear for structural measures such as tissue thickness)^{29, 31} to complex artificial intelligence techniques^{32, 33}. However, more physiological insight can be gained from the mechanistic modelling of the functional response of a biological substrate, such as the RGC and photoreceptor mosaic, because this provides a link with the underlying processes of damage. This type of modelling has been greatly advanced by the use of computational models^{7, 8}, in-vivo single cell recordings³⁴ and histology studies in human³⁵ and non-human primates³⁶⁻³⁸.

1.4. Objectives of this research

The work presented in the following chapters focuses on modelling the structure-function relationship between perimetric sensitivity and the inner retina in the macula. The research presented in this thesis had three main objectives:

1. To determine the optimal strategies to improve the accuracy of spatial mapping of VF locations tested with perimetry and the corresponding tissue in the inner retina.
2. To develop a computational approach linking spatial and temporal summation of perimetric stimuli to biological structures in the retina, accounting for cortical integration.
3. To apply these modelling strategies to study the mechanisms of inner retinal damage in disease. The two model diseases will be **diabetes** and **glaucoma**.

1.5. References

1. Bowling B. *Kanski's Clinical Ophthalmology*. Eighth edition ed. China: Elsevier; 2016.
2. Yaqoob Z, Wu J, Yang C. Spectral domain optical coherence tomography: a better OCT imaging strategy. *Biotechniques* 2005;39:S6-13.
3. Sample PA, Dannheim F, Artes PH, et al. Imaging and Perimetry Society standards and guidelines. *Optometry and vision science : official publication of the American Academy of Optometry* 2011;88:4-7.
4. Society IaP. 2010 Perimetry Standards. Imaging and Perimetry Society; 2010.
5. Pfau M, Jolly JK, Wu Z, et al. Fundus-controlled perimetry (microperimetry): Application as outcome measure in clinical trials. *Prog Retin Eye Res* 2020;100907.
6. Tyler CW, Chen CC. Signal detection theory in the 2AFC paradigm: attention, channel uncertainty and probability summation. *Vision research* 2000;40:3121-3144.
7. Pan F, Swanson WH. A cortical pooling model of spatial summation for perimetric stimuli. *J Vis* 2006;6:1159-1171.
8. Swanson WH, Felius J, Pan F. Perimetric defects and ganglion cell damage: interpreting linear relations using a two-stage neural model. *Investigative ophthalmology & visual science* 2004;45:466-472.
9. Kwon M, Liu R. Linkage between retinal ganglion cell density and the nonuniform spatial integration across the visual field. *Proc Natl Acad Sci U S A* 2019;116:3827-3836.
10. Choi AY, Nivison-Smith L, Khuu SK, Kalloniatis M. Determining Spatial Summation and Its Effect on Contrast Sensitivity across the Central 20 Degrees of Visual Field. *PLoS One* 2016;11:e0158263.
11. Khuu SK, Kalloniatis M. Spatial summation across the central visual field: implications for visual field testing. *J Vis* 2015;15:15 11 16.

12. Redmond T, Garway-Heath DF, Zlatkova MB, Anderson RS. Sensitivity loss in early glaucoma can be mapped to an enlargement of the area of complete spatial summation. *Investigative ophthalmology & visual science* 2010;51:6540-6548.
13. Sun H, Dul MW, Swanson WH. Linearity can account for the similarity among conventional, frequency-doubling, and gabor-based perimetric tests in the glaucomatous macula. *Optom Vis Sci* 2006;83:455-465.
14. Owen WG. Spatio-temporal integration in the human peripheral retina. *Vision research* 1972;12:1011-1026.
15. Barlow HB. Temporal and spatial summation in human vision at different background intensities. *J Physiol* 1958;141:337-350.
16. Glezer VD. The receptive fields of the retina. *Vision research* 1965;5:497-525.
17. Watson AB. Probability summation over time. *Vision research* 1979;19:515-522.
18. Gorea A, Tyler CW. New look at Bloch's law for contrast. *J Opt Soc Am A* 1986;3:52-61.
19. Swanson WH, Pan F, Lee BB. Chromatic temporal integration and retinal eccentricity: psychophysics, neurometric analysis and cortical pooling. *Vision research* 2008;48:2657-2662.
20. Fredericksen RE, Verstraten FA, van de Grind WA. Spatial summation and its interaction with the temporal integration mechanism in human motion perception. *Vision research* 1994;34:3171-3188.
21. Fredericksen RE, Verstraten FA, Van de Grind WA. Temporal integration of random dot apparent motion information in human central vision. *Vision research* 1994;34:461-476.
22. Fredericksen RE, Verstraten FA, van de Grind WA. An analysis of the temporal integration mechanism in human motion perception. *Vision research* 1994;34:3153-3170.
23. Mulholland P, Redmond T, Zlatkova M, Garway-Heath D, Anderson R. Temporal summation varies with visual field eccentricity for perimetric stimuli scaled to the area of complete spatial summation. *Investigative ophthalmology & visual science* 2013;54:3924-3924.
24. Mulholland PJ, Redmond T, Garway-Heath DF, Zlatkova MB, Anderson RS. Spatiotemporal Summation of Perimetric Stimuli in Early Glaucoma. *Investigative ophthalmology & visual science* 2015;56:6473-6482.
25. Anderson SJ, Burr DC. Spatial summation properties of directionally selective mechanisms in human vision. *J Opt Soc Am A* 1991;8:1330-1339.
26. Pilotto E, Convento E, Guidolin F, et al. Microperimetry Features of Geographic Atrophy Identified With En Face Optical Coherence Tomography. *JAMA ophthalmology* 2016;134:873-879.
27. Montesano G, Gervasoni A, Ferri P, et al. Structure-function relationship in early diabetic retinopathy: a spatial correlation analysis with OCT and microperimetry. *Eye* 2017;31:931-939.
28. Drasdo N, Millican CL, Katholi CR, Curcio CA. The length of Henle fibers in the human retina and a model of ganglion receptive field density in the visual field. *Vision Res* 2007;47:2901-2911.
29. Hood DC, Kardon RH. A framework for comparing structural and functional measures of glaucomatous damage. *Prog Retin Eye Res* 2007;26:688-710.
30. Malik R, Swanson WH, Garway-Heath DF. 'Structure-function relationship' in glaucoma: past thinking and current concepts. *Clin Exp Ophthalmol* 2012;40:369-380.
31. Hood DC, Raza AS, de Moraes CG, Liebmann JM, Ritch R. Glaucomatous damage of the macula. *Prog Retin Eye Res* 2013;32:1-21.
32. Kihara Y, Montesano G, Chen A, et al. Policy-Driven, Multimodal Deep Learning for Predicting Visual Fields from the Optic Disc and OCT Imaging. *Ophthalmology* 2022;129:781-791.
33. Lazaridis G, Montesano G, Afgeh SS, et al. Predicting Visual Fields From Optical Coherence Tomography via an Ensemble of Deep Representation Learners. *Am J Ophthalmol* 2022;238:52-65.
34. Swanson WH, Sun H, Lee BB, Cao D. Responses of primate retinal ganglion cells to perimetric stimuli. *Investigative ophthalmology & visual science* 2011;52:764-771.
35. Harwerth RS, Quigley HA. Visual field defects and retinal ganglion cell losses in patients with glaucoma. *Arch Ophthalmol* 2006;124:853-859.
36. Harwerth RS, Carter-Dawson L, Shen F, Smith EL, 3rd, Crawford ML. Ganglion cell losses underlying visual field defects from experimental glaucoma. *Investigative ophthalmology & visual science* 1999;40:2242-2250.
37. Harwerth RS, Wheat JL, Fredette MJ, Anderson DR. Linking structure and function in glaucoma. *Prog Retin Eye Res* 2010;29:249-271.
38. Anderson RS. The psychophysics of glaucoma: improving the structure/function relationship. *Prog Retin Eye Res* 2006;25:79-97.

2. Revisiting the Drasdo model: implications for structure-function analysis of the macular region

This paper focuses on a fundamental aspect of structure-function analyses of the macula: the correct mapping of perimetric stimuli onto the corresponding area of the inner retina. The parafoveal region is in fact characterised by a radial displacement of the ganglion cells with respect to the photoreceptors they are connected to. This displacement needs to be taken into account in structure-function analyses of the inner retina. This aspect has been explored by other investigators in the past. Most notably, the model proposed by Drasdo et al.¹ is one of the most commonly employed. However, upon starting this research project, we noticed inconsistencies between various schematic eyes used in the development of the displacement model. Moreover, we found out that the model had been applied incorrectly to structure-function analyses in the literature. Finally, the model had been proven hard to replicate, leading many researchers to simply approximate the average displacement from one of the figures in the original paper. This motivated our effort to produce an extended and more accurate version of the model developed by Drasdo et al.¹, as well as to show how this should be applied to structure-function analysis with perimetric stimuli. Finally, we made our results available through an interactive web application, to make the method easily available for other researchers. The revised model was used extensively in the rest of the research presented in this thesis and was fundamental to obtaining correct quantification of the structure-function relationship. The results were published in *Translational Vision Science and Technology (TVST)*, a journal of the Association for Research in Vision and Ophthalmology (ARVO). The paper is freely available at: <https://tvst.arvojournals.org/article.aspx?articleid=2770797>.

Contributions

- *Main contributor*: **Giovanni Montesano** (conceptualisation of research, data and statistical analysis, interpretation of the data, drafting of the manuscript).
- *Other contributors*:
 - **Giovanni Ometto** (data analysis, interpretation of the data, manuscript proofing)
 - **Ruth E. Hogg** (data collection, interpretation of the data, manuscript proofing)
 - **Luca M. Rossetti** (data collection, interpretation of the data, manuscript proofing)
 - **David F. Garway-Heath** (interpretation of the data, manuscript proofing)
 - **David P. Crabb** (supervision, interpretation of the data, manuscript proofing)

2.1. Introduction

The health of the macula is of central importance for everyday functions, such as reading and recognising faces²⁻⁴. It is now recognised that the macula can be affected by glaucoma, even in the early stages of the disease process⁵. Loss and dysfunction of Retinal Ganglion Cells (RGCs) in glaucoma is monitored using both structural and functional measurements. Structural assessment of the macular region can be performed using Spectral Domain

Optical Coherence Tomography (SD-OCT), which provides volumetric measurements of various retinal layers. The layers of most interest for glaucoma are the Retinal Nerve Fibre Layer (RNFL), the Ganglion Cell Layer (GCL) and the Inner Plexiform Layer (IPL). Together, they form the inner retina. RGC loss from glaucoma causes thinning of the RNFL (which contains RGC axons), the GCL (which contains RGC cell bodies) and the IPL (which contains the RGC dendritic arbours).

Functional assessment for glaucoma is typically measured with the visual field (VF) test in the form of Standard Automated Perimetry (SAP). For the macular region, dense testing grids, such as the standard 10-2, are used. The 10-2 spans the central 10 degrees from fixation with a spacing of 2 degrees between test locations. There is some evidence to suggest that these grids are more sensitive to early glaucoma damage in that region when compared to less dense testing grids, such as the 24-2 test pattern.^{5, 6}

Combining structural and functional information should further improve the identification of glaucomatous macular damage and the detection of its progression. Moreover, studying the relationship between the two measurements offers useful insights into the kinetics and pathophysiology of RGC loss and dysfunction in glaucoma^{7, 8}. Models seeking to match structural and functional data to histology measurements of RGC density have been used to explore this relationship⁹⁻¹². Recently, a method proposed by Raza and Hood¹³ has been used to convert the GCL thickness into RGC density in order to investigate the relationship between RGC number and SAP sensitivity^{14, 15} in healthy subjects and glaucoma patients.

The unique features of the inner retina in the macular region need to be considered when comparing structural and functional measurements. The most significant of these is the radial displacement of RGCs from the fovea so that RGCs receiving a stimulus in the parafoveal region are displaced toward the periphery with respect to the location of their corresponding photoreceptors^{1, 16, 17}. RGCs are connected to the corresponding photoreceptors via Henle's fibres, which have an oblique pathway in the parafoveal region. This displacement diminishes with eccentricity, becoming minor at around 10 visual degrees from the fovea^{1, 18}. Different numerical models, based on, or verified by, histological measurements of Henle's fibres have been proposed to account for this displacement^{1, 18-20}. The most widely used of these models is the one proposed by Drasdo et al.¹. This model is valuable in the context of structure-function analyses since the displacement calculation requires equivalence between the cumulative number of RGC Receptive Fields (RGC-RF), estimated through psychophysical measurements, and the number of RGC bodies, estimated through histology¹⁶. Theoretically, when applied correctly, this model would allow a one-to-one correspondence between the number of RGCs, estimated from structural maps, and psychophysical measurements, estimated from SAP sensitivity (which depends on the number of RGC-RFs stimulated during the test).

Although widely used, the implementation of the model reported by Drasdo et al.¹ is not straightforward. For example, Drasdo et al. only reported numerical calculations for the four principal meridians and the average displacement, in microns¹. Therefore, a method to generalise to any arbitrary meridian has not been available. A second example is that the schematic eye used by Drasdo et al.^{1, 21} to convert visual degrees to millimetres of retina assumes a spherical shape for the retina of a certain radius. However, that radius is not the same as that assumed by Curcio and Allen¹⁶ in their published histology map of RGC density. Moreover, the radius of the sphere should be adjusted for the axial length (AL), when this is available. However, Drasdo et al. only provided average displacement values regardless of axial length. A third example is that, in many cases, a simple displacement of the stimulus centres

was applied^{8, 14, 22}. However, the displacement should be applied to the perimeter of the stimulus, so that different points of the stimulus edge are independently displaced radially outward according to the model. For example, in the parafoveal region, the stimulus edge nearer the fovea is displaced further than the stimulus edge further from the fovea^{15, 23}. This is especially important when RGC counts are involved, since small differences in the area used for calculations can result in large differences in the counts.

The objective of our work was to: develop a revised version of the displacement model for any retinal location and with a customisable schematic eye, to account for variations in AL, determine the correct displacement model for circular perimetric stimulus (covering RGC-RFs) to corresponding RGC location. Moreover, we develop a web application to allow researchers to apply the revised model to their own structure-function data, in an attempt to improve the comparability of findings from different research groups.

2.2. Methods

2.2.1. Datasets

For our analyses we used two datasets. The first (Dataset 1) was a collection of macular volume scans collected for the Northern Ireland Sensory Ageing (NISA) study (<https://clinicaltrials.gov/ct2/show/NCT02788695>), which originated from a population based aging cohort (NICOLA study <https://www.qub.ac.uk/sites/NICOLA/>) conducted in Belfast at Queen's University, Belfast. Scans were acquired with a Spectralis SD-OCT (Heidelberg Engineering, Heidelberg, Germany) comprised 61 horizontal B-scans centred on the fovea (ART 9, 30 x 25 degrees with a fixed 7 degree rotation, counter-clockwise for right eyes, clockwise for left eyes). In this dataset, 417/726 scans were classified as having a healthy outer retina by 2 graders. In 299 of these eyes, AL was measured using a Lenstar LS 900 Biometer (Haag-Streit AG, Switzerland). These scans were further screened by an ophthalmologist (GM) for pathological changes of the inner retina. Seventeen scans were excluded because of poor quality that prevented a clear identification of the inner retinal layers or the Bruch's membrane within 15 degrees from the fovea, 13 scans had local thinning that could be attributed either to glaucoma or local ischemia and four were excluded for vitreoretinal alterations. The segmentation of the retinal layers was checked and manually corrected where necessary leaving 265 scans for analysis. This dataset was used exclusively to extract metrics on the shape of the GCL profile. No thickness values were measured. The median [Interquartile range] Quality Index (QI) was 30.6 [28.98, 32.26] dB.

The second dataset (Dataset 2) was a collection of SD-OCT scans acquired for a cross-sectional study on structure-function relationship in the healthy macula. The study was approved by the ethical committee Comitato Etico Milano Area 1 (code OCU_SSSF) and the data collection took place at the eye clinic at San Paolo Hospital (University of Milan) in Milan, Italy. The dataset included 28 macular scans from 28 subjects collected with a Spectralis SD-OCT and composed of 121 B-scans, centred on the fovea (ART 9, 25 x 30 degrees, oriented vertically). AL was measured using an IOL-Master V3 A-scan (Zeiss Meditec, Dublin, CA). The subjects had no known or detectable ocular disease and younger than 40 (range 23 – 37) years, to match the age range of the histological dataset collected by Curcio and Allen¹⁶ (see next section). Descriptive statistics for the two datasets are given in **Table 2.1**. Best Corrected Visual Acuity (BCVA) in Dataset 2 was 0.00 logMAR for all subjects and was

not measured further. All data collections were performed in agreement with the declaration of Helsinki after explicit written consent from the participants. All scans were of good quality and none was excluded (QI = 26.47 [25.36 – 27.47] dB).

	Dataset 1 (N = 265)	Dataset 2 (N = 28)
Median [Interquartile range]		
Age (years)	58 [63, 68]	28 [26, 31]
Male : Female	134 : 131	15 : 13
BCVA (Letters)	89 [85, 92]	-
Spherical equivalent (Diopters)	0.5 [-0.5, 1.5]	-1.19 [-3.50, 0]
Axial length (<i>mm</i>)	22.94 [23.67, 24.34]	24.50 [23.89, 25.02]
Average macular GCL thickness (μm)*	33.34 [31.36, 35.39]	35.73 [33.89, 37.64]

Table 2.1 Descriptive statistics for relevant variables in the two datasets BCVA = Best Corrected Visual Acuity. * Calculations performed on the whole thickness map within 3.5 *mm* from the fovea.

2.2.2. Histology map

The original model developed by Drasdo et al.¹ used the histology map provided by Curcio and Allen¹⁶. This reports the density of ganglion cells (cells/mm^2) obtained from six retinas of five healthy subjects, aged 27 - 37 years (range), for a retinal sphere with a radius of 11.459 *mm*. Details are reported in **Appendix 1**.

2.2.3. Schematic eye

The schematic eye used in this work replicated the one described by Drasdo and Fowler²¹ and later used by Drasdo et al.¹ for their displacement model. We used numerical ray tracing through the schematic eye to calculate the correspondence between visual degrees and *mm*, and solid visual angle (degrees^2) and mm^2 , on the retina. The data to build the schematic eye was derived from the table reported in the original paper²¹. Importantly, this approach aligns with the original methodology unlike that applied in previous studies^{18, 19}. Note the radius of the retinal sphere has been changed to match the one used for the histology map ($r_0 = 11.459 \text{ mm}$, originally 11.06 *mm* in Drasdo and Fowler²¹). The distance between the centre of the retinal sphere and the corneal vertex has also been scaled proportionally ($c_0 = 12.38 \text{ mm}$, originally 11.95 *mm*). Therefore, the default AL (AL_0) of our schematic eye was 23.84 *mm* (originally 23.01 *mm*). These changes had a small impact on the degrees-to-*mm* conversion, but a more important effect of the $\text{mm}^2/\text{solid degree}$ ratio (**Figure 2.1**). The schematic eye was coded in Matlab (The MathWorks, Natick, USA). Additional details are reported in **Appendix 2**.

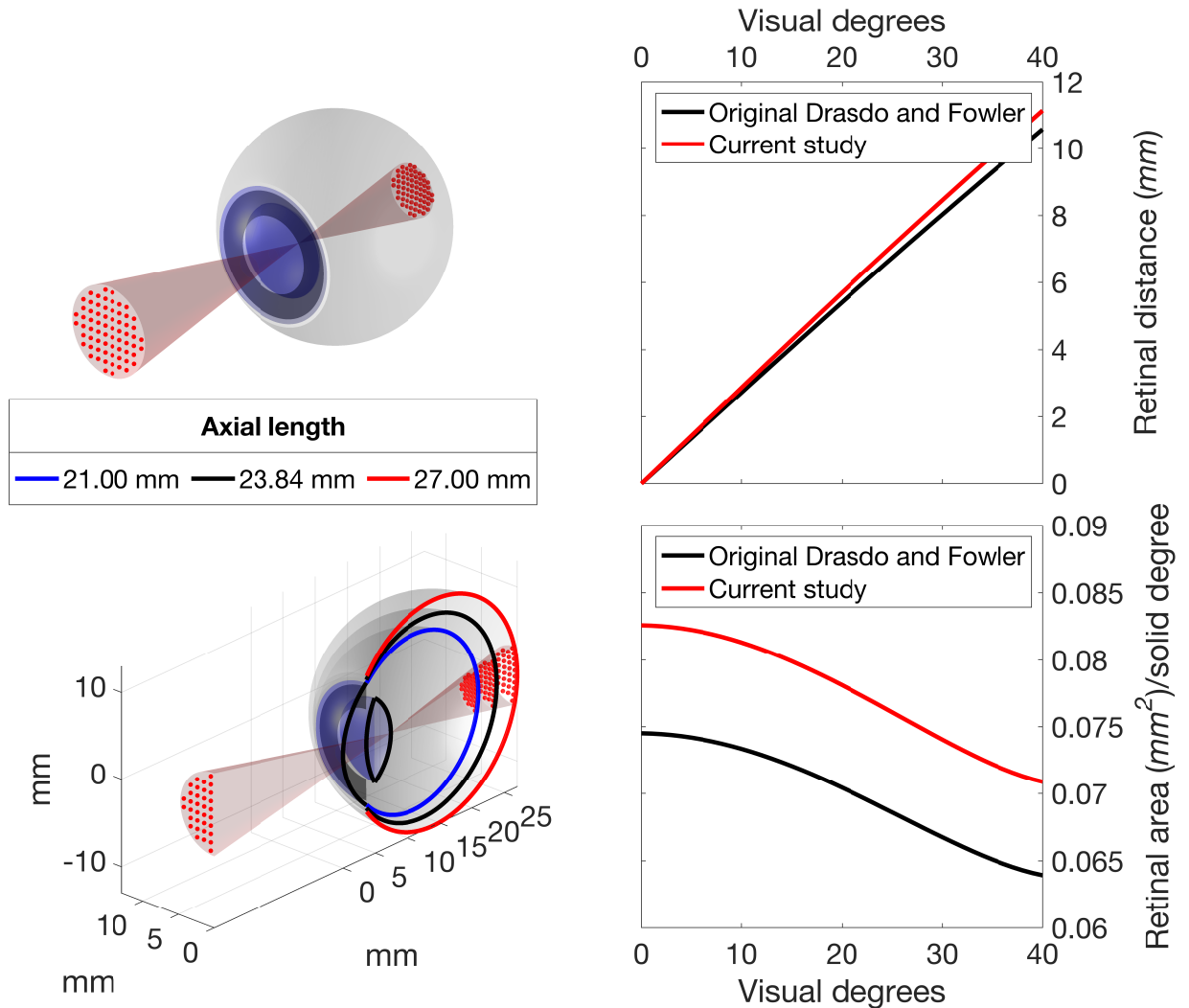


Figure 2.1 Rendering of the schematic eye, with a projection of a 10-2 grid (red dots, top panel). The bottom panel shows a cross section of the same schematic eye with additional examples of short and long axial lengths. Right panels show the distance travelled on the retina per visual degree (top) and the $mm^2/solid\ degree$ ratio at various retinal eccentricities (bottom). The latter represents the ratio between retinal areas in mm^2 to visual degrees². The curved relationship with eccentricity is a consequence of the nonlinear projection obtained by numerical calculations of ray tracing through the cornea, lens and vitreous, which varies with visual angle. It is important to acknowledge that the relationship between retinal mm and degrees of visual angle is also not linear. In black, the curves obtained from the original schematic eye described by Drasdo and Fowler²¹ (in black). In red, the results of the schematic eye used in this study.

2.2.4. Scaling of eye structures and cell density

A customised displacement model must account for how retinal structures scale with AL, especially the size of the displacement area (see later) and the planar density of ganglion cells derived from histology. The assumption of a spherical shape for the retina for all ALs is prone to the adoption of a global expansion model. In this model, the planar RGC density would scale inversely with the square of the retinal radius, whereas the radius of the displacement zone ($r_{DZ} = 4.034\ mm$ in the original paper¹) would scale linearly with the retinal

radius. The two scaling equations, where r is the retinal radius corresponding to a given AL, are given as:

$$r_{DZ}(AL) = 4.034 * \left(\frac{r}{r_0}\right) \quad (2.1)$$

$$RGC\ Density(AL) = RGC\ Density(AL_0) * \left(\frac{r_0}{r}\right)^2 \quad (2.2)$$

An alternative model to the assumption of global expansion is ‘equatorial stretch’, where the posterior pole is simply moved further away from the corneal vertex with no change in the relative size of the retinal structures. Although the actual expansion process in myopia is likely to be a mixture of the two phenomena²⁴⁻²⁶, psychophysical evidence suggests that a global expansion model is a reasonable approximation for most axial lengths²⁷⁻³⁰. Global expansion is also implied in the RGC-RF model proposed by Drasdo et al., which assumes a constant density of RFs per solid visual degree¹ (see later).

A global expansion model also implies that the amount of radial RGC displacement, when measured in mm on the retina, should increase with axial length. This is a consequence of the stretching of the retinal tissue and Henle’s fibres with increasing eye size. Although direct evidence of this is not yet available, indirect confirmation can be obtained by observing how the GCL profile scales with axial length in healthy eyes. To explore this, we used the 265 macular volume scans from Dataset 1 and identified the maximum GCL thickness peak for several meridians, centred on the anatomical fovea (**Figure 2.3**). An ellipse was then fitted through a least-squares method to the locations of the peaks. We then measured the length of the major and minor axes of the ellipse. All measurements were corrected for ocular magnification using the schematic eye defined in the previous section. The relationship between the length of the ellipse axes and the axial length was explored through linear regression. The ellipse dimensions were also predicted for an exact scaling with axial length, assuming a global expansion, by multiplying the ellipse dimensions predicted from the linear regression at AL_0 by the same scaling factor used for the r_{DZ} (geometric scaling model). The goodness-of-fit of the linear regression and the geometric scaling model were compared using the Mean Absolute Error (MAE), calculated for each model as the average of the absolute residuals.

2.2.5. OCT data processing

All OCT data were exported as RAW files (.vol) using the Heidelberg Eye Explorer. The files were then imported in Matlab using a custom routine. The segmentations were then used to generate thickness maps for the whole retina and the GCL. The maps were interpolated and smoothed to match the size of the reference infrared fundus image (768 x 768 pixels, 30 x 30 degrees field of view), padding with zeros where the OCT data were missing, i.e. outside the scanning pattern. The interpolation was performed using a thin plate spline (*tpaps* function in Matlab) with anisotropic smoothing parameters, so that smoothing was stronger across B-scans than within a B-scan. The fovea was automatically identified through a template matching. Correct detection was confirmed through visual inspection.

2.2.6. Conversion of GCL thickness maps into estimated RGC counts

We used the method proposed by Raza and Hood¹³ to convert the OCT GCL thickness maps into customised estimates of RGC density and applied this to Dataset 2. In brief, the histology map was divided point-by-point by an average healthy GCL thickness map (768 x 768 pixels), obtained as the average from all eyes in Dataset 2, after aligning the fovea and the position of the optic nerve head (ONH). This yielded a volumetric density map (RGC/mm³). The map can then be multiplied point-by-point by a GCL thickness map from a new subject to obtain a customised RGC density map (RGC/mm²). We accounted for AL by applying a magnification correction to the GCL macular volume scans and by rescaling the histology density map according to the global expansion model given by equation (2.2).

2.2.7. Displacement model

For the displacement model, we followed the same methodology proposed by Drasdo et al. in their original paper¹. The first step was to calculate the RGC-RF density along a specific meridian obtained from a generic model based on psychophysical measurements, the derivation of which is described in detail in the original paper. The final formula, where e is the eccentricity in visual degrees, D_{gcrf} is the density of RGC-RF (number/solid degree), $R_v = 0.011785$ and $R_o = 0.008333$ and k is a parameter that depends on eccentricity (see Appendix 3), is given as:

$$D_{gcrf}(e) = \frac{k * (1.12 + 0.0273 * e)}{1.155 * \left(\left(R_v \left(1 + \frac{e}{E_{2v}} \right) \right)^2 - \left(R_o \left(1 + \frac{e}{20} \right) \right)^2 \right)}. \quad (2.3)$$

The parameter E_{2v} in equation (2.3) was used by Drasdo et al. to scale the RGC-RF for each principal meridian¹. A key objective of our new approach was to determine its value for any arbitrary meridian. Similarly to Drasdo et al.¹, we performed a numerical optimization of this parameter by simply requiring that the total counts of RGC-RF and RGC bodies are equal within the maximum displacement zone (DZ). From Drasdo et al.¹, the DZ ends at 4.034 mm from the fovea and is assumed symmetric. This value was used for AL_o and was scaled proportionally with the retinal radius for different axial lengths, as previously explained. The displacement is finally computed as the difference between the eccentricities at which the cumulative count of RGC bodies (C_{gcb}) and the cumulative count of RGC-RF (C_{gcrf}) are equal. Additional details are reported in **Appendix 3**.

2.2.8. Displacement of perimetric stimuli

We compared two methods of applying the Drasdo model to perimetric stimuli. The first commonly-applied method¹⁴ (Method 1) consisted of a simple displacement of the centre of the stimuli, without any changes to its shape (**Figure 2.2**, left panel). In the alternative method (Method 2), the circumference of the stimulus (approximated with 72 points around the stimulus edge) is displaced according to the Drasdo model; this results in distorted stimulus shapes in the parafoveal region (**Figure 2.2**, right panel). We tested the accuracy of each method by requiring consistency under the Drasdo model. In fact, the model calculates the displacement by equating the number of expected RGC-RF and the number of RGC bodies at any given eccentricity (in a healthy eye). Therefore, the estimated number of RGC-RF within a given stimulus area should match the number of RGC bodies within the

displaced stimulus on the structural map, besides some minimal discrepancy due to approximation errors in the numerical calculations. For our calculations, we used a 10-2 grid and calculated the number of RGC-RF and cellular bodies for all conventional Goldman sizes, from I to V. The RGC-RF density function can change for each meridian. Hence, we generated a dense map with the same resolution as the structural map and used binary masks to calculate the number of RGC-RFs within each stimulus size. The same methodology was applied to the displaced stimuli on the structural map. The resolution used for our calculations was 2.2 μm (0.008 degrees) for the histology map and 0.0391 degrees for the structural maps in Dataset 2 (the maximum resolution of the Spectralis SD-OCT). This mainly affected the precision of the binary masks, which is important for small stimulus sizes. For the first analysis, we aimed for a very precise quantification to test the theoretical validity of the two methods. For the second analysis, we used a resolution that is likely to be applied for real data as a compromise between precision and speed of calculation.

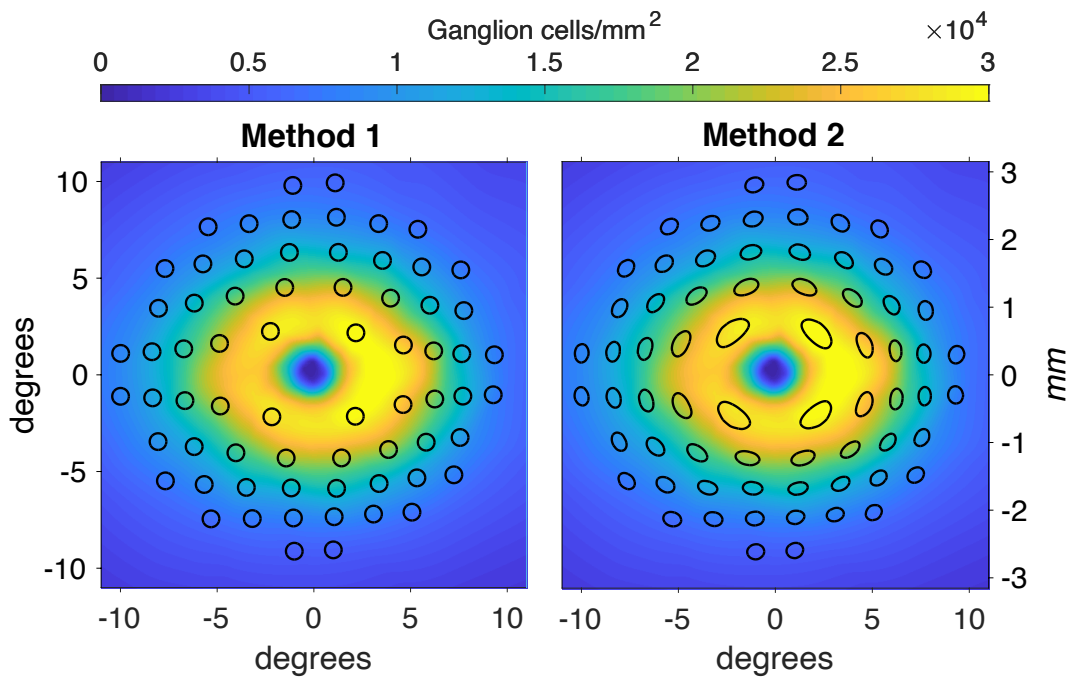


Figure 2.2 Representations of the two candidate methods to apply the displacement to perimetric stimuli. Method 1 is the one applied by Yoshioka et al.¹⁴. Method 2 is the one proposed in this paper. The colour map represents the histology density at AL0 for both graphs. The vertical axes are reported both in mm and visual degrees. The black shapes represent the areas tested by a 10-2 perimetric test, displaced with the two methods. In both images we are displaying the results of the application of the two methods on Goldmann IV stimuli, assumed circular and arranged in a regular 10-2 grid.

2.2.9. Development of the web App

A web application (App) was developed using the Shiny library³¹ for R³² (R Foundation for Statistical Computing, Vienna, Austria). The App is freely available at https://giovannimontesano.shinyapps.io/Shiny_Drasdo_Montesano_et_al/, with detailed explanations on its use. It allows the visualisation of the schematic eye and the calculation for the RGC displacement. It can also import structural maps and provide calculations for different stimulus sizes. Finally, it can also be used for batch processing of a whole dataset.

The Matlab codes for the schematic eye and the displacement model were translated in R. For faster computational execution, the displacement was pre-calculated for different *ALs* (from 18 to 35 *mm*, at 0.5 *mm* intervals). The planar displacement maps were calculated out to 7.5 *mm* from the fovea, at 0.05 *mm* intervals, then organised in a dense three-dimensional array. The displacement values are then obtained via linear interpolation of the array.

2.3. Results

2.3.1. Scaling of eye structures with axial length

The calculations were performed on the eyes from Dataset 1. Both axes of the ellipses correlated negatively with *AL* before magnification correction (major axis MAE = 0.149 *mm*, $p < 0.001$; minor axis MAE = 0.111 *mm*, $p < 0.001$) and positively after magnification correction (major axis MAE = 0.148 *mm*, $p < 0.001$; minor axis MAE = 0.112 *mm*, $p < 0.001$). A geometric scaling model offered a very similar fit (major axis MAE = 0.175 *mm*; minor axis MAE = 0.131 *mm*). The results are presented in **Figure 2.3**.

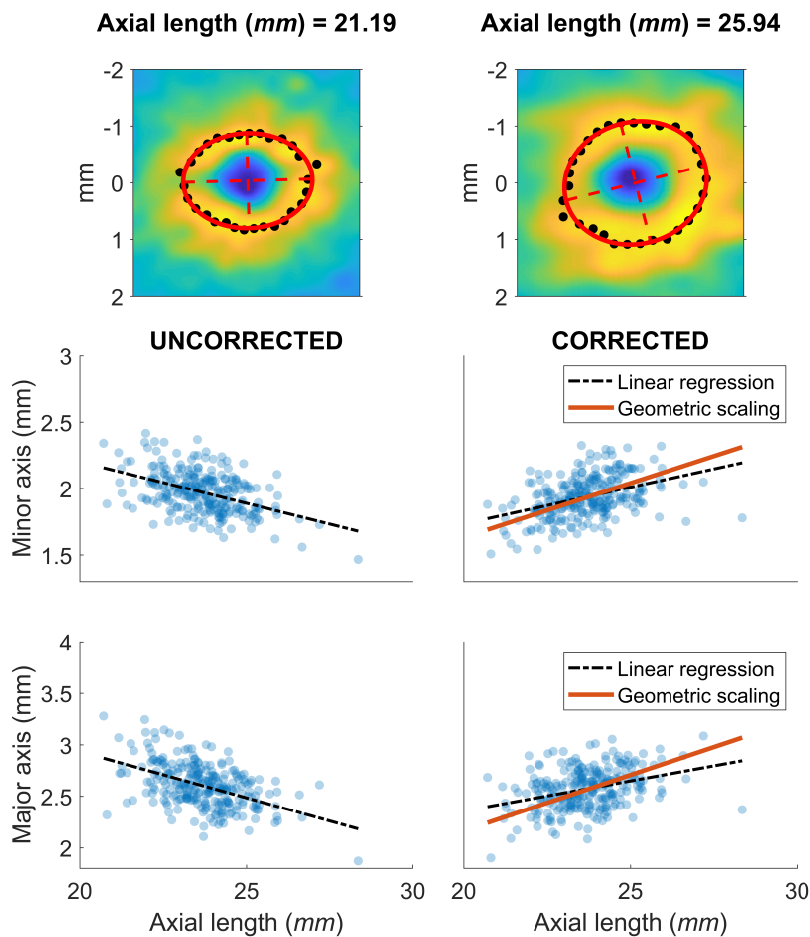


Figure 2.3 Scaling of ocular structures with axial lengths. Top panels show two examples of the calculation for the descriptive ellipses (in red), as described in the Methods. The black points identify the peaks in the GCL profile used for the fitting. Lower panels show the measurements of the major and minor axis of the ellipses before (left) and after (right) correction for ocular magnification.

2.3.2. Variability of displacement with axial length

Results of the fitting process for the parameter E_{2v} are reported in **Figure 2.4 A**. Values are very similar to those reported by Drasdo et al.¹ for the principal meridians for all considered ALs. The systematic change with axial length was small (**Figure 2.4 A**). The displacement is constant for all axial lengths when measured in degrees, as a consequence of the global expansion mechanism assumed by the model. **Figure 2.4 B** shows the displacement in degrees and in *mm* for AL_0 . The values in *mm* are very similar to the average displacement reported by Drasdo et al.¹.

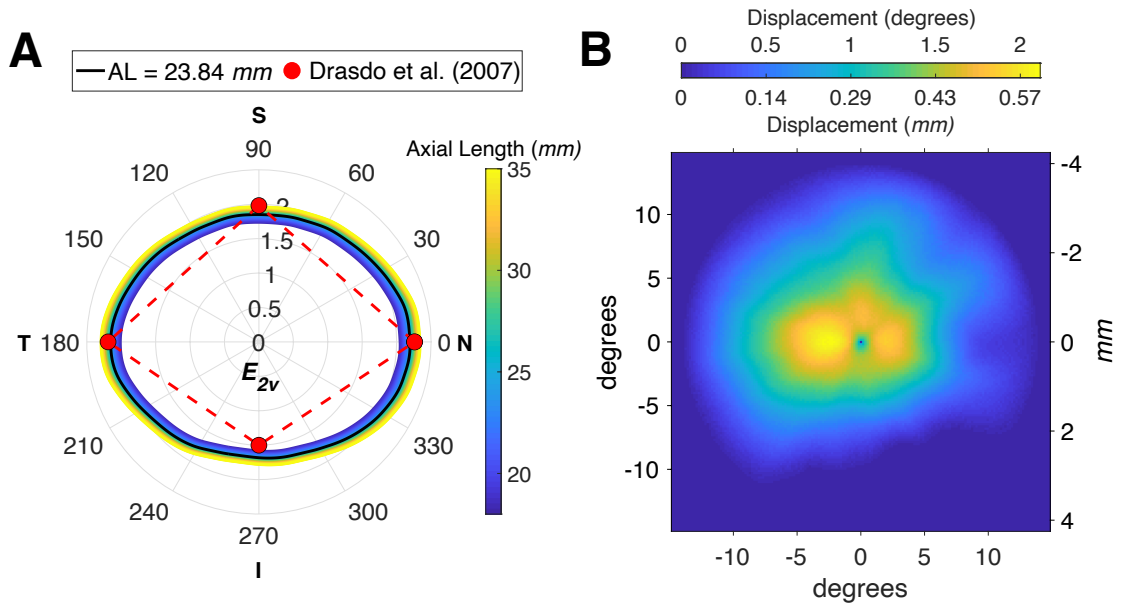


Figure 2.4 Fitting results A) Polar plot of the results of the fitting process for the parameter E_{2v} . N = Nasal; S = Superior; T = Temporal; I = Inferior. B) Displacement map calculated in degrees and *mm* at AL_0 .

2.3.3. Displacement of perimetric stimuli

Average density values (per solid degree) at different eccentricities are reported in **Table 2.2** (calculated from the counts for the G-IV stimulus size). Method 1 yielded substantial underestimation of the RGC body counts in the parafoveal region, where the displacement is largest, and a slight overestimation at larger eccentricities (**Figure 2.5** and **Table 2.2**). Conversely, Method 2 provided estimates that were very consistent with the expected number of RGC-RF. The slightly larger variability with a G-I stimulus was due to numerical approximation and completely disappears for larger stimulus sizes. When converted to dB units (**Figure 2.5**), the calculations with Method 1 yield similar results to those reported by Yoshioka et al.¹⁴ for healthy subjects. The same method was applied to the healthy macular volume SD-OCT scans in Dataset 2 (**Figure 2.6** and **Table 2.2**). The results were very similar to those obtained with the RGC histology map.

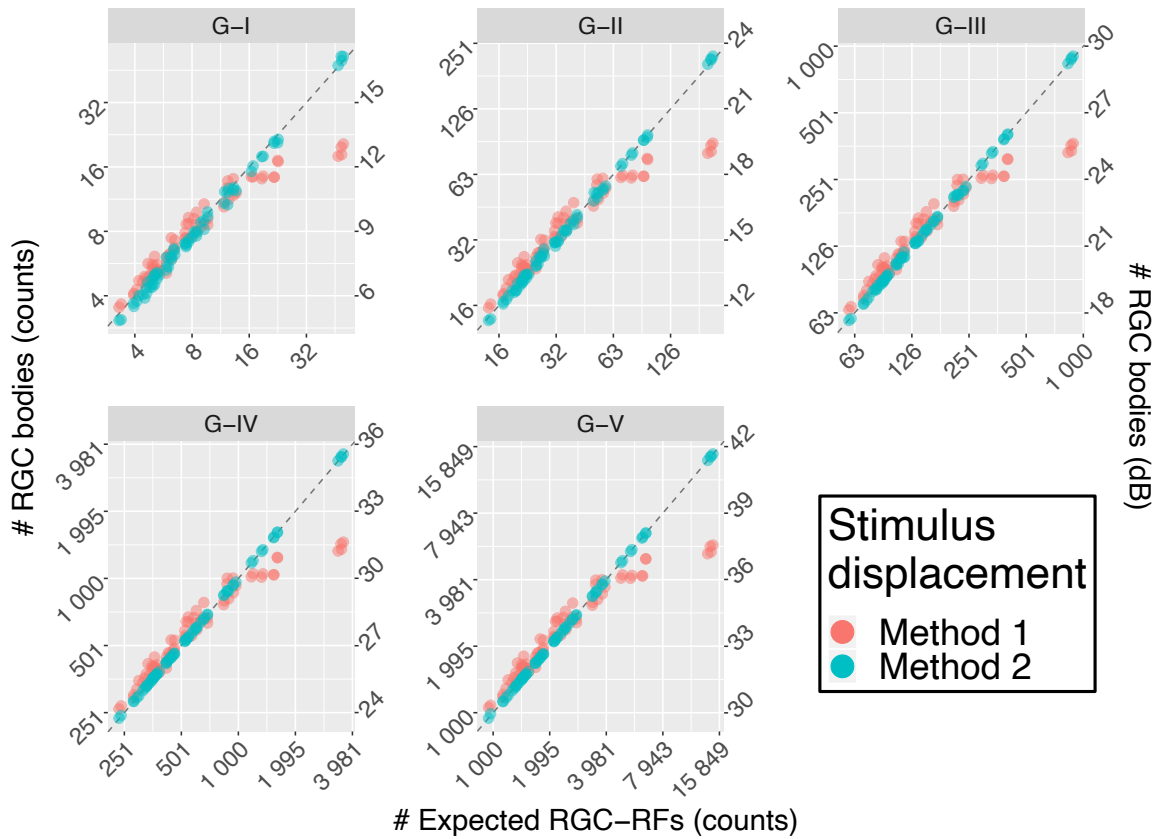


Figure 2.5 Comparison of the results between the two displacement methods for perimetric stimuli. Method 1 is the one used by Yoshioka et al.¹⁴. Method 2 is the one proposed in this paper. The horizontal axis reports the expected RGC-RF counts, calculated from the model proposed by Drasdo et al.¹, (equation (2.3)) and do not represent real subject data. The vertical axis reports the structural measurements from the RGC map both as counts (left axis) and in dB (right axis). The latter is meant for easier comparison with the results in Yoshioka et al.¹⁴. Only Method 2 yields correct estimates in the parafoveal region (higher counts). The dashed line represents the ideal line of equivalence.

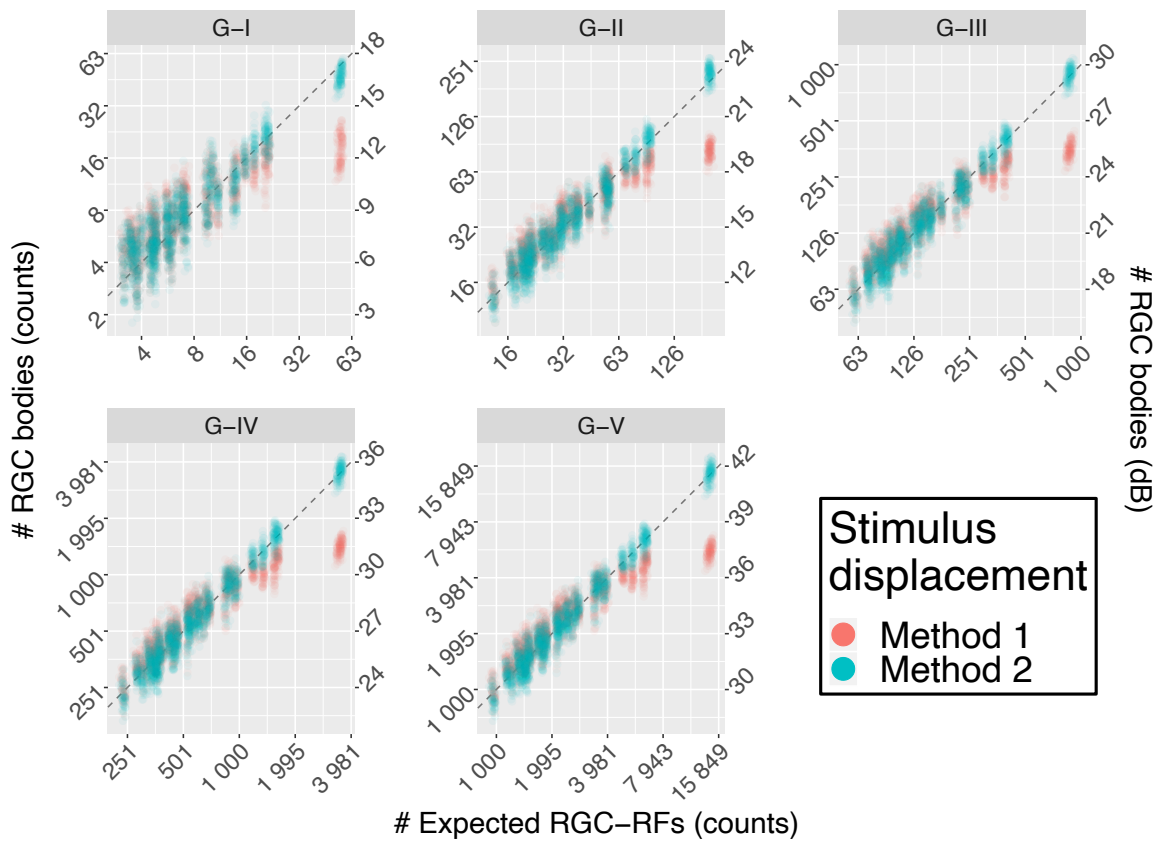


Figure 2.6 Comparison of the results between the two displacement methods for perimetric stimuli for real structural data. Method 1 is the one used by Yoshioka et al.¹⁴. Method 2 is the one proposed in this paper. The horizontal axis reports the expected RGC-RF counts, calculated from the model proposed by Drasdo et al.¹, (equation (2.3), adjusted for AL). The vertical axis reports the structural measurements from the RGC map both as counts (left axis) and in dB (right axis). The latter is meant for easier comparison with the results in Yoshioka et al.¹⁴. Only Method 2 yields correct estimates in the parafoveal region (higher counts). The dashed line represents the ideal line of equivalence.

	Eccentricity (degrees)	RGC-RF density	RGC body density	
			Method 1	Method 2
RGC his- tology map	1.41	5969 (157)	2392 (105)	5998 (173)
	3.16	2435 (307)	1868 (165)	2433 (304)
	4.24	1609 (58)	1551 (143)	1596 (62)
	5.1	1288 (210)	1332 (234)	1292 (212)
	5.83	1026 (90)	1097 (120)	1028 (90)
	7.07	783 (116)	861 (154)	785 (116)
	7.62	689 (91)	753 (94)	690 (91)
	8.6	560 (39)	609 (40)	560 (39)
	9.06	540 (102)	589 (114)	542 (102)
Database 2	1.41	5975 (145)	2424 (211)	6085 (566)
	3.16	2445 (291)	1894 (243)	2476 (388)
	4.24	1623 (54)	1520 (191)	1576 (180)
	5.1	1295 (199)	1343 (268)	1306 (269)
	5.83	1040 (87)	1105 (159)	1035 (152)
	7.07	790 (112)	859 (188)	782 (168)
	7.62	696 (87)	753 (132)	691 (127)
	8.6	568 (38)	614 (92)	563 (90)
	9.06	541 (97)	591 (146)	545 (133)

Table 2.2 Density data at different eccentricities of the 10-2 grid, derived from the counts reported in Figure 2.5 and Figure 2.6 for a G-IV stimulus size. Values are reported as Mean (SD). For the RGC histology map, the SD refers to different locations with the same eccentricity.

2.4. Discussion

In our work we revisited the RGC displacement model proposed by Drasdo et al.¹ and studied its application to perimetric data to yield consistent structure-function measurements. We also developed a web App to make our methodology easily available for other researchers, in the hope to standardise this essential aspect of structure-function analyses.

Our implementation generalised the displacement model to any arbitrary meridian. Compared to other models^{19, 20} we imposed weaker constraints on the symmetry of the displacement. The model proposed by Sjöstrand et al.²⁰ used histological measurements to derive an even displacement around the fovea. Watson¹⁹ followed an approach similar to Drasdo et al.¹, but used a different equation for the RGC-RFs and extended his calculations to arbitrary meridians by assuming an elliptical symmetry around the fovea. In contrast, our approach, as in the original paper, only assumes the maximum displacement to be the same for all meridians in the fitting process. However, as shown in **Figure 2.4 B**, such an assumption does not prevent the displacement from adapting to the measured distributions of RGC cells provided by histology. Importantly, the effective RGC displacement region extends to smaller eccentricities in the inferior retina. A similar approach for generalisation of the Drasdo model has been proposed by Turpin et al.¹⁸. Our results were in general agreement; they also showed a smaller extent of the displacement inferiorly compared to other regions.

However, the displacement for the parafoveal locations was smaller in our calculations and in good agreement with the average displacement calculated by Drasdo et al.¹. In addition to previous work, we implemented a numerical ray tracing model of the schematic eye used by Drasdo and Fowler²¹ to convert between visual degrees and distances on the retinal sphere. This allowed us to adapt the model so that the retinal sphere corresponded to the one used for the retinal histology map built by Curcio and Allen^{16, 33}. This is crucial to obtain consistent calculations, since the Drasdo model is based on that map. The implementation of the numerical model also allowed us to customise the conversion and the RGC density map based on the axial length. In this study, we assumed a global expansion model, scaling the linear structures with the radius of the retinal sphere and the density with the squared radius; this has been shown to be a good approximation by psychophysical examinations²⁷⁻³⁰. Additionally, we confirmed this by observing how the structure of the inner retina scales with axial length using a large dataset of SD-OCT data (**Figure 2.3**). We found that geometric scaling for axial length fitted the observed data adjusted for ocular magnification. Under this assumption, the displacement is conveniently equivalent for all axial lengths when calculated in degrees of visual angle. However, competing models have been proposed for eye growth in myopia and an elliptical growth model, combining equatorial stretching and global expansion, seems to be the most realistic from anatomical studies²⁴⁻²⁶. One advantage of our numerical implementation of the schematic eye is that it can be easily adapted to accommodate for different types of expansion models. One major limitation of our structural dataset was the lack of extreme axial lengths. Determining the optimal expansion model with a stratified data collection of structural and functional data will be the objective of future work.

Our work was novel because it considered two different methods of applying the displacement to perimetric stimuli in structure function analyses. We showed that simply displacing the stimulus centre (Method 1) does not provide estimates of RGC-RF counts within perimetric stimuli consistent with the counts expected from the Drasdo model. Instead, each point on the edge of the perimetric stimulus needs to be displaced independently (Method 2), resulting in distorted, ovoidal shapes. We were able to verify the validity of this approach by requiring that the RGC counts within a given displaced stimulus from the histology map be consistent with the expected RGC-RF counts assumed by the Drasdo model (equation (2.3)). Only Method 2 yielded correct estimates (**Figure 2.5**). We then verified that these results hold when the two methods are applied to structural data from young healthy subjects (**Figure 2.6**). The increase in variability in this latter analysis was due both to intra-subject differences in the structural data and to the fact that the calculations were limited to the resolution of the structural maps, as explained in the Methods. Method 1 is similar to what was used by Yoshihoka et al.¹⁴. Unfortunately, those authors did not report tabulated RGC counts or estimated density. Nevertheless, the graphs reported in their paper in **Figure 2**¹⁴ clearly show counts that, in healthy subjects, are compatible with the results of Method 1. For example, the largest RGC counts for a G-III stimulus were approximately 25.6 dB, very similar to our results in **Figure 2.5** and **Figure 2.6** for Method 1 (25.5 dB). In turn, this was crucially less than half than that derived from Method 2 (29.5 dB) and the expected RGC-RF count from equation (2.3) (29.4 dB). Moreover, the RGC-RF density derived from Method 1 for the smallest eccentricity (1.41 degrees, **Table 2.2**), when substituted into equation (2.3) to derive the corresponding visual acuity (with $E_{2v} = 2$), yields a value of 16.5 cycles/degree, unreasonably low for this eccentricity¹. In contrast, Method 2 yields 24.5 cycles/degree, much closer to the predicted 24.9 cycles/degree¹ and compatible with the

literature³⁴. These discrepancies might also be due to the fact that Yoshioka et al.¹⁴ provided age corrected structural and functional measurements at 64.5 years of age. However, the boxplots in the supplementary material for the same paper show minimal changes between age corrected and raw thickness values, too low to justify such a large difference.

Our findings are of particular importance for the interpretation of previously published results. To the extent of our knowledge, Method 2 has only been applied twice in the literature^{15, 23}. Moreover, the actual methodology to implement the Drasdo model has been rarely reported. In many cases, the displacement appears to be symmetrical around the fovea^{8, 14, 22, 35-38}. This likely indicates an application of the average displacement profile presented in the graph from Figure 2 in the original paper by Drasdo et al.¹, using a fixed degrees to *mm* conversion. Although this might be satisfactory for some simple correlation analyses, disregarding the asymmetric nature of the displacement limits studies where a more detailed structure-function relationship is sought. For instance this is important when the development of a neural model of functional response is the main goal of the research¹⁴. In fact, as shown by our results in **Figure 2.6**, a high degree of consistency with the calculations can be achieved, especially considering that, like the Drasdo displacement model, the method to estimate the number of RGC cell bodies from structural measurements¹³ is also based on the structural map produced by Curcio and Allen¹⁶.

To encourage translation, we have made our methodology available for researchers in a free user-friendly web App (**Figure 2.7**, <https://relayer.online/drasdo>). The App allows for a straightforward and customisable application of the displacement model for different axial lengths, any perimetric grids, varied stimulus sizes and structural maps. Graphical outputs are designed to provide the researcher with tools to scrutinise the steps in the process. Batch analysis can also be done on large datasets. The App will be updated with future development of the methodology; for example, when a more comprehensive expansion model is developed.

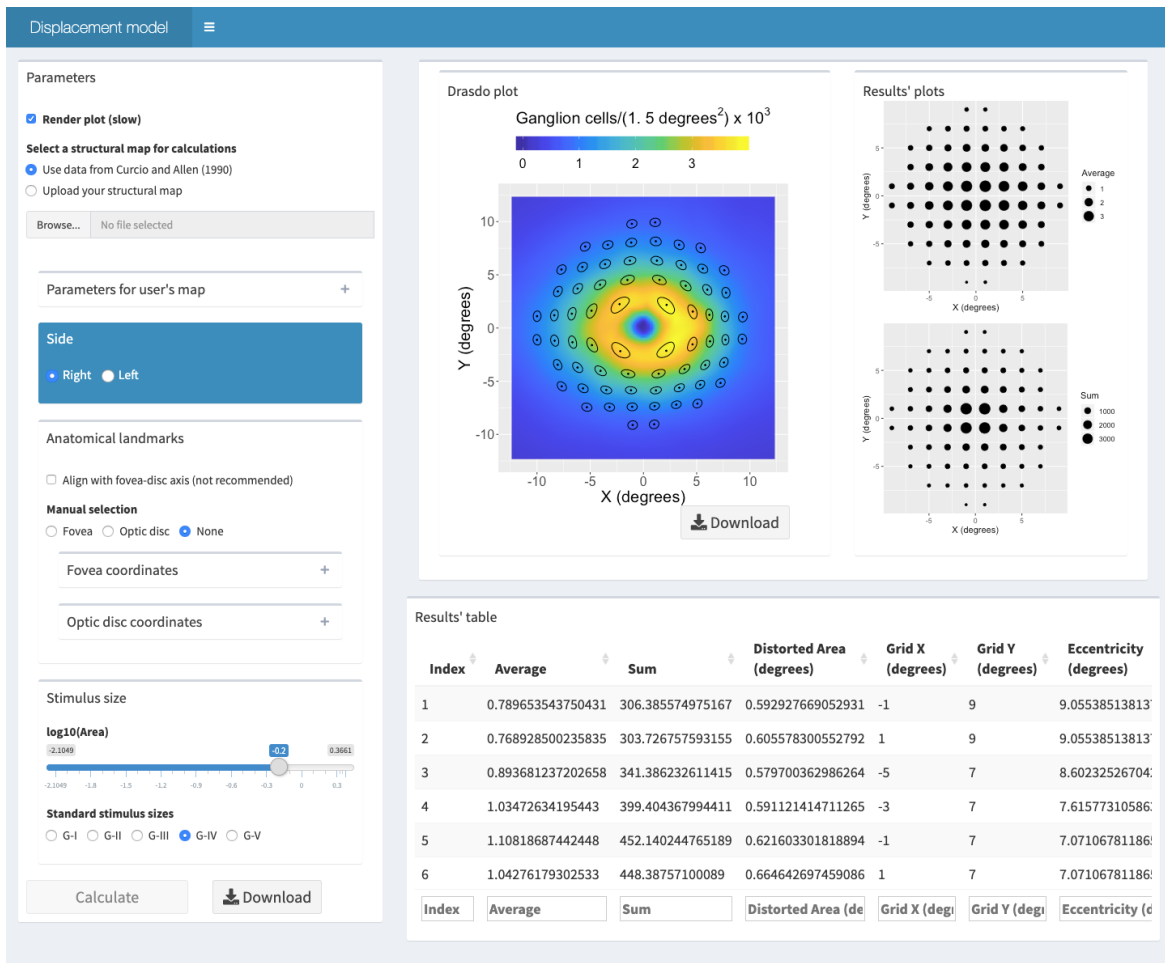


Figure 2.7 Screenshot of the second screen from the web App It presents the results for the schematic eye at AL_0 , for a G-IV stimulus size and a 10-2 perimetric grid using the histological dataset by Curcio and Allen as a structural map. The Results table extends beyond what is visible on the screen and can be easily downloaded.

2.5. Appendix

2.5.1. Appendix 1

As described in a separate paper³³, the data were recorded by Curcio and Allen using spherical coordinates, reporting co-latitude (or retinal eccentricity) and longitude (or retinal meridian) in degrees. Eccentricity is calculated from the fovea, located at (0, 0). One degree of retinal eccentricity equals $2\pi r/360$ arc length, where r is the radius of the assumed retinal sphere. From the header of the text file containing the tabulated data (<https://research-materials.christineacurcio.com/>), the assumed retinal sphere for the map is 11.459 mm. The map is built for a left eye, with the ONH at 20° eccentricity on the horizontal meridian (180° longitude). After conversion to mm, a continuous histology map was obtained through cubic interpolation. **Figure 2.8** shows the correspondence between the interpolated values and the original average counts (with standard deviations) provided by Curcio and Allen (<https://research-materials.christineacurcio.com/>) for the four principal meridians. The map was converted into a right eye by inverting the horizontal coordinates.

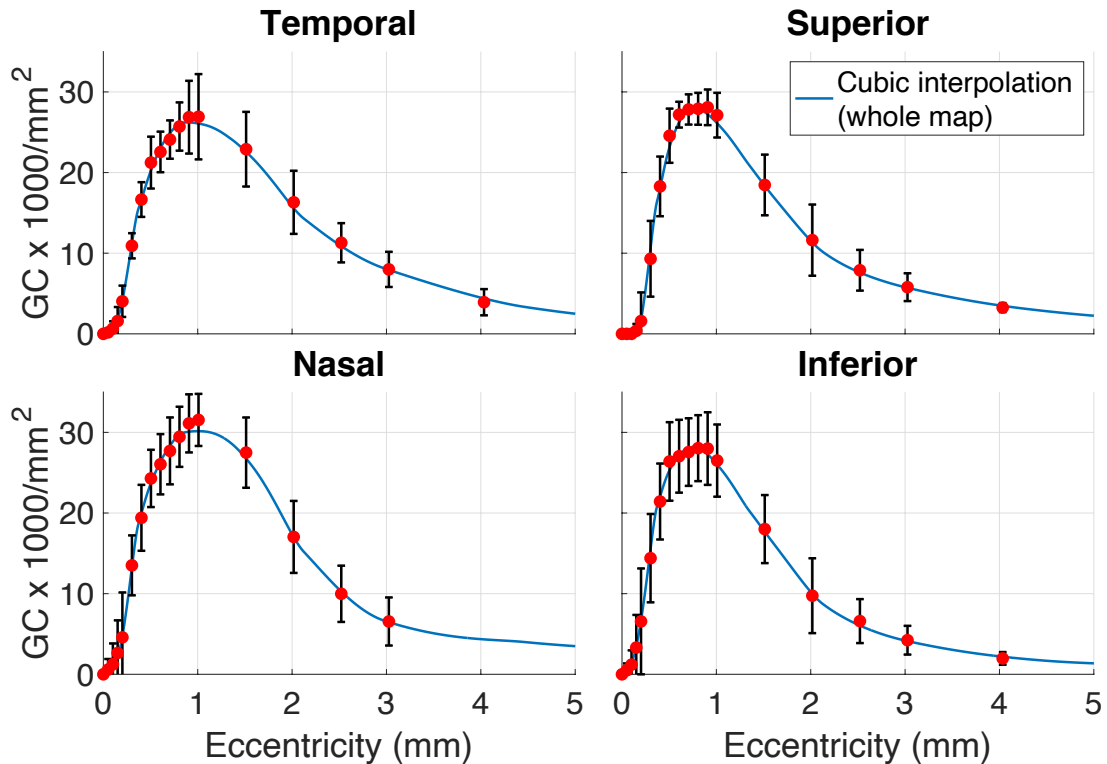


Figure 2.8 Raw averages and cubic interpolation of cell densities. Comparison of the cubic interpolation from the whole spherical map and the raw averages (red dots) and standard deviations (black vertical bars) reported by Curcio and Allen¹⁶.

2.5.2. Appendix 2

The data for the schematic eye are reported in **Table 2.3**. The ray tracing allows precise calculations for different *ALs*, which can be achieved by proportionally changing the radius and the centre location of the retinal sphere (**Figure 2.1**). The anterior part of the schematic eye is left unchanged, so that the nodal point remains the same for all *ALs*. The numerical estimate for the nodal point was obtained by averaging of 670 ray-tracings, with an angle of incidence between 0.1 and 67 degrees with respect to the optic axis. The nodal point for each incident ray was derived numerically by minimising the absolute difference between the angle of the incident and the refracted ray (after the posterior face of the lens) with respect to the optic axis. The resulting estimate was 6.93 *mm*, which is very close to the value of 6.95 *mm* reported by Drasdo and Fowler²¹. The schematic eye was assumed to be radially symmetric around the optic axis. The same schematic eye was used to correct for ocular magnification in the SD-OCT macular volume scans. In their original paper, Drasdo and Fowler did not clarify what point they used as a reference to calculate the visual angle. In accordance with the guidelines from the Imaging and Perimetry Society³⁹, we used the nodal point of the schematic eye.

	Current study	Original values ²¹
Distance from corneal vertex (mm)		
Retina (Axial length)	23.8401	23.0100
First nodal point	6.930	6.950
Anterior lens surface	3.600	3.600
Posterior lens surface	7.375	Missing
Centre of retinal sphere	12.381	11.950
Radii of curvature (mm)		
Retina	11.459	11.060
Anterior lens surface	10.000	10.000
Posterior lens surface	6.000	6.000
Apex of cornea	7.800	7.800
Eccentricity of corneal ellipse	0.500	0.500
Refractive indices		
Cornea, aqueous, vitreous	1.336	1.336
Lens	1.430	1.430

Table 2.3 Data for the schematic eye used in this paper along with the original values from Drasdo and Fowler²¹. The differences are highlighted in bold. Missing = inferred from Figure 2.1 in the original paper.

2.5.3. Appendix 3

The value of k in formula 3 also depends on eccentricity according to

$$k(e) = 1 + (1.004 - 0.007209 * e + 0.001694 * e^2 - 0.00003765 * e^3)^{-2} \quad (2.4)$$

and accounts for the change in the relative percentage of the ON and OFF midget RGC-RF with eccentricity, as reported by Drasdo et al.¹. The D_{gcrf} is converted into a density per mm^2 with the conversion ratio derived from the schematic eye (**Figure 2.1**), according to the axial length. The eccentricity in visual degrees is also converted into mm on the retina using the schematic eye. Then, a RGC-RF density profile from the fovea outward can be calculated and converted into cumulative counts for a circular sector centred at the fovea by

$$C_{gcrf}(r) = \int_0^r [2\pi r * D_{gcrf}(r)] dr \quad (2.5)$$

where r is the eccentricity from the fovea in mm and $2\pi r$ is a correction factor for the sector area increasing with eccentricity. The actual width of the sector considered acts only as a scaling factor and has no bearing on the results of the computation. When computed numerically, the integral is simply a cumulative summation for predefined steps in r . The same formula was used to compute the cumulative counts of RGC bodies (C_{gcb}). In this case, the D_{gcrf} is simply replaced by the density of RGC bodies (per mm^2) obtained from the histology map (D_{gcb}) along the same meridian, after correction for the size of the retinal sphere. The

displacement is finally computed as the difference between the eccentricities at which C_{gcb} and C_{gcrf} are equal (**Figure 2.9**). For each meridian, the displacement is zero beyond the first crossing point between the two cumulative curves. Therefore, the actual displacement might involve a smaller area than the DZ .

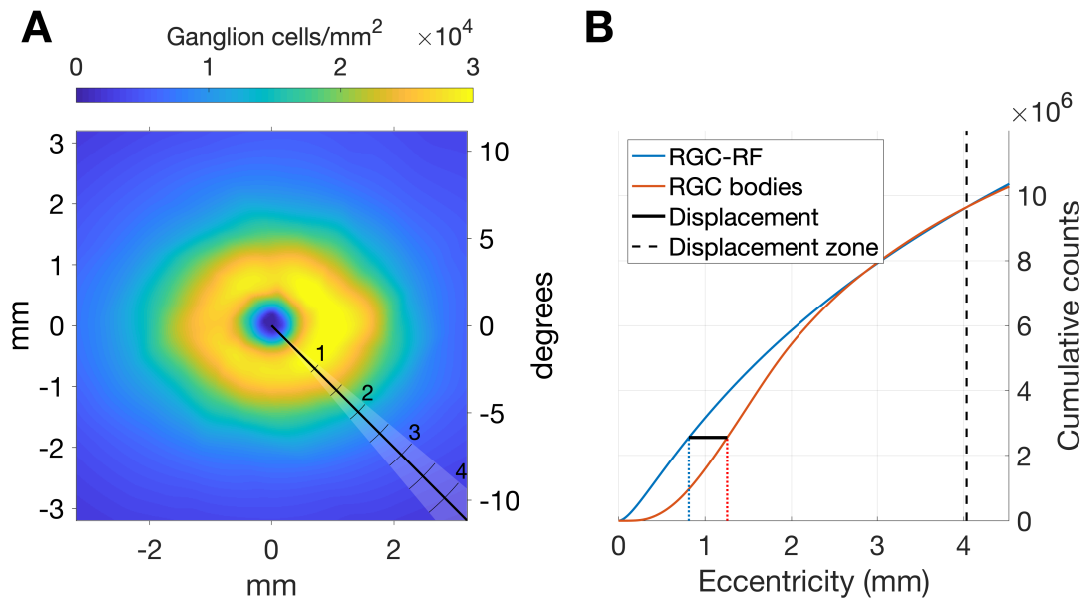


Figure 2.9 Example of how the displacement is computed along a specific meridian. A) The black line indicates the meridian analysed. The shaded area highlights the radial sector. The ticks indicate the distance in mm . The colour map represents the RGC histology density map. B) The displacement is calculated as the distance (black solid line) between the two eccentricities at which the cumulative counts of RGC-RF (blue solid line) and the RGC bodies (red solid line) are equal. The dashed vertical line indicates the eccentricity of the maximum displacement zone. The fitting process requires that the two cumulative counts are the same at this eccentricity.

2.6. Acknowledgments

We thank Christine A. Curcio and Kenneth R. Sloan from the University of Alabama at Birmingham (USA) for making the histology data available for this analysis.

We are grateful to all the participants of the NICOLA Study, and the whole NICOLA team, which includes nursing staff, research scientists, clerical staff, computer and laboratory technicians, managers and receptionists. The Atlantic Philanthropies, the Economic and Social Research Council, the UKCRC Centre of Excellence for Public Health Northern Ireland, the Centre for Ageing Research and Development in Ireland, the Office of the First Minister and Deputy First Minister, the Health and Social Care Research and Development Division of the Public Health Agency, the Wellcome Trust/Wolfson Foundation and Queen's University Belfast provide core financial support for NICOLA. The authors alone are responsible for the interpretation of the data and any views or opinions presented are solely those of the authors and do not necessarily represent those of the NICOLA Study team. The NISA study was funded by the College of Optometrists, Macular Society, RNIB, Diabetes UK and the Thomas Pocklington Trust.

2.7. References

1. Drasdo N, Millican CL, Katholi CR, Curcio CA. The length of Henle fibers in the human retina and a model of ganglion receptive field density in the visual field. *Vision research* 2007;47:2901-2911.
2. Glen FC, Crabb DP, Smith ND, Burton R, Garway-Heath DF. Do patients with glaucoma have difficulty recognizing faces? *Investigative ophthalmology & visual science* 2012;53:3629-3637.
3. Burton R, Smith ND, Crabb DP. Eye movements and reading in glaucoma: observations on patients with advanced visual field loss. *Graefe's archive for clinical and experimental ophthalmology = Albrecht von Graefes Archiv fur klinische und experimentelle Ophthalmologie* 2014;252:1621-1630.
4. Glen FC, Smith ND, Crabb DP. Saccadic eye movements and face recognition performance in patients with central glaucomatous visual field defects. *Vision research* 2013;82:42-51.
5. De Moraes CG, Hood DC, Thenappan A, et al. 24-2 Visual Fields Miss Central Defects Shown on 10-2 Tests in Glaucoma Suspects, Ocular Hypertensives, and Early Glaucoma. *Ophthalmology* 2017;124:1449-1456.
6. Grillo LM, Wang DL, Ramachandran R, et al. The 24-2 Visual Field Test Misses Central Macular Damage Confirmed by the 10-2 Visual Field Test and Optical Coherence Tomography. *Translational vision science & technology* 2016;5:15.
7. Hood DC, Kardon RH. A framework for comparing structural and functional measures of glaucomatous damage. *Prog Retin Eye Res* 2007;26:688-710.
8. Hood DC, Raza AS, de Moraes CG, Liebmann JM, Ritch R. Glaucomatous damage of the macula. *Progress in retinal and eye research* 2013;32:1-21.
9. Garway-Heath DF, Caprioli J, Fitzke FW, Hitchings RA. Scaling the hill of vision: the physiological relationship between light sensitivity and ganglion cell numbers. *Invest Ophthalmol Vis Sci* 2000;41:1774-1782.
10. Swanson WH, Felius J, Pan F. Perimetric defects and ganglion cell damage: interpreting linear relations using a two-stage neural model. *Investigative ophthalmology & visual science* 2004;45:466-472.
11. Harwerth RS, Wheat JL, Fredette MJ, Anderson DR. Linking structure and function in glaucoma. *Prog Retin Eye Res* 2010;29:249-271.
12. Anderson DR, Knighton RW. Perimetry and acuity perimetry. In: eds. SMPIKA (ed), *Perspectives in Glaucoma*. New Jersey: Slack, Inc Thorofare, NJ; 1988:59-70.
13. Raza AS, Hood DC. Evaluation of the Structure-Function Relationship in Glaucoma Using a Novel Method for Estimating the Number of Retinal Ganglion Cells in the Human Retina. *Investigative ophthalmology & visual science* 2015;56:5548-5556.
14. Yoshioka N, Zangerl B, Phu J, et al. Consistency of Structure-Function Correlation Between Spatially Scaled Visual Field Stimuli and In Vivo OCT Ganglion Cell Counts. *Investigative ophthalmology & visual science* 2018;59:1693-1703.
15. Montesano G, Rossetti LM, Allegrini D, Romano MR, Crabb DP. Improving Visual Field Examination of the Macula Using Structural Information. *Translational vision science & technology* 2018;7:36.
16. Curcio CA, Allen KA. Topography of ganglion cells in human retina. *The Journal of comparative neurology* 1990;300:5-25.
17. Lujan BJ, Roorda A, Knighton RW, Carroll J. Revealing Henle's fiber layer using spectral domain optical coherence tomography. *Investigative ophthalmology & visual science* 2011;52:1486-1492.
18. Turpin A, Chen S, Sepulveda JA, McKendrick AM. Customizing Structure-Function Displacements in the Macula for Individual Differences. *Investigative ophthalmology & visual science* 2015;56:5984-5989.
19. Watson AB. A formula for human retinal ganglion cell receptive field density as a function of visual field location. *Journal of vision* 2014;14.
20. Sjostrand J, Popovic Z, Conradi N, Marshall J. Morphometric study of the displacement of retinal ganglion cells subserving cones within the human fovea. *Graefe's archive for clinical and experimental ophthalmology = Albrecht von Graefes Archiv fur klinische und experimentelle Ophthalmologie* 1999;237:1014-1023.
21. Drasdo N, Fowler CW. Non-linear projection of the retinal image in a wide-angle schematic eye. *The British journal of ophthalmology* 1974;58:709-714.
22. Miraftebi A, Amini N, Morales E, et al. Macular SD-OCT Outcome Measures: Comparison of Local Structure-Function Relationships and Dynamic Range. *Investigative ophthalmology & visual science* 2016;57:4815-4823.

23. Hirasawa K, Matsuura M, Fujino Y, et al. Comparing Structure-Function Relationships Based on Drasdo's and Sjostrand's Retinal Ganglion Cell Displacement Models. *Investigative ophthalmology & visual science* 2020;61:10.
24. Atchison DA. Optical models for human myopic eyes. *Vision research* 2006;46:2236-2250.
25. Atchison DA, Pritchard N, Schmid KL, Scott DH, Jones CE, Pope JM. Shape of the retinal surface in emmetropia and myopia. *Investigative ophthalmology & visual science* 2005;46:2698-2707.
26. Pope JM, Verkicharla PK, Sepehrband F, Suheimat M, Schmid KL, Atchison DA. Three-dimensional MRI study of the relationship between eye dimensions, retinal shape and myopia. *Biomedical optics express* 2017;8:2386-2395.
27. Coletta NJ, Watson T. Effect of myopia on visual acuity measured with laser interference fringes. *Vision research* 2006;46:636-651.
28. Chui TY, Song H, Burns SA. Individual variations in human cone photoreceptor packing density: variations with refractive error. *Investigative ophthalmology & visual science* 2008;49:4679-4687.
29. Dabir S, Mangalesh S, Schouten JS, et al. Axial length and cone density as assessed with adaptive optics in myopia. *Indian journal of ophthalmology* 2015;63:423-426.
30. Stapley V, Anderson RS, Saunders KJ, Mulholland P. Altered Spatial Summation Optimizes Visual Function in Axial Myopia. *Scientific Reports* 2020.
31. Chang WC, Joe; Allaire, JJ; Xie, Yihui; McPherson, Jonathan. shiny: Web Application Framework for R. 2019.
32. (2019) RCT. R: A Language and Environment for Statistical Computing. Vienna, Austria: R Foundation for Statistical Computing; 2019.
33. Curcio CA, Sloan KR, Meyers D. Computer methods for sampling, reconstruction, display and analysis of retinal whole mounts. *Vision research* 1989;29:529-540.
34. Strasburger H, Rentschler I, Juttner M. Peripheral vision and pattern recognition: a review. *Journal of vision* 2011;11:13.
35. Garg A, Hood DC, Pensec N, Liebmann JM, Blumberg DM. Macular Damage, as Determined by Structure-Function Staging, Is Associated With Worse Vision-related Quality of Life in Early Glaucoma. *American journal of ophthalmology* 2018;194:88-94.
36. Hood DC, Tsamis E, Bommakanti NK, et al. Structure-Function Agreement Is Better Than Commonly Thought in Eyes With Early Glaucoma. *Investigative ophthalmology & visual science* 2019;60:4241-4248.
37. Sato S, Hirooka K, Baba T, Tenkumo K, Nitta E, Shiraga F. Correlation between the ganglion cell-inner plexiform layer thickness measured with cirrus HD-OCT and macular visual field sensitivity measured with microperimetry. *Investigative ophthalmology & visual science* 2013;54:3046-3051.
38. Ohkubo S, Higashide T, Udagawa S, et al. Focal relationship between structure and function within the central 10 degrees in glaucoma. *Investigative ophthalmology & visual science* 2014;55:5269-5277.
39. Sample PA, Dannheim F, Artes PH, et al. Imaging and Perimetry Society standards and guidelines. *Optometry and vision science : official publication of the American Academy of Optometry* 2011;88:4-7.

3. Systematic and random mapping errors in structure – function analysis of the macula

This paper focuses on investigating how perimetric stimuli are projected on the retina of healthy observers and patients with glaucoma. One common assumption in structure-function calculations (and perimetry in general) is that the observer maintains a steady fixation on a central target throughout the test. However, eye movements and damage from disease can affect the accuracy of this assumption. This is more important when using denser grids, such as the 10-2. The objective of this work was to use data from a specialised perimetry device equipped with eye-tracking and retinal imaging technology to quantify the amount of error in this assumption when performing structure-function mapping with SAP. An important outcome of this investigation was to show that the practice of rotating the 10-2 grid to align its horizontal midline with the segment connecting the fovea and the optic disc on the retina, common in previous literature^{1, 2}, did not find support in empirical evidence. Finally, we introduced a method to quantify how much fixation can be influenced by seen stimuli during perimetry and how this can affect the accuracy of the presentation of the following stimuli. This highlights the importance of steady fixation, which can be reduced by carefully instructing the tested subject. The results were published in *Translational Vision Science and Technology (TVST)*, a journal of the Association for Research in Vision and Ophthalmology (ARVO). The paper is freely available at: <https://tvst.arvojournals.org/article.aspx?articleid=2772280>.

Contributions

- *Main contributor*: **Giovanni Montesano** (conceptualisation of research, data and statistical analysis, interpretation of the data, drafting of the manuscript).
- *Other contributors*:
 - **Luca M. Rossetti** (data collection, interpretation of the data, manuscript proofing)
 - **Davide Allegrini** (data collection, interpretation of the data, manuscript proofing)
 - **Mario R. Romano** (data collection, interpretation of the data, manuscript proofing)
 - **David F. Garway-Heath** (interpretation of the data, manuscript proofing)
 - **David P. Crabb** (supervision, interpretation of the data, manuscript proofing)

3.1. Introduction

Glaucoma is characterised by structural loss of neural tissue and associated functional damage to the visual field (VF). Therefore, the spatial mapping of the location of visual function measurements to image-based measurements of retinal structure is important when evaluating the agreement of estimates of functional and structural damage.

Optical Coherence Tomography (OCT) is widely used to provide a quantitative three-dimensional assessment of thickness of different layers of the retina and optic nerve head (ONH)^{3, 4}. The most affected layers in glaucoma are the Retinal Nerve Fibre Layer (RNFL) and the Ganglion Cell Layer (GCL), which typically show localised or diffused thinning when damaged³⁻⁵. Functional (VF) loss in glaucoma is typically measured using white-on-white perimetry,⁴

⁶ where the subject is asked to fixate on a central target while stimuli of varying intensities are projected at various retinal locations. The subject presses a button every time a light stimulus is perceived. This information is then used to compute the retinal sensitivity at each tested location ⁷.

In recent years, there has been increasing interest around the study of macular damage in glaucoma^{8,9}. Macular involvement can seriously impact the visual function and vision related quality of life of patients and is now recognised to be a feature of glaucoma even in early stages¹⁰⁻¹³.

The macula can be assessed with high precision both with functional and structural tests. For example, exhaustive thickness measurements of the posterior pole can be obtained through high density OCT scans. Likewise, the 10-2 perimetric grid provides a detailed sensitivity map of the macular region, with an examination resolution of 2 degrees ^{2, 14-16}. These measurements have been combined to study the structure-function relationship in glaucoma ^{1, 2, 15-17}. Such analyses require that the spatial correspondence between tested locations and measured thickness values is established. This is challenging as a consequence of the radial displacement of the Retinal Ganglion Cells (RGCs) in the macula^{18, 19} and by the accuracy of spatial mapping of perimetry onto structural maps¹⁶. The latter is especially important in the macula, since inaccurate mapping can potentially nullify any advantage offered by the high spatial resolution of the measurements. We explore this challenge in this study.

Any mapping scheme is based on certain assumptions. Usually, it is assumed that the centre of fixation, or Preferred Retinal Locus (PRL), coincides with the anatomical fovea. However, patients can exhibit eccentric fixation, especially with advanced macular damage^{20, 21}, even in glaucoma^{16, 22}. Moreover, some researchers have proposed that the 10-2 VF grid should be rotated to match the anatomical fovea-disc axis ^{1, 2}. Such an assumption is not supported by evidence on how stimuli are projected during perimetry. Another major hurdle is fixation instability. In fact, subjects might not be able to maintain steady fixation on the central target throughout the VF test ²³⁻²⁵. This can result in projection of stimuli on the retina away from the intended location. In an attempt to solve this issue, fundus perimetry has been introduced^{21, 24, 26-29}; this employs tracking of eye movements through continuous retinal imaging and actively compensating for eye movements when projecting the stimuli. Originally designed to test patients with age related macular degeneration²¹, fundus perimetry has been successfully employed in glaucoma to improve test-retest variability and structure-function relationship^{17, 26-28}. Importantly, fundus perimetry locks the stimulus location on a reference image of the subject's retina, providing precise landmarks to accurately link perimetric data to OCT maps ¹⁶. Finally, as a useful by-product of the tracking procedure, detailed two-dimensional information on fixation behaviour of the subject during the test is provided ^{21-25, 30, 31}.

In this work, we combine structural information from an OCT device and functional data collected with a fundus perimeter from healthy subjects and glaucoma patients. The objective was to use projection and fixation data from fundus perimetry to: 1) establish whether grid rotation along the fovea-disc axis as a preferred mapping scheme is supported by evidence, and 2) quantify the spatial error of stimulus projection in perimetry when eye movements are not compensated, as in traditional VF test.

3.2. Methods

3.2.1. Data collection

This was a retrospective analysis of data collected for a previously published study¹⁶. The study adhered to the tenets of the Declaration of Helsinki and was approved by the local ethical committee¹⁶ (Humanitas–Gavazzeni Hospital Ethical Committee, reference number 161/18gav). After obtaining written consent, we collected data from 17 visually healthy subjects and 31 glaucoma patients. All glaucoma patients and 9 of the healthy subjects had previous experience with perimetry, but not with the fundus perimeter used in this study. All subjects were instructed to maintain central fixation, as in traditional perimetry. The data collection has been described elsewhere³². In brief, Spectral Domain OCT (SD-OCT) high density volume scans (121 vertical b-scans) of the macular region were acquired with a fundus tracked device, the Spectralis (Heidelberg Engineering, Heidelberg, Germany). Axial length was measured with an IOL-Master V3 A-scan (Zeiss Meditec, Dublin, CA, USA). The 10-2 VF field test was performed on these 38 subjects with a fundus perimeter (Compass [CMP], CenterVue, Padua, Italy). Twenty additional glaucoma patients were also tested with a custom small grid for the main experiment and were not included in this analysis³². The CMP has a tracking speed of 25 Hz using an infrared fundus camera, with an approximate resolution of 32 pixel/degree. The theoretical maximum resolution of the tracking is equivalent to that of the camera (0.03 degrees), but can be reduced by blurred or low quality images. The device has a background illumination of 31.5 asb and uses a Bayesian testing strategy (Zippy Estimation through Sequential Testing, ZEST^{28, 33}) to determine retinal sensitivity. The device tracks the eye for 10 seconds at the beginning of the test to determine the PRL on the retina²³. The testing grid is then centred on this location, which might be different from the anatomical fovea. The position of the tested locations is calculated in degrees from fixation (PRL) as in conventional perimetry.

3.2.2. Analysis of fixation and projection data

We extracted the complete tracking recordings of fixation during the test for each exam; these are composed of retina displacements over time (in milliseconds) in the horizontal and vertical direction (in degrees) with respect to a reference image acquired at the beginning of the test^{16, 23}. We also extracted the time, intensity, position relative to the PRL and response time (button press) of all the stimulus projections occurring during the test¹⁶. The two tracks (fixation and projections) were then matched using the time reference to quantify fixation behaviour before and after each stimulus projection.

First, we used this information to detect eye movements that were likely caused by gaze attraction from seen stimuli. We called these movements *evoked displacements*. The methodology for this analysis has been previously presented (Modarelli A, et al. IOVS 2018;59:ARVO E-Abstract 5131) and is reported in detail in the Appendix. In brief, a filter identifies eye movements, above an individualised noise threshold, directed towards a stimulus projection. These eye movements can either be removed from the fixation track, to give a more robust quantification of fixation, or they can be analysed as a separate component of spatial projection error (see below).

To quantify fixation behaviour, we calculated the 95% Bivariate Contour Ellipse Area (95% BCEA)^{23, 25} of fixation positions before and after the removal of the evoked displacements. We also calculated the average displacement of fixation from the PRL during the test, as this

can be easily related to common fixation tracks provided by traditional perimeters^{34, 35}, such as the Humphrey Field Analyzer (Zeiss Meditec, Dublin, California).

3.2.3. Structural mapping

Fundus images from the CMP and the Spectralis can be used to match VF test locations to structural maps¹⁶. For this analysis, we were only interested in detecting the anatomical fovea and the position of the ONH. The former was automatically detected using a template matching technique on the OCT measurement of the whole retinal thickness¹⁶ and the latter was manually identified on the wide-field CMP image.

Once a geometric projective transformation¹⁶ is estimated by matching the fundus images from the two devices, the positions of the anatomical landmarks, the tested locations and the fixation track can be mapped into the coordinates of either device.

In this study, we assumed that the retinal rotation during the VF test was the one observed in the fundus image from the CMP. Therefore, when stimulus locations were reported on the maps from the Spectralis, such a rotation was preserved. It is important to notice that the projection of the 10-2 grid in the CMP is analogous to any non-fundus tracked perimeter, i.e. stimuli are presented at predefined eccentricities with no rotation, regardless of the relative position of the fovea or ONH. However, differently from other devices, the retinal image can be used to assess the rotation of the eye relative to the grid during the test. The results from this analysis are therefore generalizable to structure-function analyses performed with any perimeter. For objective (1), the effect of artificial grid rotation (to align the horizontal axis of the VF grid to the fovea-disc axis) on the mapping error was calculated as the Euclidean distance between the locations of the rotated or non-rotated grids, centred on the fovea, and the actual locations on the Spectralis maps (**Figure 3.1 A**). This approach preserves the real observed retinal rotation but removes fixation bias (see next section). Therefore, all grids were assumed to be centred in the fovea and the effect of rotation was isolated.

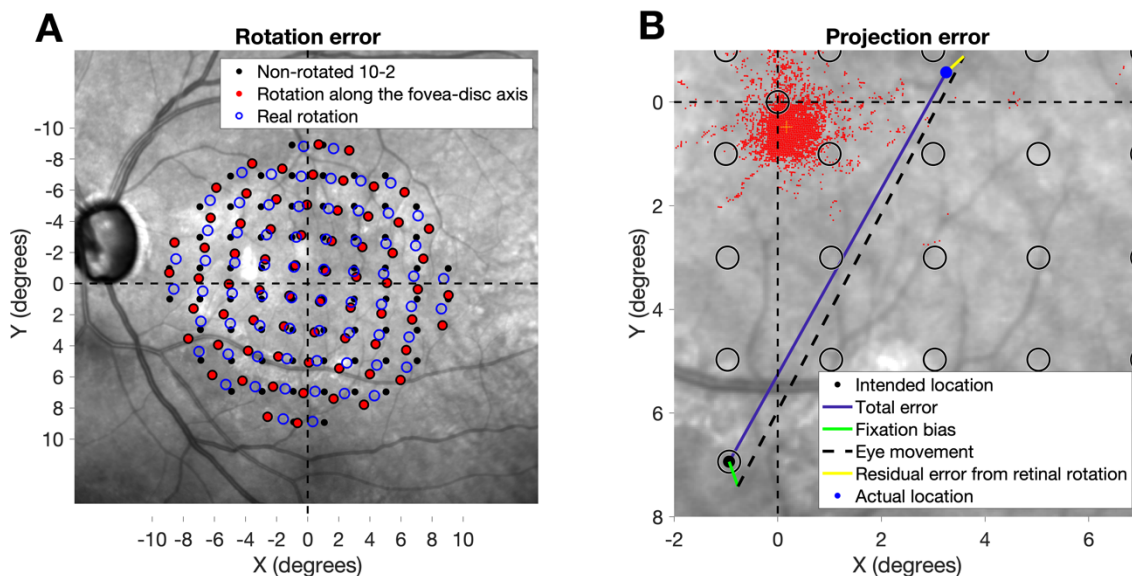


Figure 3.1 Examples of mapping errors A) Spectralis fundus picture showing different mapping schemes. All are centred in the fovea. The filled black points represent the non-rotated 10-2 grid (i.e. assuming the horizontal axis of the VF is horizontal on the retina). The filled

red points show the 10-2 grid rotated to match the horizontal axis with fovea-disc axis of the subject. Finally, the empty blue circles represent the grid with the real observed rotation from the CMP. The (0,0) coordinate represents the location of the anatomical fovea. B) Calculation of the projection error. The different segments show different component of the error. The empty black circles represent the intended test locations for the 10-2 grid referenced to the anatomical fovea. The small red dots represent the cloud of fixation positions during the exam. The offset of its centre from the anatomical fovea indicates the fixation bias. The (0,0) coordinate represents the location of the anatomical fovea.

3.2.4. Quantification of projection errors

Our main goal was to quantify projection errors occurring when eye movements are not compensated. This happens in conventional perimetry, when performing structure-function analysis. We defined projection errors as the spatial distance (in degrees) between the actual location of the projection on the retina (had there been no fundus tracking) and its intended location, in this case the stimulus coordinates of a 10-2 grid centred on the anatomical fovea. One important aspect of fundus perimetry is that it locks the stimuli on fixed positions on the retina based on the initial estimation of the PRL. However, this is not what happens in conventional perimetry. Therefore, in our calculations for objective (2), we estimated the actual projection location during the test by adding the last fixation offset (recorded immediately before the stimulus projection) to its intended position, in degrees from the anatomical fovea. Finally, the small differences in retinal rotation between the fundus images from the CMP and the Spectralis (**Figure 3.1 B**) were also added.

We considered the total projection error for each test to be composed of two different additive elements:

- *Fixation bias*: this is a consistent offset of the PRL from the anatomical fovea. In our analysis, the fixation bias was calculated as the average offset in the horizontal and vertical directions of the fixation positions after the evoked displacements had been removed. The fixation bias was then removed before calculating the following components.
- *Eye movements*: these are gaze displacements occurring during the test and can be classified into two types:
- *Evoked displacements*: these are eye movements caused by gaze attraction from perceived stimuli. The exact method for their detection is explained in the Appendix. To quantify their effect, the error for each projection was identified as being a consequence of an evoked displacement if such a displacement happened during the previous presentation. Therefore, an evoked displacement caused by one stimulus presentation is assumed to influence the error of the following projection. This happens if the subject does not return to central fixation after the evoked displacement.
- *Random displacements*: these are eye movements caused by random fixation instability. They are composed of all the calculated projection errors that are not attributed to evoked displacements.

We finally defined the *unbiased error* to be the ensemble of evoked and random displacements (i.e. after removing the fixation bias from all projection errors). All calculations for the image and track analyses were performed in Matlab (The MathWorks Inc., Natick, Massachusetts).

3.2.5. Statistical analysis

Changes in the 95% BCEA before and after removal of evoked displacements^{23, 25}, was modelled using a generalised linear model (GLM) with a Gamma distribution of the statistical error and a log link function for the BCEA. Such an approach accounts for the skewed distribution of the BCEA (strictly positive) and models the effect of the predictors as proportional (additive in log-scale). This is consistent with previous reports studying the log-transformed BCEA. Differently from a log-transformation, GLMs allow a direct estimate of the mean and standard error in the original scale of the dependent variable. Random intercepts were added to account for the repeated measures from the same eye (BCEA with and without evoked displacements). The marginal (population) estimates from mixed model with a non-linear link function (log in this case) are, however, conditional to specific values of the random intercept³⁶. Unconditional marginal estimates were derived numerically using the *glmmadaptive* package³⁷ for R (R Foundation for Statistical Computing, Vienna, Austria). Differences in 95% BCEA with and without evoked displacements between the healthy and glaucoma cohort were calculated through a single model which included an interaction between the group (Healthy or Glaucoma) and the type of displacement (Random or Evoked). The projection error in our analysis is defined as a distance; the distribution of this variable is also expected to be positive and right-skewed. Therefore, GLMs with a proportional effect of the predictors can be suitable in this case as well. However, for ease of interpretation, it is convenient instead to model the effects on the error as additive. Hence, we used simple linear mixed effect models, with a random intercept term to account for correlations among observations from the same test, for all the statistics describing the projection errors (*lme4* package for R³⁸). The effect of evoked displacements was coded for each presentation as a binary fixed effect predictor in the GLM. The specific effect of evoked displacements was analysed using the unbiased error. The linear model expressed the difference in projection error for presentations following likely evoked displacements compared to the other presentations. The differences in the frequency of evoked displacements between the healthy and glaucoma cohort was studied using a logistic regression with random intercepts. This is also a GLM with a non-linear link function (logit). The population estimates were therefore also obtained with the *GLMMadaptive* package³⁷. Differences between random and evoked displacements between the healthy and glaucoma cohort were calculated through a single model which included an interaction between the group (Healthy or Glaucoma) and the type of displacement (Random or Evoked).

Age (years) was always included as a covariate, except when calculating the error introduced by rotation, since this was not dependent on functional factors. Age adjusted estimates and 95% confidence intervals (CIs) are reported at the average age of the overall sample (61 years). The level of statistical significance for the analyses was set to 0.05. The Tukey-Kramer method was used to correct for multiple testing when performing pairwise comparisons. All statistical analyses were performed in R.

3.3. Results

Demographic characteristics of the final sample are reported in **Table 3.1**. On average, the healthy cohort was younger than the glaucoma cohort. The two cohorts overlapped in the range between 34 and 62 years of age, which included 20 (43%) subjects. The fixation track could not be extracted for 3 healthy subjects. One glaucoma subject was excluded because, despite correct initial alignment and PRL detection, the centre of fixation was several

degrees away from the central target throughout the exam. The patient reported seeing a ghost image of the central target projected superiorly.

	Healthy (N = 17)	Glaucoma (N = 30)
Age (years)	42 [27, 60]	74 [44, 87]
Axial length (mm)	24.17 [22.06, 25.84]	24.18 [22.24, 26.33]
BCVA (decimals)	1.0 [0.80, 1.00]	0.70 [0.22, 1.00]
HFA 24-2 (dB)	-	-14.42 [-27.67, -3.12]
CMP 10-2 MD (dB)	-0.28 [-1.89, 0.56]	-13.00 [-26.16, -6.40]
Exam duration (minutes)	6.6 [5.7, 14.5]	9.9 [7.3, 16.5]

Table 3.1 Demographics of the sample. All values are reported as Median [95% quantiles]. 24-2 data for glaucoma patients were obtained from clinical charts. CMP = Compass; HFA = Humphrey Field Analyzer

3.3.1. Mapping error introduced by grid rotation

The effect of aligning the horizontal axis of the 10-2 grid with the fovea-disc axis (rotation) is shown in **Figure 3.2**. The reference was the actual rotation of the grid observed with the CMP. The error was 0.80 [0.73, 0.86] degrees (Mean [95% CIs] for the rotated grid and 0.30 [0.23, 0.36] degrees for the non-rotated grid ($p < 0.001$). Grid rotation introduced a systematic error that was larger for more eccentric locations and increased proportionally with the amplitude of the fovea-disc angle ($p < 0.001$), i.e. with the amount of rotation required (**Figure 3.2**). No significant systematic error was introduced with the non-rotated grid.

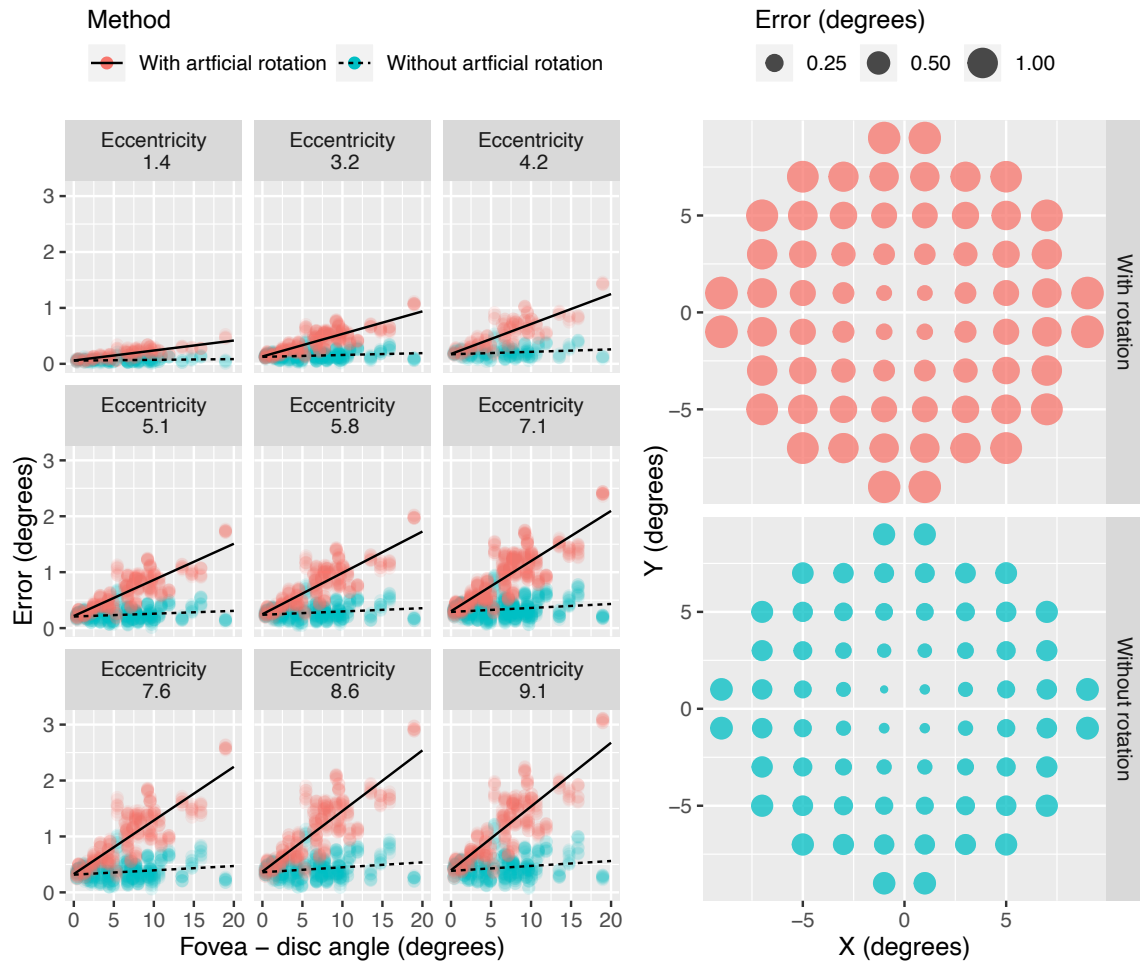


Figure 3.2 Error introduced by grid rotation. The left panel shows the systematic error introduced by artificial grid rotation at different eccentricities according to the measured fovea-disc angle. The right panel shows the mean error estimated from the model at different locations with and without grid rotation to match the fovea-disc axis.

3.3.2. Projection errors due to fixation movement

Projection errors from four different example subjects are reported in **Figure 3.3**.

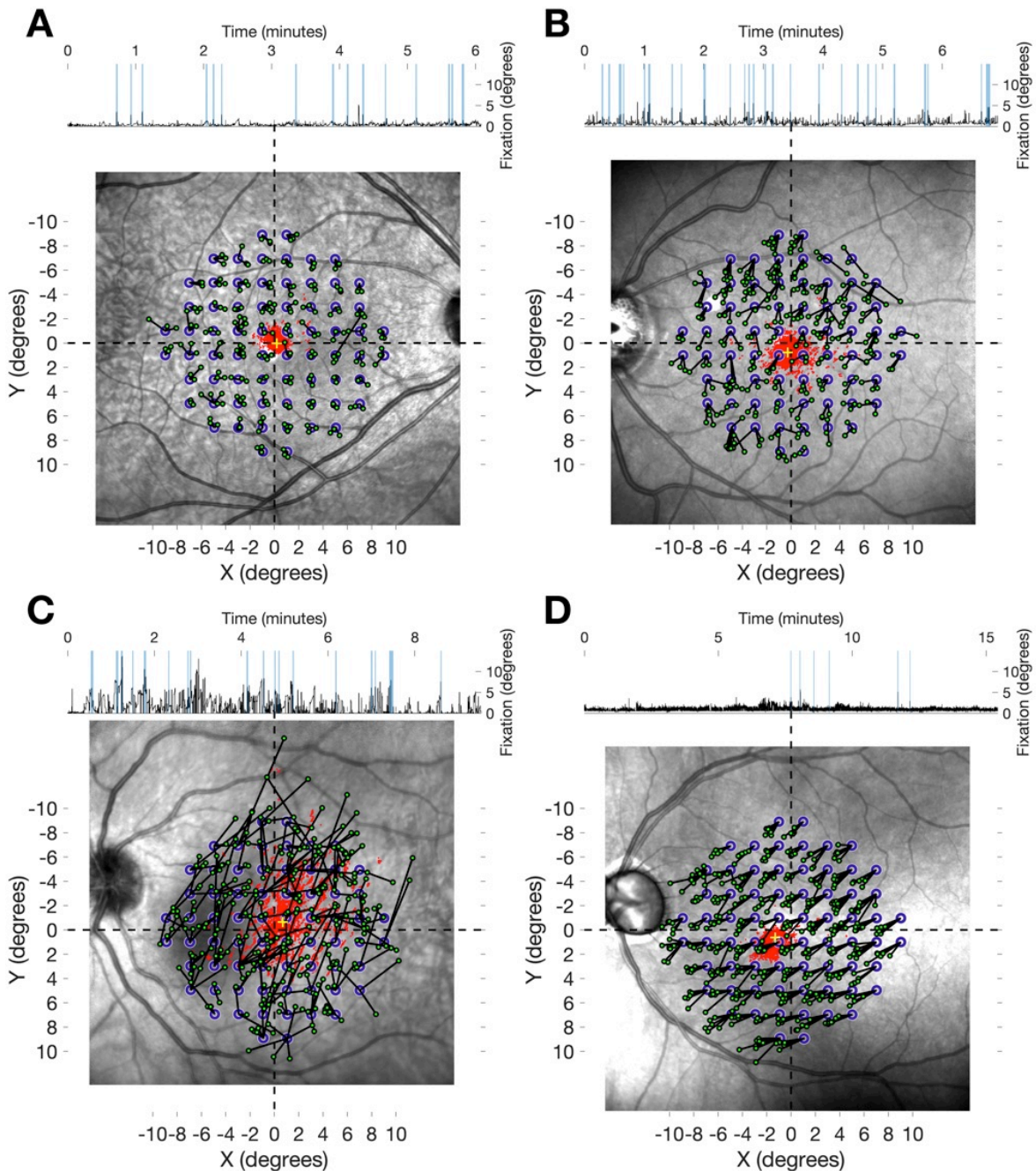


Figure 3.3 Examples from four different subjects of projection errors during a 10-2 VF test. All images are centred on the anatomical fovea. The small red dots represent the cloud of fixation positions during the test. The yellow cross corresponds to the fixation bias. The blue empty circles represent the intended position of the tested location. The small green circles represent the actual location of each projection on the retina, connected to its intended location by a black line. The top track represents the fixation displacement from the initial PRL. The shaded blue vertical bands in the track indicate evoked displacements. A) Small fixation bias, stable fixation; B) Larger fixation bias, more unstable fixation. C) Extremely chaotic fixation; D) Stable fixation with large fixation bias.

Age corrected estimates of the 95% BCEA were lower in glaucoma patients than in healthy subjects but the difference did not reach significance (**Table 3.2**, $p = 0.062$). The 95% BCEA recalculated excluding the evoked displacements was significantly smaller, both in glaucoma patients and healthy subjects ($p < 0.001$), but showed no significant differences between the two groups ($p = 0.886$). Healthy subjects showed a significantly larger reduction in 95% BCEA when evoked displacements were removed compared to glaucoma patients ($p = 0.034$). The age corrected 95% BCEA was also significantly positively correlated with the 10-2 MD (4.9% increase/dB, $p = 0.014$) in glaucoma subjects but no significant relationship could be found between the MD and the 95% BCEA after the removal of evoked displacements ($p = 0.265$). The frequency of evoked displacements was significantly higher ($p = 0.047$, logistic regression) in healthy subjects (6% [4%, 8%]) than in glaucoma patients (4% [3%, 5%]).

	Median [95% quantiles]		Age-corrected Mean [95% CIs]	
	Healthy	Glaucoma	Healthy	Glaucoma
Fixation				
95% BCEA (degrees²)	3.91 [0.38, 21.45]	3.76 [0.64, 20.98]	8.02 [4.78, 13.46]	4.09 [2.93, 5.7]
95% BCEA (degrees²) w/o Evoked displacements	0.68 [0.23, 3.45]	2.54 [0.34, 6.31]	1.98 [1.05, 3.75]	1.86 [1.21, 2.86]
Fixation bias (degrees)	0.47 [0.06, 0.95]	0.52 [0.18, 1.55]	-	-
Projection errors (degrees)				
Total	0.63 [0.16, 2.27]	0.73 [0.19, 2.45]	0.99 [0.75, 1.23]	0.89 [0.73, 1.05]
Unbiased Evoked	0.53 [0.13, 3.13]	0.49 [0.12, 2.88]	1.04 [0.82, 1.25]	0.81 [0.67, 0.96]
Random	0.43 [0.11, 1.73]	0.46 [0.11, 1.68]	0.78 [0.56, 0.97]	0.55 [0.41, 0.68]
Time interval between presentations (seconds)				
	1.43 [0.89, 2.32]	1.7 [1.1, 2.56]	1.54 [1.46, 1.63]	1.76 [1.68, 1.84]

Table 3.2 Fixation metrics and projection errors. Fixation metrics (top) and projection error (bottom) reported as Median [95% quantiles] (left) and as age corrected estimates of the mean [95% confidence intervals]. The mean values are estimated at the overall average age of the sample (61 years). The estimates for evoked and random errors quantify the amount of unbiased error for presentations following likely evoked displacements (Evoked) and all the other presentations (Random).

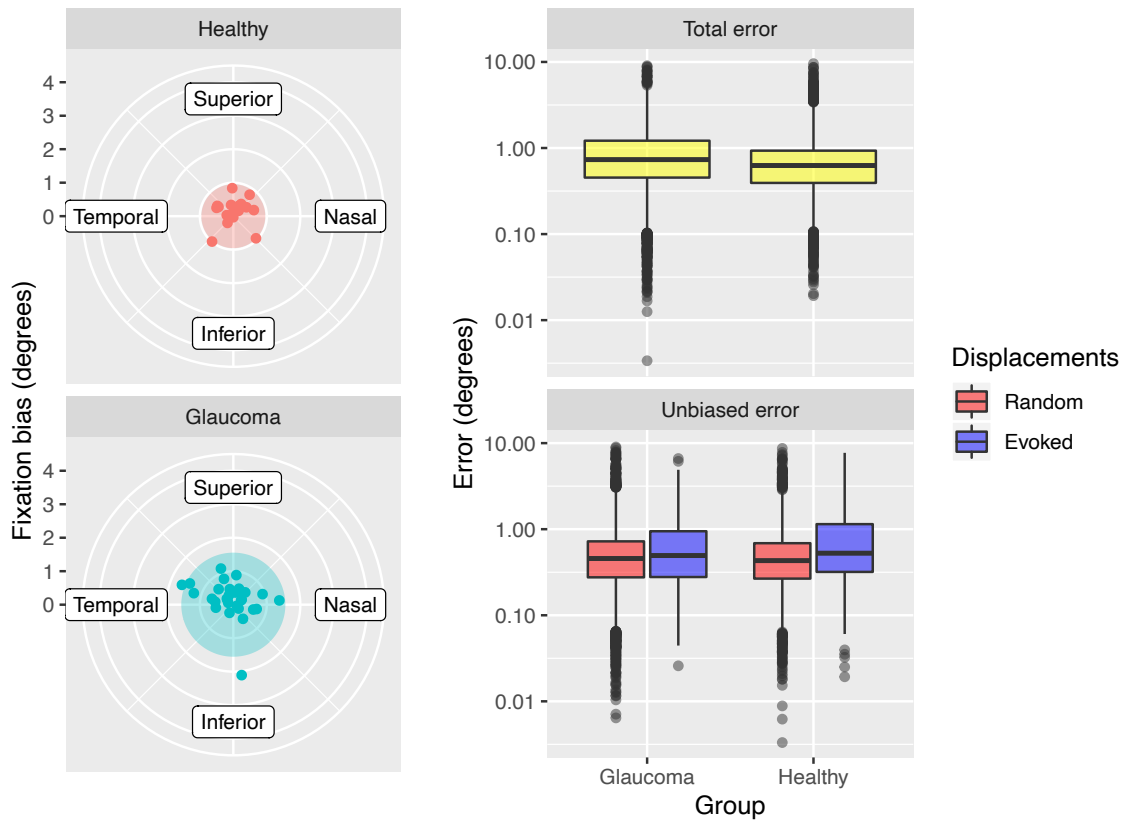


Figure 3.4 Fixation bias and mapping errors. The left panel shows the fixation bias of each subject. The centre of the polar plots represents the anatomical fovea. The dots represent the position of the average fixation during the test. The shaded circle encloses the 95% quantile value of the distance of the centre of fixation from the fovea for each group. The panel on the right shows the total error (top) for glaucoma and healthy subjects and the unbiased error (bottom) broken down into evoked and random displacements. The spacing of the vertical axis is in log₁₀ steps.

Average fixation bias was greater (**Table 3.2** and **Figure 3.4**, left panel) for glaucoma patients but this difference did not reach statistical significance ($p = 0.15$). Age corrected estimates for mean projection error were not significantly different between glaucoma patients and healthy subjects (**Table 3.2**, **Figure 3.4** right panel), neither for the total error ($p = 0.53$) nor for the unbiased error ($p = 0.13$). Removing the fixation bias significantly reduced the error in both healthy and glaucoma subjects ($p < 0.001$), with a significantly larger effect on glaucoma patients ($p < 0.001$). Evoked displacements significantly increased the error both in glaucoma patients ($p < 0.001$) and healthy subjects ($p < 0.001$) and the effect was not different between the two groups ($p = 0.839$).

Both the total and the unbiased average errors were very well predicted by the average fixation track displacement ($R^2 = 0.77$ for the total error; $R^2 = 0.60$ for the unbiased error; $p < 0.001$) through a simple linear relationship (**Figure 3.5**).

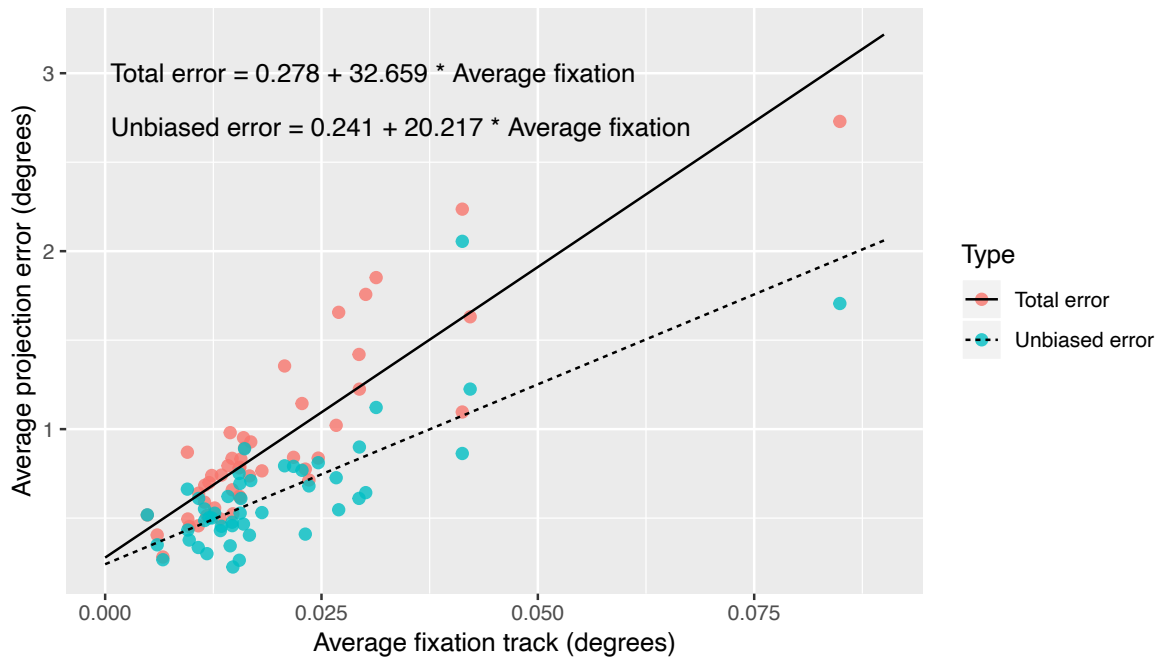


Figure 3.5 Projection error prediction. Linear regression of the average total and unbiased error according to the average displacement of the fixation track for each subject. Equations of the linear fit are given.

3.4. Discussion

3.4.1. Mapping error introduced by grid rotation

The first objective of our work was to test whether rotating the 10-2 grid to match the fovea-disc axis was the best mapping scheme for structure-function analysis. We compared the error with and without rotation using the actual eye rotation observed with a fundus perimeter as a ground truth. With our data, we did not find any evidence to support that grid rotation provides a better mapping of the tested locations on the retina. Moreover, we found that rotating the 10-2 grid introduced a systematic error proportional to the fovea-disc angle. This finding has some important consequences for previously published results^{1, 2}, where grid rotation was applied. Since most of these results relied on pointwise topographical analyses, their validity now seems questionable. These studies did not use a fundus perimeter, so the actual location of the stimuli cannot be known. However, our findings easily generalise to conventional perimetry since the head positioning of the patient and the projection of the stimuli are identical²⁸. The CMP, in fact, projects the 10-2 grid exactly as it would be in a traditional perimeter, with no regard for the relative position of fovea and the ONH. Of course, with the aid of imaging and fundus perimetry, the 10-2 grid could be forcedly aligned with the fovea disc axis. However, further studies, for example on how the anatomy of the RGCs changes with the position of the ONH, are needed to understand whether such a change would provide any advantage in structure-function analyses and diagnostic ability.

3.4.2. Projection errors due to fixation movement

The second objective was to quantify how eye movements contributed to errors in the projection of perimetric stimuli on the retina. Here we used fixation and projection data from

the CMP and structural data from a SD-OCT to model what would happen in conventional perimetry. We specifically isolated the effect of gaze attraction from projected stimuli in what we called evoked displacements. We found that removing these evoked displacements from fixation data significantly shrunk the 95% BCEA both in healthy subjects and in glaucoma patients ($p < 0.001$). This reduction was significantly more pronounced in healthy subjects ($p = 0.034$), as evoked displacements were significantly more frequent in this group ($p = 0.047$). This could be partially explained by the fact that healthy subjects were less experienced with perimetry than glaucoma patients. However, rather than an actual change in fixation behaviour, we attribute this difference to a higher number of seen presentations in healthy subjects, which is a consequence of the way threshold strategies probe VF sensitivity^{7, 33}. This is also corroborated by the finding that the 10-2 MD was positively correlated with the 95% BCEA in glaucoma subjects (larger for more initial damage), but such a relationship was not significant when evoked displacements were removed. Notably, all glaucoma subjects were experienced test takers. We then found that the projection error of stimulus presentations preceded by an evoked displacement was significantly increased compared to the rest of the presentations ($p < 0.001$, **Figure 3.4**). This is not an obvious result, as the time interval between presentations (**Table 3.2**) could allow subjects to return to central fixation. Previous work investigating fixation area in fundus perimetry found a significantly increased 95% BCEA in glaucoma patients^{30, 31}. In a previous study²³, however, we analysed data from the PRL assessment phase in the CMP on a different dataset and found no difference between healthy subjects and glaucoma patients, irrespective of their level of damage. However, there was a significant difference in other fixation metrics²³. This is confirmed by the results of this study, as no difference was found in the 95% BCEA between glaucoma and healthy subjects. Interestingly, Longhin et al.³⁰ reported an increase in BCEA during the perimetric test, compared to the initial PRL assessment phase, during which time no stimuli are projected. They speculated that this spread in fixation area could be the effect of projected stimuli attracting fixation, and this is consistent with our findings. Another component of the error that we analysed was the fixation bias. We could not find a statistically significant difference between healthy subjects and patients with glaucoma ($p = 0.12$). Yet, removing the fixation bias significantly reduced the projection error in both groups, with a significantly larger effect in glaucoma patients ($p < 0.001$). This apparent discrepancy can be explained by the sample size, since in the first analysis it is limited to the number of subjects included in the study ($N = 47$), whereas the second result is based on the analysis of each presentation from the VF tests on those subjects ($N = 14343$ data points). This finding has important consequences. Regarding structure-function analyses, it obviously challenges the notion that the centre of the perimetric grid should be centred on the fovea when mapping perimetric thresholds onto structural data. Similar results have been shown for patients with other optic neuropathies with central damage³⁹. This issue can be addressed by fundus perimetry, as the position of the stimulus projection is known with higher precision and can be used to obtain more accurate mapping^{16, 22}. Other solutions might include methods based on structural analyses of the macular damage or on ad-hoc fixation analyses derived from other fundus tracking devices, such as the Spectralis³⁹. Additionally, such a consistent shift in fixation has important consequences for deriving normative databases in perimetry. At present, the additional variability introduced by a fixation bias, which effectively changes the location of the projected stimuli, is not taken into account. It has to be noted that this latter issue is not solved by fundus tracked perimetry, since the centre of the perimetric grid is determined by an initial functional assessment of

the PRL. One possible solution would be to integrate fundus perimetry and OCT imaging to detect the location of the anatomical fovea and ensure that this is used as the centre of the perimetric grid instead.

We also showed that the error can be reliably predicted from the fixation track (**Figure 3.5**). This could be useful for researchers not using fundus perimetry to determine the amount of error in their measurements. In fact, the fixation tracks produced by fundus perimetry can be easily related to similar graphs produced by traditional perimeters with pupillary fixation monitors. A method for the quantitative analysis of these tracks has been proposed by Ishiyama et al.^{34, 35}, for example. However, studies are needed to establish the exact correspondence between the results of fundus and pupillary tracking.

Finally, it is important to notice that our work did not aim at quantifying the effect of eye movements on perimetric sensitivity. We instead estimated the error induced by fixation and artificial grid rotation when reporting retinal sensitivities onto structural maps. Previous work thoroughly investigated the effect of eye movements on perimetric sensitivity⁴⁰⁻⁴². Also, in our previous report on the CMP²⁸, we showed that, despite improving test-retest variability for global indices, fundus tracking had only a modest effect on discrimination ability compared to traditional perimetry. However, our previous study compared two different devices, with two different testing strategies, using a 24-2 grid, whose locations are 6 degrees apart²⁸. This could have limited the detection of the impact of tracking. In fact, even with very chaotic fixation (**Figure 3.3 C**), errors ≥ 6 degrees are extremely unlikely (0.2% in our sample, compared to 3.8% ≥ 2 degrees, see **Appendix, Figure 3.6**). A more precise quantification of the effect of fundus tracking on perimetric sensitivity and test-retest variability using a 10-2 grid will be the objective of future work.

3.4.3. Limitations

One limitation of our work is the relatively small sample size. This might have prevented the detection of significant differences in some fixation metrics between healthy subjects and glaucoma patients (e.g., the fixation bias caused by central glaucoma damage). However, we exploited the large amount of information contained in each VF test by analysing each projection, increasing the statistical power as much as possible. Like for many other fundus tracking device, CMP fundus tracking speed of only 25 Hz is a technical limitation for our study. Therefore, we were only able to analyse fixation up to this resolution and faster eye movements are likely to have gone undetected. Faster tracking is available with pupillary monitors⁴³. However, these have the disadvantage of not using retinal images as a reference, eliminating an essential piece of information for our analyses. Nevertheless, further studies using pupillary tracking would be extremely useful to better characterise the effect of evoked displacements both on projection accuracy and on fixation metrics, such as the BCEA.

Finally, the structural and functional tests were not performed through the same optical system but instead relied on a post-hoc matching of fundus images from two devices. This could induce further uncertainty and could only be solved with an integrated OCT - fundus perimeter system⁴⁴.

3.5. Appendix

3.5.1. Identification of evoked displacements

For each exam, the fixation track was matched with the sequence of the presentations, which reported the intensity, the location and the time of the stimulus projections. The whole fixation track was subdivided into segments delimited by projections times. For example, the fixation segment between the onset of one stimulus (t_0) and the following projection (t_1) was assigned to the projection started at t_0 . Fundus tracking ensured that the stimuli were projected at the intended retinal location (relative to the PRL) Therefore, for each segment the coordinates of the first position were subtracted from the rest of the segment positions. Therefore, all the following positions within a segment were referenced to the last tracked position before the presentation of the stimulus, set as zero. For each presentation, the displacement was calculated as the maximum distance from zero reached within the fixation segment (**Figure 3.6 A**). To quantify how much each displacement was directed toward the stimulus, d the orthogonal projection of the displacement onto a line joining the centre of the grid (the initial PRL) with the location of the stimulus was calculated (**Figure 3.6 A**). We named this the concordant displacement (CD). So, a displacement exactly reaching the stimulus location would produce the maximum CD, whereas displacements at 90 degrees with respect to the stimulus direction would produce a null CD. Finally, a displacement pointing in the opposite direction would produce a negative CD. These values can then be used to build a graph where the vertical axis reports the CD (in degrees) and the horizontal axis reports the intensity of the stimulus projection at each location as a difference from the final threshold determined for that same location (in dB, **Figure 3.6 B**). Therefore, negative values in the horizontal axis indicate stimulus intensities dimmer than threshold while positive values indicate intensities brighter than threshold.

To detect significantly positive CDs, indicating evoked displacements, we estimated the individualised noise from the negative part of the graph on the vertical axis, under the assumption that negative CDs were just a consequence of random gaze movements during the projection of the stimuli. Hence, we calculated a 5% noise threshold that was then reflected on the positive part of the graph. We considered as evoked displacements all the segments with a CD value above the noise threshold and evoked by a projection within at least 10 dB below threshold (-10 dB on the graph, **Figure 3.6 B**). It is important to notice that this filter does not simply remove large gaze movements based on their magnitude but only acts on those that are likely caused by stimulus projections.

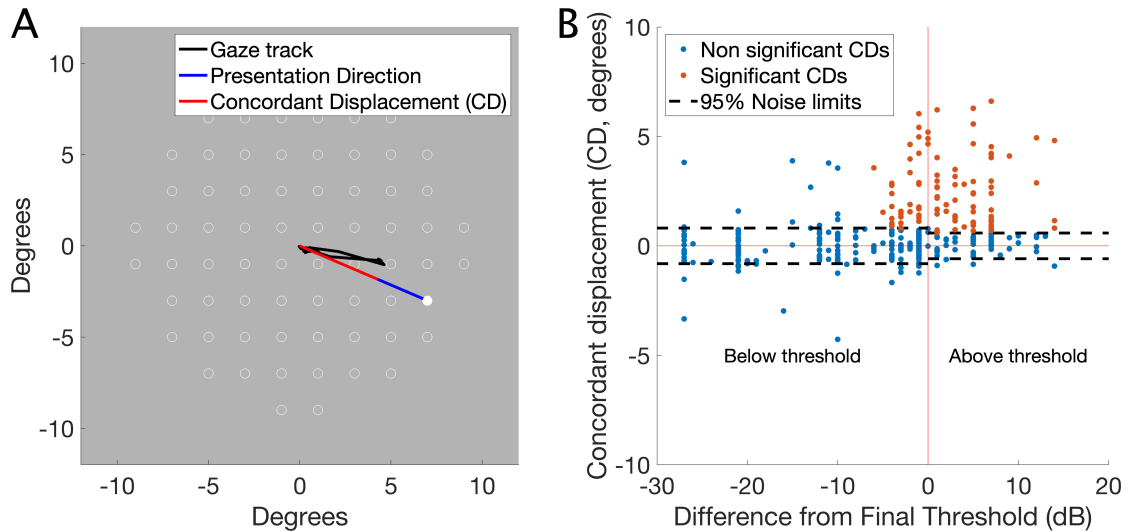


Figure 3.6 Calculation of concordant displacements A) The red track represents in the top image represents the gaze displacement evoked by the projection of the stimulus, indicated by the solid white dot, overlaid to the fundus image. The bottom graph shows the same displacement (in blue) in visual field coordinates. The black segment represents the PRL – stimulus direction, while the red segment represents the orthogonal projection of the maximum displacement on the black segment (the concordant displacement, CDs). B) Red dots represent the significant positive CDs (evoked by the stimulus). Dashed lines represent the 95% noise limits calculated from the negative CDs and reflected on the positive upper half of the graph. Different noise levels were calculated for projections below (negative on the horizontal axis) and above (negative on the horizontal axis) the threshold.

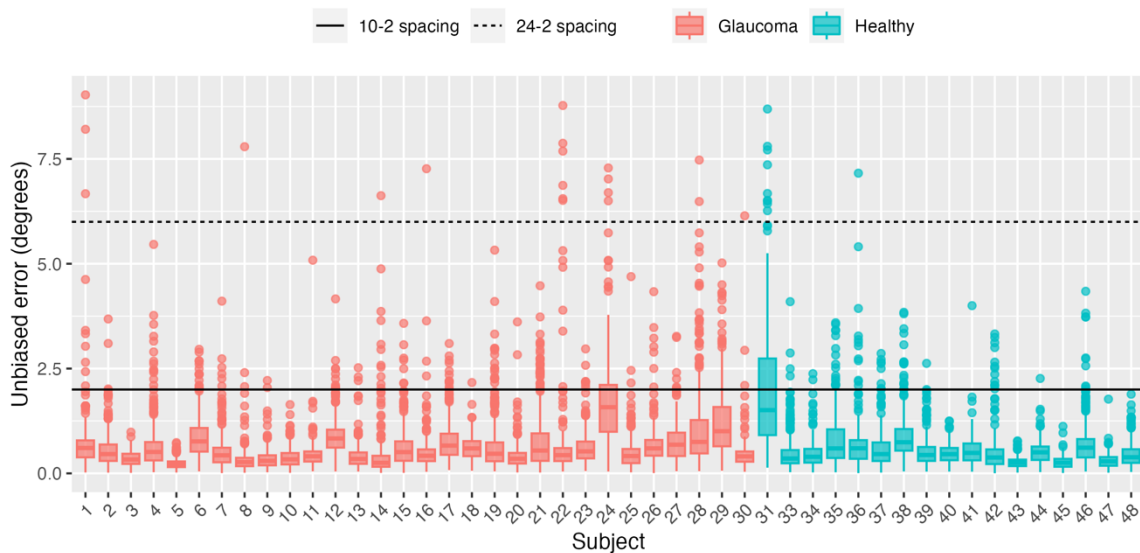


Figure 3.7 Box-plots of the unbiased error for each subject. The boxes include the interquartile range, the whiskers extend to the 95% quantiles and the horizontal midline represents the median. The two horizontal black lines represent the spacing between locations of a 10-2 grid and of a 24-2 grid as a reference.

3.6. References

1. Yoshioka N, Zangerl B, Phu J, et al. Consistency of Structure-Function Correlation Between Spatially Scaled Visual Field Stimuli and In Vivo OCT Ganglion Cell Counts. *Investigative ophthalmology & visual science* 2018;59:1693-1703.
2. Miraftebi A, Amini N, Morales E, et al. Macular SD-OCT Outcome Measures: Comparison of Local Structure-Function Relationships and Dynamic Range. *Investigative ophthalmology & visual science* 2016;57:4815-4823.
3. Bussell, II, Wollstein G, Schuman JS. OCT for glaucoma diagnosis, screening and detection of glaucoma progression. *Br J Ophthalmol* 2014;98 Suppl 2:ii15-19.
4. Weinreb RN, Aung T, Medeiros FA. The pathophysiology and treatment of glaucoma: a review. *JAMA* 2014;311:1901-1911.
5. Garway-Heath DF, Hitchings RA. Quantitative evaluation of the optic nerve head in early glaucoma. *Br J Ophthalmol* 1998;82:352-361.
6. Malik R, Swanson WH, Garway-Heath DF. 'Structure-function relationship' in glaucoma: past thinking and current concepts. *Clinical & experimental ophthalmology* 2012;40:369-380.
7. Turpin A, McKendrick AM, Johnson CA, Vingrys AJ. Properties of perimetric threshold estimates from full threshold, ZEST, and SITA-like strategies, as determined by computer simulation. *Investigative ophthalmology & visual science* 2003;44:4787-4795.
8. Hood DC, Raza AS, de Moraes CG, Liebmann JM, Ritch R. Glaucomatous damage of the macula. *Progress in retinal and eye research* 2013;32:1-21.
9. Zeimer R, Asrani S, Zou S, Quigley H, Jampel H. Quantitative detection of glaucomatous damage at the posterior pole by retinal thickness mapping. A pilot study. *Ophthalmology* 1998;105:224-231.
10. Traynis I, De Moraes CG, Raza AS, Liebmann JM, Ritch R, Hood DC. Prevalence and nature of early glaucomatous defects in the central 10 degrees of the visual field. *JAMA ophthalmology* 2014;132:291-297.
11. Wu Z, Medeiros FA, Weinreb RN, Zangwill LM. Performance of the 10-2 and 24-2 Visual Field Tests for Detecting Central Visual Field Abnormalities in Glaucoma. *American journal of ophthalmology* 2018.
12. De Moraes CG, Hood DC, Thenappan A, et al. 24-2 Visual Fields Miss Central Defects Shown on 10-2 Tests in Glaucoma Suspects, Ocular Hypertensives, and Early Glaucoma. *Ophthalmology* 2017;124:1449-1456.
13. Grillo LM, Wang DL, Ramachandran R, et al. The 24-2 Visual Field Test Misses Central Macular Damage Confirmed by the 10-2 Visual Field Test and Optical Coherence Tomography. *Translational vision science & technology* 2016;5:15.
14. Kim S, Lee JY, Kim SO, Kook MS. Macular structure-function relationship at various spatial locations in glaucoma. *The British journal of ophthalmology* 2015;99:1412-1418.
15. Ohkubo S, Higashide T, Udagawa S, et al. Focal relationship between structure and function within the central 10 degrees in glaucoma. *Investigative ophthalmology & visual science* 2014;55:5269-5277.
16. Montesano G, Rossetti LM, Allegrini D, Romano MR, Crabb DP. Improving Visual Field Examination of the Macula Using Structural Information. *Translational vision science & technology* 2018;7:36.
17. Matsuura M, Murata H, Fujino Y, Hirasawa K, Yanagisawa M, Asaoka R. Evaluating the Usefulness of MP-3 Microperimetry in Glaucoma Patients. *American journal of ophthalmology* 2018;187:1-9.
18. Drasdo N, Millican CL, Katholi CR, Curcio CA. The length of Henle fibers in the human retina and a model of ganglion receptive field density in the visual field. *Vision research* 2007;47:2901-2911.
19. Turpin A, Chen S, Sepulveda JA, McKendrick AM. Customizing Structure-Function Displacements in the Macula for Individual Differences. *Investigative ophthalmology & visual science* 2015;56:5984-5989.
20. Greenstein VC, Santos RA, Tsang SH, Smith RT, Barile GR, Seiple W. Preferred retinal locus in macular disease: characteristics and clinical implications. *Retina* 2008;28:1234-1240.
21. Hanout M, Horan N, Do DV. Introduction to microperimetry and its use in analysis of geographic atrophy in age-related macular degeneration. *Current opinion in ophthalmology* 2015;26:149-156.
22. Montesano G, Fogagnolo P, Digiuni M, Rossetti LM. How glaucoma shapes fixation: structure-function analysis using COMPASS fundus perimeter and SD-OCT. *Investigative ophthalmology & visual science* 2017;58:5827-5827.
23. Montesano G, Crabb DP, Jones PR, Fogagnolo P, Digiuni M, Rossetti LM. Evidence for alterations in fixational eye movements in glaucoma. *BMC ophthalmology* 2018;18:191.
24. Crossland MD, Dunbar HM, Rubin GS. Fixation stability measurement using the MP1 microperimeter. *Retina* 2009;29:651-656.

25. Crossland MD, Sims M, Galbraith RF, Rubin GS. Evaluation of a new quantitative technique to assess the number and extent of preferred retinal loci in macular disease. *Vision research* 2004;44:1537-1546.
26. Rossetti L, Digiuni M, Rosso A, et al. Compass: clinical evaluation of a new instrument for the diagnosis of glaucoma. *PloS one* 2015;10:e0122157.
27. Fogagnolo P, Modarelli A, Oddone F, et al. Comparison of Compass and Humphrey perimeters in detecting glaucomatous defects. *European journal of ophthalmology* 2016;26:598-606.
28. Montesano G, Bryan SR, Crabb DP, et al. A Comparison between the Compass Fundus Perimeter and the Humphrey Field Analyzer. *Ophthalmology* 2018.
29. Rohrschneider K, Bultmann S, Springer C. Use of fundus perimetry (microperimetry) to quantify macular sensitivity. *Progress in retinal and eye research* 2008;27:536-548.
30. Longhin E, Convento E, Pilotto E, et al. Static and dynamic retinal fixation stability in microperimetry. *Canadian journal of ophthalmology Journal canadien d'ophtalmologie* 2013;48:375-380.
31. Shi Y, Liu M, Wang X, Zhang C, Huang P. Fixation behavior in primary open angle glaucoma at early and moderate stage assessed by the MicroPerimeter MP-1. *Journal of glaucoma* 2013;22:169-173.
32. Montesano G, Gervasoni A, Ferri P, et al. Structure-function relationship in early diabetic retinopathy: a spatial correlation analysis with OCT and microperimetry. *Eye* 2017;31:931-939.
33. King-Smith PE, Grigsby SS, Vingrys AJ, Benes SC, Supowit A. Efficient and unbiased modifications of the QUEST threshold method: theory, simulations, experimental evaluation and practical implementation. *Vision research* 1994;34:885-912.
34. Ishiyama Y, Murata H, Asaoka R. The Usefulness of Gaze Tracking as an Index of Visual Field Reliability in Glaucoma Patients. *Investigative ophthalmology & visual science* 2015;56:6233-6236.
35. Ishiyama Y, Murata H, Mayama C, Asaoka R. An objective evaluation of gaze tracking in Humphrey perimetry and the relation with the reproducibility of visual fields: a pilot study in glaucoma. *Investigative ophthalmology & visual science* 2014;55:8149-8152.
36. Pavlou M, Ambler G, Seaman S, Omar RZ. A note on obtaining correct marginal predictions from a random intercepts model for binary outcomes. *BMC Medical Research Methodology* 2015;15:59.
37. Rizopoulos D. GLMMadaptive: Generalized Linear Mixed Models using Adaptive Gaussian Quadrature. 2020.
38. Bates D, Mächler M, Bolker B, Walker S. Fitting Linear Mixed-Effects Models Using lme4. *Journal of Statistical Software* 2015;67.
39. Mallery RM, Poolman P, Thurtell MJ, et al. The Pattern of Visual Fixation Eccentricity and Instability in Optic Neuropathy and Its Spatial Relationship to Retinal Ganglion Cell Layer Thickness. *Investigative ophthalmology & visual science* 2016;57:OCT429-437.
40. Demirel SJ, CA; Fendrich, R; Vingrys, AJ. The slope of frequency-of-seeing curves in normal amblyopic and pathologic vision. *Vision science and its applications. J Opt Soc Am Technical Digest Series* 1997;244-247.
41. Fendrich RW, CM; Marshall, D; Johnson, CA. Stabilized image perimetry: Evaluating the influence of eye movements on perimetry data. *Vision science and its applications. J Opt Soc Am Technical Digest Series* 1995;254-257.
42. Henson DB, Evans J, Chauhan BC, Lane C. Influence of fixation accuracy on threshold variability in patients with open angle glaucoma. *Investigative ophthalmology & visual science* 1996;37:444-450.
43. Asfaw DS, Jones PR, Monter VM, Smith ND, Crabb DP. Does Glaucoma Alter Eye Movements When Viewing Images of Natural Scenes? A Between-Eye Study. *Investigative ophthalmology & visual science* 2018;59:3189-3198.
44. Anastasakis A, McAnany JJ, Fishman GA, Seiple WH. Clinical value, normative retinal sensitivity values, and intrasession repeatability using a combined spectral domain optical coherence tomography/scanning laser ophthalmoscope microperimeter. *Eye (Lond)* 2011;25:245-251.

4. Evidence for structural and functional damage of the inner retina in diabetes with no diabetic retinopathy

This paper applied the methodology developed in the previous two chapters and an established neural model of perimetric sensitivity to investigate early neuronal damage in diabetic patients without diabetic retinopathy. The paper found that, despite significant changes in the thickness of the inner retinal layers, diabetic patients did not display a statistically significant perimetric loss. Importantly, the structure-function relationship between perimetric sensitivity and structural estimates of RGC counts was compatible with partial summation conditions. We hypothesised that this was the reason behind the structure-function discrepancy: a substantial loss of RGCs from neuronal damage can result in a small change in perimetric sensitivity when tested with relatively large stimuli. We then calculated that smaller stimuli, for the same amount of estimated RGC loss, might have been able to highlight the functional damage from diabetes. This paper highlighted the importance of an appropriate choice of perimetric stimuli to improve functional testing and optimise structure-function concordance in the macula. The results were published in *Investigative Ophthalmology & Visual Science* (IOVS), a journal of the Association for Research in Vision and Ophthalmology (ARVO). The paper is freely available at: <https://iovs.arvojournals.org/article.aspx?articleid=2772422>.

Contributions

- *Main contributor:* **Giovanni Montesano** (conceptualisation of research, data and statistical analysis, interpretation of the data, drafting of the manuscript).
- *Other contributors:*
 - **Giovanni Ometto** (data analysis, interpretation of the data, manuscript proofing)
 - **Bethany E. Higgins** (interpretation of the data, manuscript proofing)
 - **Radha Das** (manuscript proofing)
 - **Katie W. Graham** (manuscript proofing)
 - **Usha Chakravarthy** (interpretation of the data, manuscript proofing)
 - **Bernadette McGuinness** (data collection, manuscript proofing)
 - **Bethany E. Higgins** (interpretation of the data, manuscript proofing)
 - **Ian S. Young** (project funding, manuscript proofing)
 - **Frank Kee** (project management, manuscript proofing)
 - **David M. Wright** (interpretation of the data, manuscript proofing)
 - **David P. Crabb** (supervision, interpretation of the data, manuscript proofing)
 - **Ruth E. Hogg** (supervision, interpretation of the data, manuscript proofing)

4.1. Introduction

Diabetic retinopathy (DR) is the leading cause of blindness worldwide in working-age adults¹⁻³. The role of vascular damage and new vessel proliferation is widely recognised and is ultimately responsible for the loss of sight^{1, 3}. However, recent evidence suggests that direct retinal neuronal damage in diabetic patients might precede evident changes to the

retinal blood vessels⁴ and be a risk factor for progression to DR⁵. The damage mainly manifests as Retinal Ganglion Cell (RGC) loss through apoptosis, resembling other neuro-degenerative diseases⁶⁻⁸.

Both functional and structural evidence has been provided to support RGC loss in diabetic patients. Several imaging studies, earlier with scanning laser polarimetry⁹⁻¹¹ and more recently with Spectral Domain Optical Coherence Tomography (SD-OCT), observed thinning of the Ganglion Cell Layer (GCL), Retinal Nerve Fibre Layer (RNFL) and Inner Plexiform Layer (IPL) in patients with minimal or no vascular diabetic retinopathy^{4, 12-17}. A wide array of tests have also been employed to detect the functional implications of such structural changes. Besides visual acuity, reported in almost all studies, functional tests have included Pelli-Robson contrast sensitivity¹⁸⁻²⁰, microperimetry²⁰⁻²⁴, Rarebit perimetry^{18, 25, 26}, Frequency Doubling Technology perimetry (FDT)^{18, 19, 27-29}, Standard Automated Perimetry (SAP)^{18, 28-31} and quick contrast sensitivity function (qCSF)¹⁸. All these functional assessments have been able to show, to a different extent, some degree of functional impairment in patients with diabetes mellitus (DM) with no or minimal DR when compared to people without DM. Microperimetry is particularly appealing for its high spatial accuracy and has been used for topographical structure-function mapping of early diabetic damage^{20, 22}. FDT perimetry has also shown promising results in this context and is particularly valuable for its sensitivity to inner retina damage^{19, 32}. Jackson et al.¹⁹, Parravano et al.²⁹, Joltikov et al.¹⁸ and Bao et al.²⁷ all reported reduced sensitivity to FDT stimuli in patients with early or no DR.

Many of these effects on visual function are, however, subtle and difficult to identify. Although structural analyses on large databases of OCT scans exist^{16, 17}, functional tests have been performed on much smaller cohorts, especially when considering diabetic people with no vascular damage. The only large scale functional testing results in people with DM and no DR come from a screening survey performed in the United States²⁷ with a suprathreshold FDT test. The study confirmed the usefulness of FDT as an indicator of early inner retinal damage in diabetes. However, the absence of measured sensitivity thresholds and structural data prevented a comprehensive quantification of the structural and functional damage and their relationship.

In this work, we use prospectively collected structural (SD-OCT) and functional data from a large cohort of healthy people and diabetic patients with no DR to characterise early neuronal damage in diabetes. The data are part of a population-based collection, the Northern Ireland Sensory Ageing (NISA) study (<https://clinicaltrials.gov/ct2/show/NCT02788695>), conducted at Queen's University Belfast (QUB). The functional data include Best Corrected Visual Acuity (BCVA), Pelli-Robson log₁₀ Contrast Sensitivity (PR-logCS), microperimetry and FDT threshold perimetry. We use these data to test the hypothesis that structural and functional damage of the inner retina is present in DM prior to clinically evident vascular changes.

4.2. Methods

4.2.1. Data collection

The NISA study (<https://clinicaltrials.gov/ct2/show/NCT02788695>) is a follow-up to the NICOLA study (<https://www.qub.ac.uk/sites/NICOLA/>), a prospective population based study of early imaging and functional biomarkers of DR and age-related macular degeneration (AMD). The selection steps are illustrated in a flowchart in the **Appendix**. The NICOLA study

involved a computer assisted home interview followed by a health assessment at the Northern Ireland Clinical Research Facility (NICRF), including an evaluation of eye health. People from the NICOLA cohort with at least one of the following characteristics were invited for the NISA follow-up data collection: 1) no retinal diseases; 2) self-reported diagnosis of DM either during the home interview or the health assessment; 3) early or intermediate AMD. The sample of diabetic people (type I or type II) was then extended with patients recruited directly from the Belfast Trust Diabetic Retinopathy Hospital Clinics at QUB. Participants underwent Best Corrected Visual Acuity (BCVA) test with an Early Treatment Diabetic Retinopathy Study (ETDRS) chart, PR-logCS test with a Pelli-Robson chart, microperimetry and FDT perimetry (described in detail in the following paragraphs), an SD-OCT scan (described in detail in the next paragraph), fundus colour picture (CX-1 Digital Fundus Camera, Canon U.S.A., Inc, Tokyo, Japan), colour Ultra Wide Field Imaging (UWFI) images centred on the fovea (Optomap Panoramic 200Tx scanning laser ophthalmoscope, Optos PLC, Dunfermline, Scotland, UK) and a measurement of axial length (AL, Lenstar LS 900 Biometer, Haag-Streit AG, Switzerland). Lens opacity in phakic eyes was graded with a Pentacam Scheimpflug System (Oculus, Wetzlar, Germany) using the Pentacam Nucleus Staging (PNS) classification³³. All imaging was performed after pharmacological dilation with tropicamide 1%. For all participants, the eye with better BCVA was selected for the study, choosing at random if they were both eligible.

Fundus colour pictures for all participants were classified by two graders (authors RD and UC) to identify signs of AMD (Beckmann classification³⁴) and DR. Disc and macula colour images and UWFI were assessed for characteristic DR features in the central and peripheral retina and then staged using the national screening for DR system for England and Wales into four levels: none (R0), background (R1), pre-proliferative (R2) and proliferative (R3). Subjects not recruited from the DR clinic were identified as diabetic if they self-reported a diagnosis of diabetes mellitus. The duration of the disease was also recorded when provided. All subjects over 50 years of age and all diabetic patients were also invited to have a blood sample taken to measure the concentration of plasma glycated haemoglobin (HbA1C). Participants with no record of diabetes were classified as diabetic if the HbA1C was $\geq 6.5\%$. Refusal to have the blood sample taken did not prevent inclusion.

Only healthy subjects (starting N = 406) or diabetic patients classified as R0 (starting N = 159) were considered for this analysis. Eyes with intermediate or advanced AMD were excluded (N = 17). People with signs of early AMD were included in the analysis to avoid over-selection of participants, especially for the no DM cohort. Of the remaining 548, we only selected people for whom either microperimetry or FDT was available (N = 545). Hence, the following selection steps were applied to a starting sample of 395 healthy participants and 150 diabetic patients.

4.2.1.1. SD-OCT Scans

Structural data were collected using a Spectralis SD-OCT (Heidelberg Engineering, Heidelberg, Germany). A macular volume scan was acquired for each study eye. The volume was composed of 61 horizontal B-Scans (ART 9) covering a rectangular patch 30 x 25 degrees tilted by 7 degrees (counter-clockwise for right eyes, clockwise for left eyes) to match the average inclination of the fovea-disc axis (**Figure 4.1**). The scans were tracked on the retina using a Scanning Laser Ophthalmoscope (SLO) which continuously captured an infrared fundus picture to compensate for eye movements. A circumpapillary RNFL (cp-RNFL) scan was also collected for the study eye. All images were evaluated by two graders (authors RD &

UC) to identify poor quality scans and manually correct the segmentations where necessary. Poor quality was defined as the inability to accurately identify all retinal layers either because of low signal strength or because of partially or totally out-of-frame scans. An ophthalmologist (GM) visually inspected all scans from eyes that matched the inclusion criteria (described above) to identify people with vitreo-retinal alterations (such as vitreo-retinal tractions or epiretinal membranes), focal loss of the inner retina on macular scans or of the RNFL on the cp-RNFL scans (either from vascular occlusions or possible glaucoma), as well as diffused advanced cp-RNFL thinning and/or Optic Nerve Head (ONH) cupping likely attributable to glaucomatous damage. Standard white-on-white perimetry and a measurement of the intraocular pressure were not obtained for this data collection. Hence, a careful selection based on structural criteria was necessary. A total of 14 eyes were excluded due to poor quality of the scans, 10 due to the presence of vitreo-retinal diseases and 16 due to focal inner retinal loss or possible glaucoma. The same criteria were applied to cp-RNFL scans for participants whose macular scan was included, leading to the exclusion of 119/505 scans (14 from diabetic patients), all because of poor quality. The absence of a viable cp-RNFL did not prevent inclusion in the analysis. Hence, selection was only based on the macular scans. For the final selection of scans, the Median (Interquartile Range) Quality Index was 30.7 [28.9, 32.5] dB for the macular scans and 29.3 [23, 34.7] dB for the cp-RNFL scans.

4.2.1.2. Microperimetry

Microperimetric data were collected using a MAcular Integrity Assessment device (MAIA, CenterVue, Padua, Italy). The MAIA performs continuous infrared imaging of the retina to track and compensate for eye movements occurring during the test³⁵⁻³⁷. The test was performed in mesopic conditions (1.27 cd/m² background illumination) with an achromatic stimulus (0.43 degrees diameter) using a 4-2 staircase strategy. At the beginning of the test, a 10 second fixation trial was used to locate the Preferred Retinal Locus (PRL) of fixation, used as the centre of the perimetric grid. Notice that this might not coincide with the anatomical fovea. All tests were preceded by a training phase with the 'Fast' protocol to minimise learning effect. The grid was composed of 44 locations distributed on 5 concentric rings at 1, 2.3, 4, 6 and 10 degrees of eccentricity from the PRL. No exclusion was performed based on fixation metrics or blind spot responses since, given the use of fundus tracking, these metrics are unlikely to be related to the reliability of the test. Furthermore, in a previous analysis, we have shown both these metrics to be poor predictors of test-retest variability in microperimetry³⁸.

4.2.1.3. FDT perimetry

FDT data were collected with a Matrix device (Zeiss Meditec, Dublin, CA, USA). The test was performed with the 24-2 threshold program. The stimuli were 5-degree squares with a vertical sine wave grating (0.5 cycles/degree) counterphase flickered at 18 Hz. The threshold was measured using a Zippy Estimation through Sequential Testing (ZEST)³⁹ strategy. Only one eye per subject was tested (the same as microperimetry when both were performed). In contrast to microperimetry and standard SAP, Matrix FDT uses Michaelson's definition of contrast instead of Weber's⁴⁰. In the context of sinusoidal grating stimuli they are, however, equivalent⁴¹. Importantly, the Matrix FDT defines the sensitivity scale so that change of one log₁₀ unit of contrast corresponds to 20 dB, instead of 10 dB as in microperimetry and SAP⁴⁰. Two tests were excluded due to high false positive errors (> 33%).

4.2.2. Data analysis

4.2.2.1. Structural metrics

All OCT data were exported as RAW files (.vol) using the Heidelberg Eye Explorer. The files were then read in Matlab (The Mathworks, Natick, USA) using a custom-made code. The segmentations were used to generate thickness maps for the whole retina, the RNFL, the GCL, the IPL and the outer retina (from the outer limit of the IPL to the Bruch's membrane). The maps were interpolated and smoothed to match the size of the reference infrared fundus image (768 x 768 pixels, 30 x 30 degrees field of view), padding with zeros where the OCT data were missing, i.e. outside the scanning pattern. The interpolation was performed using a thin plate spline (*tpaps* function in Matlab) with anisotropic smoothing parameters, so that smoothing was stronger across B-scans than within a B-scan. The fovea was automatically identified through template matching. Correct detection was confirmed through visual inspection.

Topographic average thickness values for all layers were measured using a standard ETDRS grid, with three concentric rings of 1 mm, 3 mm and 6 mm external diameter. The two outermost rings were divided into four sectors (superior, inferior, nasal and temporal). The size of the grid was corrected for AL using our implementation of a schematic eye⁴² proposed by Drasdo and Fowler⁴³. The statistical analysis was performed in R (R Foundation for Statistical Computing, Vienna, Austria) using a linear mixed effect model with a random intercept to account for multiple measurements (different sectors) from the same eye. The response variable was the measured thickness and the model included a categorical fixed effect for the group (either healthy or diabetic), a categorical fixed effect for the sector, the interaction between the two fixed effects and age (years) as a continuous predictor. The p-values were corrected for multiple comparisons (N = 9 tests) with the Bonferroni-Holm method⁴⁴. Finally, global differences between the two groups across all sectors were tested for each layer by setting the sector as a crossed random effect. Global age corrected differences are reported as Estimate [95% Confidences Intervals (CIs)]. The alpha level was 0.05 for all analyses.

Cp-RNFL scans were corrected for ocular magnification using the formula provided by Kang et al.⁴⁵. However, such a compensation, and other similar methods proposed, introduce a positive correlation with AL which then needs to be accounted for in the analysis^{45, 46}. Therefore, when analysing the cp-RNFL scans, we included AL as a covariate, together with age.

4.2.2.2. Functional metrics

Microperimetric and FDT data were exported as XML files and read in Matlab. The mean sensitivity (MS) for MAIA tests was calculated excluding the foveal location, which was not used for the structure-function analysis (see later). The Matrix FDT provides a calculation of the global Mean Deviation (MD), Pattern Standard Deviation (PSD) and values for the point-wise sensitivity, total deviation (TD) and pattern deviation (PD). We additionally calculated the global MS as the average of the 52 locations within the 24-2 grid, excluding the two blind spot locations. Since our main analysis focussed on the macular region, we only used point-wise data for the 12 central locations (within 10 degrees from fixation). Global indices for the macula were also calculated as the average of the 12 corresponding central TD values (central Mean Deviation, cMD) and the central sensitivity values (central Mean Sensitivity, cMS). All statistical comparisons, including for BCVA and PR-logCS, were performed with simple multivariate linear models with age as a covariate, except for the MD and the

cMD which already account for normal ageing. BCVA was converted from letter counts to \log_{10} Minimum Angle of Resolution (logMAR) for analysis.

4.2.2.3. Structure-function relationship

For our main structure-function analysis, we focused on the GCL, assumed to be mostly composed of the bodies of the RGC neurons. The GCL thickness maps were transformed into estimates of local RGC density using the method proposed by Raza and Hood⁴⁷ and based on the histology maps by Curcio and Allen⁴⁸. The maps were corrected for axial length assuming a global expansion model, as previously described⁴². These density maps can then be used to derive customised local or global RGC counts.

4.2.2.3.1. Global structure-function relationship

The global structure-function relationship was studied using the MS for the MAIA and the cMD and cMS for the FDT. The functional metric was used as the response variable. The structural parameter was the total number of RGCs within 12 degrees from the fovea, covering the area tested by both the 12 central FDT and the MAIA grid after accounting for RGC displacements (see next paragraph). The MS for the MAIA and FDT tests was analysed using a multivariate model that included age as a covariate. The RGC counts were \log_{10} transformed prior to analysis to match the scale of perimetric data. This is also a widely applied method to relate RGC counts to perimetric sensitivities^{42, 49-51} (see also the **Appendix**). A secondary analysis of the correlation between global FDT MS with the average cp-RNFL (corrected for ocular magnification⁴⁵) thickness was also performed, with age and AL as covariates.

4.2.2.3.2. Topographic structure-function relationship

We used point-wise data to explore the local structure-function relationship at different eccentricities. The structural metric was the local RGC count corresponding to each location. We accounted for RGC displacement in the macular region using our generalised implementation⁴² of the model proposed by Drasdo et al.⁵². Instead of simply displacing the centre of the tested locations, we displaced the whole perimeter of the stimuli, since we have previously proven this to be the correct method to obtain accurate structurally derived RGC counts⁴² (**Figure 4.1**).

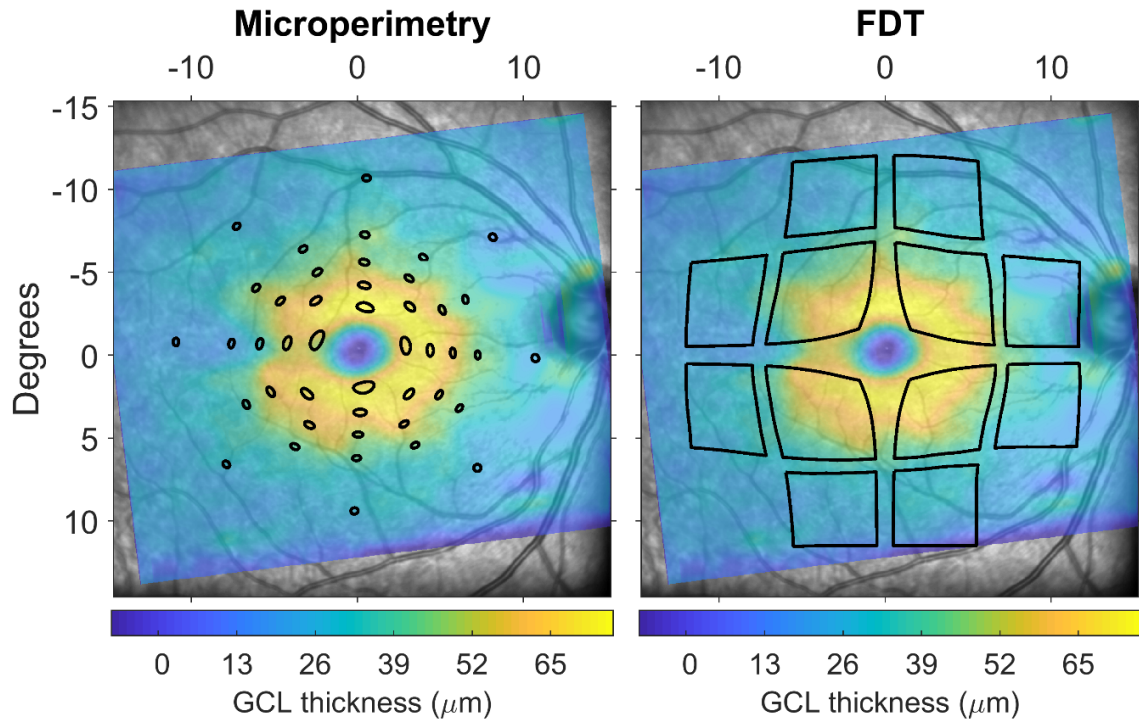


Figure 4.1 Schematic of the stimulus displacement applied for the topographic structure-function analysis, overlaid to the GCL thickness map from the Spectralis SD-OCT. Areas enclosed within the black lines were used for calculations. Microperimetric stimuli were mapped by aligning the fundus images from the MAIA and the Spectralis. FDT stimuli were centred on the fovea. FDT = Frequency Doubling Technology; GCL = Ganglion Cell Layer

Since the same RGC count could produce a different psychophysical sensation (i.e. sensitivity) at different eccentricities, especially in the perifoveal region, our structure-function models used a categorical fixed effect to account for eccentricity. An interaction term with the $\log_{10}(\text{RGC counts})$ also allowed for a different slope for each eccentricity. Finally, an interaction term between the eccentricity fixed effect and the group fixed effect (healthy or diabetic) allowed for formal testing of statistically significant differences in slopes between the two groups, which would indicate different change in sensitivities for the same change in RGC count. A more detailed explanation of the model and its interpretation is given in the **Appendix**. For FDT data, the categorical fixed effect identified each one of the 12 central locations as a separate level. For the MAIA, locations were instead grouped by their eccentricity from the PRL. Prior to analysis, the fundus image from the MAIA was matched with the SLO fundus picture from the Spectralis SD-OCT using an affine or projective transformation, so that the tested locations could be accurately reported onto the structural maps. The alignment was performed in Matlab and visually inspected (GM) to ensure it was correct. When incorrect, the alignment was repeated by placing manual landmarks on the two images. A satisfactory alignment could be obtained for all the included OCT/MAIA pairs. Manual intervention was required for 327/486 alignments.

4.3. Results

4.3.1. Sample description

Descriptive statistics of the selected sample are reported in **Table 4.1**. Some participants were unable to complete the entire imaging and functional testing protocol due to fatigue or time constraints. Only people with a viable macular scan and either the FDT or microperimetric test available were included. **Table 4.1** also reports the number of participants for whom each variable/test was available. Eleven participants (10 healthy) had an intraocular lens implant. Three healthy subjects and six diabetic patients had a PNS > 1. The AL was measured for 495 participants and was derived through linear regression from the spherical equivalent for the remaining 10 participants (none of whom were pseudophakic). Despite a small difference in the average age composition, the two groups largely overlapped and the main age clusters for diabetic patients were well represented in the healthy cohort. Microperimetry and FDT were available together for 412 participants (117 with DM). Thirteen subjects were diagnosed with diabetes during the study because of their HbA1C value. Nineteen patients in this cohort had type I diabetes. Twenty-three participants had signs of early AMD, all in the no DM cohort. The cp-RNFL scan was available for 386 people (118 with diabetes). All of these had performed the FDT test.

	No DM				DM			N (No DM/DM)
Age (years)	61 [51, 66]				67 [58, 72]			371/134
Sex (M:F)	208:163				88:46			371/134
Duration of diabetes (years)	-				0.20 [0.10, 0.43]			- /133
HbA1C (%)	5.57 [5.31, 5.89]				7.21 [6.52, 8.28]			271/118
Spherical equivalent (D)	0.38 [-0.75, 1.38]				0.38 [-0.62, 1.47]			369/134
Axial length (mm)	23.65 [22.96, 24.40]				23.49 [22.81, 24.15]			371/134
BCVA (logMAR)	-0.08 [-0.14, 0]				-0.02 [-0.08, 0.04]			371/133
PR-logCS (log)	1.65 [1.65, 1.65]				1.50 [1.50, 1.65]			370/133
MAIA (MS, dB)	27.23 [26.09, 28.11]				26.56 [25.42, 27.88]			360/126
FDT (Global MD, dB)	-1.53 [-3.45, 0.17]				-2.32 [-4.43, -0.05]			306/125
Age cluster (years)	< 30	30-39	40-49	50-59	60-69	70-79	> 80	
Healthy (N)	36 (10%)	23 (6%)	26 (7%)	84 (23%)	155 (42%)	45 (12%)	2 (1%)	
Diabetes (N)	3 (2%)	8 (6%)	3 (2%)	23 (17%)	47 (35%)	45 (34%)	5 (4%)	

Table 4.1 Descriptive statistics of the analysed sample. Continuous variables are reported as Median [Interquartile Range]. DM = Diabetes Mellitus; HbA1C = glycated haemoglobin plasma concentration; D = Dioptres; BCVA = Best Corrected Visual Acuity; logMAR = \log_{10} Minimum Angle of Resolution; PR-logCS = Pelli-Robson \log_{10} Contrast Sensitivity; MS = Mean Sensitivity; FDT = Frequency Doubling Technology; MD = Mean Deviation

4.3.2. Structural metrics

Global average thickness across all sectors was significantly reduced in patients with DM for the whole retina (difference estimate [95% CIs]: -3.47 [-6.09, -0.84] μm , $p = 0.010$), the GCL -1.04 [-1.74, -0.35] μm , $p = 0.003$) and the IPL (-1.89 [-3.09, -0.69] μm , $p = 0.002$). No significant difference was found for the RNFL (0.11 [-0.52, 0.74] μm , $p = 0.730$). The outer retina was generally thinner in the DM group, but this difference did not reach statistical significance (-1.65 [-3.37, 0.07] μm , $p = 0.061$). The total macular \log_{10} (RGC count) was also

significantly smaller in diabetic patients (0.011 [0.004, 0.019] log₁₀-unit reduction, $p = 0.036$). All comparisons were age-corrected by including age as a covariate, which was significantly negative correlated with the thickness of all retinal layers ($p < 0.001$). Sector differences are reported in **Figure 4.2**. Significant differences (Bonferroni-Holm corrected $p < 0.05$) were found for the GCL and IPL in all 3 mm ring sectors and for the 6 mm nasal sector for all layers except the RNFL. In the DM cohort, the thickness of none of the layers was significantly correlated with either the HbA1C or the duration of diabetes. The average cp-RNFL, compensated for ocular magnification⁴⁵ and corrected by age and axial length, was also significantly thinner in the DM cohort (-2.27 [-0.22, -4.64] μm , $p = 0.032$).

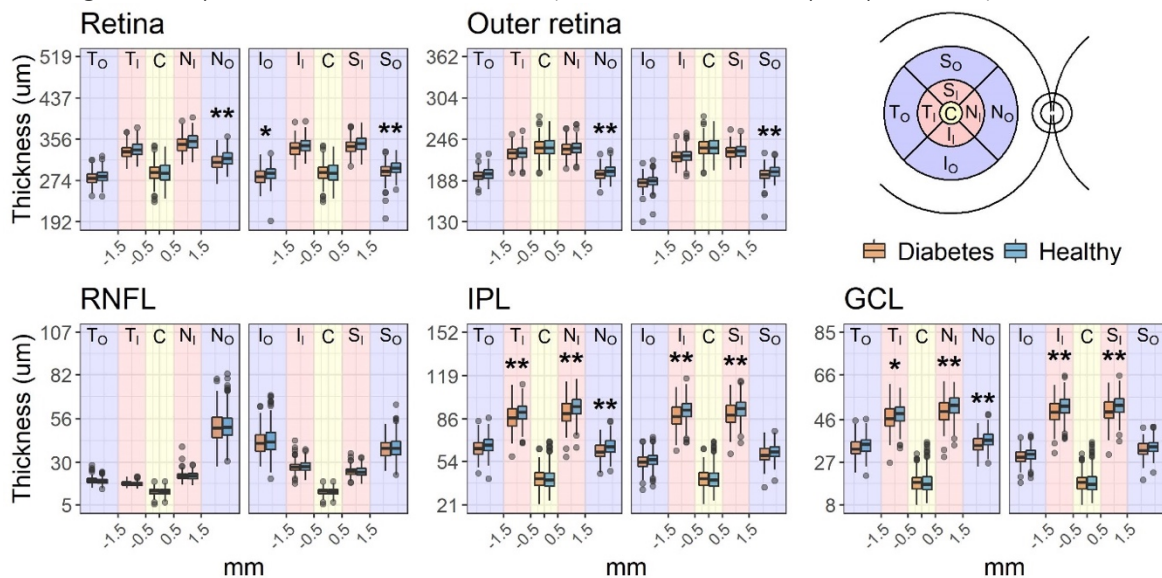


Figure 4.2 Box-plots of the average thickness values recorded for each ETDRS sector. The boxes enclose the interquartile range, the whiskers extend to the 95% quantiles. P -values corrected for 9 tests with the Bonferroni-Holm method for an age-corrected comparisons. * = $p < 0.05$; ** = $p < 0.01$; RNFL = Retinal Nerve Fibre Layer; GCL = Ganglion Cell Layer; IPL = Inner Plexiform Layer.

4.3.3. Functional metrics

Diabetic people had a significantly lower PR-logCS (age-corrected estimated difference: -0.09 [-0.11, -0.06], $p < 0.001$) and the BCVA (0.05 [0.03, 0.07] logMAR, $p < 0.001$). There was no significant difference in microperimetric MS in the age-corrected comparison (-0.21 [-0.52, 0.1] dB, $p = 0.188$). There was however a statistically significant difference in FDT cMD (-0.94 [-1.65, -0.23] dB, $p = 0.010$) and FDT MD (-0.83 [-1.53, -0.13], $p = 0.021$). A significant difference was also found for the age-corrected FDT cMS (-1.02 [-1.75, -0.28], $p = 0.007$). In the DM cohort, none of the functional metrics were significantly correlated with either the HbA1C or the duration of diabetes.

4.3.4. Structure-function relationship

4.3.4.1. Global structure-function relationship

A significant correlation with the total macular log₁₀(RGC Count) was found for the microperimetric MS ($p = 0.0212$) and for both central FDT metrics (cMD, $p = 0.002$; MS, $p < 0.001$). There was no significant difference in slopes between diabetic and healthy participants for either test ($p = 0.055$ for microperimetry; $p = 0.885$ for FDT cMD, $p = 0.894$ for FDT cMS).

The slope was steeper for the FDT cMD (13.3 dB/log₁₀(RGC Count)) and FDT cMS (15.5 dB/log₁₀(RGC Count)) than microperimetry MS (4.3 dB/log₁₀(RGC Count)). However, this result needs to be interpreted in the context of the different definitions of the dB scale used by the two devices (see Discussion) and considering the small loss in RGC count effectively observed for diabetic people in this sample (see previous paragraph). A significant difference in intercepts was found for the FDT cMS ($p = 0.030$) but not for FDT cMD ($p = 0.062$) and microperimetry MS ($p = 0.339$). The relationships with age-corrected microperimetric MS and FDT cMS are shown in **Figure 4.3**. There was a significant correlation between the average cp-RNFL and the global FDT MS (0.04 dB/ μm , $p = 0.028$). The relationship with the global MD, however, did not reach significance, despite being very similar in magnitude (0.03 dB/ μm , $p = 0.074$). All comparisons with MS were corrected for age in the statistical model. The average cp-RNFL was also compensated for ocular magnification⁴⁵ and corrected by AL.

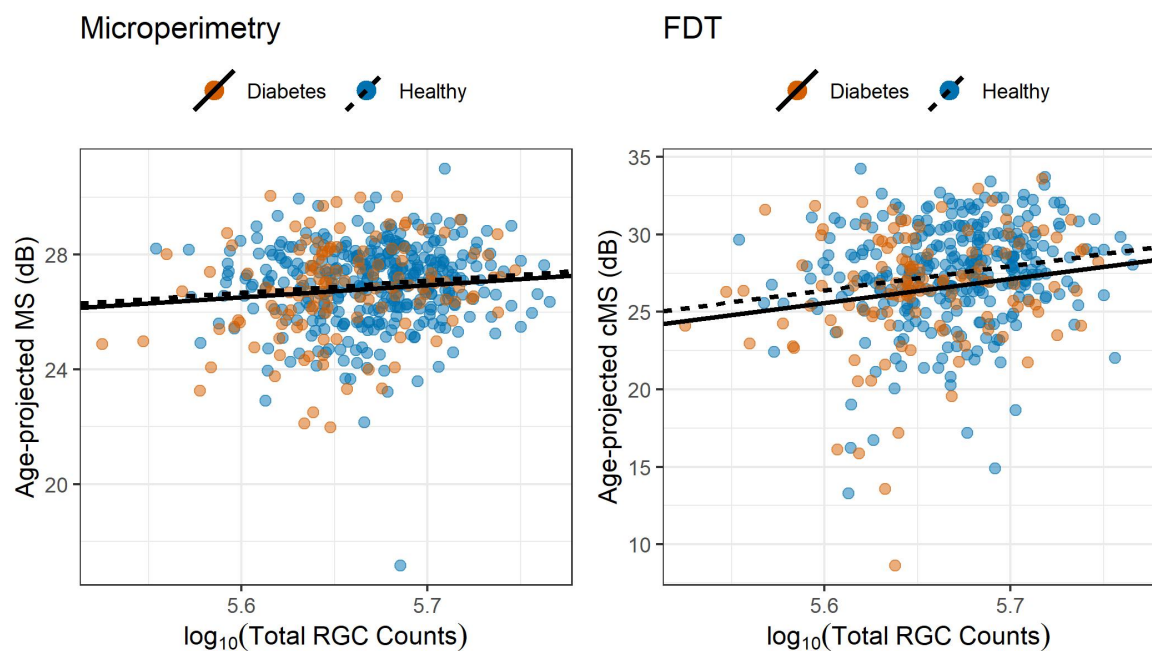


Figure 4.3 Scatter plot and regression lines for the global structure-function relationship. The regression lines have the same slope for both healthy and diabetic people. The total RGC count was calculated within the central 12 degrees from the fovea. The MS and cMS are projected to the average age of the sample (58 years old). RGC = Retinal Ganglion Cell; cMS = central Mean Sensitivity (12 central locations).

4.3.4.2. Topographic structure-function relationship

The point-wise structure-function slopes for microperimetry were shallow (**Figure 4.4**), as expected in partial summation condition (see **Appendix**). The slopes were however all statistically significant ($p < 0.05$) except at 1 degree of eccentricity ($p = 0.068$). The only significant difference in intercepts between healthy and diabetic patients was found at 1 degree ($p = 0.036$). As expected, there was no significant difference in slopes between healthy and diabetic patients ($p = 0.178$).

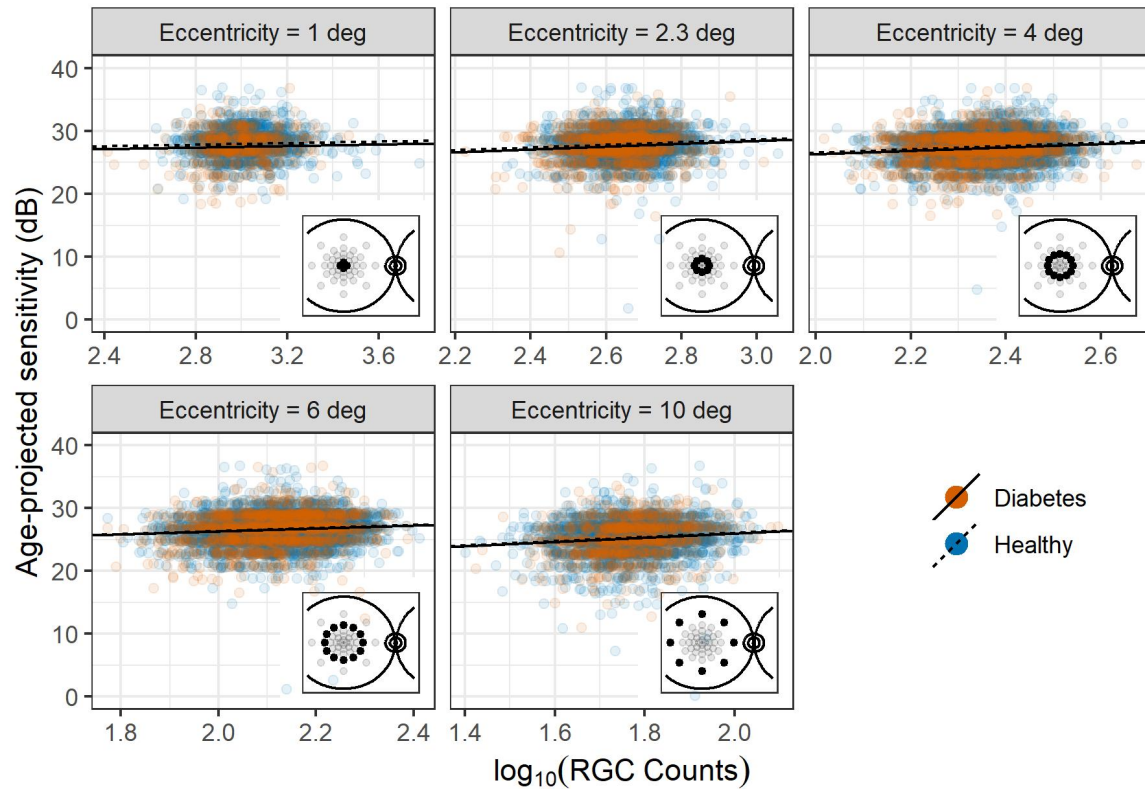


Figure 4.4 Scatter plot and regression lines for the topographic structure-function relationship for microperimetry The regression lines have the same slope for both healthy and diabetic patients. Local counts account for RGC displacement. The microperimetric sensitivity is projected to the average age of the sample (58 years old). RGC = Retinal Ganglion Cell.

The point-wise structure-function slopes for FDT sensitivity values (**Figure 4.5**) were also shallow. The significance for slopes and differences in intercepts between the two groups is reported in **Figure 4.5** for each location. A significant difference in intercepts was found for 5 locations. A significant structure-function slope was found for 9 locations. As expected, there was no significant difference in slopes between healthy and diabetic patients ($p = 0.270$).

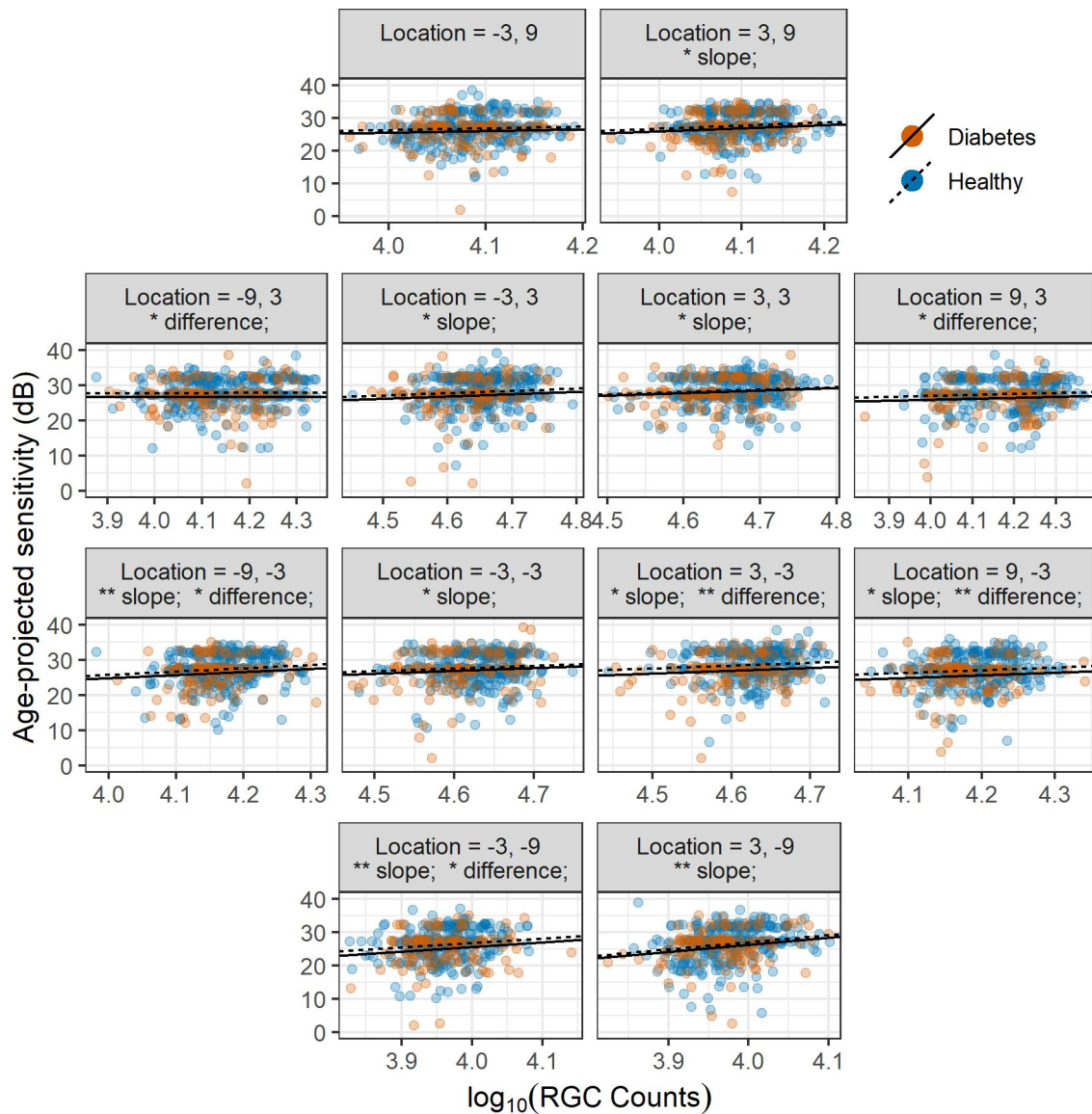


Figure 4.5 Scatter plot and regression lines for the topographic structure-function relationship for FDT. The regression lines have the same slope for both healthy and diabetic patients. Local counts account for RGC displacement. * = $p < 0.05$; ** = $p < 0.01$; RGC = Retinal Ganglion Cell; difference = difference in intercepts between healthy and diabetic patients.

4.4. Discussion

We analysed structural and functional data in a large number of patients with DM ($n = 134$) with no signs of DR and 371 healthy controls. Our results support the hypothesis of inner retinal loss prior to clinically evident vascular alterations in diabetes. Critically, we could test this hypothesis by excluding patients with DR allowing us to isolate the effect of early neuronal loss. Another strength of our study is that the diagnosis of DM for many of the diabetic patients was fairly recent (**Table 4.1**). This constitutes an optimal condition to study neuronal loss in its earliest phase, suggesting that it might happen soon after or even before the clinical diagnosis of DM. Another novel important aspect of our analysis is that the results are framed in the context of an accepted neural model for perimetric stimuli, which allowed us to provide a mechanistic interpretation of the observed structure-function

relationship rather than simply reporting statistical associations between structural and functional metrics. Such a model constitutes an accepted paradigm for glaucoma but has not been previously tested for early neuronal loss in diabetes.

4.4.1. Structural metrics

The largest significant reduction in retinal thickness was recorded for the GCL and IPL, with some mild, non-significant changes to the outer-retina. This is in agreement with previous findings, showing thinning of the inner retina in patients with no or mild DR^{4, 12-17}. Despite some local variations, the neural loss appeared mostly diffuse. However, most of the significant differences were found in sectors where the layer of interest is normally thicker, indicating a likely effect of a larger signal-to-noise ratio in areas where measurements are more robust and have more room for variation. Such a result is in agreement with Van Dijk et al.^{12, 13, 26}, who reported significant changes only in peri-foveal region. This can also explain the lack of observable differences in the RNFL, notoriously thin and difficult to measure in the macular region. Indeed, when the normally thicker cp-RNFL was analysed, a significant, albeit small, loss was identified in patients with DM. It is important to note that retinal thinning is not the only structural change observed in patients with DM and minimal DR. A comprehensive analysis by Gerendas et al.⁵³ showed GCL-IPL thickening and attributed it to initial diffuse swelling prior to the development of evident macular oedema. However, these findings pertained to patients with type-1 diabetes, including people with mild DR. Instead, in our study, we carefully focused our analysis on patients with no signs of DR to specifically examine evidence of neural degeneration. Our DM cohort only contained 19 patients with type-1 diabetes, too few to be analysed separately. However, despite not being significant, this group showed an average thinning of the GCL compared to the healthy subjects both in the raw (-0.47 μm) and age corrected (-1.28 μm) estimates, in agreement with the general trend for the DM cohort. Nevertheless, this is an important aspect to consider when interpreting the structure-function relationship (discussed later).

4.4.2. Functional metrics

In agreement with previous results¹⁸⁻²⁰, PR-logCS was significantly reduced in diabetic patients (19% average age-corrected reduction in CS). A significant reduction was also observed in the BCVA, although the effect was smaller (12% average age-corrected increase in MAR). Such a small difference might explain why this parameter failed to show significant differences in previous reports^{18, 20}.

Importantly, we found a significant reduction in sensitivity with FDT perimetry in diabetic patients, confirming and expanding previous findings. Previous studies were mainly limited by the small sample size and the lack of a specific analysis of the macular region^{18, 19, 27-29}. In our analysis, we showed that the differences between healthy and diabetic patients are larger for the central locations (cMD) than the whole field (MD). This strengthens the evidence for neural damage, since tests of the central visual field are usually more reliable⁵⁴. We did not find any significant differences between healthy and diabetic patients in the age-corrected MS with microperimetry, despite a significant correlation with the RGC count. This can be explained by a more careful analysis of the structure-function relationship (see next paragraph). Of note, the MAIA, differently from the Matrix FDT perimeter, does not provide deviation values, hence the need for statistical correction for age. However, the same age-corrected model used for the central FDT MS still showed a strongly significant difference between the two groups, ruling out a lack of power in the statistical approach.

Of course, one limitation of our dataset is the lack of either the FDT or the microperimetry data for some of the participants. This could have been avoided by only analysing complete data (76% of the overall sample, 88% of the diabetic cohort). However, we decided to include all participants that had performed at least one of the two perimetric tests to minimise the risk of bias and to maximise the power of our statistical analyses, conditioning our selection only on the presence of the macular OCT scan.

4.4.3. Structure-function relationship

One core aspect of our analysis was the detailed study of the structure-function relationship, especially in the macular region. This is important in order to interpret our findings in the context of accepted neural models for perimetric responses. Unlike previous reports^{18, 20, 26}, we transformed the measured GCL thickness into an estimate of RGC counts and this was a novel step. Such an approach allows a more direct interpretation of the functional findings in light of the observed structural changes. Both FDT and MAIA measurements showed a significant correlation with structural parameters in the global and topographical analyses. For the global parameters, the slopes were steeper (greater effect) for measurements from the FDT when compared to those from MAIA. However, it is important to keep in mind that the Matrix FDT equates one \log_{10} step to 20 dB instead of 10 dB. To transform the FDT values to the same scale as microperimetry, it is sufficient to divide sensitivity and slopes by 2. This calculation brings the structure-function slope observed for the FDT cMS with the total central RGC count to 7.75 dB/ \log_{10} (RGC count), much closer to the value observed for microperimetry (4.3 dB/ \log_{10} (RGC count)), but still steeper.

Despite both tests showing a significant correlation with structural parameters, with global and local measurements, only the FDT was able to show a significant difference between diabetic and healthy participants. The lack of significant differences for microperimetry can be explained by considering point-wise sensitivities and the effect of spatial summation on perimetric stimuli and this is worthy of some discussion here and in the **Appendix**. Indeed, the relationship between the number of RGCs and perimetric sensitivity becomes very shallow if the number of stimulated RGCs is larger than a critical amount (conventionally $> 10^{1.5}$ for SAP stimuli⁴⁹), reducing the ability of the test to discriminate early functional damage. This happens in the macular region for G-III stimuli (used in microperimetry) because of the high density of RGCs^{49, 50}. Total summation conditions could be obtained for the macula by changing the size or the duration of the stimuli^{49, 55}. This would be particularly valuable for detecting the effect of early neural degeneration in diabetes. In fact, under-sampling due to RGC loss is expected to have a greater effect on sensitivity for small test targets compared to large test targets (see appendix). However, FDT was able to discriminate between the two groups regardless of this limitation. Although such simple reasoning is more difficult to apply to FDT stimuli, the even larger stimulus size is likely to produce partial summation (see **Appendix**). One explanation for this difference is that FDT might be able to detect early cell dysfunction occurring in diabetic patients, in addition to the changes explained by pure structural loss. This is concordant with the finding that a significant difference in the intercepts was detected in the structure-function relationship for FDT metrics (with no significant differences in slope), effectively highlighting a residual functional defect in diabetic patients unexplained by structural changes. This residual defect could be the consequence of concomitant changes in the functionality of the outer retina. However, given the lack of significant thinning of the outer layers, this seems unlikely for our dataset. Of course, such a difference in intercepts could also be explained by the limitations of the structural OCT

measurements. One key assumption in our structure-function analyses is that changes in the measured thickness values accurately represent the loss of neural tissue. This is known not to be the case and is one of the reasons for the floor effect in structural measurements, especially with more advanced damage^{47, 56}. For example, our quantification of RGCs assumes that cellular density within a given volume of tissue remains constant and the change in RGCs is accurately reflected by the change in volume. Moreover, as previously mentioned, inner retinal tissue thickening has also been described⁵³ in diabetic patients, likely due to subtle swelling of the neural tissue. This would make our assumption of constant density unreliable. However, it is unlikely for these factors to have played a major role in our analyses, given the absence of eyes with DR and the relatively early loss of inner retinal tissue, far from the floor effect. Indeed, such inaccuracies should have caused a significant difference in intercepts between the two groups also for microperimetry, which was not seen. This opens up potential applications of complex stimuli to more accurately investigate inner retinal damage in diabetes. However, in other reports, traditional SAP was also shown to be effective in detecting retinal dysfunction in diabetes^{18, 28-31} and performed similarly to FDT when compared directly¹⁸. The recent introduction of wide-field photopic white-on-white perimeters equipped with fundus tracking technology⁵⁷ might combine the accuracy of microperimetry with the benefit of traditional SAP. The obvious advantage of circular stimuli is that, not having to accommodate for patterns, they can be designed to be arbitrarily localised (small), potentially increasing spatial precision. However, as mentioned earlier, the characteristics of the stimulus (duration/size) should ideally be optimised to detect fine changes in the macular region (this point is further expanded the **Appendix**).

4.4.4. Effect of disease duration and HbA1C

We could not find any significant correlations of the structural or functional parameters with either the duration of the disease or the percentage HbA1C in diabetic patients. The measured impact of these factors on neuronal damage has been variable across different reports^{13, 21, 53, 58}. In our study population, the average duration of the disease was short. This was expected from our selection criteria, since patients with type-2 diabetes and no DR are likely to have only been recently diagnosed. This also means that the recorded duration is unlikely to accurately reflect the actual time course of the disease. Longer durations were recorded for patients with type-1 diabetes, a small fraction of our sample.

A similar consideration can be made for the HbA1C, since the value measured in our cohort is representative of the metabolic control under treatment, with little connection to the metabolic imbalance that would have determined the initial neural damage. One limitation of this analysis was the fact that the HbA1C was not available for all participants (88% of diabetic patients and 73% of healthy participants). This constitutes a limitation also for the exclusion of type II DM in the healthy cohort. However, only 37 of the healthy participants (10% of the overall healthy cohort) for whom HbA1C was not measured were older than 40 years of age and therefore at reasonable risk of having undetected type II DM. Thus, such a misclassification might have reduced the observed differences between the two cohorts in our dataset, but is unlikely to have produced a large effect.

4.4.5. Conclusions

Our data provide structural and functional evidence to support the hypothesis of neuronal damage in DM, prior to clinically evident vascular changes, in a large cohort of diabetic patients and healthy controls. However, most of these modifications are subtle and difficult to

detect. The macular region has the potential to be the optimal ‘ground’ to integrate structural and functional information for early detection of neural degeneration. Although these changes are too small to directly impact on patients’ vision, their detection is clinically meaningful, as it could help predict the insurgence of clinically evident vascular alterations⁵. However, functional tests should be optimised to better probe the central visual field, taking the effect of neural summation into account, for example. Future investigations with better designed functional tests are needed to assess the clinical effectiveness of structure-function integration to detect early neural damage in diabetes. Our data also confirm that a simple measurement of BCVA might be insufficient to fully characterise the changes in visual function observed in diabetes and that perimetric tests should be considered by researchers investigating diabetic neuronal damage. It is also important to highlight that clinical studies such as this cannot entirely rule out the presence of pre-existing micro-alterations of the retinal vasculature as a primary source of neuronal damage, since only clinically evident vascular alterations can be excluded in patients. Further structure-function analyses including parameters from OCT-angiography scans might help shed light into this aspect and will be the subject of future work.

4.5. Appendix

4.5.1. Flowchart of the selection steps

The flowchart in **Figure 4.A1** reports the selection steps applied to the initial samples. The criteria for patients to be invited for the NISA study were based on the information collected at the time of the NICOLA study. For example, people with early AMD during the NICOLA study might have converted to intermediate/advanced AMD and therefore later excluded from this analysis. No such prior information was available for the diabetic cohort from the Belfast Trust Diabetic Retinopathy Hospital Clinics at QUB.

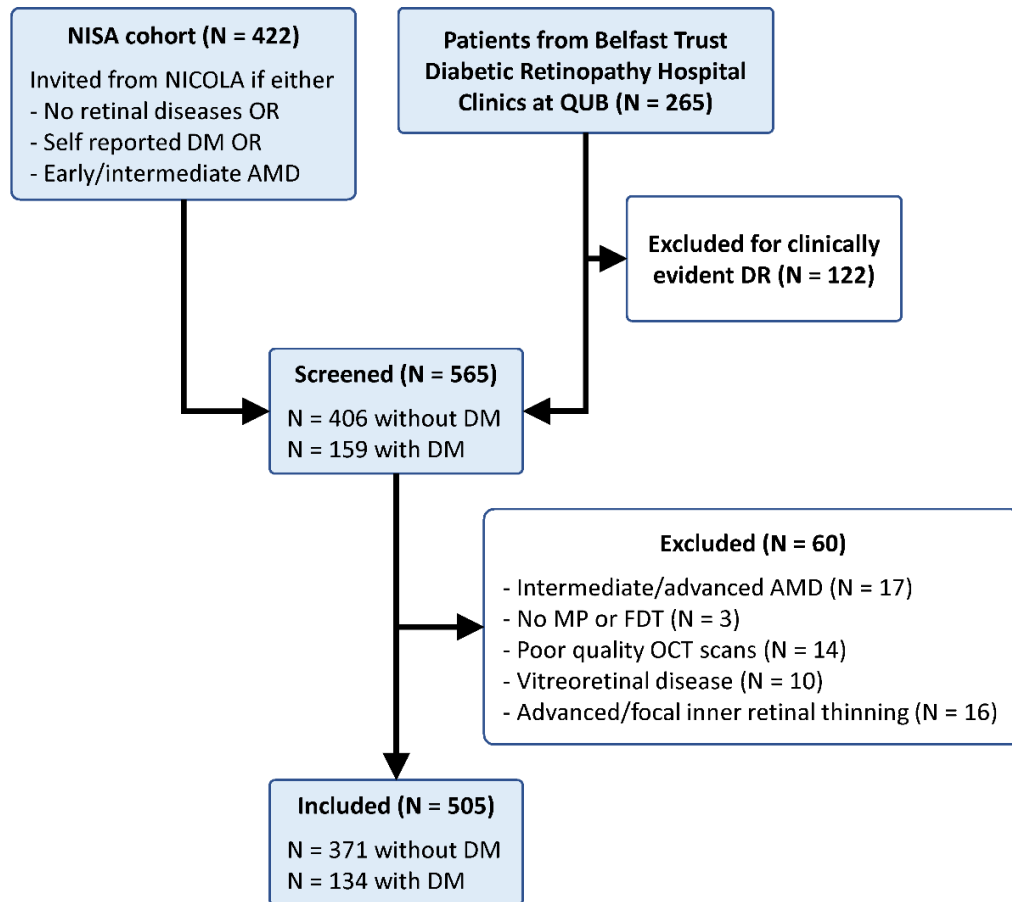


Figure 4.6 Flowchart of the selection steps detailed in the methods. DM = Diabetes Mellitus; DR = Diabetic Retinopathy; AMD = Age Related Macular Degeneration; QUB = Queen’s University Belfast.

4.5.2. Spatial summation of perimetric stimuli

Spatial summation describes how sensory systems combine input from multiple channels to produce the final psychophysical sensation (in this case, perimetric sensitivity). For simple circular perimetric stimuli, such as in the case of the MAIA, the number of channels is often equated to the number of RGCs being stimulated^{49, 59}. This number can change because of the size of the stimulus or the local density of RGCs^{49, 55, 59}. In SAP, the relationship between the \log_{10} (RGC count) and sensitivity in dB has a slope of 10 up to a certain RGC count (total or complete summation) after which the slope becomes much shallower, usually 2.5 (partial summation). In traditional SAP with photopic background illumination (10 cd/m^2) and 200 ms round stimuli, the break point is conventionally located at $10^{1.5}$ RGCs⁴⁹. Although using a mesopic background (1.27 cd/m^2), such as in the MAIA, could change the location of the breakpoint^{60, 61}, large differences are not expected for changes of less than 1 \log_{10} unit in background illumination, as in this case. In fact, the theoretical framework is confirmed by our experimental data. **Figure 4.7**, left panel, shows the relationship between the \log_{10} (RGC count) and microperimetric sensitivity. The empirical slope fitted using the overall dataset yielded a value of 2.29 [95% CIs: 2.22, 2.37] dB/ \log_{10} (RGC Count), remarkably close to the theoretical prediction. Indeed, even for the most peripheral locations, the number of stimulated ganglion cells was mostly beyond the critical $10^{1.5}$. Of note, the empirical slope was

fitted using a linear mixed model with random intercepts to account for correlated measures from the same eye and with age as a covariate to account for ageing effect beyond the normal loss of RGCs. In this framework, significant differences in intercepts between the diabetic patients and healthy controls would indicate a sensitivity loss unexplained by the structural loss, for example in the case of dysfunction. This was not observed for microperimetric stimuli.

Such a theoretical framework can be applied for FDT stimuli, although harder to interpret due to their complex features⁴¹. Nevertheless, the much larger stimulus size is likely to produce partial summation conditions. Indeed, the observed slope was 2.29 [95% CIs: 1.97, 2.62] dB/ \log_{10} (RGC Count). This is however much shallower than microperimetry, considering that for the Matrix FDT one \log_{10} step corresponds to 20 dB instead of 10 dB, leading to slope estimates that are doubled in value. In this case, as for the main analysis, there was a significant difference in the intercept between the two groups ($p = 0.0105$) and this is represented in **Figure 4.7**, right panel.

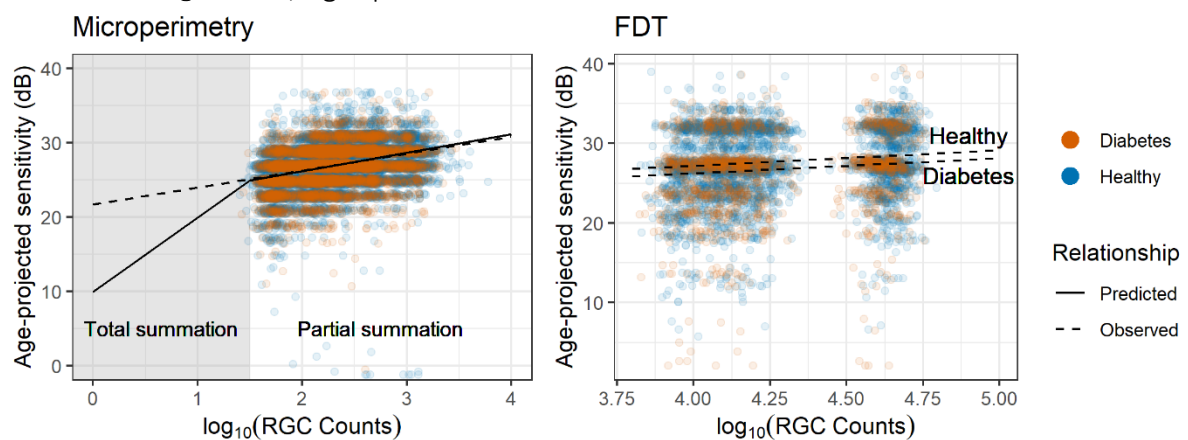


Figure 4.7 Observed structure-function relationship compared to the theoretical framework of spatial summation. The observed relationship for the FDT is plotted as two separate lines to reflect the significant difference in intercepts between the diabetic and healthy participants. Sensitivity is projected to the average age of the sample (58 years old). RGC = Retinal Ganglion Cell

Figure 4.8 shows how different results could be obtained by performing the microperimetric test in total summation conditions, for example by reducing the stimulus size. For this calculation, we scaled the \log_{10} (RGC count) estimated for Goldmann III stimuli to other stimulus sizes. We then calculated the expected sensitivity for the corresponding number of stimulated RGCs according to the model and added the residuals calculated from the real data. The estimated average difference between the two groups (and its standard error) were then calculated combining the values at different locations using a linear mixed model. As expected, the difference became larger for smaller stimulus sizes (**Figure 4.8 B**) and reached significance with a Goldmann I. This calculation does not account for possible changes in the variability of the perimetric response that could be introduced when testing with smaller stimulus sizes. However, this is not an intrinsic limitation of the test, since strategies can be devised to maintain constant variability at different sensitivities⁶². Moreover, the breakpoint location might change based on adaptation conditions and background luminance^{60, 61}, but a Goldmann I stimulus is expected to be within the range of total summation in the macula even for mesopic testing conditions⁶³.

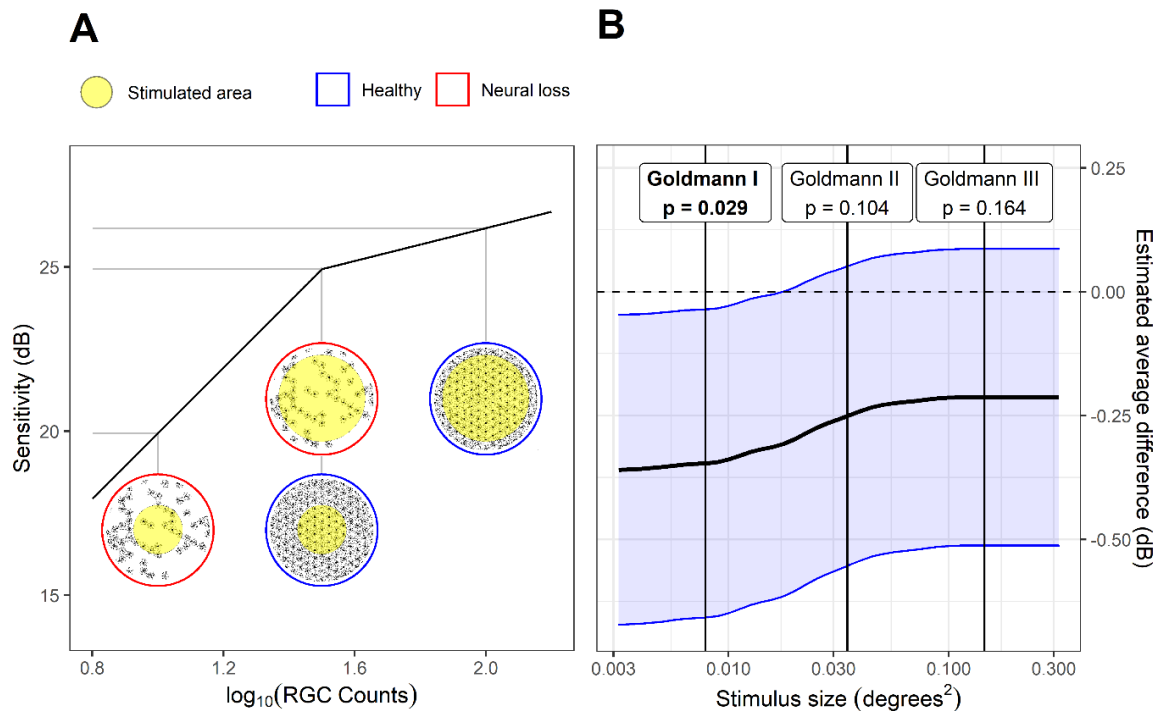


Figure 4.8 Example of how the microperimetric test could be modified to improve detection of neural damage. Panel A shows how the differences between perimetric responses from a healthy and degraded RGC mosaic are amplified by smaller stimuli that operate in total summation conditions. The grey lines connect the number of RGCs stimulated in each condition with the predicted sensitivity. Their difference can be read on the vertical axis. Panel B shows how this principle might have provided different results for microperimetry in this study; the black line represents the estimated average difference in sensitivity with different stimulus sizes, according to the model; the blue shaded area encloses the 95% Confidence Intervals for the difference, estimated from a linear mixed model. The vertical lines indicate the size of typical Goldmann stimuli. The estimated difference was significant with a Goldmann I stimulus (p -values reported at the top).

4.6. Acknowledgements

“We are grateful to all the participants of the NICOLA Study, and the whole NICOLA team, which includes nursing staff, research scientists, clerical staff, computer and laboratory technicians, managers and receptionists. The Atlantic Philanthropies, the Economic and Social Research Council, the UKCRC Centre of Excellence for Public Health Northern Ireland, the Centre for Ageing Research and Development in Ireland, the Office of the First Minister and Deputy First Minister, the Health and Social Care Research and Development Division of the Public Health Agency, the Wellcome Trust/Wolfson Foundation and Queen’s University Belfast provide core financial support for NICOLA. The authors alone are responsible for the interpretation of the data and any views or opinions presented are solely those of the authors and do not necessarily represent those of the NICOLA Study team.”

NISA Study was funded by grants from the College of Optometrists. Diabetes UK, Macular Society, Guidedogs for the Blind, Thomas Pocklington Trust and the Belfast Association for the Blind.

4.7. References

1. Lee R, Wong TY, Sabanayagam C. Epidemiology of diabetic retinopathy, diabetic macular edema and related vision loss. *Eye Vis (Lond)* 2015;2:17.
2. Cheung N, Mitchell P, Wong TY. Diabetic retinopathy. *Lancet* 2010;376:124-136.
3. Yau JW, Rogers SL, Kawasaki R, et al. Global prevalence and major risk factors of diabetic retinopathy. *Diabetes Care* 2012;35:556-564.
4. Sohn EH, van Dijk HW, Jiao C, et al. Retinal neurodegeneration may precede microvascular changes characteristic of diabetic retinopathy in diabetes mellitus. *Proc Natl Acad Sci U S A* 2016;113:E2655-2664.
5. Kim K, Kim ES, Yu SY. Longitudinal Relationship Between Retinal Diabetic Neurodegeneration and Progression of Diabetic Retinopathy in Patients With Type 2 Diabetes. *Am J Ophthalmol* 2018;196:165-172.
6. Barber AJ. A new view of diabetic retinopathy: a neurodegenerative disease of the eye. *Prog Neuropsychopharmacol Biol Psychiatry* 2003;27:283-290.
7. Barber AJ, Baccouche B. Neurodegeneration in diabetic retinopathy: Potential for novel therapies. *Vision Res* 2017;139:82-92.
8. Barber AJ, Gardner TW, Abcouwer SF. The significance of vascular and neural apoptosis to the pathology of diabetic retinopathy. *Invest Ophthalmol Vis Sci* 2011;52:1156-1163.
9. Lopes de Faria JM, Russ H, Costa VP. Retinal nerve fibre layer loss in patients with type 1 diabetes mellitus without retinopathy. *Br J Ophthalmol* 2002;86:725-728.
10. Ozdek S, Lonneville YH, Onol M, Yetkin I, Hasanreisoglu BB. Assessment of nerve fiber layer in diabetic patients with scanning laser polarimetry. *Eye (Lond)* 2002;16:761-765.
11. Takahashi H, Goto T, Shoji T, Tanito M, Park M, Chihara E. Diabetes-associated retinal nerve fiber damage evaluated with scanning laser polarimetry. *Am J Ophthalmol* 2006;142:88-94.
12. van Dijk HW, Kok PH, Garvin M, et al. Selective loss of inner retinal layer thickness in type 1 diabetic patients with minimal diabetic retinopathy. *Invest Ophthalmol Vis Sci* 2009;50:3404-3409.
13. van Dijk HW, Verbraak FD, Kok PH, et al. Early neurodegeneration in the retina of type 2 diabetic patients. *Invest Ophthalmol Vis Sci* 2012;53:2715-2719.
14. Cabrera DeBuc D, Somfai GM. Early detection of retinal thickness changes in diabetes using Optical Coherence Tomography. *Med Sci Monit* 2010;16:MT15-21.
15. Chhablani J, Sharma A, Goud A, et al. Neurodegeneration in Type 2 Diabetes: Evidence From Spectral-Domain Optical Coherence Tomography. *Invest Ophthalmol Vis Sci* 2015;56:6333-6338.
16. Carpineto P, Toto L, Aloia R, et al. Neuroretinal alterations in the early stages of diabetic retinopathy in patients with type 2 diabetes mellitus. *Eye (Lond)* 2016;30:673-679.
17. Ng DS, Chiang PP, Tan G, et al. Retinal ganglion cell neuronal damage in diabetes and diabetic retinopathy. *Clin Exp Ophthalmol* 2016;44:243-250.
18. Joltikov KA, de Castro VM, Davila JR, et al. Multidimensional Functional and Structural Evaluation Reveals Neuroretinal Impairment in Early Diabetic Retinopathy. *Invest Ophthalmol Vis Sci* 2017;58: BIO277-BIO290.
19. Jackson GR, Scott IU, Quillen DA, Walter LE, Gardner TW. Inner retinal visual dysfunction is a sensitive marker of non-proliferative diabetic retinopathy. *Br J Ophthalmol* 2012;96:699-703.
20. Montesano G, Gervasoni A, Ferri P, et al. Structure-function relationship in early diabetic retinopathy: a spatial correlation analysis with OCT and microperimetry. *Eye (Lond)* 2017;31:931-939.
21. Verma A, Rani PK, Raman R, et al. Is neuronal dysfunction an early sign of diabetic retinopathy? Microperimetry and spectral domain optical coherence tomography (SD-OCT) study in individuals with diabetes, but no diabetic retinopathy. *Eye (Lond)* 2009;23:1824-1830.
22. Sacconi R, Lamanna F, Borrelli E, et al. Morphofunctional analysis of the retina in patients with type 1 diabetes without complications after 30 years of disease. *Sci Rep* 2020;10:206.
23. Nittala MG, Gella L, Raman R, Sharma T. Measuring retinal sensitivity with the microperimeter in patients with diabetes. *Retina* 2012;32:1302-1309.
24. Park JC, Chen YF, Liu M, Liu K, McAnany JJ. Structural and Functional Abnormalities in Early-stage Diabetic Retinopathy. *Curr Eye Res* 2020;45:975-985.
25. Nilsson M, von Wendt G, Wanger P, Martin L. Early detection of macular changes in patients with diabetes using Rarebit Fovea Test and optical coherence tomography. *Br J Ophthalmol* 2007;91:1596-1598.
26. van Dijk HW, Verbraak FD, Stehouwer M, et al. Association of visual function and ganglion cell layer thickness in patients with diabetes mellitus type 1 and no or minimal diabetic retinopathy. *Vision Res* 2011;51:224-228.

27. Bao YK, Yan Y, Gordon M, McGill JB, Kass M, Rajagopal R. Visual Field Loss in Patients With Diabetes in the Absence of Clinically-Detectable Vascular Retinopathy in a Nationally Representative Survey. *Invest Ophthalmol Vis Sci* 2019;60:4711-4716.
28. Parravano M, Oddone F, Boccassini B, et al. Functional retinal impairment in type 1 diabetic patients without any signs of retinopathy. *Ophthalmic Res* 2013;50:108-112.
29. Parravano M, Oddone F, Mineo D, et al. The role of Humphrey Matrix testing in the early diagnosis of retinopathy in type 1 diabetes. *Br J Ophthalmol* 2008;92:1656-1660.
30. Bengtsson B, Heijl A, Agardh E. Visual fields correlate better than visual acuity to severity of diabetic retinopathy. *Diabetologia* 2005;48:2494-2500.
31. Hellgren KJ, Agardh E, Bengtsson B. Progression of early retinal dysfunction in diabetes over time: results of a long-term prospective clinical study. *Diabetes* 2014;63:3104-3111.
32. Anderson AJ, Johnson CA. Frequency-doubling technology perimetry. *Ophthalmol Clin North Am* 2003;16:213-225.
33. Mayer WJ, Klaproth OK, Hengerer FH, Kohnen T. Impact of crystalline lens opacification on effective phacoemulsification time in femtosecond laser-assisted cataract surgery. *Am J Ophthalmol* 2014;157:426-432 e421.
34. Ferris FL, 3rd, Wilkinson CP, Bird A, et al. Clinical classification of age-related macular degeneration. *Ophthalmology* 2013;120:844-851.
35. Wu Z, Ayton LN, Guymer RH, Luu CD. Intrasession test-retest variability of microperimetry in age-related macular degeneration. *Invest Ophthalmol Vis Sci* 2013;54:7378-7385.
36. Cassels NK, Wild JM, Margrain TH, Chong V, Acton JH. The use of microperimetry in assessing visual function in age-related macular degeneration. *Surv Ophthalmol* 2018;63:40-55.
37. Pfau M, Jolly JK, Wu Z, et al. Fundus-controlled perimetry (microperimetry): Application as outcome measure in clinical trials. *Prog Retin Eye Res* 2020;100907.
38. Montesano G, Naska TK, Higgins BE, Wright DM, Hogg RE, Crabb DP. Determinants of Test Variability in Scotopic Microperimetry: Effects of Dark Adaptation and Test Indices. *Translational Vision Science & Technology* 2021;10:26-26.
39. King-Smith PE, Grigsby SS, Vingrys AJ, Benes SC, Supowit A. Efficient and unbiased modifications of the QUEST threshold method: theory, simulations, experimental evaluation and practical implementation. *Vision Res* 1994;34:885-912.
40. Anderson AJ, Johnson CA, Fingeret M, et al. Characteristics of the normative database for the Humphrey matrix perimeter. *Invest Ophthalmol Vis Sci* 2005;46:1540-1548.
41. Sun H, Dul MW, Swanson WH. Linearity can account for the similarity among conventional, frequency-doubling, and gabor-based perimetric tests in the glaucomatous macula. *Optom Vis Sci* 2006;83:455-465.
42. Montesano G, Ometto G, Hogg RE, Rossetti LM, Garway-Heath DF, Crabb DP. Revisiting the Drasdo Model: Implications for Structure-Function Analysis of the Macular Region. *Transl Vis Sci Technol* 2020;9:15.
43. Drasdo N, Fowler CW. Non-linear projection of the retinal image in a wide-angle schematic eye. *Br J Ophthalmol* 1974;58:709-714.
44. Holm S. A Simple Sequentially Rejective Multiple Test Procedure. *Scandinavian Journal of Statistics* 1979;6:65-70.
45. Kang SH, Hong SW, Im SK, Lee SH, Ahn MD. Effect of myopia on the thickness of the retinal nerve fiber layer measured by Cirrus HD optical coherence tomography. *Invest Ophthalmol Vis Sci* 2010;51:4075-4083.
46. Nowroozizadeh S, Cirineo N, Amini N, et al. Influence of correction of ocular magnification on spectral-domain OCT retinal nerve fiber layer measurement variability and performance. *Invest Ophthalmol Vis Sci* 2014;55:3439-3446.
47. Raza AS, Hood DC. Evaluation of the Structure-Function Relationship in Glaucoma Using a Novel Method for Estimating the Number of Retinal Ganglion Cells in the Human Retina. *Investigative ophthalmology & visual science* 2015;56:5548-5556.
48. Curcio CA, Allen KA. Topography of ganglion cells in human retina. *The Journal of comparative neurology* 1990;300:5-25.
49. Swanson WH, Felius J, Pan F. Perimetric defects and ganglion cell damage: interpreting linear relations using a two-stage neural model. *Investigative ophthalmology & visual science* 2004;45:466-472.
50. Garway-Heath DF, Caprioli J, Fitzke FW, Hitchings RA. Scaling the hill of vision: the physiological relationship between light sensitivity and ganglion cell numbers. *Invest Ophthalmol Vis Sci* 2000;41:1774-1782.

51. Yoshioka N, Zangerl B, Phu J, et al. Consistency of Structure-Function Correlation Between Spatially Scaled Visual Field Stimuli and In Vivo OCT Ganglion Cell Counts. *Invest Ophthalmol Vis Sci* 2018;59:1693-1703.
52. Drasdo N, Millican CL, Katholi CR, Curcio CA. The length of Henle fibers in the human retina and a model of ganglion receptive field density in the visual field. *Vision Res* 2007;47:2901-2911.
53. Gerendas BS, Hatz K, Kaider A, et al. Ganglion cell layer thickening in well-controlled patients with type 1 diabetes: an early sign for diabetic retinopathy? *Acta Ophthalmol* 2020;98:e292-e300.
54. Heijl A, Lindgren G, Olsson J. Normal variability of static perimetric threshold values across the central visual field. *Arch Ophthalmol* 1987;105:1544-1549.
55. Redmond T, Garway-Heath DF, Zlatkova MB, Anderson RS. Sensitivity loss in early glaucoma can be mapped to an enlargement of the area of complete spatial summation. *Investigative ophthalmology & visual science* 2010;51:6540-6548.
56. Hood DC, Kardon RH. A framework for comparing structural and functional measures of glaucomatous damage. *Prog Retin Eye Res* 2007;26:688-710.
57. Montesano G, Bryan SR, Crabb DP, et al. A Comparison between the Compass Fundus Perimeter and the Humphrey Field Analyzer. *Ophthalmology* 2019;126:242-251.
58. Sharanjeet K, Ismail SA, Mutalib HA, Ngah NF. HbA1c and retinal sensitivity in diabetics using microperimetry. *J Optom* 2019;12:174-179.
59. Pan F, Swanson WH. A cortical pooling model of spatial summation for perimetric stimuli. *J Vis* 2006;6:1159-1171.
60. Barlow HB. Temporal and spatial summation in human vision at different background intensities. *J Physiol* 1958;141:337-350.
61. Owen WG. Spatio-temporal integration in the human peripheral retina. *Vision research* 1972;12:1011-1026.
62. Gardiner SK. Effect of a variability-adjusted algorithm on the efficiency of perimetric testing. *Invest Ophthalmol Vis Sci* 2014;55:2983-2992.
63. Hunter AML, Anderson R, Redmond T, Garway-Heath DF, Crossland M, Mulholland PJ. Investigating the Effect of Visual Field Eccentricity on Spatial Summation in Mesopic Microperimetry. *Investigative Ophthalmology & Visual Science* 2019;60:1171-1171.

5. Spatiotemporal summation of perimetric stimuli in healthy observers

The motivation for this paper was to develop a computational model of perimetric sensitivity based on a mosaic of RGCs and photoreceptors and that included the effect of cortical processing. In particular, the model needed to capture some important features observed in experimental data collected in healthy observers and patients with eye disease, mainly glaucoma. The first aspect was the interaction between spatial and temporal summation. The second was the effect of cones and RGC density at various eccentricity on spatiotemporal summation. The third was the change in the critical area and critical duration observed in glaucoma. We collected perimetric and imaging data from healthy observers with various combinations of stimulus sizes and durations to develop and test the model. The study produced a relatively simple computational model that accounted for all the features previously outlined. Importantly, the model could replicate the effect observed in glaucoma from RGC loss or damage and could therefore be used to test the mechanism of damage in this particular disease. Moreover, the results of this work showed how similar changes in perimetric sensitivity can be obtained by combinations of stimulus sizes and duration and how these can be linked to an underlying biological substrate, opening the possibility for novel paradigms of perimetric testing. Key to the development of the computational model was the accurate quantification of the RGC displacement in the macula, which allowed personalised estimates of RGC densities through imaging of the subject's retinas. The results were published in the *Journal of Vision* (JOV), a journal of the Association for Research in Vision and Ophthalmology (ARVO). The paper is freely available at: <https://jov.arvojournals.org/article.aspx?articleid=2785499>.

Contributions

- *Main contributor*: **Giovanni Montesano** (conceptualisation of research, development of testing software, data collection, data and statistical analysis, interpretation of the data, drafting of the manuscript).
- *Other contributors*:
 - **Pádraig J. Mulholland** (supervision, conceptualisation of research, interpretation of the data, manuscript proofing)
 - **David F. Garway-Heath** (supervision, interpretation of the data, manuscript proofing)
 - **Josephine Evans** (data collection, manuscript proofing)
 - **Giovanni Ometto** (data analysis, interpretation of the data, manuscript proofing)
 - **David P. Crabb** (supervision, interpretation of the data, manuscript proofing)

5.1. Introduction

Measuring how contrast sensitivity varies according to different stimulus sizes and durations has proven invaluable for investigating the psychophysical and physiological basis of transient stimulus detection¹⁻⁵ and how the underlying physiology is altered by disease⁶⁻¹⁰. In fact, change in sensitivity with increasing stimulus size (*spatial summation*) and duration (*temporal summation*) has been shown to be altered following retinal ganglion cell (RGC) loss from glaucoma^{6-9, 11}. Both spatial and temporal summation are characterised by a

biphasic response, with a steeper reciprocal relationship between stimulus area/duration and contrast at threshold for smaller/shorter stimuli (total summation) and a shallower change for larger/longer stimuli (partial summation). The response is often characterised in terms of the point of transition between these two phases (*critical size/duration*)¹². The physiological basis of spatial and temporal summation has been extensively studied. Although models solely based on RGCs exist¹³, spatial summation has been linked to cortical magnification and to the convergence of RGCs onto cells of the visual cortex¹⁰. This phenomenon is often referred to as *cortical pooling* and it is the favoured model for explaining spatial summation^{1, 10}. Cortical pooling can be modelled through a linear combination of filter elements tuned to different spatial frequencies¹.

One aspect that has been explored to a lesser extent is the interaction between stimulus size and duration and its effect on sensitivity (*spatiotemporal summation*). Models exist to describe temporal summation in isolation¹⁴⁻¹⁶. Many of these authors acknowledge the effect of stimulus configuration^{14, 15} and adaptation state¹⁷ on critical duration. Direct experimental evidence of the interaction between size and duration for simple circular stimuli^{11, 18, 19} suggests a combined integration of the total input by the visual system. Some attempts have been made to describe such an interaction, mainly in the field of motion detection^{20, 21}, but this phenomenon has been little explored for perimetry¹⁹. Another aspect that has been overlooked is the effect of retinal convergence. One common assumption is that spatial summation at different eccentricities can be exclusively explained by the change in density of RGCs¹⁰. However, similarly to cortical convergence, individual RGCs' might carry a different weight in terms of retinal input at different eccentricities because they receive input from a different number of photoreceptors (larger in the periphery), with significant changes in the composition and density of their mosaic.

Understanding these aspects is essential for many clinical applications of psychophysics. White-on-white perimetry is one of the most performed tests in clinical practice to diagnose and monitor the progression of a variety of diseases. In its most common implementation, the test is a 'yes/no' task in which an observer is asked to press a button every time a stimulus is perceived. The response needs to be provided within a set time window following stimulus onset, with no response indicating that the stimulus was not seen. The stimulus is projected on a bowl with a uniform white background and usually consists of a circular target with sharp edges and 0.43 degrees in diameter (size III according to Goldmann²²) and a duration between 100 and 200 ms. The intensity of the target is varied to estimate the 50% seen contrast threshold, using a variety of strategies. The target is presented at various locations around the fixation target, according to a set of pre-determined testing grids, so that the 50% threshold can be estimated at each of these locations. This produces a sensitivity map that can be used to identify and monitor visual field defects. The objective of our work was to collect experimental data to build and validate a spatiotemporal summation model, able to capture the combined effect of retinal convergence, stimulus size and stimulus duration for perimetric stimuli.

5.2. Methods

5.2.1. Participants

Ten visually healthy participants between 18 and 40 years of age were recruited on a voluntary basis at City, University of London, London, United Kingdom. All participants gave

their written informed consent. The study was approved by the local Ethics board (Optometry Proportionate Review Committee, approval number ETH2021-1728) and adhered to the tenets of the declaration of Helsinki. All participants underwent an ophthalmic assessment by an ophthalmologist (GM), which included objective refraction and measurement of the intraocular pressure (IOP) with a non-contact tonometer and auto-refractor (TRK-1P, Topcon, Tokyo, Japan), best corrected visual acuity (BCVA) with Snellen charts, slit lamp assessment of the anterior segment and indirect funduscopy. Reasons for exclusion were any abnormality of the retina or of the optic nerve head (ONH), IOP > 21 mmHg and a BCVA < 6/6 in the test eye. If both eyes were eligible, the one with the smallest refractive error was selected.

5.2.2. Psychophysical experimental procedure

5.2.2.1. Testing apparatus

All experiments were carried out on an Octopus 900 bowl perimeter (Haag Streit AG, Koeniz, Switzerland) controlled through the Open Perimetry Interface²³. The bowl is 30 cm in radius. The perimeter is equipped with a chinrest and an infrared camera to monitor eye position and pupil size. Chinrest position was adjusted by the operator as required, to maintain good centration of the pupil. A central target (four small dots in a diamond arrangement) encouraged fixation and avoided interference with centrally presented stimuli. A near-vision lens addition of approximately +2.50 D was used to reduce strain from accommodation, refined with subjective assessment of optimal visibility by the subject. Lenses were placed on an adjustable lens holder in-built to the instrument. The background illumination was 10 cd/m². Calibration was performed in a dark room before every experiment through an automated procedure implemented by the manufacturer. As is convention in perimetry, the intensity of the stimulus in dB is expressed as attenuation of the maximum possible stimulus intensity (3185 cd/m²), so that higher contrast equates to lower dB values. This quantity can be converted to Weber contrast (W_c) using the equation

$$W_c = \frac{3185/10^{DLS}}{10}. \quad (5.1)$$

However, for simplicity in our calculations, we report the values as Differential Light Sensitivity (DLS), which is simply the sensitivity value in dB/10.

5.2.2.2. Spatiotemporal summation

In the first experiment, we estimated contrast sensitivity at twelve locations in the central visual field (VF) with different stimulus sizes and durations for one test eye of all ten participants. The locations' coordinates ($\{X; Y\}$) in visual degrees from fixation were: $\{\pm 7; \pm 7\}$; $\{\pm 4, \pm 4\}$; $\{\pm 1, \pm 1\}$. Stimuli were round achromatic targets with five different diameters (Goldmann sizes, G): 0.10 (G-I); 0.21 (G-II); 0.43 (G-III); 0.86 (G-IV); 1.72 deg. (G-V). All locations were tested with all stimulus sizes. The locations at $\{\pm 7; \pm 7\}$ were additionally tested with five different stimulus durations (for all stimulus sizes): 15 ms; 30 ms; 55 ms; 105 ms; 200 ms. Four combinations (G-I/15 ms; G-I/200 ms; G-V/15 ms; G-V/200 ms) were tested twice so that more robust estimates of their threshold were available for the measurement of the frequency of seeing (FoS) curves (see next section).

The threshold was determined with a yes/no task. The observer was asked to press a button every time a stimulus was perceived. We assumed that no response within a predetermined time window (1500 ms) corresponded to "not seen". The threshold was estimated through a

Bayesian strategy, the Zippy Estimation through Sequential Testing (ZEST)²⁴, as implemented on the OPI. For our test, the strategy was set to have a uniform prior distribution between 0 and 50 dB (the range of the instrument). The likelihood function was a Gaussian cumulative distribution function (CDF) with a standard deviation (SD) of 1 dB and a guess/lapse rate of 3%. The prior distribution was updated at each response to generate a posterior distribution. The posterior distribution was used as the prior distribution for next step in the strategy. The stimulus was chosen as the mean of the prior distribution at each step, rounded to the closest integer dB value. This has been shown to provide unbiased estimates of the 50% detection threshold for a yes/no task²⁴. The determination of each threshold terminated when the posterior distribution reached a standard deviation < 1.5 dB (dynamic termination criterion).

Each combination of stimulus size and duration at each location was treated as a separate independent “thread” by the strategy (140 in total). The threads were randomly subdivided into four blocks, to allow for breaks within the test. Each block of testing lasted for approximately 15 minutes (~350 presentations). Individual presentations within each block were fully randomised. A block was completed when all the 35 threads assigned to it reached the termination criterion. A pause between individual presentations was also introduced, calculated as (1000 ms – response time, minimum 200 ms) plus an additional pause, randomly sampled from a uniform distribution between 0 and 100 ms. All responses occurring within the pause or less than 180 ms after stimulus onset stimulus²⁵ were considered as false responses and discarded.

5.2.2.3. Frequency of seeing curves

For a subset of five participants, FoS curves were determined for four stimulus combinations (G-I/15 ms; G-I/200 ms; G-V/15 ms; G-V/200 ms) at coordinates {±7; ±7} degrees (four locations) using a Method of Constant Stimuli (MOCS) procedure. Following others⁸, we used a two-stage approach. First, we obtained a coarse estimate of the FOS curve through a multidimensional Bayesian strategy, QUEST²⁶. Such a strategy is similar in principle to ZEST but uses entropy to determine the next presentation and allows for multiple parameters to be estimated. In our procedure, the FOS curve was parametrised as the CDF of a Gaussian distribution, with a fixed guess/lapse rate of 3%. The mean and SD (which model the 50% threshold and the slope of the FOS curve respectively) were simultaneously fitted as free parameters. The test was terminated when the entropy of the combined posterior distribution was ≤ 4.5. For the purpose of this preliminary step, the four spatial locations were considered as interchangeable. Therefore, only four FOS curves were determined, one for each stimulus combination. The prior distribution for the mean was itself a Gaussian distribution with a SD of 4 dB, centred on the average of the sensitivity estimates obtained from the ZEST procedure for the tested locations (8 estimates for each stimulus combination, i.e. 4 locations each tested twice) and limited over a domain of ±5 dB around its mean. The prior distribution for the SD of the FOS curve was a uniform between 1 and 10 dB, with steps of 0.5 dB.

The estimated SD for the Gaussian FOS curves were used to determine the contrast levels to be tested for each stimulus combinations in the actual MOCS. We tested seven steps for each location and each condition. The steps were placed at the following quantiles of the Gaussian FOS (neglecting lapse/guess rate): {0.0001, 0.1, 0.3, 0.5, 0.7, 0.9, 0.9999}. We however ensured that all the steps were at least 1 dB apart (the minimum interval allowed by the device) and that the two most extreme contrast levels were at least 10 dB above and

below the estimated 50% threshold. The 50% threshold was calculated as the average of the two test results obtained from the ZEST strategy for each location. Each contrast level was presented 25 times and each spatial location was tested fully and independently, for a total of 2800 presentations. A break of at least 10 minutes was introduced every 350 presentations and the whole test was split into two sessions performed on two separate days. The individual presentations were fully randomised across test locations, stimulus area/duration combinations and contrast levels. Pauses between presentations and false responses were determined as described above for the main experiment.

MOCS data were fitted using a Bayesian hierarchical model, similarly to Prins²⁷. The results of the test performed on each subject were fitted independently. The psychometric function was modelled with the CDF of a Gaussian function (Φ), where the mean (μ), SD (σ), lapse rate (λ) and guess rate (γ) were free parameters, with the formula

$$p_{seen} = 1 - (\gamma + (1 - \gamma - \lambda) * \Phi(\mu, \sigma)). \quad (5.2)$$

Mean (μ) and σ were hierarchical parameters that varied for each of the four tested locations. Information was however propagated across different locations to improve the robustness of the fit of the parameters for each testing condition. Lapses and guesses were instead modelled as global parameters for the whole test. Details of the implementation of the Bayesian model are reported in the **Appendix**.

5.2.3. Imaging

Retinal imaging was performed using a Spectralis Spectral Domain Optical Coherence Tomography (SD-OCT, Heidelberg Engineering, Heidelberg, Germany) scanner. Dense macular volume scans spanning the central 25 x 30 visual degrees (121 vertical B-scans, 9 averaged scans) were segmented and exported as RAW files using the Heidelberg Eye Explorer (HEYEX, Heidelberg Engineering, Heidelberg, Germany). Retinal ganglion cell layer (RGCL) thickness maps were built from segmentation data and converted to customised estimates of local RGC counts by combining thickness data with histology data provided by Curcio and Allen²⁸, using previously published methodology^{29,30}. Local customised RGC density was calculated for each location tested in the psychophysical procedure by accounting for RGC displacement^{30,31}, using methodology detailed elsewhere³⁰.

5.2.4. Modelling of perimetric sensitivity

One of the objectives of this study was to provide a model that was simple, but sufficient to describe the change in sensitivity observed with different combinations of sizes and durations for perimetric stimuli. Our working hypothesis, derived from previous work^{11, 18, 19, 32}, was that the combined effect of these two parameters, at any given location, could be described by taking the product of stimulus area and stimulus duration. We called this product the *spatiotemporal input*. We integrated the spatiotemporal input into a computational model of the response of RGC mosaics, partially based on the work by Pan et al.¹ and Bradley et al.³³. The key novel aspect of our modelling was that the linear response from the RGC mosaic was pooled and integrated over time so that changes in duration and size of the stimulus would both simultaneously affect the temporal and spatial response of the system. We further modelled the retina as a two-stage mosaic, where the response from individual photoreceptors active in photopic adaptation conditions (cones) was integrated by the RGC mosaic, to explore the effect of retinal convergence in the central visual field. The density of the two mosaics was varied to reproduce the effect of eccentricity. We refer to the

combined effect of the spatiotemporal input and changes in retinal structure (i.e. density of the photoreceptor and RGC mosaics) as *total retinal input*. The model was implemented in Matlab (The MathWorks, Natick, USA) and is described in detail below.

5.2.4.1. Hexagonal mosaics

Following Swanson et al.⁷, we modelled multiple detectors organised in a regular hexagonal lattice. This organisation is reflective of many naturally occurring cell mosaics as it represents the most efficient packing scheme for objects with circular/spherical geometries³⁴. For our purposes, we simplified the retina as being composed of two stacked mosaics, the photoreceptor mosaic and the RGC mosaic. Being interested in the results of experiments performed in photopic conditions (background illumination = 10 cd/m²), we only modelled the cone mosaic. In this retinal model, individual RGCs pool the response from the photoreceptors according to their Receptive Fields (RFs). To improve the efficiency of computation, each hexagonal lattice was rearranged in a regular lattice with anisotropic spacing (See **Figure 5.A1**). This simplifies the pooling operation, which can be computed via simple convolution of the regularised lattice with the RGC-RF filter (see next section), also rearranged according on the same regular lattice. The response of the photoreceptor mosaic was simply computed by multiplying the mosaic by the stimulus. In its simplest form, this is equivalent to assigning a value of 1 to all the photoreceptors that fall within the stimulus area, leaving the others to 0. However, in its final implementation, this was modified to include the effect of optical blur (see later). Only the Parasol OFF RGC mosaic was used for the calculations (P-OFF-RGC), assuming that the ON and OFF mosaic operate on parallel redundant channels for the detection of simple round stimuli. Parasol cells were chosen because there is experimental evidence that these cells preferentially mediate sensitivity to briefly flashed stimuli, such as those used in perimetry. The calculations were repeated with the midget OFF RGC mosaic (mOFF-RGC) and reported as **supplementary material** for comparison with some previous literature¹⁰.

5.2.4.2. RGC receptive field

The spatial filters for the RGC-RF were modelled with a Difference of Gaussian (DoG, **Figure 5.1 A**), using the median parameters estimated by Croner and Kaplan³⁵ from electrophysiology on macaque's retina. In their work, they showed that, although the scaling factors for the relative width and height of the inhibitory and excitatory Gaussian components of the filter changed with eccentricity, their ratios remained approximately constant. In this model, the surround inhibitory component has peak sensitivity $K_s = 0.01 * K_c$, where K_c is the peak sensitivity of the excitatory centre. The standard deviation (SD) of the surround was 6.7 times larger than the SD for the centre (average reported by Croner and Kaplan³⁵). The SD for the centre was scaled so that the *radius* of the centre component was equal to the inter-cell spacing of the mosaic (defined by its density). The radius was defined by Croner and Kaplan as the distance from the centre at which the excitatory Gaussian component has value K_c/e . The corresponding SD was approximated as $SD = \text{Cell spacing}/1.414$. Note that, while the centre-surround proportions are based on Croner and Kaplan³⁵, the actual extent of the RGC-RFs in our model depends only on the inter-cell spacing of the RGC mosaic.

5.2.4.3. Cone-RGC convergence

The number of cones that converge onto a RGC is known to increase with eccentricity^{28, 31, 36}. In our model, this corresponds to an increasing number of photoreceptors pooled by the

RGC-RF per unit area. This can be achieved by increasing the density of the cone photoreceptor mosaic, also provided by Curcio and Allen³⁷. The convergence rate can be calculated by taking the ratio of the density of cones over the density of P-OFF-RGCs (**Figure 5.1 B**). Because of how the hexagonal matrix has been re-arranged for calculations (fig.1), the intercell spacing for the RGC mosaic needs to be an exact multiple of that of the cone mosaic. This limits the possible Cones:RGCs ratios that can be calculated. However, changing the convergence ratio is equivalent to simply multiplying the response of the RGC obtained with a 1:1 convergence ratio by a scaling factor. This is easily demonstrated by the graph in **Figure 5.1 B**. This method was therefore chosen to account for the change in convergence across the VF in a smooth fashion.

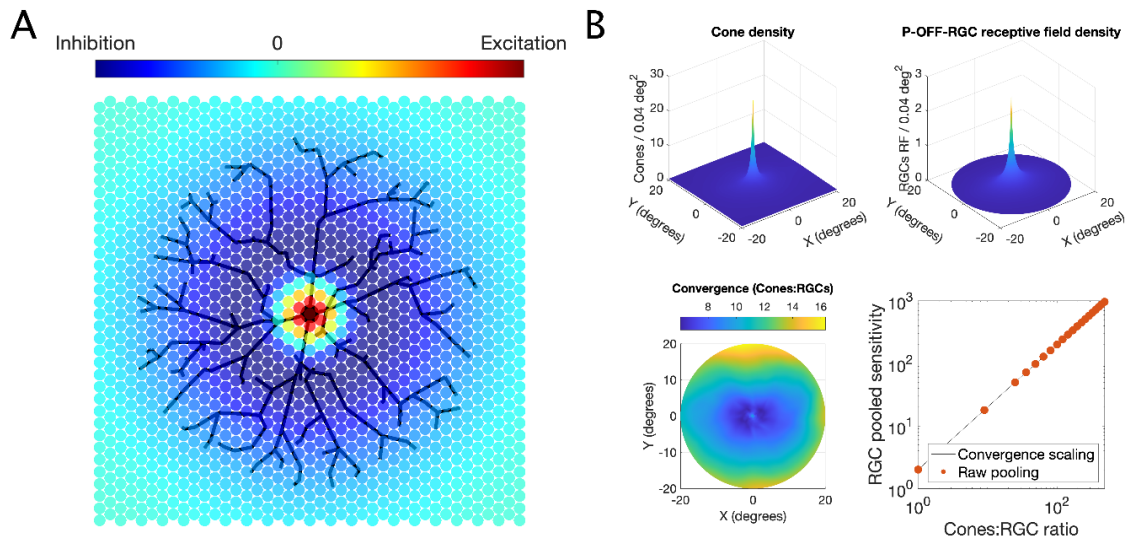


Figure 5.1 Retinal Ganglion Cell (RGC) receptive field (RF) modelling. A) Schematic example of how a RGC samples the input from the photoreceptor mosaic, according to its Difference-of-Gaussian RF. The strength of inhibitory surround has been exaggerated here for clarity. B) Estimated density for Cones (top left) and RGC-RF (top right) and a map of Cones:RGCs convergence (bottom left). The bottom-right panel shows a comparison between the predicted (unscaled) sensitivity for the numerical calculations from the mosaic with discrete changes in convergence (dots) and continuous factor scaling (line).

5.2.4.4. Modelling of optical factors

The effect of natural optics was modelled using the formula for the average Modulation Transfer Function (MTF) of the human eye proposed by Watson³⁸. In this formula, the square-root of the diffraction limited (DL) MTF, which depends only on the pupil size, is multiplied by a Lorentzian function whose parameters are fitted so that the product would approximate the average human MTF. A multiplicative correction factor, that depends on age and eye pigmentation, is then additionally applied to the MTF to account for light scattering. **Figure 5.2** reports examples of the effect of optical blur on different stimulus sizes for different pupil apertures using the MTF (without accounting for scattering)³⁸. The calculations are performed by multiplying the two-dimensional Fourier transform of the stimulus by the MTF and then back-transforming in the spatial domain. The blurred stimulus can then be sampled with the photoreceptor mosaic. For each subject, we used the average pupil size recorded by the Octopus perimeter during the test to model the results of our experiments.

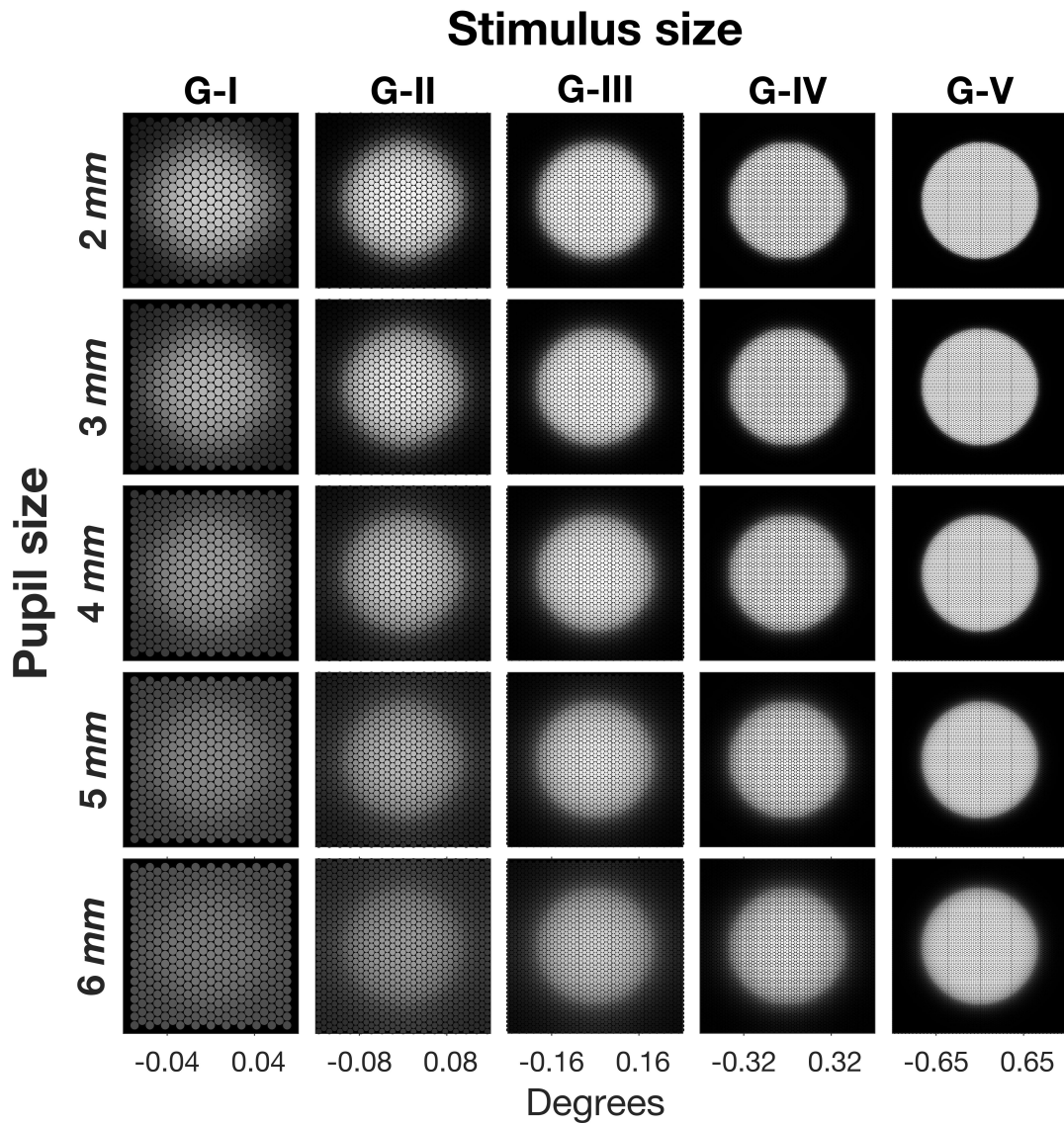


Figure 5.2. Effect of optical blur for different pupil sizes. The images represent the projection of the blurred stimulus on the photoreceptor mosaic.

5.2.4.5. Proposed spatiotemporal model

One desired property of our proposed model was that the size and duration of the stimulus interacted so that longer stimuli would decrease Ricco's area (upper limit of complete spatial summation) and larger stimuli would shorten the critical duration (upper limit of complete temporal summation). One solution to achieve this is to use a pooling operation that integrates the spatial input over time. The integration, however, must not solely take into account the duration of the stimulus, but also the amount of RGCs stimulated (i.e., the amount of spatial input). In other words, the temporal integration is to be performed by a cortical pooler on the total spatial input rather than by individual detectors prior to pooling. The simplest model, with the smallest number of parameters, is a capacitor (equation 5.5), which is convolved with the temporal profile of the stimulus and then integrated over time according to equation (5.6) to obtain the response (in the equations, the symbol "*" indicates convolution):

$$h(t, \tau, S) = e^{\left(-\frac{t}{\tau/S}\right)} \quad (5.5)$$

$$R = \left(\int_0^{\infty} |f(t) * h(t, \tau, S)|^k dt S \right)^{1/k} \quad (5.6)$$

where τ is the integration constant, k is the summation exponent (4 in this study)^{1, 7, 39-42} and S is the total spatial input defined as

$$S = \sum_i R_i \quad (5.7)$$

where R_i is the response of an individual ganglion cell to the stimulus. Note the contribution of individual RGCs (R_i) can change both because of the location of the RGC with respect to the stimulus (edge as opposed to centre) and the effect of retinal convergence (RGCs in the periphery will have a bigger contribution when fully stimulated because of their larger pooling from the photoreceptors). The temporal profile of the stimulus is represented by $f(t)$, which is a step function with value 1 when the stimulus is on and 0 otherwise. As previously mentioned, the combined effect of stimulus size, stimulus duration, RGC density and retinal convergence defines the *total retinal input*. Much like other temporal filters, this operation can also be implemented through temporal convolution. Note that such an approach to spatiotemporal summation is very similar to what was described in Frederiksen et al.²¹ and Anderson and Burr²⁰ for motion detection. Since only the P-OFF-RGC mosaic was considered for our calculations, the RGCs that were assigned a negative input were considered as inhibited by the stimulus. Their negative contribution to the sum can be interpreted as an inhibition of their background activity. Obviously, such a simple approach would not account for other filter choices with a strong biphasic response, where a simple summation would always result in a zero net sum. From the examples in **Figure 5.3**, we can see that this pooler has the desired properties when the response is computed for different stimulus sizes and durations, i.e. a shorter duration determines a larger critical area and vice-versa. One additional convenient property of this pooler is that the critical size and duration depend on the integration constant τ . The integration constant τ is therefore the scaling factor of the pooler and can be used to test the hypothesis of constant input integration across the VF. If the hypothesis of constant integration response for the same amount of total retinal input is correct, we do not expect important changes in the integration constant across different testing conditions and eccentricities. An alternative approach would be to model individual RGCs (or higher order visual detectors) as separate spatiotemporal integrators and to pool their response by vector summation^{1, 39}. Such an approach has the advantage of allowing the modelling of the response from specific classes of RGCs and produces sensible spatial and temporal summation responses. However, it fails to reproduce the interaction between spatial and temporal input that would be expected. For example, Ricco's areas in spatial summation curves would be unaffected by changes in stimulus duration. This is in contrast with evidence from the literature^{11, 18, 19, 32}. It is worth noting that the current model could be extended to include the temporal response of individual classes of RGCs prior to pooling. However, this would increase the number of tuneable parameters and would be beyond the objectives of the current study and what could be determined with our experiments.

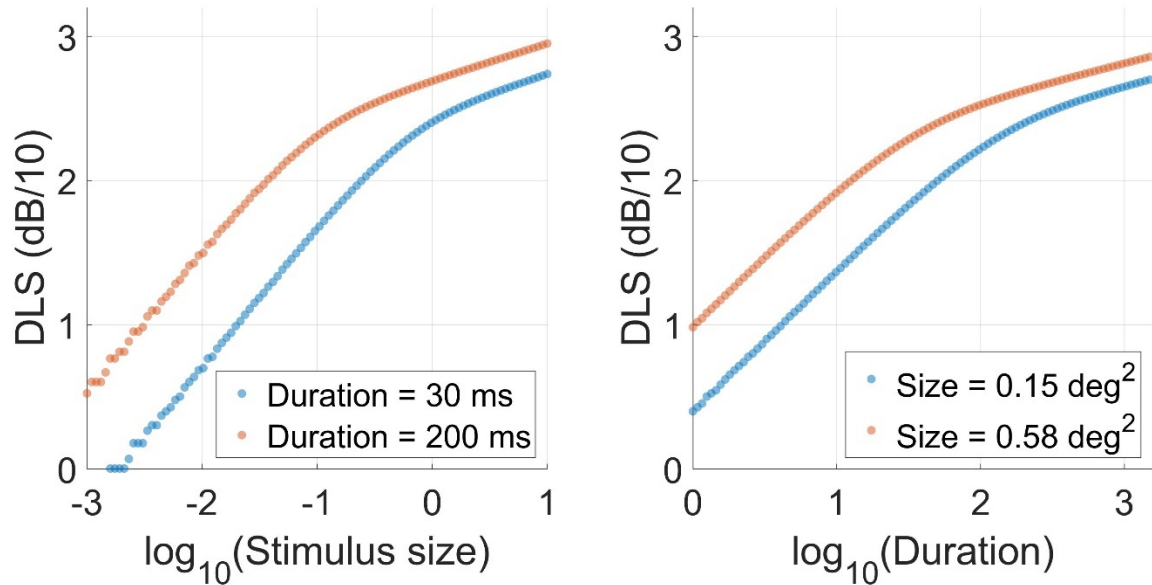


Figure 5.3 Example of the interaction of stimulus size and duration in the proposed model. Changing the stimulus duration translates the spatial summation curve along the horizontal axis (left panel). The same is true for the temporal summation curve when changing the stimulus area (right panel).

5.2.4.6. Fitting procedure

The model described by equation (5.6) was fitted to the data using an iterative algorithm (Nelder-Mead Simplex Method, *fminsearch* function in Matlab⁴³) to minimise the Root Mean Squared Error (RMSE). The summation exponent was set to $k = 4^{1, 7, 39-42}$ and the RGC mosaic density was varied according to the eccentricity following the model by Drasdo et al.^{30, 31}. These estimates were corrected with individual imaging data obtained from the OCT scans, as previously reported^{29, 30}. The model was fitted by tuning the parameter τ , which represents the integration constant of the spatiotemporal input. An additional parameter (additive in log-scale) allowed translation along the vertical axis (log-DLS, Offset term).

5.2.4.7. Calculation of critical size

The transition from total to partial summation is smooth for the curves generated by our model. The response curve is fully characterised by the integration constant τ and the amount of retinal input. The calculation of the critical (Ricco's) area is therefore dependent on an arbitrary threshold and is only performed for comparison with previous literature. For our calculations, the transition point was the retinal input at which the slope of the summation curve is 0.5 (Piper's law). Note that the retinal input scales perfectly with stimulus size for our chosen implementation of the model, but non linearities are introduced if taking the sum of the module in equation (5.7). For consistency with our supplementary analyses (see later), the conversion between stimulus area and retinal input for each mosaic was calculated numerically and locally approximated with a linear function in $\log_{10} - \log_{10}$ scale. The parameters for the curves were fitted accounting for the optical blur (based on each participant's average pupil size and iris pigmentation). Densely sampled curves were numerically calculated using these parameters to estimate Ricco's area. These curves were calculated without the effect of optical blur. This simulates removing the estimated effect of optics on

the size of Ricco’s area. Note that accounting for convergence in the fitting process will not change Ricco’s area, as parameters are optimised to fit the same data.

5.2.4.8. Statistical analysis

Statistical comparisons were performed using linear mixed models to account for correlations between observations from the same subject. When data from multiple locations were used, individual locations were used as a nested random factor within the subject. When multiple comparisons were compared, the p-values were corrected using a Bonferroni-Holm correction. All calculations were performed in R (R Foundation for Statistical Computing, Vienna, Austria) using the *lme4* package⁴⁴. All comparisons were performed on log₁₀-transformed values of Ricco’s area, integration constant and number of P-OFF-RGCs, unless otherwise specified. Eccentricity was treated as a discrete factor.

5.3. Results

5.3.1. Average response

In this section, we show plots of the average DLS for different experimental conditions to give an intuitive representation of the phenomena under investigation. Characteristics of each eye in the sample are reported in **Table 5.1**. **Figure 5.4A** reports the average DLS for the spatial summation experiment at different eccentricities. As expected, the summation curves are separated by a horizontal shift, owing to the effect of the changes in the retinal mosaic. Interestingly, simply transforming the stimulus area into the corresponding estimated number of RGC-RFs underlying the stimulus did not fully account for the effect of eccentricity. Most of the effect was instead removed by considering the product of stimulus area, RGC-RF density and Cones:RGC convergence ratio. We evaluated this by comparing the results of a simple 2nd degree polynomial fit of the DLS using either the log₁₀(stimulus area), the raw log₁₀(number of RGCs) or the convergence weighted log₁₀(number of RGCs) as predictors in a mixed effect model. The unexplained residual variance (including random effects) was 1.93 dB² for the log₁₀(stimulus area), 1.79 dB² for the unweighted log₁₀(number of RGCs) (7.2% reduction) and 1.77 dB² for the convergence weighted log₁₀(number of RGCs) (8.1% reduction).

Subject ID	Age (years)	Study eye	Sphere (D)	Cylinder (D)	Axis (deg)	BCVA (logMAR)	IOP (mmHg)	Average Macular thickness (µm)	Average GCL thickness (µm)	Average RNFL thickness (µm)
S 1	33	Left	-3.00	-1.00	154	0.02	16	306.4	37.9	110.9
S 2	25	Right	+0.25	-0.75	31	-0.10	14	308.1	39.7	92.2
S 3	33	Left	-3.25	-0.25	111	0.01	18	339.5	42.5	106.2
S 4	27	Left	-0.25	-0.50	171	-0.10	14	330.0	42.2	98.9
S 5	25	Left	+0.75	-0.75	8	0.00	15	311.3	37.4	111.9
S 6	26	Right	-0.25			0.01	11	311.3	40.9	104.6
S 7	36	Left	+0.25	-1.00	173	0.00	19	314.7	42.7	104.6
S 8	28	Right	-2.25	-0.50	43	0.00	15	298.6	33.7	81.5
S 9	26	Right	-0.75	-0.25	7	0.02	16	311.1	38.0	105.6
S 10	32	Right	-2.00			0.00	15	295.4	40.8	90.3

Table 5.1 Characteristic of each eye in the sample. All subjects had their sensitivity tested with the ZEST strategy for all the duration and size combinations for all tested locations. Psychometric functions were estimated for subjects from 1 to 5 using the method of constant stimuli. D = Diopter; BCVA = Best Corrected Visual Acuity; logMAR = log-Minimum

Angle of Resolution; IOP = Intraocular Pressure; GCL = macular Ganglion Cell Layer; RNFL = peripapillary Retinal Nerve Fibre Layer. Average macular and GLC thickness were measured for the area corresponding to the central 10 degrees.

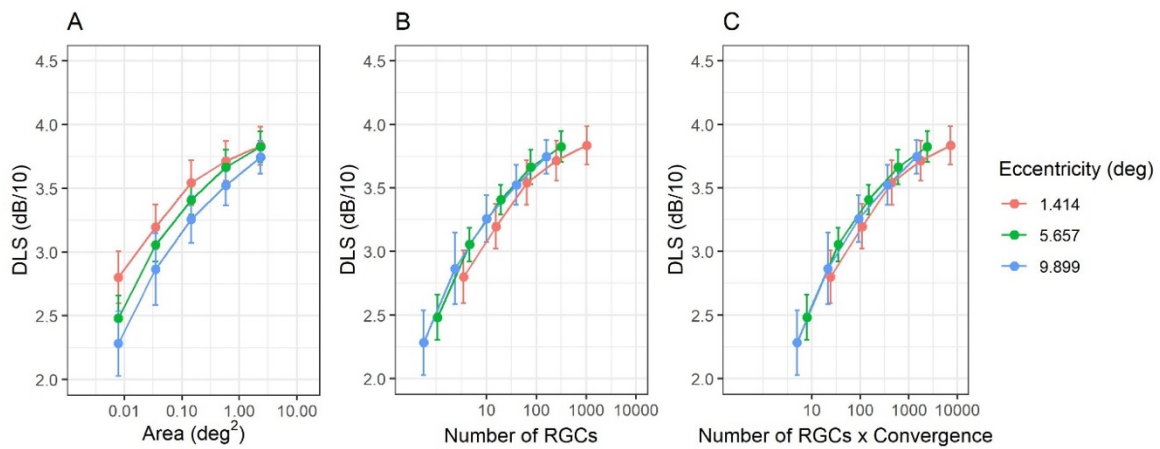


Figure 5.4 Spatial summation curves. Average (dots) and standard deviation (error bars) for Differential Light Sensitivity (DLS) for the three tested eccentricities at different stimulus sizes **(A)**, the corresponding P-OFF-RGC-RF count underlying the stimuli **(B)** and the corresponding P-OFF-RGC-RF count underlying the stimuli weighted by convergence **(C)**. RGC = Retinal Ganglion Cell (average across subjects at each stimulus size in these graphs).

Taken together, these results and plots support the hypothesis that the main determinant of DLS is the total retinal input to higher visual centres, influenced by both the number of stimulated RGCs, retinal convergence and duration of the stimulus.

5.3.2. Results from the spatiotemporal model

5.3.2.1. Spatial summation – effect of eccentricity

The parameters of the model were fitted independently for each location using the data collected with different stimulus sizes and 200 ms stimulus duration (the only duration tested at all eccentricities). **Figure 5.5** reports the estimated critical size (Ricco's area) at different eccentricities. The average RMSE of the model fits was 0.85 ± 0.39 dB (Mean \pm SD). As expected, the estimated Ricco's area increased towards the periphery (**Figure 5.5 C** and **Table 5.2**), with no significant differences between the areas calculated with and without accounting for convergence. However, such a change did not correspond to a constant number of P-OFF-RGCs being stimulated. Instead, the estimated number of P-OFF-RGCs at Ricco's area was consistently larger towards the fovea (**Figure 5.5 D**). This was mirrored by a change in the integration constant τ with eccentricity. However, this trend in τ was completely eliminated by accounting for the change in Cones:RGCs convergence (**Figure 5.5 A** and **Table 5.2**). This effect of convergence was larger when modelling the mOFF-RGC mosaic (**supplementary material**). This result can alternatively be visualised by multiplying the number of P-OFF-RGCs at Ricco's area by the corresponding convergence factor (**Figure 5.5 D** and **Table 5.2**). Note that this is a post-hoc calculation and not an output from the model (accounting for convergence is expected to have an effect on the model's parameters but not on Ricco's area and the shape of the fitted response profile). There was a small significant increase in the vertical Offset with eccentricity, which was reduced by accounting for convergence (**Figure 5.5 B** and **Table 5.2**).

		Eccentricity (degrees)			Comparisons		
		1.414 (A)	5.657 (B)	9.899 (C)	A vs B	A vs C	B vs C
Uncorrected	τ ($\times 10^2$)	12.11 [6.83, 20.08]	9.36 [6.54, 14.33]	6.32 [4.85, 9.45]	0.2208	0.0061	0.1125
	Offset (dB/10)	2.52 [2.46, 2.61]	2.64 [2.57, 2.73]	2.63 [2.54, 2.7]	< 0.0001	0.0001	0.3271
	Ricco's area (deg^2)	0.039 [0.023, 0.067]	0.111 [0.067, 0.152]	0.143 [0.104, 0.199]	< 0.0001	< 0.0001	0.0158
	# P-OFF-RGCs*	17.54 [9.96, 29.18]	13.48 [9.42, 20.72]	9.11 [6.96, 13.62]	0.2210	0.0059	0.1099
Convergence weighted	τ ($\times 10^2$)	86.25 [46.48, 137.29]	71.28 [49.2, 105.41]	57.89 [43.7, 88.97]	0.8884	0.4579	0.8884
	Offset (dB/10)	2.31 [2.25, 2.41]	2.42 [2.36, 2.51]	2.4 [2.3, 2.46]	< 0.0001	0.0243	0.0311
	Ricco's area (deg^2)	0.039 [0.023, 0.067]	0.11 [0.068, 0.152]	0.142 [0.103, 0.197]	< 0.0001	< 0.0001	0.0175
	# P-OFF-RGCs†	125.05 [67.88, 199.52]	102.51 [70.89, 153.1]	83.42 [63.2, 128.13]	0.8765	0.4502	0.8765

Table 5.2 Model fit results for spatial summation data. Median [Interquartile Range] of the different outputs from the model fits. Comparisons were performed on log-transformed values but reported in linear scale (except for the Offset, which was tested and reported in log-scale and represents the shift in the relationship along the vertical axis). P-OFF-RGC = Parasol OFF retinal ganglion cells. *Obtained by taking the product of Ricco's area and local P-OFF-RGC density; † Obtained by taking the product of Ricco's area and local P-OFF-RGC density scaled by retinal convergence.

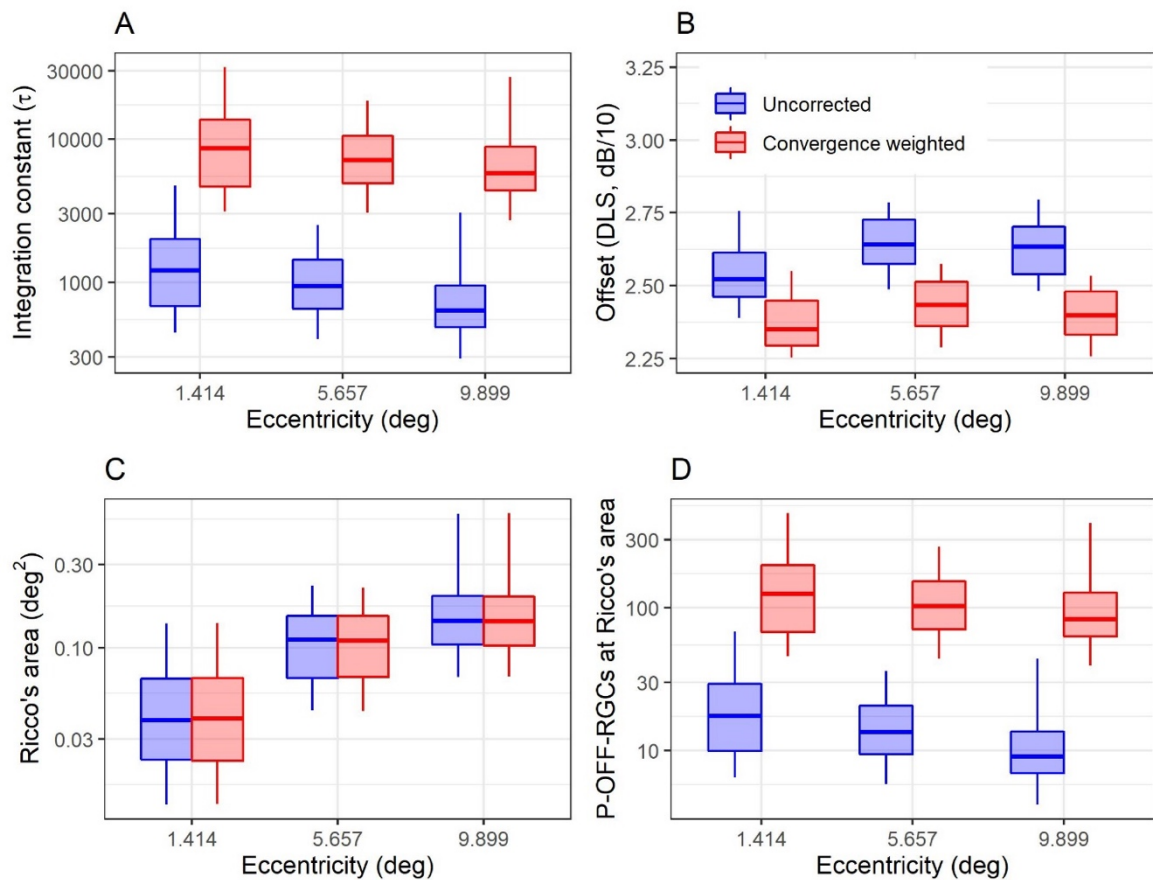


Figure 5.5 Model fit results for spatial summation data. Boxplots of the different parameters and estimates derived from the model for spatial summation data. Note that the

convergence weighted values in **(D)** are obtained by simply multiplying the uncorrected number of P-OFF-RGCs at Ricco's area by the convergence rate. The box encloses the interquartile range, the horizontal midline indicates the median and the error bars extend from the 5% to the 95% quantiles. The vertical axis is \log_{10} -spaced. RGC = Retinal Ganglion Cell

5.3.2.2. Spatiotemporal summation

The same spatiotemporal model was used to analyse data from locations $\{\pm 7; \pm 7\}$ with all different combinations of stimulus sizes and durations. The data were collated to obtain a single estimate of the integration constant and accounting for retinal convergence. The global average RMSE for this fit was 1.67 ± 0.52 dB (Mean \pm SD) and 1.40 ± 0.41 dB for the 200 ms stimuli. This can be compared to the 0.96 ± 0.35 dB average RMSE obtained from fitting the 200 ms data alone at the same eccentricity. For context, the root mean squared difference in sensitivity between the two repetitions of the retested combinations was 2.44 dB and the root mean squared deviation from the average of the two repetitions was 1.22 dB. An example of the calculation for one location in one subject is also shown (**Figure 5.6 A and B**). There was a strong correlation between the parameter estimates obtained by fitting data from all stimulus durations and 200 ms alone (previous section), at the same eccentricity (correlation coefficient: 0.83 for $\log_{10}(\tau)$ and 0.89 for the sensitivity offset, **Figure 5.6 C and D**). However, the two estimates appeared to have a consistent significant difference ($p < 0.0001$), approximately constant in \log_{10} -scale. The Median [Interquartile Range] was $34.65 [25.31, 56.04] \times 10^2$ for the τ constant and $2.36 [2.31, 2.42]$ dB/10 for the offset. These values were both significantly smaller than those reported in **Table 5.2** for the same eccentricity ($p < 0.0001$ and $p = 0.00298$ respectively). Significant differences were also present for all the other parameters, including Ricco's area and the number of P-OFF-RGCs at Ricco's area (all $p < 0.0001$). Numeric values of Ricco's area and corresponding P-OFF-RGC counts are reported in **Table 5.3** for all durations. Differences in Ricco's areas between different durations were not tested as such differences are assumed by the model.

	Ricco's area (deg ²)	# P-OFF-RGCs* (Uncorrected)	# P-OFF-RGCs [†] (Convergence weighted)
Durations 15 ms	1.088 [0.773, 1.913]	71.63 [55.75, 116.9]	655.48 [510.59, 1082.06]
30 ms	0.545 [0.388, 0.961]	35.91 [27.87, 58.76]	328.64 [255.54, 543.92]
55 ms	0.298 [0.212, 0.525]	19.59 [15.2, 32.12]	179.27 [139.13, 297.32]
105 ms	0.156 [0.111, 0.275]	10.28 [7.96, 16.8]	94.05 [73.01, 155.51]
200 ms	0.082 [0.059, 0.144]	5.42 [4.18, 8.84]	49.56 [38.21, 81.87]

Table 5.3 Model fit results for spatiotemporal summation data. Median [Interquartile Range] of the different outputs from the model fits with the different stimulus durations. P-OFF-RGC = Parasol OFF retinal ganglion cells. *Obtained by taking the product of Ricco's area and local P-OFF-RGC density; † Obtained by taking the product of Ricco's area and local P-OFF-RGC density scaled by retinal convergence.

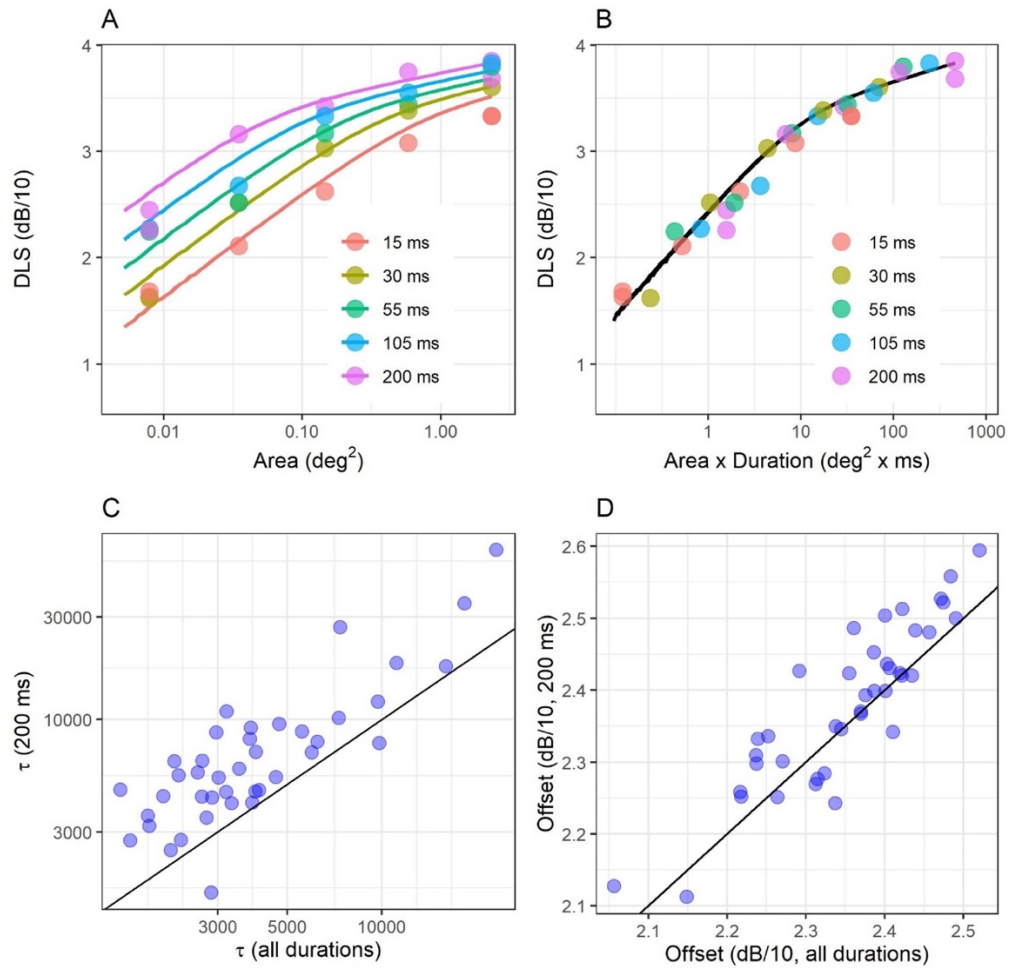


Figure 5.6 Model fit results for spatiotemporal summation data. The two top panels show an example fit from one location in one subject, with the horizontal axis reporting the stimulus area (A) and the product of area and duration (B). Correlation between the parameter estimates obtained by combining all durations and by only using data obtained with the 200 ms stimulus for the integration constant (C) and the offset (D). The diagonal line indicates equivalence.

5.3.3. Frequency of seeing curves

We estimated the FoS curves for the four most extreme combinations of stimulus size and duration at locations $\{\pm 7; \pm 7\}$ using the MOCS data for five subjects. The results of the Bayesian fitting are shown in **Figure 5.7**. The FoS was modelled using the CDF of a Gaussian distribution. The average of the estimates for μ , σ , λ and γ are reported as **Supplementary material**.

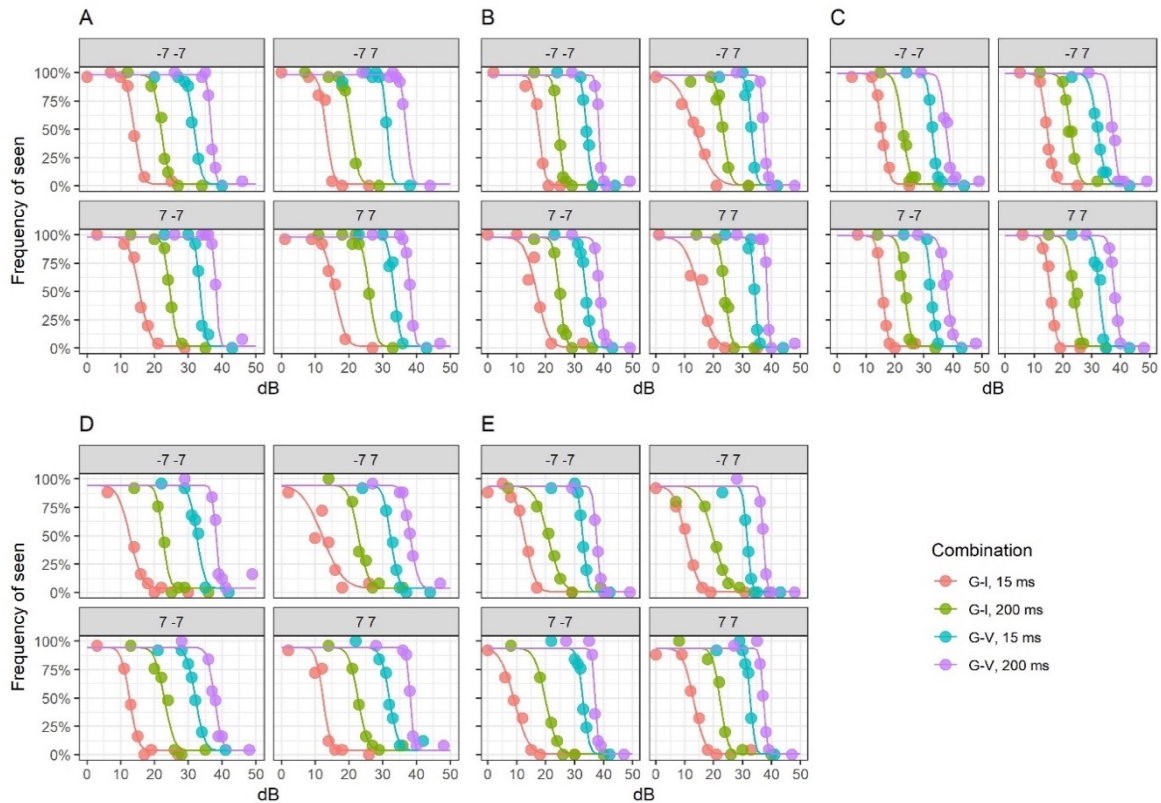


Figure 5.7 Psychometric functions. The curves were obtained from the Method of Constant Stimuli (MOCS) experiment at the four tested locations in five subjects with four different combinations of stimulus size and duration. Parameters are provided as Supplementary material.

In general, there was a tendency for slopes (σ) to be shallower for conditions where sensitivity was lower (μ). This agrees with previous literature^{45, 46}. **Figure 5.8** shows this relationship. Estimates from Henson et al.⁴⁵ are also reported for comparison.

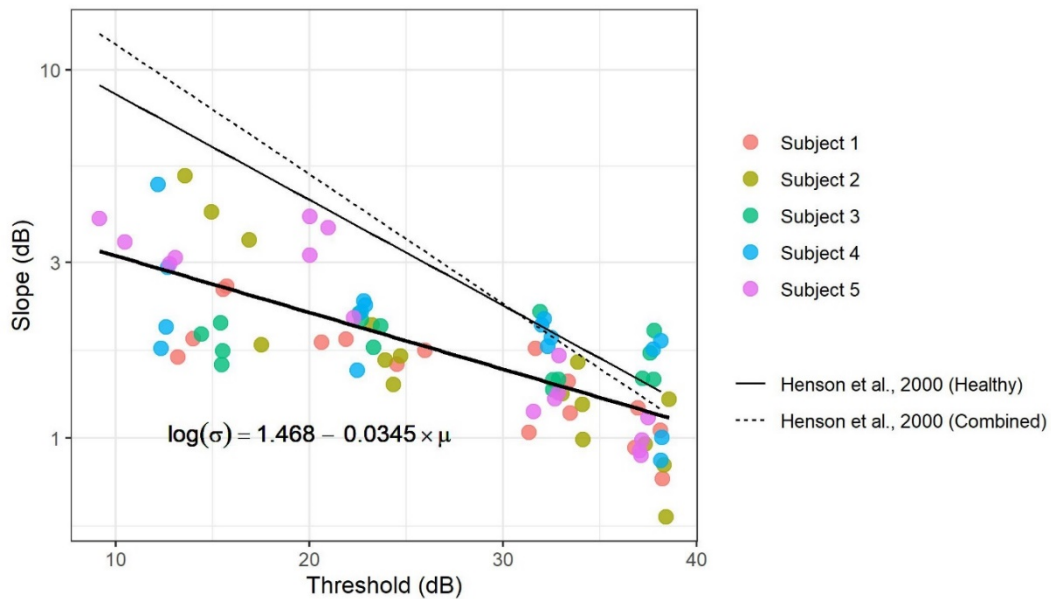


Figure 5.8. Change in psychometric slope. Relationship between the slope (σ) of the psychometric function and the 50% threshold (μ). The regression line is also reported. The relationship was statistically significant ($p < 0.0001$).

5.4. Discussion

Constant integration of visual input has been regarded as a fundamental principle governing the perception of visual stimuli^{18, 19}. However, the interaction of stimulus duration and size has been rarely and incompletely explored in perimetry¹¹. Our data support constant input integration as a fundamental principle in perimetric response in healthy observers. Such a principle has translational value as it provides a simple framework for the interpretation and prediction of perimetric responses in healthy subjects and allows speculations on the expected changes from disease.

The first important result is the change in Ricco's area with different stimulus durations. The size of Ricco's area has often been interpreted considering cortical magnification¹⁰, linking the number of RGCs within Ricco's area to the number of RGCs contacting V1 cells in the visual cortex. Such a line of reasoning seems however questionable if Ricco's area can vary with stimulus duration, because duration would have no effect on the spatial extent of RGC-V1 connections. Rather, temporal and spatial summation appear to operate in concert to maintain a consistent behaviour in response to the same amount of visual input, be it from changes in stimulus size or duration. Fredericksen et al.²¹ also proposed a similar integration model in the context of motion detection, suggesting that spatiotemporal summation likely arise from diffuse cortical integration rather than specific temporal or spatial processes. Our model captures such a spatiotemporal interaction by only requiring the fitting of one parameter (the integration constant τ), while providing good predictions of the experimental results. Other models, while not specifically investigating the interaction between stimulus size and duration, also showed that the spatial scale of the visual system could be modelled independently of the underlying RGC density and their RFs using cortical filters with different spatial scales^{1, 7}. Our model also decouples spatial summation from the extent of the retinal spatial filters (in this case, the extent of the DoG filter used to model RGCs' responses). This has important implications for modelling the effect of disease that will be discussed later. It should be noted that other authors have proposed that these effects could be explained by a dynamic change in the "functional" receptive field size as a function of stimulus duration and background luminance¹³. More realistically, this could correspond to a selection of cortical filters of different sizes for different stimulus characteristics or to the response envelope of multiple filters combined by probability summation whose sensitivity can be selectively changed by different stimulation conditions¹. Further research is needed to understand how this would apply in the case of disease, such as RGC loss (see later). Such a mechanism is further explored in a dedicated paragraph in the **Appendix**.

The model described by equations (5.5) and (5.6) can be modified to incorporate different impulse response functions. In this study, it was a simple capacitor equation, as this was deemed sufficient to model our data by fitting only two parameters. This is likely to be simplistic for many other applications. For example, our model does not include any response delay. Our results can be largely replicated with the monophasic response filter used by Gorea and Tyler¹⁵ and first described by Watson⁴⁷. Such an impulse response can also be tuned to produce different critical durations by changing an integration constant, while keeping all the other parameters fixed. Using this impulse response only produced minimal differences (one example is provided as **Supplementary Material**). A drop in sensitivity has been shown for very long stimulus durations⁴⁸⁻⁵⁰ and modelled with a biphasic impulse response integrated over a limited time window¹⁵. Our stimuli would not be long enough for this to be evident. Our temporal integral in Equation (5.6) extends to infinity, similarly to

Watson¹⁴. Gorea and Tyler¹⁵ highlighted the implausibility in this assumption, because an observer that integrates over an infinite time window will never make a decision to respond. A practical choice for our experiments would be to use the maximum time interval allowed for a response (1500 ms) as an integration window. However, this is so much longer than the longest stimulus (200 ms) that it would be practically equivalent to infinity.

It should be mentioned that both temporal and spatial summation, and contrast sensitivity in general, can be largely affected by background adaptation. For the background illumination used in this study (10 cd/m²) threshold behaviour should be close to Weber's law at least for a G-III stimulus^{51, 52}. Retinal illuminance can be reduced by media opacity (such as cataract) but this is likely to be negligible in a young healthy cohort. Pupil size can also affect retinal illuminance, especially if below 3 mm⁵¹, but the average pupil size in our cohort was 5.9 ± 0.8 mm.

The model can be used to investigate the effect of eccentricity on spatial summation. Our results show that Ricco's area significantly increased with eccentricity, as expected²⁻⁴. However, this did not correspond to a constant number of P-OFF-RGCs being stimulated, this number being comparably larger at smaller eccentricity. This is mirrored by the identical trend for the integration constant τ , indicating that more P-OFF-RGCs need to be stimulated to achieve the same change in sensitivity closer to the fovea. This trend is even bigger when modelling the response from the mOFF-RGC mosaic (**supplementary material**). Our results agree with Kwon and Liu¹⁰, who also observed a notable departure from a constant number of mOFF-RGCs at Ricco's area and a trend with eccentricity. However, they concluded that this was likely a result of inaccuracies in the estimates of RGC density. We propose a different explanation: the trend in the number of RGCs, and in the integration constant, appeared to be completely eliminated by weighting the contribution of each RGC by the Cones:OFF-RGC convergence ratio. This observation suggests that, much like the effect of change in stimulus duration, convergence can change the "contribution" provided by each RGC in terms of retinal input. Our model is able to account for this, because the contribution of each RGC can be weighted by its convergence rate prior to summation in equation (5.6). Our experiments would not allow us to uncover a specific mechanism for this phenomenon. However, a reasonable hypothesis is that increased convergence could change the contrast gain determining the spiking rate of the RGC for a given level of contrast. For our main analysis we considered one possible class of RGCs, P-OFF-RGCs. This is important for our assumption of hexagonal tiling, because different classes of RGCs form independent and overlapping mosaics^{53, 54}. mOFF-RGCs were also modelled (**supplementary material**) for comparison with Kwon and Liu¹⁰. Their choice was justified by the fact that these are the most prevalent type of RGCs in humans^{31, 54}. However, previous literature showed that briefly flashed stimuli, such as those used in perimetry, might preferentially stimulate parasol RGCs⁵⁵, and this was the reason for our choice to model P-OFF-RGCs instead. It should be noted that the effect of eccentricity, and the importance of Cones:RGC convergence, was much more pronounced for mOFF-RGCs. However, accounting for convergence eliminated significant differences in the number of stimulated RGC at Ricco's area and in the integration constant between the smallest and the largest eccentricity for both modelling choices. Interestingly, when weighted by convergence, the results were effectively identical to those obtained with the P-OFF-RGC mosaic, because the higher convergence ratio for the mOFF mosaic effectively produced the same scaled input. It should be noted that there is no clear anatomical evidence of increased Cones:P-OFF-RGC convergence with eccentricity. However, this seems a reasonable assumption because the Cones: RGC ratio calculated from

histology data^{37, 56} increases with eccentricity in a similar fashion for both the midget and parasol cells. The similarity between our results and those reported by Kwon and Liu¹⁰ should be interpreted with caution, because it can be explained by the fact that both our estimates and theirs were derived from those provided by Drasdo et al.^{30, 31}, which are in turn based on a small histology dataset by Curcio and Allen²⁸. Despite our attempt to improve precision by customising Drasdo's estimates using individualised structural OCT data³⁰, the results are unlikely to be greatly altered. Therefore, Kwon and Liu's¹⁰ results cannot be considered a fully independent confirmation of our findings. Finally, it should be noted that the compensation of the effect of eccentricity with the convergence ratio might be coincidental and could be explained by other factors, such as optical aberrations. The effect of natural ocular optics on spatial summation in the parafoveal retina is debated⁵⁷⁻⁵⁹. In our model, we included the effect of optical aberrations and glare using the average MTF for the human eye proposed by Watson³⁸: the data were fitted accounting for optical factors, but the summation curves were generated without the effect of optics. This was an attempt at estimating the pure neural contribution to spatial summation. However, the effect on the results largely depends on other assumptions within the model, particularly the choice of whether the summation in equation (5.7) is taken over the signed or absolute value or the RGC response. Our choice of summing the signed contribution was based on some desirable properties of the model, particularly the perfect linear scaling of the response with the change in RGC density and filter size. This produced a very small effect from ocular optics, because the total power of the stimulus was simply spread over a larger area. Taking the summation over the absolute value instead produced a much greater effect (results reported in **Supplementary material**) because negative contributions from "inhibited" RGCs were transformed into positive contributions, greatly amplifying the effect of optical blur. Our choice of modelling produced an average change in Ricco's area due to optical factors of $0.056 \log_{10}$ units, which is very similar to the change measured by Tuten et al.⁵⁷ with adaptive optics (AO). Taking the summation over the absolute value instead produced an average change of $0.37 \log_{10}$ units, which is closer to what was reported by Dalimier and Dainity⁵⁸ for similar experiments. Ultimately, a definitive answer to these questions could only be obtained by performing these same experiments with coupled AO corrected stimuli and imaging, so that accurate estimates of individual RGCs can be obtained and the effect of optical aberrations eliminated⁶⁰.

Another important result is the effect of different stimulus durations and sizes on the shape of the psychometric function. In general, and in agreement with previous reports^{45, 46}, we have found that the change in the slope of the psychometric function was largely explained by a change in sensitivity and was reasonably described by a log-linear relationship (**Figure 5.9**). This effect is indicative of the presence of multiplicative noise in the response⁴⁰. However, it is difficult to identify the exact origin of such noise (quantal fluctuations; eye movements; noise from the instrument). This has however important implications, because it confirms that the increase in variability of perimetric responses with sensitivity is not uniquely linked to disease but can be replicated in healthy observers. The MOCS experiments were designed to replicate the simple detection task involved in perimetry, where observers are asked to continuously monitor the presence of a signal in sequential intervals. This can be modelled as a task with a variable observer-defined "criterion" (i.e. rate of false alarm or response bias)⁶¹. In our FoS curves, this bias is accounted for by estimating the guess rate as a lower asymptote (the γ term in equation (5.2)). This framework is rooted in high-threshold theory and widely adopted in the field of perimetry⁶². It should be kept in

mind that, under the alternative signal detection theory, the bias correction would be performed after z-score transformation and would require numerous catch trials to determine the individual response bias⁶¹. In our data, the response bias and lapse rate were estimated from the response to stimuli that were likely to be much above or below the 50% threshold (as determined using a pilot using QUEST+ to estimate threshold and psychometric function slope) and all participants were encouraged to maintain a low false-alarm rate during the experiments. Both the guess and lapse rates were very close to 0 and are therefore unlikely to have greatly affected the estimates of the psychometric function.

Our choice of placing our testing locations along the diagonals limits our ability to appreciate the previously reported dissociation in between ganglion cell number and perimetric sensitivity in nasal visual field⁶³. We however found a significantly smaller number of P-OFF-RGCs within Ricco's area for the nasal locations, indicating a smaller spatial scale compared to temporal locations ($p = 0.005$). This comparison was performed for the \log_{10} -RGC number with a linear mixed model using the hemifield as a fixed effect and the eccentricity as a random effect, nested within the subject, to perform a paired same-eccentricity comparison.

It is interesting to consider the implications of our results and modelling approach for the interpretation of changes observed in disease. Redmond et al.⁹ have demonstrated an increase in Ricco's area in patients with glaucoma, which could be accounted for by a shift of the summation curves along the horizontal axis (stimulus size). According to some models^{7, 10}, such a change could only occur by scaling the spatial filters to increase spatial convergence (equivalent to changing the cortical magnification factor), which would imply some sort of "restructuring" of either the pooling mechanism (for example the spatial extent of RGC-V1 connections) or an enlargement of RGCs' RFs. The latter seems implausible, because most histologic studies have shown dendritic pruning and shrinkage⁶⁴, which would imply smaller RGCs' RFs. The first hypothesis also lacks solid support from experiments: Wang et al.⁶⁵ observed changes in the cortical magnification factor in patients with glaucoma tested with functional magnetic resonance imaging; such changes, however, are indicative of increased retina-V1 divergence, and therefore do not clearly support the hypothesis of an increased magnification factor. Our model makes no such assumptions. Instead, the change in Ricco's area is a consequence of the reduction in retinal input owing to a loss of RGCs in glaucoma. In **Figure 5.9 A**, data from healthy participants in Redmond et al.⁹ were fitted with our model, assuming a mosaic of P-OFF-RGCs with density estimated from Drasdo et al.^{30, 31}. The mosaic was then randomly degraded to achieve 73% RGC loss, equivalent to the reported proportional average change in Ricco's area. The figure plots the average response of 100 randomly degraded mosaics. The model correctly predicted a horizontal shift of the curve, in agreement with the data. A horizontal shift in the response could also be explained by RGC loss preferentially affecting higher frequency cortical filters, whose loss in sensitivity might determine a horizontal shift of their probability summation envelope¹. Our model also predicts that temporal summation curves can be equated between healthy and glaucoma by appropriately scaling stimulus size. This is shown in **Figure 5.9 B**, for the same mosaics simulated in **Figure 5.9 A**. Mulholland et al.¹¹ provided experimental evidence that using Ricco-scaled stimuli could reduce the difference in temporal summation observed between glaucoma patients and healthy controls with G-III stimuli, although some residual differences were still present. This is further proof of the interaction between stimulus size and duration. However, more research is needed to fully characterise such an interaction in glaucoma. Finally, our model also predicts changes in spatial and temporal

summation with photoreceptor loss, such as from diseases of the external retina. However, studies investigating this with perimetric stimuli are still lacking and will need further research.

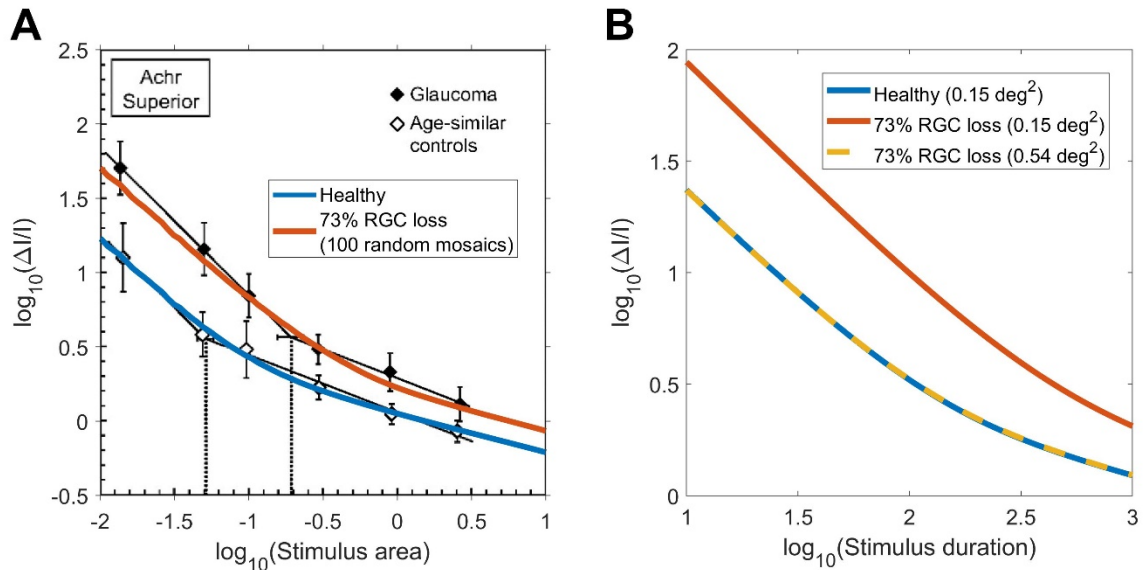


Figure 5.9. Application to glaucoma. A) Change in Ricco’s area in patients with glaucoma compared to age-matched controls, adapted from Redmond et al.⁹. B) Temporal summation curves can be equated when RGC loss is compensated by an increase in the stimulus size. RGC = retinal ganglion cells.

Other questions remain, particularly pertaining to the systematic difference between the estimates of the model parameters obtained with 200 ms stimuli only or with all stimulus durations combined. Small inaccuracies in the delivery of the stimulus might produce variations in the intended durations, skewing the results of the combined analysis. Another consideration is that our model, despite describing most of the variability in the data, might not be capturing all aspects of the effect of stimulus duration on sensitivity. In fact, the model was not meant to be a complete description of the psychophysical response to all the features of the stimulus, but rather aimed at providing a coherent framework to explain important experimental observations from the data that are often neglected by other modelling attempts.

5.5. Conclusions

We show that the amount of total retinal input can account for most of the characteristic of spatiotemporal summation with perimetric stimuli in healthy observers, including the effect of eccentricity. This could have important implications for the interpretation and design of perimetric examinations in diseased eyes as well as providing a framework for analysing spatiotemporal integration in healthy observers.

5.6. Appendix

5.6.1. MOCS fitting

MOCS data were fitted using a Bayesian hierarchical model. Each subject was fitted independently. The four combinations of stimulus size and duration were modelled as fixed

effect factors on the parameters μ and σ of the psychometric function, as defined in equation (5.2). The parameters for each stimulus combination are denoted as μ_c and σ_c . The four locations were modelled as hierarchical random effects on μ_c and σ_c , with no correlations between the two parameters. The lapse rate (λ) and guess rate (γ) were modelled as global parameters for the whole test. The response (yes/no) was modelled as binomial process with 25 trials. Following Prins et al.²⁷, the prior distribution for the mean of the parameter μ_c and σ_c for each stimulus combination was a non-informative normal distribution with a standard deviation of 30 dB. The prior distribution for the variance of the parameters μ_c and σ_c for each stimulus combination was a non-informative uniform distribution between 0 and 1000 dB. The random effects for each location were modelled as a normal distribution with mean μ_c and standard deviation σ_c . The prior distribution was linked to the parameter σ_c via a logarithmic function. The parameters γ and λ were non-hierarchical and had a Beta prior distribution with shape parameters 2 and 50. The model was fitted by running two parallel MCMCs in Just Another Gibbs Sampler (JAGS)⁶⁶. We used 5,000 burn-in iterations. After that, the model was run for 10,000 iterations. All parameters achieved a Gelman-Rubin diagnostic < 1.2 ⁶⁷.

5.6.2. Mosaic arrangement for computation

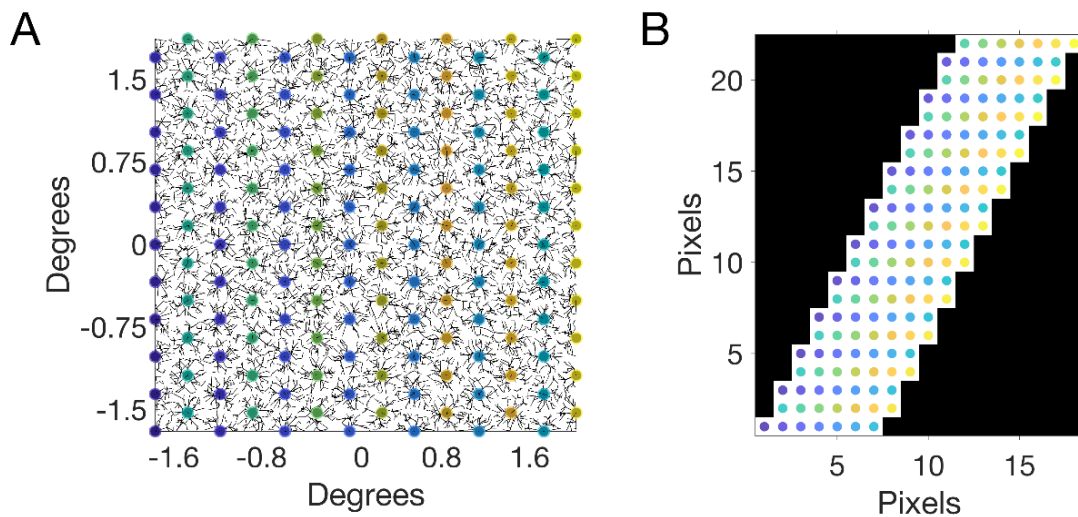


Figure 5.10. Implementation of the mosaic. Example of how a cellular mosaic (RGCs in this case, left panel) is rearranged into a regular matrix with anisotropic spacing (right panel).

5.6.3. A multiscale filter hypothesis for spatiotemporal integration

Many possible mechanisms could replicate the interaction between spatial and temporal summation reported in the literature and observed in our experiments. Our modelling approach is able to capture this aspect of the response. Nevertheless, it is useful to hypothesize how such an interaction could be implemented in the visual system. Glezer et al.¹³ proposed that this be achieved by a dynamic change in the “functional” RGC-RFs in the retina in response to changes in stimulation conditions, such as background illumination. However, there is no clear evidence of such a change occurring in the retina. Furthermore, Glezer et al.¹³ proposed such changes to occur through alterations in the weighting of the centre and surround of centre-surround receptive fields. Despite this, Ricco’s area was

observed to alter in response to glaucomatous RGC loss in glaucoma patients⁹ and background luminance in healthy subjects⁶⁸ in the s-cone pathway, in which a centre-surround receptive field organisation is absent⁶⁹. A more reasonable hypothesis, that fits more closely with experimental observations, is that a set of spatial cortical filters exist and can be optimally selected based on the amount of retinal input. **Figure 5.11** shows a hypothetical response of an array of cortical neurons employing a biphasic first gaussian derivative filter (D1) with a gaussian envelope. This filter was chosen because it produces a smooth monotonic spatial summation curve, as shown by Pan and Swanson¹. Note that the locations of the cortical neurons in the schematic indicate their projection into the visual space, rather than their anatomical arrangement in the visual cortex. In the schematic, selecting a larger filter corresponds to selecting a sparser mosaic of cortical neurons, since the extent of the filter is scaled with the inter-cellular spacing. This is equivalent to proportionally scaling the same mosaic. As expected, the summation curves with larger filters are shifted along the horizontal axis towards larger stimulus sizes. These mosaics can be obtained by selecting subsets of neurons from the same array (as in this example) or be constituted of separate sets of neurons. It should be mentioned that the summation curves produced by a more realistic implementation of this model (with cortical neurons sampling the response of RGCs with static RF sizes) would largely reproduce this behaviour but would not be an exact horizontal translation of the same response (see later).

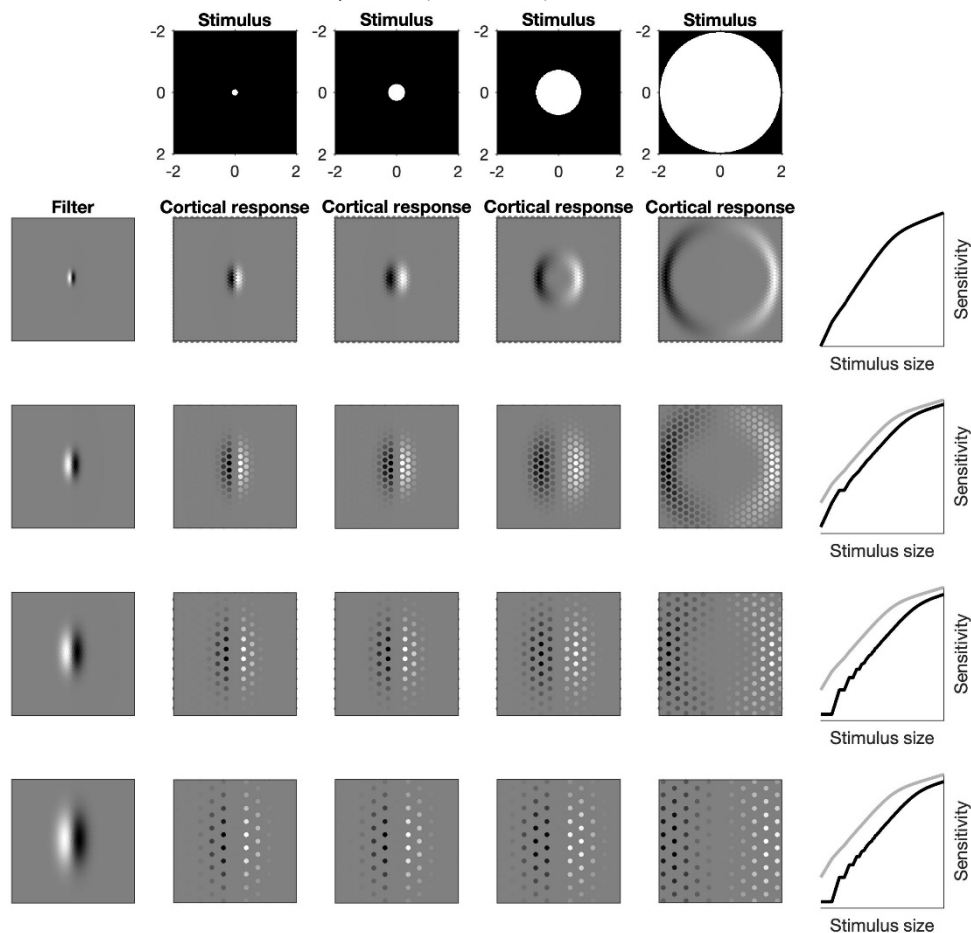


Figure 5.11. Example of how a change in scale results in a horizontal translation of the spatial summation curve. The cortical response is obtained by convolution of the spatial filter (left column) with the stimulus (top row). The summation curves (right column) are calculated as in Pan and Swanson¹ with an exponent of 2. For this specific spatial filter, this

corresponds to a partial summation slope of 0.25 in the $\log_{10} - \log_{10}$ plot, the same as in our model. The spatial summation curve with the smallest filter is shown in grey for reference.

The change in spatial scale with different stimulus durations can therefore be replicated by a horizontal shift (in $\log_{10} - \log_{10}$ coordinates) of the same template response by an amount equivalent to the \log_{10} change in duration. Note that the selection of the filter scale does not need to depend solely on the stimulus duration, but more generically on the retinal input, to include the effect of Cones:RGC convergence, duration, background illumination or, for example, RGC loss in disease. For the sake of simplicity, everything except duration was held constant for these calculations. The combined effect is best represented by a summation surface, shown in **Figure 5.12**. In the figure, three summation curves are isolated by cutting through the surface at different stimulus durations and correspond to using a different filter scale. Importantly, temporal summation responses can be obtained by cutting through the surface along the orthogonal (duration) axis. Because the surface is obtained by proportionally translating the same spatial summation curve, temporal summation responses also follow the same template curve, proportionally shifted with different stimulus sizes. This would produce the same results obtained with our more generic input summation model. With this interpretation, although a strict retina-V1 convergence cannot be defined, testing in partial summation condition (i.e. long stimulus durations and high background illumination) would allow the calculation of the smallest possible spatial scale for a given retinal location.

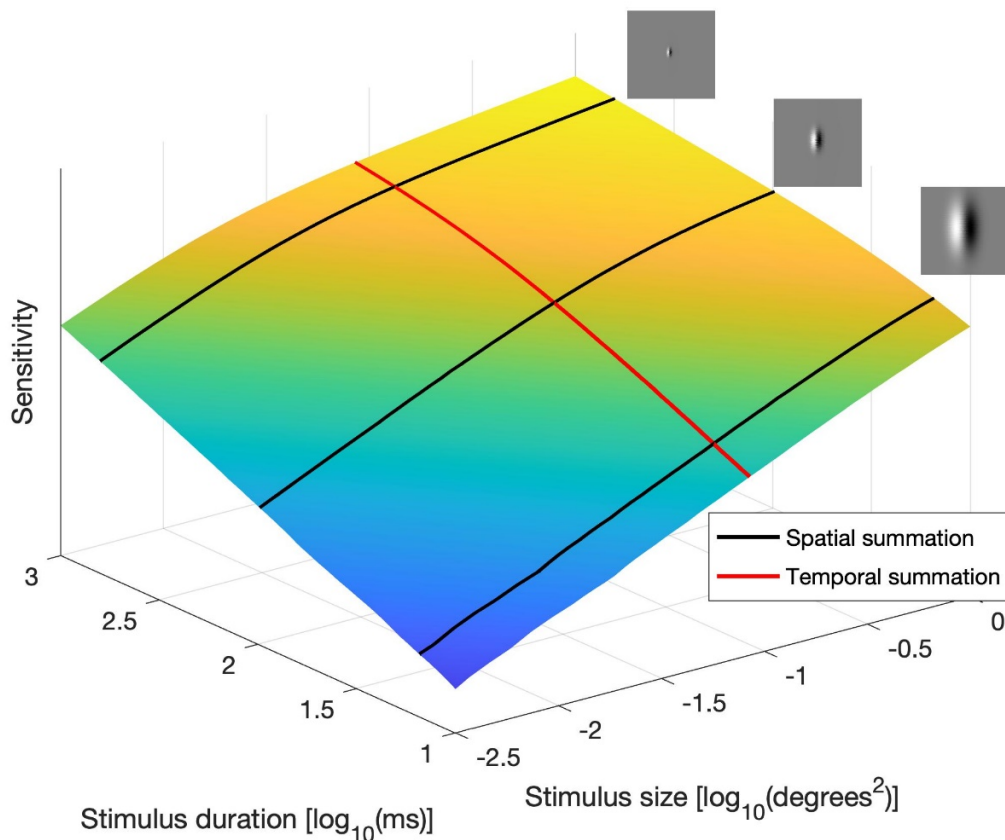


Figure 5.12. Spatiotemporal response surface. The surface was obtained by shifting the spatial summation curve by an amount equivalent to changes in duration, in \log_{10} scale. Spatial and temporal summation curves are shifted versions of the same curve and can be

obtained by cutting through the surface along different axes. The small insets show the change in the spatial filter for three different stimulus durations, producing the spatial summation curves identified by the black profiles.

Another possibility, proposed by Pan and Swanson¹, is that different stimulus features, such as adaptation state and stimulus duration, might alter the relative sensitivity of individual filters and change the combined response “envelope” obtained through probability summation. For simplicity, we demonstrate this concept in **Figure 5.13** by selectively combining the response of filters with progressively smaller spatial scales. The resulting response envelope is a simple translation of the same curve.

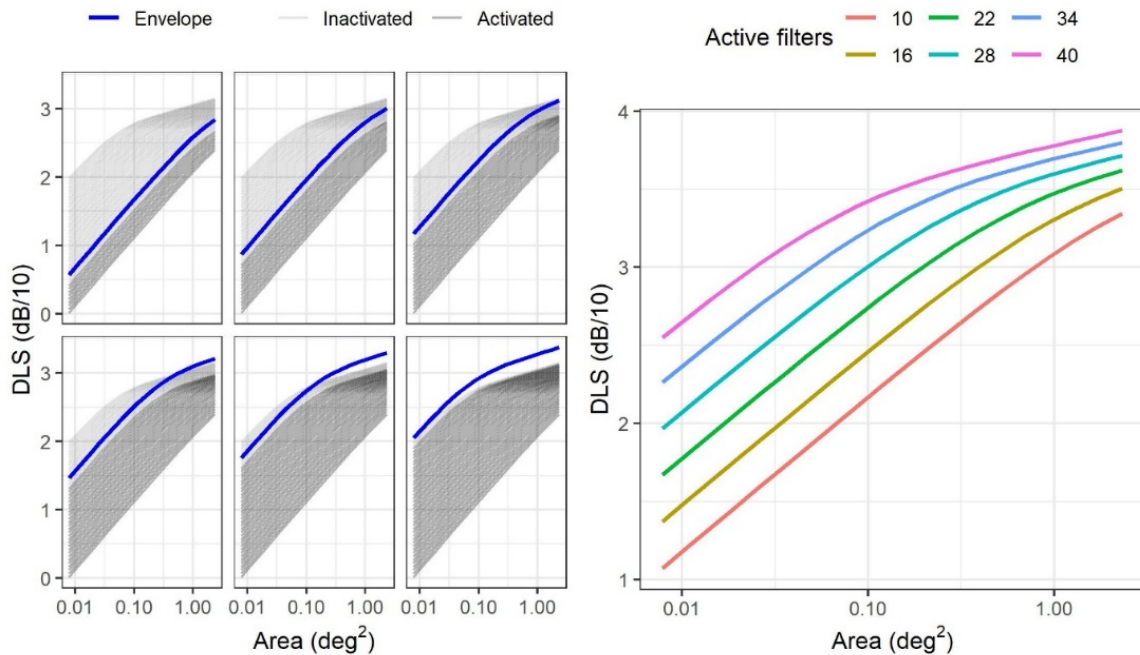


Figure 5.13. Response envelope modelling. The blue lines in the left panels represent the envelope of the combine responses of the cortical filters whose responses are shown as black likes (inactive filters are in light grey). The right panel reports the same response envelopes, color-coded according to the number of hypothetical filters combined to generate the response.

We finally implemented a more realistic two-stage version⁷⁰ of the cortical pooling model presented in **Figure 5.11**, where an array of cortical cells would sample the response of an array of RGCs like the one used in our main model. The cortical cell array was the same as the RGC array but used a D1 filter as their receptive field. **Figure 5.14** shows the responses produced by both the multiscale filters and the combination envelope. These largely replicate our experimental results (horizontal translation of the same response), with some small changes at different scales introduced by the fact that the size of the RGCs did not scale with the chosen cortical filter. Like in Swanson et al.⁷⁰, this modelling exercise shows that Ricco’s area can be entirely determined by cortical filters without changing the RGC density or the size of the RGC-RF.

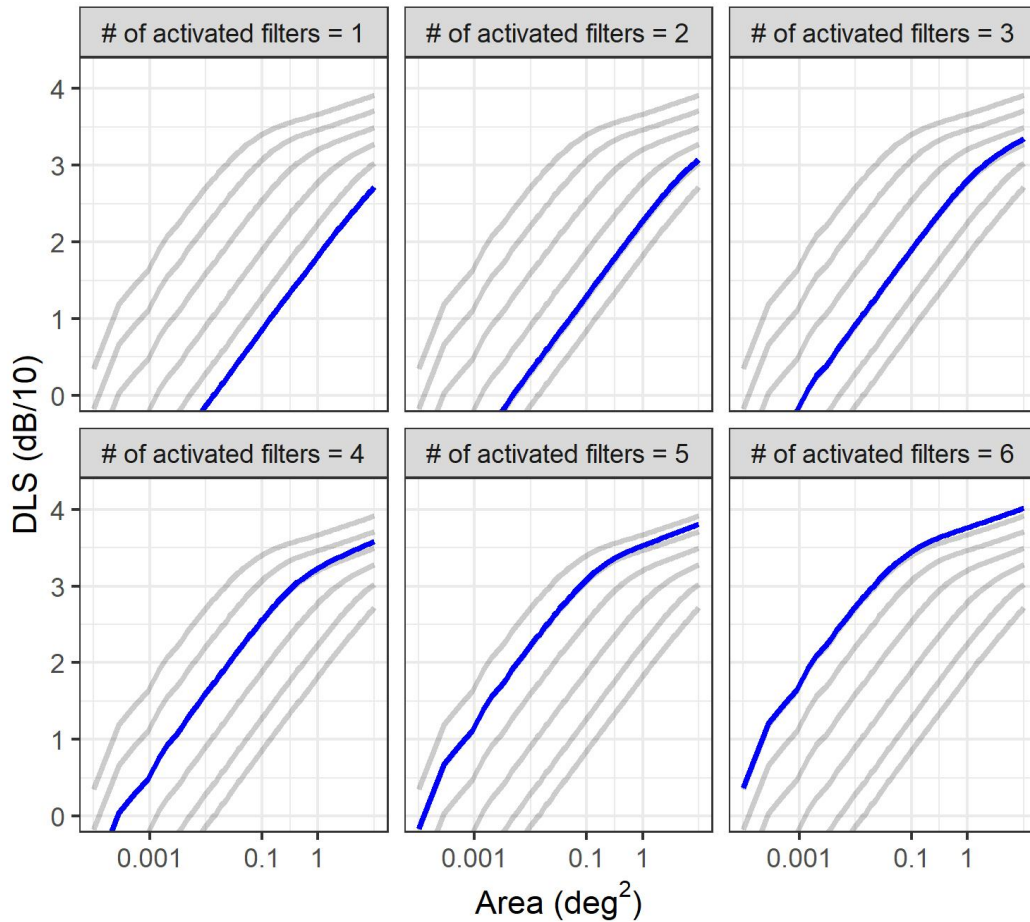


Figure 5.14 Replication of the model in cortical filter model using a two-stage model. The individual filter responses at different scales are reported in grey. The blue line represents the response envelope obtained by combining, through probability summation, the responses of filters with progressively smaller spatial scales. For example, in the top-right panel, the envelope is obtained by combining the responses of the filters with the three largest scales, while excluding the remaining 3 with a smaller spatial scale.

5.7. Supplementary material

5.7.1. Spatial summation with midget OFF retinal ganglion cells

		Eccentricity (degrees)			Comparisons		
		1.414 (A)	5.657 (B)	9.899 (C)	A vs B	A vs C	B vs C
Uncorrected	τ (x 10 ²)	66.53 [39.12, 110.42]	30.46 [21.03, 46.24]	15.18 [11.14, 22.68]	< 0.0001	< 0.0001	0.0002
	Offset (dB/10)	2.34 [2.28, 2.43]	2.51 [2.45, 2.6]	2.54 [2.44, 2.61]	< 0.0001	< 0.0001	0.4201
	Ricco's area (deg ²)	0.039 [0.024, 0.068]	0.109 [0.068, 0.149]	0.144 [0.104, 0.197]	< 0.0001	< 0.0001	0.0171
	# mOFF-RGCs*	95.72 [55.66, 159.1]	44.04 [30.39, 67.08]	22.02 [16.06, 32.7]	< 0.0001	< 0.0001	0.0002
Convergence weighted	τ (x 10 ²)	84.28 [51.02, 137.96]	71.01 [48.86, 105.18]	57.62 [43.78, 92.11]	0.9442	0.4883	0.9442
	Offset (dB/10)	2.31 [2.25, 2.41]	2.42 [2.35, 2.5]	2.4 [2.3, 2.46]	< 0.0001	0.0175	0.0403
	Ricco's area (deg ²)	0.039 [0.024, 0.068]	0.11 [0.067, 0.148]	0.143 [0.103, 0.198]	< 0.0001	< 0.0001	0.0153
	# mOFF-RGCs†	121.39 [72.82, 198.81]	102.5 [70.58, 152.3]	83.61 [63.67, 132.72]	0.9326	0.4854	0.9326

Table 5.4. Model fit results with midget RGCs. Median [Interquartile Range] of the different outputs from the model fits. Comparisons were performed on log-transformed values but reported in linear scale (except for the Offset, which was tested and reported in log-scale). mOFF-RGC = midget OFF retinal ganglion cells. *Obtained by taking the product of Ricco's area and local mOFF-RGC density; † Obtained by taking the product of Ricco's area and local mOFF-RGC density scaled by retinal convergence.

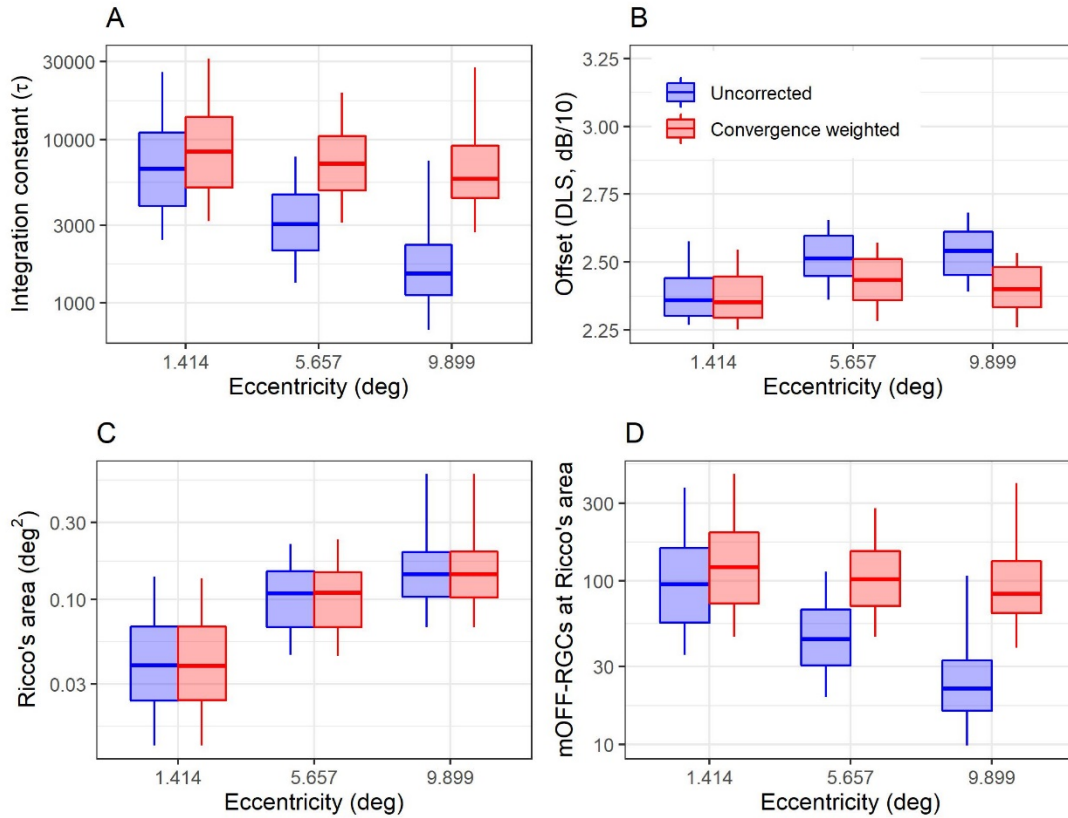


Figure 5.15. Model fit results with midget RGCs. Box-plots of the different parameters and estimates derived from the model for spatial summation data. Note that the convergence weighted values in (D) are obtained by simply multiplying the uncorrected number of midget OFF-RGCs at Ricco's area by the convergence rate. The box encloses the interquartile range, the horizontal midline indicates the median and the error bars extend from the 5% to the 95% quantiles. The vertical axis is \log_{10} -spaced. RGC = Retinal Ganglion Cell

5.7.2. Effect of optical factor compensation

		Eccentricity (degrees)			Comparisons		
		1.414 (A)	5.657 (B)	9.899 (C)	A vs B	A vs C	B vs C
Uncorrected	τ ($\times 10^2$)	72.54 [42.4, 119.38]	53.5 [36.78, 86.51]	32.35 [22.6, 53.44]	0.1386	0.0006	0.0413
	Offset (dB/10)	2.33 [2.28, 2.43]	2.49 [2.43, 2.59]	2.5 [2.41, 2.58]	< 0.0001	< 0.0001	0.8806
	Ricco's area (deg^2)	0.019 [0.011, 0.037]	0.101 [0.059, 0.139]	0.143 [0.091, 0.219]	< 0.0001	< 0.0001	0.0017
	# P-OFF-RGCs*	9.46 [5.17, 16.99]	11.5 [7.59, 20.01]	9.02 [6.05, 15.54]	0.5253	0.8895	0.8895
Convergence weighted	τ ($\times 10^2$)	90.12 [54.7, 148.87]	124.47 [85.97, 201.38]	126.58 [83.64, 210]	0.0324	0.0071	0.5050
	Offset (dB/10)	2.31 [2.25, 2.41]	2.4 [2.34, 2.5]	2.36 [2.27, 2.43]	0.0006	0.2574	0.0163
	Ricco's area (deg^2)	0.019 [0.011, 0.037]	0.101 [0.058, 0.14]	0.143 [0.094, 0.207]	< 0.0001	< 0.0001	0.0020
	# P-OFF-RGCs†	64.77 [36.86, 116.88]	85.95 [57.42, 150.81]	84.08 [53.29, 145.9]	0.1166	0.0701	0.7000

Table 5.5. Effect of optical factors on model fit results. Median [Interquartile Range] of the different outputs from the model fits by taking the summation over the module (absolute value) of the RGC. Comparisons were performed on log-transformed values but reported in linear scale (except for the Offset, which was tested and reported in log-scale).

P-OFF-RGC = parasol OFF retinal ganglion cells. * Obtained by taking the product of Ricco's area and local, P-OFF-RGC density; † Obtained by taking the product of Ricco's area and local P-OFF-RGC density scaled by retinal convergence.

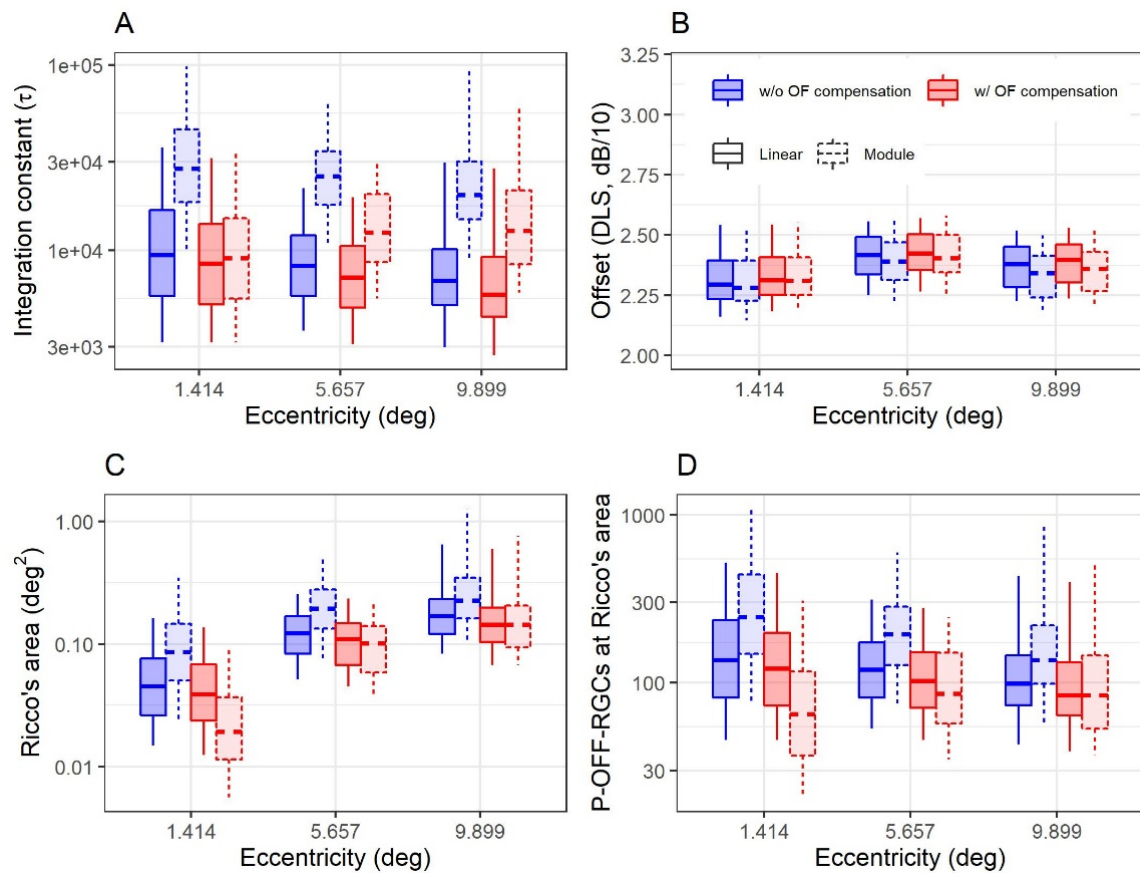


Figure 5.16. Effect of optical factors on model fit results. Box-plots of the different parameters and estimates derived from the model for spatial summation data. The shading indicates whether the summation in equation (5.6) in the text was taken over the absolute value (module) or the signed (linear) RGC input. The box encloses the interquartile range, the horizontal midline indicates the median and the error bars extend from the 5% to the 95% quantiles. The vertical axis is \log_{10} -spaced. RGC = Retinal Ganglion Cell; OF = Optical factors (average modulation transfer function of the eye)

5.7.3. Average parameters for the psychometric functions

Stimulus	Location {X, Y}	μ, σ (dB)				
		Subject 1	Subject 2	Subject 3	Subject 4	Subject 5
G-I, 15 ms	{-7, -7}	13.99, 1.86	17.52, 1.79	15.43, 2.06	12.68, 2.90	12.79, 2.97
	{-7, 7}	13.22, 1.66	13.59, 5.15	14.41, 1.92	12.17, 4.89	10.46, 3.41
	{7, -7}	15.55, 2.54	16.88, 3.45	15.48, 1.58	12.60, 2.00	9.16, 3.94
	{7, 7}	15.72, 2.58	14.95, 4.12	15.52, 1.72	12.35, 1.75	13.08, 3.09
G-I, 200 ms	{-7, -7}	21.90, 1.86	24.35, 1.4	22.67, 2.10	22.46, 1.53	20.97, 3.73
	{-7, 7}	20.63, 1.82	23.24, 2.03	22.56, 2.18	22.80, 2.36	20.03, 3.99
	{7, -7}	24.54, 1.59	24.70, 1.67	23.32, 1.76	22.90, 2.29	20.03, 3.13
	{7, 7}	25.96, 1.73	23.92, 1.63	23.68, 2.02	22.69, 2.20	22.28, 2.12
G-V, 15 ms	{-7, -7}	31.69, 1.75	34.09, 1.24	32.87, 1.44	32.49, 1.88	32.86, 1.33
	{-7, 7}	31.34, 1.04	33.06, 1.32	31.91, 2.20	32.30, 1.77	31.56, 1.18
	{7, -7}	33.47, 1.17	33.86, 1.61	32.56, 1.35	32.12, 2.11	32.90, 1.68
	{7, 7}	33.37, 1.43	34.12, 0.99	32.57, 1.44	32.00, 2.03	32.67, 1.28
G-V, 200 ms	{-7, -7}	36.81, 0.94	38.31, 0.85	37.61, 1.70	38.21, 1.00	37.49, 1.13
	{-7, 7}	36.96, 1.21	37.33, 0.96	37.20, 1.45	38.15, 1.84	37.11, 0.90
	{7, -7}	38.23, 0.77	38.57, 1.27	37.80, 1.96	37.75, 1.74	37.05, 0.92
	{7, 7}	38.13, 1.05	38.41, 0.61	37.80, 1.44	38.14, 0.87	37.17, 0.99
	γ	0.018	0.024	0.009	0.055	0.063
	λ	0.017	0.008	0.016	0.039	0.008

Table 5.6. Parameters for the psychometric functions. Fitted parameters for the psychometric function obtained from the Method of Constant Stimuli (MOCS) experiment at the four tested locations in five subjects with four different combinations of stimulus size and duration. Lapses (λ) and guesses (γ) were modelled as global parameters for the whole MOCS experiment in each eye.

5.7.4. Results with an alternative temporal impulse response

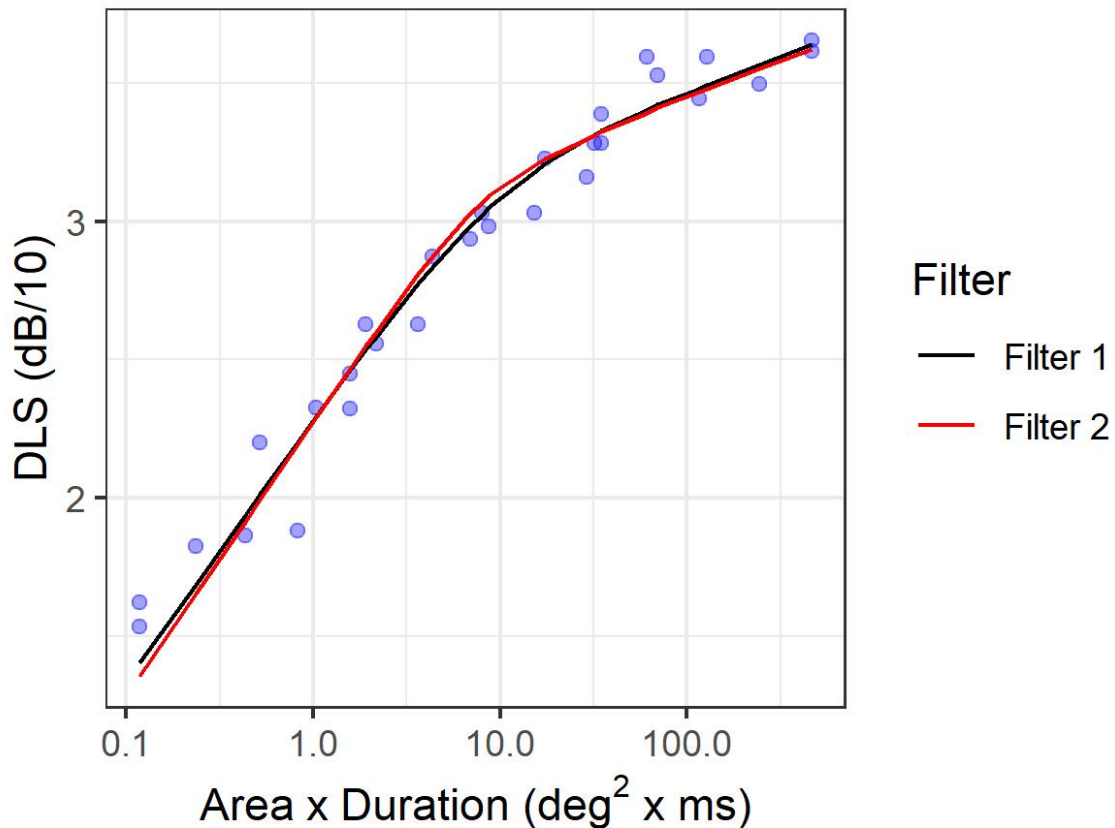


Figure 5.17. Effect of different impulse response functions. Example of the fitted response of the model with the impulse response used in the main calculations (Filter 1) and with the monophasic impulse response used by Gorea and Tyler¹⁵ and described by Watson⁴⁷ (Filter 2).

5.8. References

1. Pan F, Swanson WH. A cortical pooling model of spatial summation for perimetric stimuli. *J Vis* 2006;6:1159-1171.
2. Choi AY, Nivison-Smith L, Khuu SK, Kalloniatis M. Determining Spatial Summation and Its Effect on Contrast Sensitivity across the Central 20 Degrees of Visual Field. *PLoS One* 2016;11:e0158263.
3. Khuu SK, Kalloniatis M. Spatial summation across the central visual field: implications for visual field testing. *J Vis* 2015;15:15 11 16.
4. Khuu SK, Kalloniatis M. Standard Automated Perimetry: Determining Spatial Summation and Its Effect on Contrast Sensitivity Across the Visual Field. *Investigative ophthalmology & visual science* 2015;56:3565-3576.
5. Phu J, Khuu SK, Zangerl B, Kalloniatis M. A comparison of Goldmann III, V and spatially equated test stimuli in visual field testing: the importance of complete and partial spatial summation. *Ophthalmic Physiol Opt* 2017;37:160-176.
6. Yoshioka N, Zangerl B, Phu J, et al. Consistency of Structure-Function Correlation Between Spatially Scaled Visual Field Stimuli and In Vivo OCT Ganglion Cell Counts. *Investigative ophthalmology & visual science* 2018;59:1693-1703.
7. Swanson WH, Felius J, Pan F. Perimetric defects and ganglion cell damage: interpreting linear relations using a two-stage neural model. *Investigative ophthalmology & visual science* 2004;45:466-472.

8. Rountree L, Mulholland PJ, Anderson RS, Garway-Heath DF, Morgan JE, Redmond T. Optimising the glaucoma signal/noise ratio by mapping changes in spatial summation with area-modulated perimetric stimuli. *Sci Rep* 2018;8:2172.
9. Redmond T, Garway-Heath DF, Zlatkova MB, Anderson RS. Sensitivity loss in early glaucoma can be mapped to an enlargement of the area of complete spatial summation. *Investigative ophthalmology & visual science* 2010;51:6540-6548.
10. Kwon M, Liu R. Linkage between retinal ganglion cell density and the nonuniform spatial integration across the visual field. *Proc Natl Acad Sci U S A* 2019;116:3827-3836.
11. Mulholland PJ, Redmond T, Garway-Heath DF, Zlatkova MB, Anderson RS. Spatiotemporal Summation of Perimetric Stimuli in Early Glaucoma. *Investigative ophthalmology & visual science* 2015;56:6473-6482.
12. Mulholland PJ, Redmond T, Garway-Heath DF, Zlatkova MB, Anderson RS. Estimating the critical duration for temporal summation of standard achromatic perimetric stimuli. *Investigative ophthalmology & visual science* 2014;56:431-437.
13. Glezer VD. The receptive fields of the retina. *Vision research* 1965;5:497-525.
14. Watson AB. Probability summation over time. *Vision research* 1979;19:515-522.
15. Gorea A, Tyler CW. New look at Bloch's law for contrast. *J Opt Soc Am A* 1986;3:52-61.
16. Swanson WH, Pan F, Lee BB. Chromatic temporal integration and retinal eccentricity: psychophysics, neurometric analysis and cortical pooling. *Vision research* 2008;48:2657-2662.
17. Swanson WH, Ueno T, Smith VC, Pokorny J. Temporal modulation sensitivity and pulse-detection thresholds for chromatic and luminance perturbations. *J Opt Soc Am A* 1987;4:1992-2005.
18. Barlow HB. Temporal and spatial summation in human vision at different background intensities. *J Physiol* 1958;141:337-350.
19. Owen WG. Spatio-temporal integration in the human peripheral retina. *Vision research* 1972;12:1011-1026.
20. Anderson SJ, Burr DC. Spatial summation properties of directionally selective mechanisms in human vision. *J Opt Soc Am A* 1991;8:1330-1339.
21. Fredericksen RE, Verstraten FA, van de Grind WA. Spatial summation and its interaction with the temporal integration mechanism in human motion perception. *Vision research* 1994;34:3171-3188.
22. Goldmann H. Fundamentals of exact perimetry. 1945. *Optom Vis Sci* 1999;76:599-604.
23. Turpin A, Artes PH, McKendrick AM. The Open Perimetry Interface: an enabling tool for clinical visual psychophysics. *J Vis* 2012;12.
24. King-Smith PE, Grigsby SS, Vingrys AJ, Benes SC, Supowit A. Efficient and unbiased modifications of the QUEST threshold method: theory, simulations, experimental evaluation and practical implementation. *Vision Res* 1994;34:885-912.
25. Olsson J, Bengtsson B, Heijl A, Rootzen H. An improved method to estimate frequency of false positive answers in computerized perimetry. *Acta Ophthalmol Scand* 1997;75:181-183.
26. Watson AB. QUEST+: A general multidimensional Bayesian adaptive psychometric method. *J Vis* 2017;17:10.
27. Prins N. Hierarchical Bayesian modeling of the psychometric function (and an example application in an experiment on correspondence matching in long-range motion). *Journal of Vision* 2019;19:287b-287b.
28. Curcio CA, Allen KA. Topography of ganglion cells in human retina. *The Journal of comparative neurology* 1990;300:5-25.
29. Raza AS, Hood DC. Evaluation of the Structure-Function Relationship in Glaucoma Using a Novel Method for Estimating the Number of Retinal Ganglion Cells in the Human Retina. *Investigative ophthalmology & visual science* 2015;56:5548-5556.
30. Montesano G, Ometto G, Hogg RE, Rossetti LM, Garway-Heath DF, Crabb DP. Revisiting the Drasdo Model: Implications for Structure-Function Analysis of the Macular Region. *Transl Vis Sci Technol* 2020;9:15.
31. Drasdo N, Millican CL, Katholi CR, Curcio CA. The length of Henle fibers in the human retina and a model of ganglion receptive field density in the visual field. *Vision Res* 2007;47:2901-2911.
32. Baumgardt E. Visual spatial and temporal summation. *Nature* 1959;184(Suppl 25):1951-1952.
33. Bradley C, Abrams J, Geisler WS. Retina-V1 model of detectability across the visual field. *J Vis* 2014;14.
34. Legras R, Gaudric A, Woog K. Distribution of cone density, spacing and arrangement in adult healthy retinas with adaptive optics flood illumination. *PLoS One* 2018;13:e0191141.
35. Croner LJ, Kaplan E. Receptive fields of P and M ganglion cells across the primate retina. *Vision research* 1995;35:7-24.
36. Sjostrand J, Olsson V, Popovic Z, Conradi N. Quantitative estimations of foveal and extra-foveal retinal circuitry in humans. *Vision research* 1999;39:2987-2998.

37. Curcio CA, Sloan KR, Kalina RE, Hendrickson AE. Human photoreceptor topography. *The Journal of comparative neurology* 1990;292:497-523.
38. Watson AB. A formula for the mean human optical modulation transfer function as a function of pupil size. *J Vis* 2013;13:18.
39. Quick RF, Jr. A vector-magnitude model of contrast detection. *Kybernetik* 1974;16:65-67.
40. Tyler CW, Chen CC. Signal detection theory in the 2AFC paradigm: attention, channel uncertainty and probability summation. *Vision research* 2000;40:3121-3144.
41. Meese TS, Williams CB. Probability summation for multiple patches of luminance modulation. *Vision research* 2000;40:2101-2113.
42. Robson JG, Graham N. Probability summation and regional variation in contrast sensitivity across the visual field. *Vision research* 1981;21:409-418.
43. Lagarias JC, Reeds JA, Wright MH, Wright PE. Convergence Properties of the Nelder--Mead Simplex Method in Low Dimensions. *SIAM Journal on Optimization* 1998;9:112-147.
44. Bates D, Mächler M, Bolker B, Walker S. Fitting Linear Mixed-Effects Models Using lme4. *Journal of Statistical Software* 2015;67:1 - 48.
45. Henson DB, Chaudry S, Artes PH, Faragher EB, Ansons A. Response variability in the visual field: comparison of optic neuritis, glaucoma, ocular hypertension, and normal eyes. *Invest Ophthalmol Vis Sci* 2000;41:417-421.
46. Gardiner SK, Demirel S, Johnson CA. Modeling the sensitivity to variability relationship in perimetry. *Vision research* 2006;46:1732-1745.
47. Watson AB. Derivation of the impulse response: comments on the method of Roufs and Blommaert. *Vision Res* 1982;22:1335-1337.
48. Kelly DH, Savoie RE. Theory of flicker and transient responses. III. An essential nonlinearity. *J Opt Soc Am* 1978;68:1481-1490.
49. Roufs JA. Dynamic properties of vision. IV. Thresholds of decremental flashes, incremental flashes and doublets in relation to flicker fusion. *Vision Res* 1974;14:831-851.
50. Breitmeyer BG, Ganz L. Temporal studies with flashed gratings: Inferences about human transient and sustained channels. *Vision Research* 1977;17:861-865.
51. Swanson WH, Dul MW, Horner DG, Liu T, Tran I. Assessing spatial and temporal properties of perimetric stimuli for resistance to clinical variations in retinal illumination. *Investigative ophthalmology & visual science* 2014;55:353-359.
52. Bierings R, de Boer MH, Jansonius NM. Visual Performance as a Function of Luminance in Glaucoma: The De Vries-Rose, Weber's, and Ferry-Porter's Law. *Investigative ophthalmology & visual science* 2018;59:3416-3423.
53. Dacey DM, Petersen MR. Dendritic field size and morphology of midget and parasol ganglion cells of the human retina. *Proc Natl Acad Sci U S A* 1992;89:9666-9670.
54. Dacey DM. The mosaic of midget ganglion cells in the human retina. *J Neurosci* 1993;13:5334-5355.
55. Swanson WH, Sun H, Lee BB, Cao D. Responses of primate retinal ganglion cells to perimetric stimuli. *Investigative ophthalmology & visual science* 2011;52:764-771.
56. Curcio CA, Allen KA. Topography of ganglion cells in human retina. *J Comp Neurol* 1990;300:5-25.
57. Tuten WS, Cooper RF, Tiruveedhula P, et al. Spatial summation in the human fovea: Do normal optical aberrations and fixational eye movements have an effect? *J Vis* 2018;18:6.
58. Dalimier E, Dainty C. Role of ocular aberrations in photopic spatial summation in the fovea. *Opt Lett* 2010;35:589-591.
59. Davila KD, Geisler WS. The relative contributions of pre-neural and neural factors to areal summation in the fovea. *Vision research* 1991;31:1369-1380.
60. Liu Z, Kurokawa K, Zhang F, Lee JJ, Miller DT. Imaging and quantifying ganglion cells and other transparent neurons in the living human retina. *Proc Natl Acad Sci U S A* 2017;114:12803-12808.
61. Klein SA. Measuring, estimating, and understanding the psychometric function: a commentary. *Percept Psychophys* 2001;63:1421-1455.
62. Rubinstein NJ, Turpin A, Denniss J, McKendrick AM. Effects of Criterion Bias on Perimetric Sensitivity and Response Variability in Glaucoma. *Transl Vis Sci Technol* 2021;10:18.
63. Keltgen KM, Swanson WH. Estimation of spatial scale across the visual field using sinusoidal stimuli. *Invest Ophthalmol Vis Sci* 2012;53:633-639.
64. Liu M, Duggan J, Salt TE, Cordeiro MF. Dendritic changes in visual pathways in glaucoma and other neurodegenerative conditions. *Exp Eye Res* 2011;92:244-250.

65. Wang B, Yan T, Zhou J, et al. Altered fMRI-derived functional connectivity in patients with high-tension glaucoma. *J Neuroradiol* 2021;48:94-98.
66. Plummer M. JAGS: A program for analysis of Bayesian graphical models using Gibbs sampling. 2003.
67. Gelman A, Rubin DB. Inference from Iterative Simulation Using Multiple Sequences. *Statistical Science* 1992;7:457-472, 416.
68. Redmond T, Zlatkova MB, Vassilev A, Garway-Heath DF, Anderson RS. Changes in Ricco's area with background luminance in the S-cone pathway. *Optom Vis Sci* 2013;90:66-74.
69. Dacey DM, Lee BB. The 'blue-on' opponent pathway in primate retina originates from a distinct bistratified ganglion cell type. *Nature* 1994;367:731-735.
70. Swanson WH, Felius J, Pan F. Perimetric defects and ganglion cell damage: interpreting linear relations using a two-stage neural model. *Invest Ophthalmol Vis Sci* 2004;45:466-472.

6. Spatial summation in the glaucomatous macula: a link with retinal ganglion cell damage

This paper tested the computational model developed in the previous chapter in patients with glaucoma. In particular, we showed that the spatial summation profile generated by the computational model in response to RGC loss or damage could be replicated by a simple horizontal translation of the same curve (a template). This would effectively lead to a change in the critical area in glaucoma. This property was used to fit the template to data from glaucoma patients and healthy age-matched controls. The results demonstrated a good agreement with the predictions from the computational model for different levels of glaucoma damage. Importantly, this was the first investigation of its kind in the macula of patients with glaucoma, including patients with advanced damage. The results were also in good agreement with previous literature in animal models. The key element of novelty was the use of a computational model to link the changes observed in glaucoma patients to a biological substrate. The paper also investigated the empirical structure-function relationship using imaging data. Importantly, we confirmed that local measurements of structural damage suffer from a significantly restricted dynamic range that prevents accurate quantification of advanced damage. This has important implications for both clinical applications of imaging technology and for the interpretation of experimental results. Additional insight could be gathered by using, in the future, more advanced imaging techniques able to resolve individual RGCs¹. The manuscript is currently under revision at *Investigative Ophthalmology & Visual Science* (IOVS), a journal of the Association for Research in Vision and Ophthalmology (ARVO).

Contributions

- *Main contributor*: **Giovanni Montesano** (conceptualisation of research, development of testing software, data collection, data and statistical analysis, interpretation of the data, drafting of the manuscript).
- *Other contributors*:
 - **Tony Redmond** (supervision, interpretation of the data, manuscript proofing)
 - **Pádraig J. Mulholland** (supervision, interpretation of the data, manuscript proofing)
 - **David F. Garway-Heath** (supervision, interpretation of the data, manuscript proofing)
 - **Giovanni Ometto** (data analysis, interpretation of the data, manuscript proofing)
 - **Dario Romano** (data collection, manuscript proofing)
 - **Federica Antonacci** (data collection, manuscript proofing)
 - **Lucia Tanga** (data collection, manuscript proofing)
 - **Carmela Carnevale** (data collection, manuscript proofing)
 - **Luca M. Rossetti** (data collection, manuscript proofing)
 - **David P. Crabb** (supervision, interpretation of the data, manuscript proofing)
 - **Francesco Oddone** (supervision, interpretation of the data, manuscript proofing)

6.1. Introduction

Glaucoma is characterized by progressive loss of the visual field (VF) as a consequence of damage to, and death of, Retinal Ganglion Cells (RGCs).^{2, 3} VF damage is usually detected and monitored with Standard Automated Perimetry (SAP), in which circular stimuli of constant area and duration are modulated in luminance on a uniform background at different VF locations. The test aims to estimate, for each location, the stimulus luminance that represents the just noticeable difference from the background luminance. This is expressed as VF sensitivity, where decibel units measure the attenuation of the brightest stimulus (higher dB indicating dimmer stimuli). Despite a long-established understanding that perimetric sensitivity is associated with RGC density,⁴⁻⁷ in that they co-vary in disease such as glaucoma, their exact relationship has proven difficult to elucidate.

Useful insights into the pathophysiology of visual loss in glaucoma can be gathered by studying how perimetric sensitivity changes with stimulus area. For a given duration and background luminance, sensitivity is known to increase with the area of the stimulus (*spatial summation*).⁸ The change in sensitivity is steeper and directly proportional to the area of the stimulus (*complete spatial summation*) up to a certain critical area (Ricco's area, or the area of complete spatial summation). After this point, sensitivity still increases with stimulus area but by a smaller amount (*partial summation*). Ricco's area is known to enlarge with eccentricity and different stimulating conditions and it has been hypothesized that a critical number of RGCs underlies Ricco's area across different eccentricities⁹⁻¹⁵, this varying with adaptation level¹⁶. Similar scaling of Ricco's area with RGC density has been hypothesized to hold true with RGC loss in glaucoma¹⁷. Redmond et al. demonstrated that Ricco's area is enlarged in glaucoma, which can account for the difference in sensitivity between patients and healthy controls for conventional Goldmann III stimuli¹⁷. Antwi-Boasiako et al. showed similar results in non-human primates¹⁸.

The use of computational models has been pivotal to the understanding of these phenomena. Swanson et al.¹⁹ showed that spatial summation can be reproduced by a two-stage hierarchical process involving RGC density as well as the spatial tuning of cortical filters, which can be independent of the underlying density of RGCs. Further research by Pan & Swanson suggested that probability summation across RGCs cannot explain spatial summation of perimetric stimuli, whereas it may be explained instead by cortical pooling by multiple spatial mechanisms²⁰. We have recently proposed a computational model able to reproduce the interaction between stimulus area and duration in the response of a synthetic RGC mosaic in healthy observers²¹. In that work, we also hypothesised, in partial agreement with Swanson et al.²², that the retinal input would determine the selection of different cortical filters, altering spatial summation. We hypothesised that this retinal input could also be altered by a change in the density of RGCs. Under this assumption, we showed that our model would be able to reproduce the results presented by Redmond et al.¹⁷ in glaucoma.

Glaucoma damage in the macula has been documented extensively in the literature^{23, 24}, but has gained increasing attention in recent years after reports that it can be affected in early disease,²⁵⁻²⁷ albeit often going undetected clinically until later in the condition,^{28, 29} and that it affects quality of life of patients at all stages of disease³⁰. In the healthy eye, sensitivity measured with the Goldmann III stimulus adopted in SAP (0.43 deg in diameter) in photopic conditions are determined by complete spatial summation only outside the central 15 degrees^{9-11, 22}. This means that early macular damage from glaucoma would produce only small changes in SAP sensitivity until a very large proportion of RGCs is lost^{17, 19, 31, 32}.

Despite its relevance, only two studies have investigated spatial summation in glaucomatous macula, one in non-human primates¹⁸ and one in glaucoma patients^{18, 33}. However, they limited their analysis to early damage. Moreover, the investigation in glaucoma patients³³ only correlated sensitivity with coarse RGC count estimates from Optical Coherence Tomography (OCT) imaging, rather than attempting to model the underlying latent process of damage.

In the current study, we wished to test the hypothesis that changes in sensitivity in the macula of patients with glaucoma could be explained by a change in the spatial scale used by the visual system that relates to RGC loss or damage. Here, we perform five separate SAP examinations, each with a different fixed-area luminance-modulated stimulus on a 10-2 grid, in eyes with glaucoma with different levels of damage and age-similar healthy control eyes, as well as in young healthy eyes. We then compare our functional RGC density estimates derived from the spatial summation model with structural estimates from high-density OCT scans, to determine the extent to which VF damage can be predicted from clinical measures of tissue loss in the macula.

6.2. Methods

6.2.1. Study population

Data were collected in the eye clinic at Santi Paolo e Carlo Hospital – University of Milan, Milan, Italy and in the glaucoma clinic at IRCCS Fondazione G.B. Bietti, Rome, Italy.

Thirty young healthy participants were recruited among staff and students on a voluntary basis. Inclusion criteria for this cohort were: 1) age between 18 and 40 years; 2) best corrected visual acuity (BCVA) of 0 logMAR or better; 3) Intraocular pressure (IOP) < 21 mmHg; 4) no evidence of ocular disease on preliminary ophthalmoscopic examination; 5) no history or evidence of systemic disease that might affect the VF or compromise the execution of the test. Individuals were excluded if the macular or optic nerve head (ONH) OCT scans collected for the study showed any signs of ocular disease (details of the imaging and macular testing protocols are reported later). A 24-2 Swedish Interactive Thresholding Algorithm (SITA) VF test was performed for descriptive purposes for the study but was not used to assess inclusion.

Glaucoma patients and the age-similar healthy participants were recruited on a voluntary basis. Glaucoma patients' charts were screened by clinicians in order to identify potentially eligible candidates. To meet eligibility criteria, patients were required to have a confirmed clinical diagnosis of open angle glaucoma (which could include pseudoexfoliative and pigment dispersion glaucoma), regardless of the integrity of their VF. Glaucoma patients were stratified by level of damage according to the Mean Deviation (MD) value from their most recent reliable (FP < 15%) 24-2 SITA test and classified as early (MD better than -6 dB), moderate (MD between -6 dB and -12 dB) or advanced (MD worse than -12 dB), with the aim of recruiting 10 participants for each class. Other inclusion criteria were: 1) age greater than 18 years; 2) BCVA of 0.2 logMAR or better; 3) no history or evidence of other ocular or systemic diseases, other than glaucoma, that might affect the VF or compromise the execution of the test. Age-matched controls were recruited among members of staff and patients' spouses, partners and relatives. Inclusion criteria were the same as for the healthy young cohort, but with no upward age limit and the requirement for VA to be better than or equal to 0.2 logMAR.

Written informed consent was obtained from all participants. The study adhered to the tenets of the Declaration of Helsinki and was approved by local ethics committees (Comitato Etico Milano Area 1 -code OCU_SSSF; Comitato Etico Centrale IRCCS Lazio N. 90/19/FB).

6.2.2. Study protocol

All healthy participants underwent an ophthalmoscopic examination and measurement of their BCVA and IOP (Goldmann Applanation Tonometry) in order to confirm eligibility. Their BCVA was not tested beyond 0 logMAR. BCVA and IOP were not recorded for the study and only used to assess the exclusion criteria. Axial length and corneal curvature were measured with an IOLMaster (Carl Zeiss Meditec, Dublin, USA) and recorded for the study.

Only one eye per participant was included in the study. Where both eyes of healthy controls were eligible, one was chosen arbitrarily by the researcher for testing. In the glaucoma cohort, if the two eyes were classified as having a different stage of glaucoma, one was chosen to populate the severity group, as needed. Otherwise, one was chosen arbitrarily by the researcher.

6.2.2.1. Standard Automated Perimetry

All VF tests were performed with a Humphrey Field Analyzer (HFA, Carl Zeiss Meditec, Dublin, USA). Participants' near correction was used where required. For young healthy participants, near correction was used according to their preference. All healthy participants underwent a 24-2 SITA Standard test to obtain MD and Pattern Standard Deviation (PSD) values for descriptive purposes and for the purposes of disease severity classification.

Separate macular perimetric tests were performed with a 10-2 grid, Full-threshold strategy, each with a different Goldmann stimulus diameter (in degrees): G-I (0.10); G-II (0.21); G-III (0.43); G-IV (0.86); G-V (1.72). The order of these tests was randomized following a computer generated sequence of tests, one for each subject. For the young healthy cohort, the G-I test was repeated twice, because results with this stimulus were expected to be more variable²¹. For glaucoma patients and age matched controls, the G-III test was performed twice instead, to produce a more reliable estimate of the age-corrected sensitivity loss, because normative databases in the HFA are only available for the G-III stimulus. All participants performed a total of six 10-2 SAP tests. Based on previous literature for full-threshold tests,³⁴ reliability of the tests was only assessed with the percentage of FP errors (< 33%). For the healthy participants, a limit of 33% on false negative errors was also set. The operator was instructed to carefully monitor the participants and ensure good fixation throughout the test. If unreliable, the test, but not the participant, was excluded from analysis. Fixation losses were not used to determine good fixation because of their poor reliability as a fixation metric³⁴.

6.2.2.2. OCT imaging

Spectral Domain OCT (SD-OCT) imaging was performed with a Spectralis SD-OCT (Heidelberg Engineering, Heidelberg, Germany). A circumpapillary Retinal Nerve Fibre Layer (cp-RNFL) scan and a high-density macular cube (121 vertical B-scans, 30 x 25 degrees) were acquired. These scans were inspected by an ophthalmologist (the author, GM) to confirm the absence of any abnormality in the healthy cohorts and of any ocular disease other than glaucoma in the glaucoma cohort. Scans were judged of sufficient quality if all the layers could be clearly identified in the central 15 degrees around the fovea. No scans were removed because of poor quality.

Macular volumes were then exported in RAW binary format (.vol) using the Heidelberg Eye Explorer platform and read into R (R Foundation for Statistical Computing, Vienna, Austria). This file contained raw image files and segmentations of retinal layers, including the Inner limiting membrane (ILM), Bruch's membrane (BM), the RNFL, and Ganglion Cell Layer (GCL). These segmentations were checked for errors by an ophthalmologist (the author, GM) and corrected where needed. Retinal thickness and GCL thickness maps were generated and processed as previously described to obtain localised estimates of the number of RGCs underlying each stimulus area at all locations in the 10-2 grid^{21, 31, 35}. Briefly, the fovea was automatically located via template matching on the retinal thickness map. The GCL thickness map was transformed into a RGC density map with histology data from Curcio and Allen³⁶ using a method proposed by Raza and Hood.³⁷ This method accounts for eccentricity because the histology-derived volumetric density varies at different positions on the retina. The area covered by the stimuli was displaced and distorted to account for RGC displacement according to a revised version of the model proposed by Drasdo et al.^{31, 35, 38} (**Figure 6.1**). Note that our method for displacement is different from the one used by a similar previous study in the field,³³ and produces different RGC counts especially in the parafoveal region. However, our method was confirmed to be accurate.^{35, 39} All calculations were performed in visual degrees because we have previously shown that, under a spherical expansion model of the eye, calculations of RGC density in visual degrees are unaffected by axial length³⁵. There is anatomical³⁵ and psychophysical⁴⁰ evidence to support a spherical expansion model, at least for moderate refractive errors.

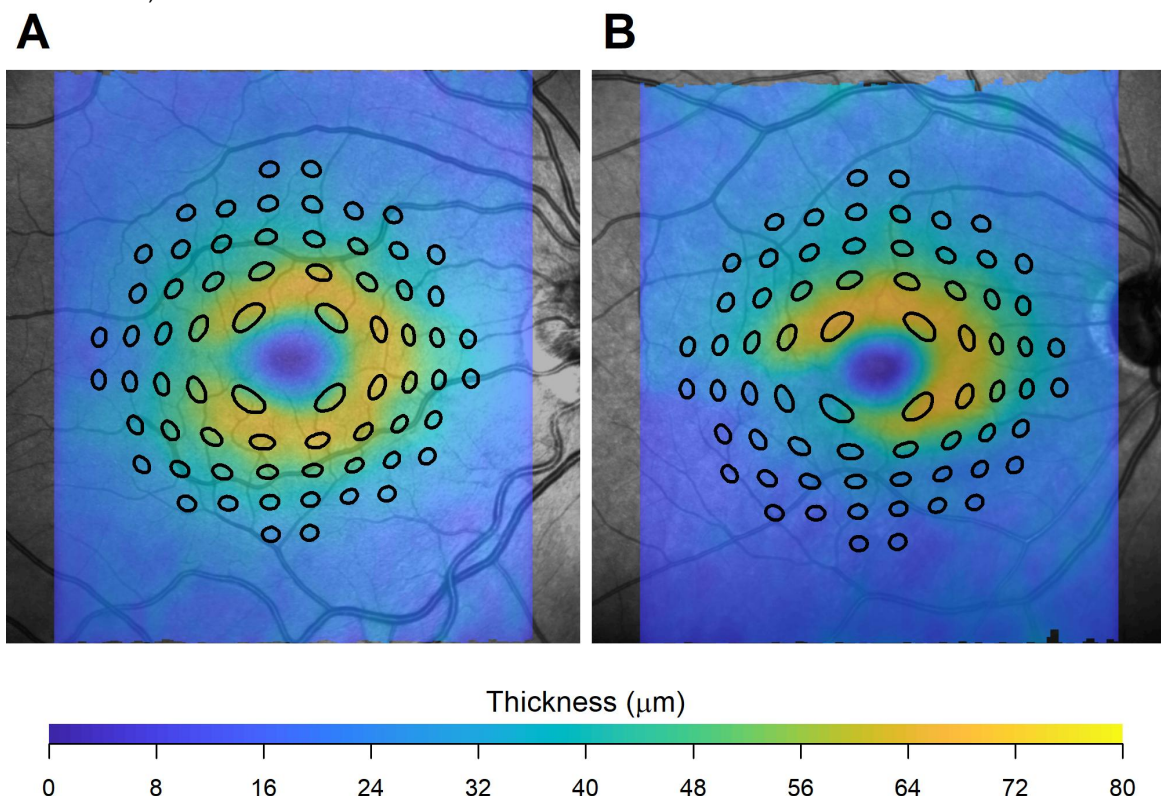


Figure 6.1. Displacement of perimetric stimuli. Test locations of the 10-2 grid distorted and displaced to cover the corresponding area on the ganglion cell layer thickness map in a healthy eye (A) and an eye with glaucoma (B). This example is for a G-V stimulus, for ease of visualization.

6.2.3. Spatial summation model

A previously described summation model²¹ was used to generate a template to fit the sensitivity vs stimulus area data. The summation model is described in more detail in the **Appendix**. In brief, the model integrates the total retina input, which is the product of stimulus area, stimulus duration, RGC density and Cone-to-RGC convergence ratio at a specific location. For this application, the stimulus duration was fixed at 200ms. The model predicts a biphasic relationship between retinal input and sensitivity, with a gradual transition from total to partial summation (**Figure 6.2**). The model accounts for the Cone-to-RGC convergence ratio because we found, in previous experiments and calculations,⁴¹ that the spatial summation response profile (and Ricco's area) did not scale perfectly with the number of RGCs at different eccentricities, but that the number of RGCs needed to be weighted by the number of cones converging onto each RGC. Because different classes of RGCs tile the retina with independent and partially overlapping mosaics, we only consider Parasol (or magnocellular) OFF RGCs (P-OFF-RGCs) for our calculations^{42,43} because P-RGCs have been shown to be preferentially stimulated by briefly flashed stimuli.^{44,45} However, for a given location, the effect of stimulus area can be explained by a change in the number of RGCs being stimulated. This indicates a scaling of recruited cortical filters with the amount of total retinal input, at least in healthy observers. Note that we do not attribute any specific role to OFF-RGCs, although a preferential involvement of this sub-class of RGCs has been suggested in glaucoma⁴⁶. This sub-class was simply chosen to model a hexagonal mosaic of non-overlapping RGCs^{38,43} and because OFF-RGCs are the most abundant in the human retina⁴⁶. Modelling ON-RGCs would have no material effect on our results other than proportionally scaling the underlying RGC density in the model.

In the current study, we wanted to test the hypothesis that such a cortical filter scaling would also occur with RGC damage in glaucoma. This can be done by testing whether the change in sensitivity from RGC damage in glaucoma could be explained by a simple horizontal shift of a summation template predicted by the model, similarly to what was reported by Redmond et al.¹⁷ This corresponds to a change in Ricco's area (**Figure 6.2**). To test this hypothesis, we made two assumptions:

- 1) RGC death and dysfunction would be indistinguishable, meaning that the model would not be able to distinguish whether the reduced input is provided by a smaller number of fully functional cells or a larger amount of dysfunctional cells⁴⁷.
- 2) The change in sensitivity would be predominantly a consequence of RGC loss and not of photoreceptor damage, media opacity or other conditions.

An alternative hypothesis was to assume *no change in spatial scaling*. This corresponds to modelling the change in sensitivity in glaucoma as a vertical shift in the summation template, i.e. change in sensitivity without any change in Ricco's area. Note that the actual value of Ricco's area is not reported as part of the results because it is not relevant for testing our hypothesis and because it is not univocally defined for a summation curve with a smooth transition from total to partial summation.

The model template was calibrated with data from the young healthy cohort and tested on glaucoma patients and age matched controls.

6.2.3.1. Model calibration

The model has three parameters (see Formula in the **Appendix**): α determines the vertical offset of the template (in \log_{10} scale); τ determines the transition from total to partial summation; κ determines the slope of the partial summation portion of the curve (slope = $1/\kappa$).

The model was calibrated with RGC count estimates and perimetric sensitivity values from the healthy young cohort. The RGC count estimates are more likely to be accurate in this group because of the low likelihood of retinal damage and the close similarity in age with the retinae in the original histology dataset by Curcio and Allen³⁶.

The parameters were estimated via numerical optimization (*fminsearch* function in Matlab R2018b, The Mathworks, Natick, USA) and 95%-Confidence Intervals (CIs) for the parameters were computed via bootstrap, resampling individual eyes rather than observations to preserve the correlation structure of the data. The calibrated model was used to generate a template to fit the rest of the data and test our hypothesis, as explained in the next section.

6.2.3.2. Template fitting to glaucoma patients and controls

Both the main and alternative hypothesis (*spatial scaling vs no spatial scaling* in glaucoma) can be tested by fitting the summation template to the perimetric data with different assumptions. Fitting the template presents significant challenges, especially because of the involvement of eyes with advanced damage. The main technical issues are the presence of censored data, because the HFA is not capable of presenting stimuli with luminance greater than 3,185 cd/m² (0 dB), and a consequent lack of sensitivity values for more damaged locations. This can, on the one hand, bias the estimates. On the other hand, it makes it difficult to obtain stable estimates for these locations when only few sensitivity values are available at this level of damage. Bayesian computation and hierarchical models can offer a solution because data censoring can be easily incorporated in complex models, avoiding the bias from censored data (i.e. sensitivities < 0 dB), and estimates at individual locations can be made more robust by efficiently distributing information across different levels of the hierarchy.

Details about the implementation of the Bayesian hierarchical model for this study are reported in the **Appendix**. In brief, for the main hypothesis (*spatial scaling*), the model estimated the density of RGCs at each location, in log₁₀-scale, by optimising the horizontal shift of the template to fit the observed sensitivity values for each stimulus area (**Figure 6.2**). The first level of the hierarchy was the population level, modelling the average RGC count. This was then propagated at the eye level and then at each location. The eye and location levels can be considered nested Gaussian random effects. Because of the hierarchical structure, all the data were fitted concomitantly and the estimate at each location was also informed by the data at other locations within the same eye and by the general behaviour of the population. The template was used as a link function to model the expected sensitivity at each stimulus area given the modelled RGC density estimate. The response variable was the sensitivity, which was censored at 0 dB. Note that using a link function for the expected sensitivity is different from modelling an inverse transformation of the data. The fitting process also modelled a vertical shift of the template at the population level, to optimise the average centration of the template. The alternative hypothesis (*no change in spatial scaling*) was implemented with a similar model. In this case, the hierarchical parameter was the vertical shift of the template and the horizontal shift (Ricco's area) was only modelled at the population level. This fitting process assumes no change in spatial scaling across subjects, while the change in sensitivity is only modelled through the vertical shift of the template.

Note that it is not possible to model a vertical and a horizontal shift of the template simultaneously, because the solution would be undefined in locations for which the tested stimulus area sizes do not encompass Ricco's area. For example, a location for which all tested

stimulus sizes are smaller than Ricco's area can be fitted by arbitrary combinations of vertical and horizontal shifts of the template. Therefore, we used the alternative hypothesis of no spatial scaling as a comparator to assess the significance of our results under the main hypothesis (see next section). Normally, statistical significance can be assessed by quantifying the uncertainty around parameters' estimates. However, because each version of the model is forced to fit the data with either a horizontal or a vertical shift of the template, the parameter estimate associated with the modelled shift is likely to be significantly different from zero (no shift) in both cases and cannot be used to accept or reject the tested hypothesis.

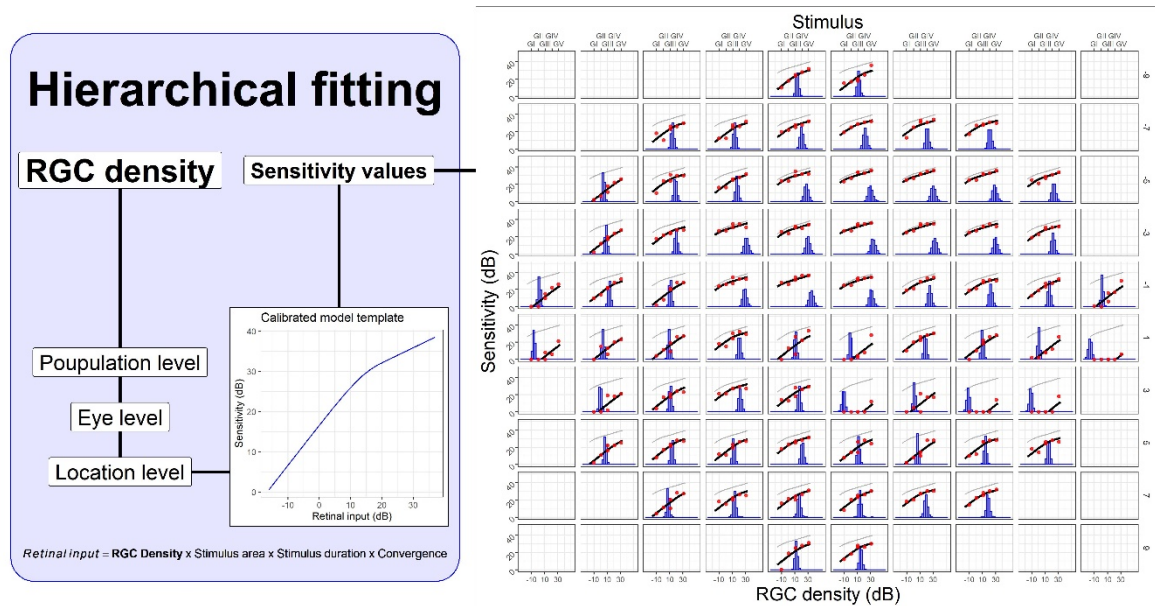


Figure 6.2. Schematic illustrating the hierarchical fitting process for the template. The template shown on the left is shifted horizontally to match the data. The example on the right shows the result of the fit. The top horizontal axis reports the stimulus size. The bottom horizontal axis refers to the histograms, which represent the estimated Retinal Ganglion Cell (RGC) density (in dB) for each location. The histograms show all the iterations of the Bayesian fitting procedure. The red dots are the measured sensitivity, the black lines are the shifted templates (the original “healthy” template is reported in light grey).

6.2.3.3. Data analysis

All data, including those from the young healthy cohort, were used in the fitting, but only data from the glaucoma patients and age-similar healthy controls were used to calculate goodness of fit statistics. The R^2 was calculated for the sensitivity predicted with the template fitted at each location and expressed as the percentage of variance explained. Confidence intervals for the R^2 were calculated via bootstrap (1000 samples) using the subject as the resampling unit. The Root Mean Squared Error (RMSE) was also calculated, for comparison with the structural predictions (see below).

The structure-function analysis was performed in a similar fashion, using the point-wise structural RGC density, calculated as described above, with estimates of GCL thickness from the SD-OCT scans (calculated as the average density from the five different stimulus sizes). However, because there was no fitting involved in the structure-function predictions, only the RMSE was calculated. Both RGC density estimates were expressed in dB ($10 \cdot \log_{10}(\text{Density})$). We also calculated the dynamic range for the structural and functional density

estimates as the width of the 2.5% - 97.5% interval, to report the structural floor effect. All the analyses were performed in R.

When referring to estimates of the total retinal input, we will use the term *functional retinal input* to refer to the total retinal input calculated with local RGC density values estimated by fitting the functional data. The *structural retinal input* was instead calculated using structurally derived local RGC density values.

6.3. Results

6.3.1. Study population

Descriptive statistics for the sample are reported in **Table 6.1**. One individual in the healthy cohort was excluded because they completed only two of the six tests. None of the tests was unreliable.

	Healthy < 40 years old (N = 29)	Age matched controls (N = 20)	Glaucoma		
			Early (N = 10)	Moderate (N = 10)	Advanced (N = 10)
Age (age)	28 (3)	62 (11)	66 (9)	59 (10)	62 (11)
AL (mm)	24.40 (1.05)	24.00 (0.94)	23.56 (0.65)	24.75 (1.35)	23.71 (1.18)
24-2 MD (dB)	-0.67 (0.91)	0.16 (1.36)	-2.26 (1.56)	-8.21 (2.13)	-18.51 (5.78)
24-2 PSD (dB)	1.45 (0.37)	1.91 (0.58)	3.24 (1.60)	11.10 (2.35)	11.61 (1.99)
cpRNFL (μm)	96.8 (9.2)	93.8 (9.5)	72.0 (10.4)	61.3 (15.4)	47.1 (6.9)
WRT (μm)	311.1 (13.8)	303.1 (13.9)	290.5 (17.7)	280.8 (16.2)	275.5 (8.7)
GCL (μm)	39.6 (3.10)	37.1 (3.2)	31.8 (4.9)	26.8 (5.4)	23.2 (3.8)
RGCs (dB)	5.58 (0.03)	5.54 (0.04)	5.47 (0.08)	5.39 (0.10)	5.32 (0.08)

Table 6.1. Descriptive statistics of the sample. The values are reported as Mean (Standard deviation). AL = Axial Length; MD = Mean Deviation; PSD = Pattern Standard Deviation; cpRNFL = circumpapillary Retinal Nerve Fibre Layer; WRT = Whole Retinal Thickness; GCL = Ganglion Cell Layer; RGCs = Retinal Ganglion Cell count (in $10 \cdot \log_{10}$ scale). The structural metrics are total or average values calculated within the central 10 degrees from the fovea.

6.3.2. Model calibration

The parameter estimates for the model fitted in the young healthy cohort were (Mean [95% - CIs]): $\alpha = 1.42 [1.29, 1.57]$; $\log_{10}(\tau) = 3.58 [3.44, 3.70]$; $k = 2.59 [2.45, 2.78]$ (corresponding to a partial summation slope of $0.39 [0.36, 0.40]$). The slope was notably different from the commonly chosen 0.25 ($p < 0.001$)^{20, 22} but not dissimilar to the 0.369 reported by Antwi-Boasiako et al. ($p = 0.146$)¹⁸. The result of the fitting is shown in **Figure 6.3**.

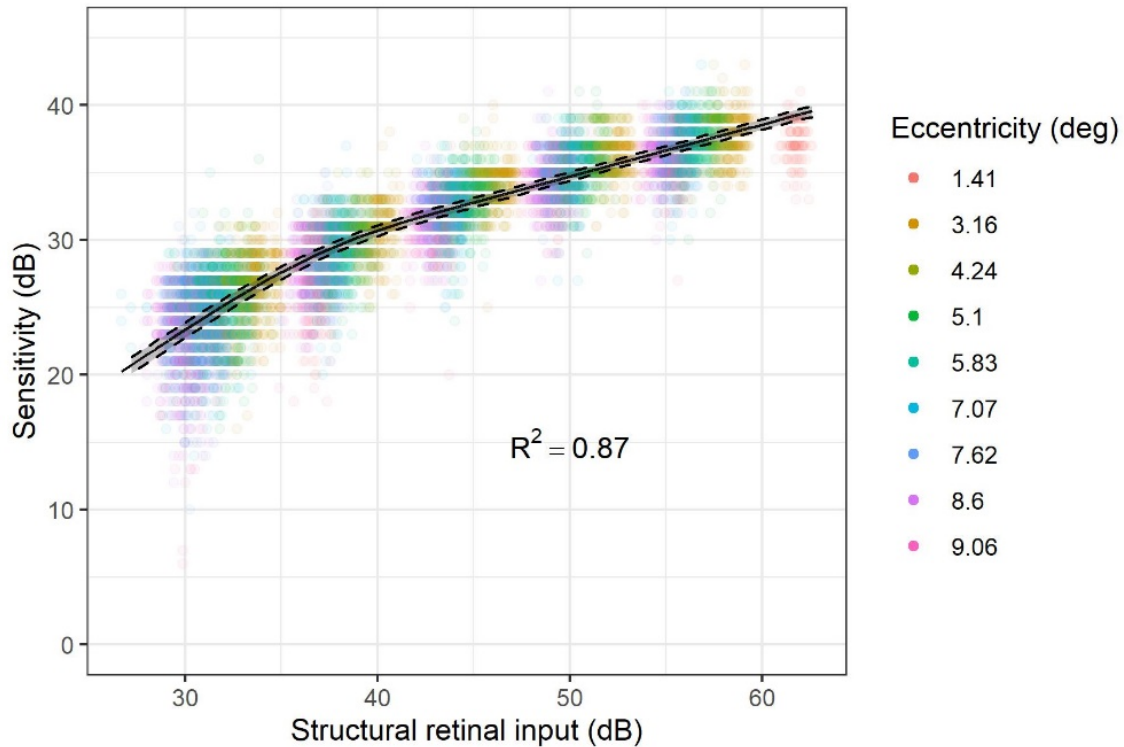


Figure 6.3. Template calibration. Results of the calibration procedure of the template on the data from the young healthy cohort. The Dashed lines represent the 2.5%-97.5% confidence bands for the template estimated via bootstrap. The data are clustered due the different stimulus diameters used.

6.3.3. Template fitting

The horizontal shift of the template (which assumes a change in Ricco's area from RGC damage) explained 95.2% [95%-CIs: 94%, 96.2%] of the overall variance in the data, a significant improvement over assuming no change in Ricco's area ($p < 0.001$). **Table 6.2** reports the R^2 and RMSE values for the healthy subjects and the glaucoma patients at different stages of damage. **Figure 6.4** shows the fitting results. **Supplementary Figure 6.8** shows the same results for each location (horizontal shift). The average error per subject for the horizontal shift of the template was not significantly affected by age (linear regression, $p = 0.819$), indicating that modelling a change in Ricco's area was able to account for most of the effect of ageing. The differences in accuracy between the two alternative models were more evident in the glaucoma cohort with intermediate damage, where a transition from partial to complete summation would be more evident if RGC damage was indeed causing a change in Ricco's area. **Supplementary Figure 6.9** shows the fitting error, stratified by sensitivity, of the two alternative models compared to the test-retest noise. Fitting the template with a horizontal shift produced the closest error to the test-retest noise, consistently below that obtained with a vertical shift.

Estimate [95%-CIs]

Group	Altered Ricco's area		Unchanged Ricco's area		Improvement (%)		
	R ² (%)	RMSE (dB)	R ² (%)	RMSE (dB)	R ²	RMSE	
All	95.2 [93.9-96.1]	2.09 [1.92-2.26]	93.2 [91.5-94.5]	2.49 [2.24-2.72]	2.1 [1.6-2.7]	15.9 [12.6-18.3]	
Healthy	91.3 [90.4-92.1]	1.56 [1.44-1.71]	89.8 [88.8-90.8]	1.69 [1.58-1.83]	1.7 [0.8-2.5]	7.7 [4.0-11.5]	
Glaucoma	Early	91.6 [89.5-93.1]	2.21 [1.74-2.64]	88.4 [86.6-90.0]	2.59 [1.99-3.10]	3.4 [2.4-4.2]	14.5 [9.70-18.7]
	Moderate	93.2 [90.9-95.3]	2.96 [2.50-3.39]	89.6 [85.4-93.1]	3.66 [2.98-4.29]	3.9 [2.1-6.2]	19.2 [14.3-22.5]
	Advanced	95.3 [93.7-96.3]	2.99 [2.70-3.29]	92.3 [89.1-94.3]	3.83 [3.33-4.32]	3.1 [1.9-5.0]	21.8 [17.1-25.2]

Table 6.2. Template fitting error. R² and Root Mean Squared Error (RMSE) statistics for the hierarchical fitting of the template. The 95%-Confidence Intervals were estimated via bootstrap. These statistics exclude the data from the young healthy cohort used for calibration. Improvement was calculated as percent increase in R² and percent reduction in RMSE fitting a horizontal shift of the template over fitting a vertical shift. All improvements were significant ($p < 0.001$).

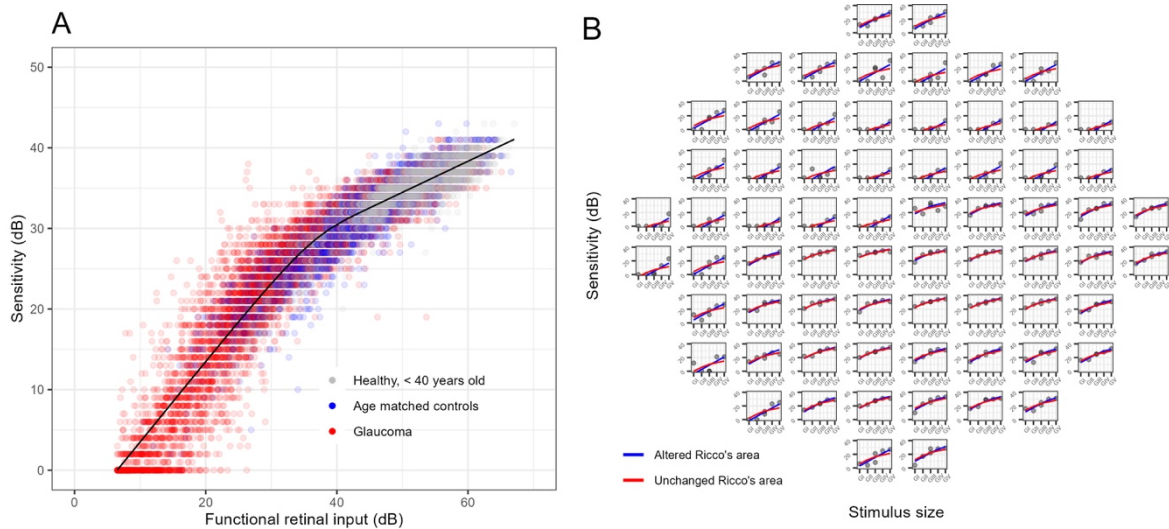


Figure 6.4. Template fitting results. **A)** Results of the template fitting via horizontal shift on the overall sample. For this graph, the observations from each location were shifted horizontally according to their estimated parasol OFF Retinal Ganglion Cell (RGC) density. **B)** Example (one eye with glaucoma) comparing the fit obtained via horizontal (altered Ricco's area) and vertical (unchanged Ricco's area) shift of the template.

When broken down into different stimulus sizes, some locations appeared to have their sensitivity underestimated by the model for the largest stimuli. We identified these locations as those that were greater than 97.5% of the prediction error (4.9 dB) above the prediction with the G-V stimulus (**Figure 6.5**). The sensitivity for these locations also appeared to increase more steeply than predicted by complete summation for smaller stimulus sizes^{48, 49}. We hypothesized that this could be a consequence of testing at the edge of scotomas. When plotted in the 10-2 grid, these locations were in fact mostly located in regions of sharp change in the modelled RGC density estimates (**Figure 6.5**). We further tested this hypothesis by simulating the response from an RGC mosaic with a sharp change in cell density and we were able to reproduce the same behaviour (**Supplementary**).

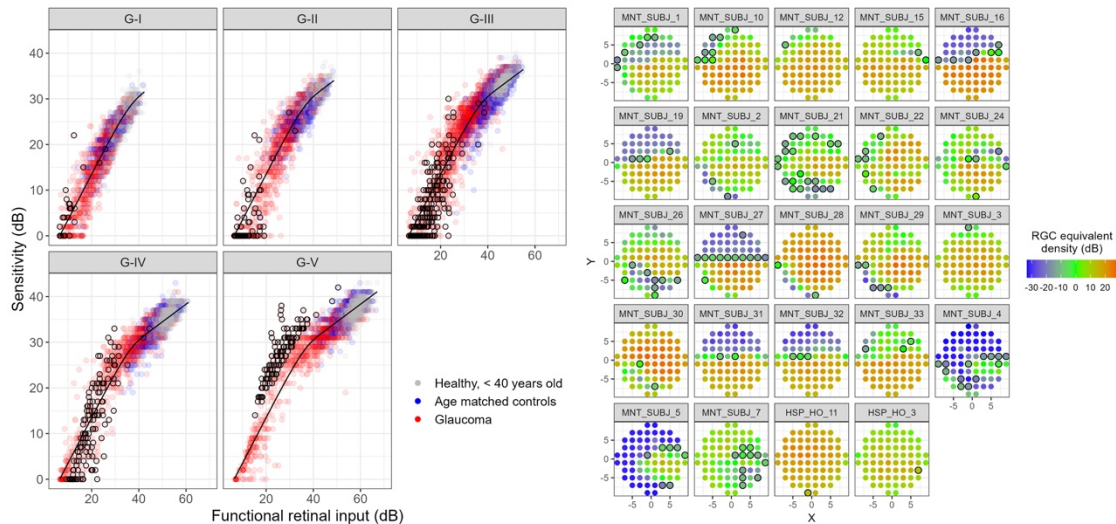


Figure 6.5. Effect of stimulus size. Fitting results split by stimulus size (left panels). The observations circled in black are those that exceeded the 97.5% limit of the prediction error for the G-V stimulus. The same locations are reported on the map on the right, representing the modelled RGC density.

6.3.4. Structure-function relationship

The structural and functional estimates of RGC density are plotted in **Figure 6.6**. The overall agreement was poor (**Table 6.3**), mostly due to the limited dynamic range of the structural estimates, which was, on average, only 11% ($\pm 2\%$) of the functional estimates.

Using the template to predict the sensitivity from the structural RGC estimates generally provided poor prediction accuracy (**Table 6.3**). These predictions are reported in **Figure 6.7**. The predictions were improved, as expected, by only analysing locations where sensitivity with a G-I stimulus was greater than 10 dB. This latter sub-analysis was performed for comparison with the work of Antwi-Boasiako et al.¹⁸

Group	Structural RMSE (dB) [95%-CIs]		
	Sensitivity, all locations	Sensitivity, locations ≥ 10 dB	Functional RGC Density
All	10.6 [8.4-12.5]	3.5 [2.9-3.7]	14.3 [11-17.6]
Healthy	3.0 [2.1-3.9]	3.0 [2.2-3.7]	4.0 [2.5-5.3]
Early	5.9 [3.7-7.5]	3.1 [2.4-3.8]	7.2 [4.5-9.3]
Glaucoma Moderate	11.8 [9.2-14.1]	4.2 [3.3-4.6]	15.2 [11.6-18.5]
Advanced	18.8 [15.7-21.8]	4.8 [3.3-4.9]	26.5 [20.7-31.8]

Table 6.3. Structure-function model fitting error. Root Mean Squared Error (RMSE) for structure-function predictions. For sensitivity, structural predictions were generated using the spatial summation template with structural estimates of the parasol OFF Retinal Ganglion Cell (RGC) number as an input. For the RGC density estimates, we report the RMSE of structural estimates of local parasol OFF RGC density predicting the corresponding functional estimates from the fitting of the template.

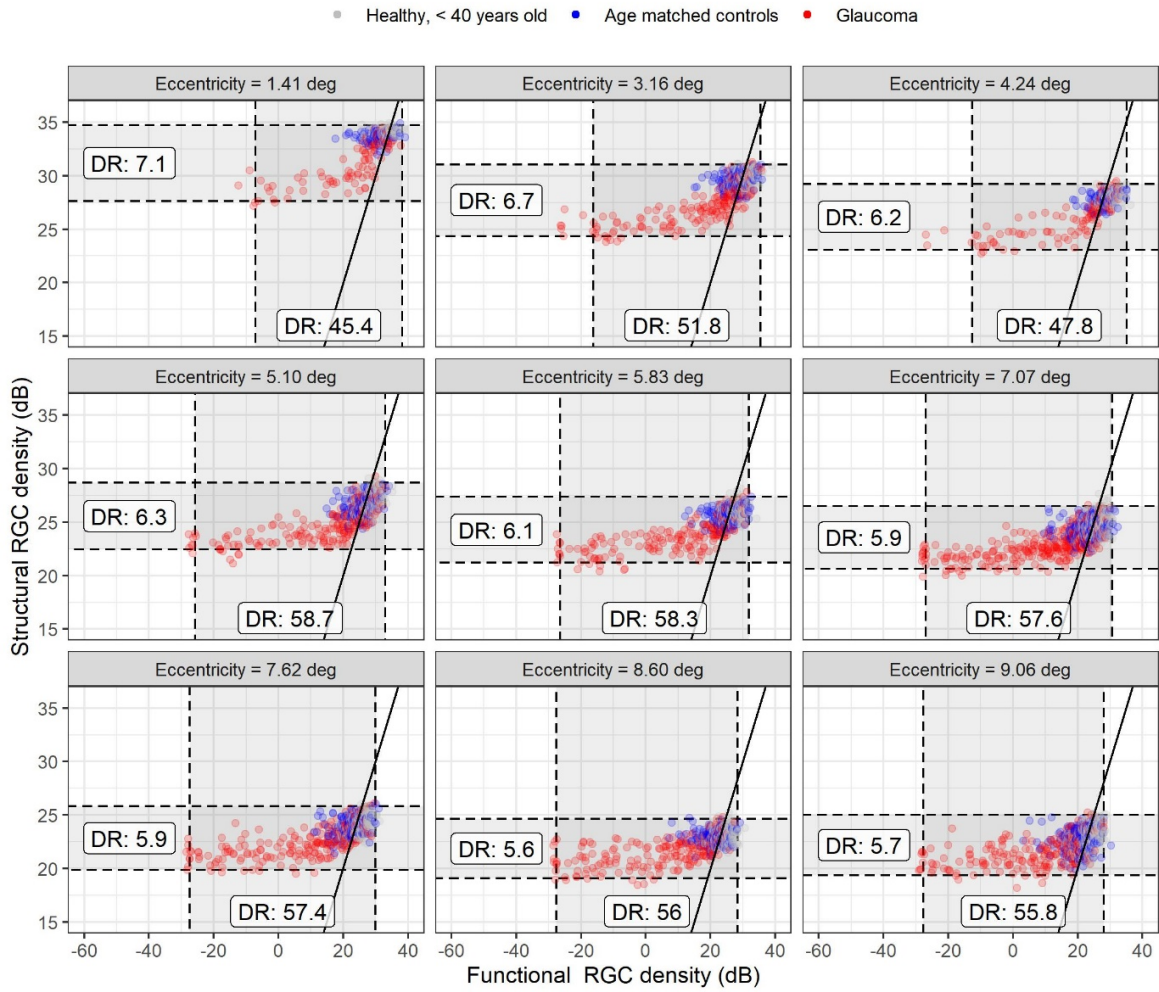


Figure 6.6. Structure-function relationship. Structural and functional estimates of the Par- asol OFF Retinal Ganglion Cell (RGC) density at each location. The solid line indicates the identity. The dashed line represents the dynamic range (DR) of the structural and functional estimates.

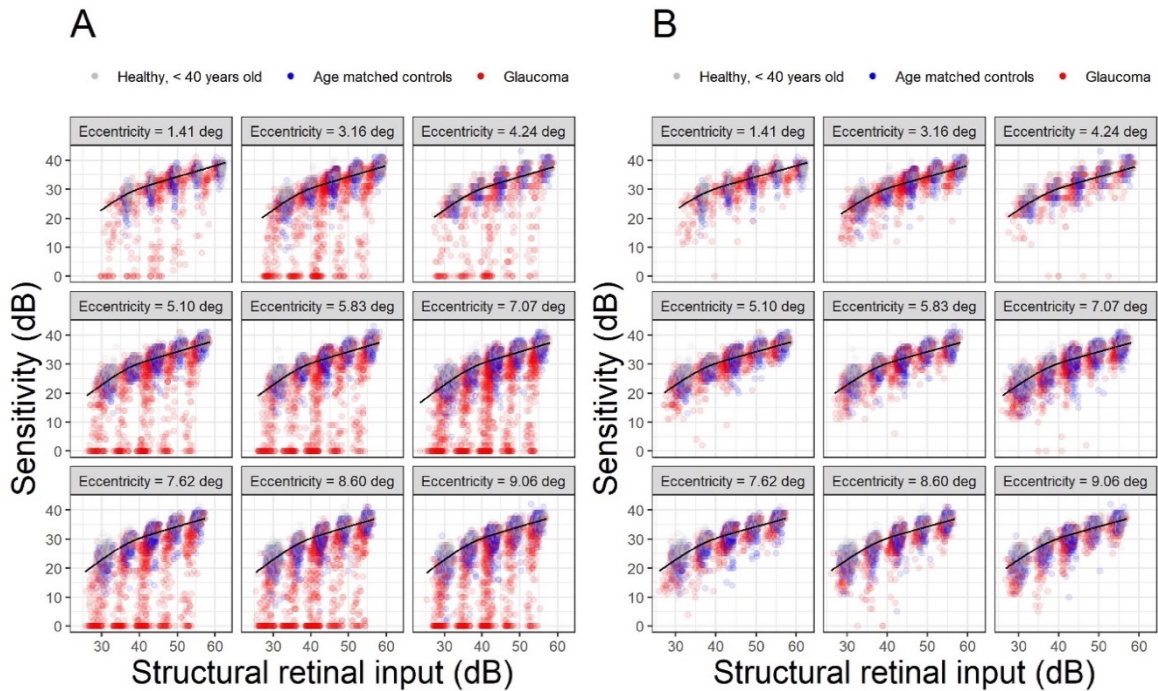


Figure 6.7. Structure-function model fitting results. Structure-function predictions based on the template for the whole sample (A) and for locations where sensitivity was > 10 dB with a G-I (B). The structural retinal input was calculated identically to the functional retinal input, but using structural estimates of local parasol OFF retinal ganglion cell density instead of the functional ones, derived from fitting the template (as in Figure 6.4 and 5). This is identical to the retinal input calculated for the young healthy cohort for calibration (Figure 6.3), which was also derived from structure.

6.4. Discussion

We evaluated the hypothesis that changes in perimetric sensitivity from modelled RGC damage or loss in the glaucomatous macula could be explained by a change in the spatial scaling of the response of visual system. We tested this by fitting experimental perimetric data in human observers (patients with glaucoma and healthy controls) with a template that models a change in Ricco's area, and showed that a horizontal shift of the template, modelling an enlargement of Ricco's area, could explain 95% of the overall variance in the data. This explained the data significantly better than a vertical shift of the template, which would model a change in sensitivity without a change in Ricco's area. We then showed that the local functional loss was not entirely captured by structural measurements from SD-OCT. Our findings support the hypothesis that RGC damage from glaucoma produces a perimetric functional loss that can be explained by an enlargement of Ricco's area¹⁷. This was speculated to be a consequence of the loss of RGCs, leading to the hypothesis that Ricco's area would scale with RGC density, to include a constant number of RGCs. In general, this hypothesis has been shown to hold true in healthy eyes when tested at different eccentricities⁹⁻¹⁵ and in glaucoma patients when assessed with computational models similar to the one used in this work²². However, Swanson et al.²² showed that the extent of Ricco's area depends on the spatial scale of the cortical filters, regardless of the underlying density of RGCs. In fact, previous work has shown that the extent of Ricco's area (and thus the number of RGCs underlying a Ricco's area scaled stimulus¹⁶) at any given location can be altered, in healthy observers, by stimulation conditions, such as background luminance⁵⁰⁻⁵², duration

of the stimulus^{21, 51, 53, 54} or by high frequency background noise²⁰. This makes it clear that VF sensitivity cannot be explained solely by RGC density and likely also involves further processing at a cortical level.

Redmond et al.¹⁷ provided experimental evidence of such a change in the spatial scaling occurring in patients with glaucoma. However, the same phenomenon has not been extensively investigated in advanced glaucomatous damage and in the macular region. While there is no specific reason to expect spatial summation to behave differently in the macula, its impact would be the greatest in this region for standard perimetry with a G-III stimulus^{9-11, 22, 31}. This is because the high initial RGC density in the healthy macula would determine a transition between partial and total summation, as RGCs are lost in glaucoma. Moreover, the macula allows direct individualised point-wise structural OCT measurements, which are not usually available for the more peripheral retina. One study by Yoshioka et al.³³ investigated the effect of spatial summation on the association between perimetric sensitivity and retinal structure in the macula of eyes with early glaucomatous damage and showed that it is improved with smaller stimulus-sizes. This is compatible with our findings, since smaller stimulus sizes would operate under complete spatial summation in both healthy and glaucomatous eyes, making the slope of the relationship between the number of RGCs and sensitivity steeper. One important difference was the method used to displace the stimuli to account for RGC displacement, which, in the case of Yoshioka et al.³³, was later shown to yield inaccurate results, especially in the parafoveal region³⁵. This was then also confirmed by the same group in later work⁵⁵. More recently, a detailed analysis has been presented by Antwi-Boasiako et al.¹⁸, who studied the relationship between macular RGC counts and perimetric sensitivity in non-human primates with experimental glaucoma. Antwi-Boasiako et al.¹⁸ also analysed their data within the framework of spatial summation. Some of their results were confirmed in our study. Importantly, the partial summation slope estimated by our data (0.39, corresponding to an exponent k of 2.59) was very close to their estimate (0.369). This is noteworthy, because there is still uncertainty about the most accurate choice of slope to describe partial summation for perimetric stimuli in studies of this kind. In computational models of sensitivity, this mainly depends on the choice of the spatial filter and of the Minkowski summation exponent k ²⁰. Common choices for the exponent are between 2 and 4. For most symmetric filter choices (except some Gaussian derivatives used to model cortical responses), these values correspond to a partial summation slope of 0.5 (Piper's law) and 0.25. An exponent of 4 was used in a previous implementation of our model²¹ and by others^{20, 22}. However, an intermediate value for the exponent seems more reasonable given the experimental results from this work and Antwi-Boasiako et al.¹⁸.

Differently from Antwi-Boasiako et al.¹⁸, we found that structural measurements were not able to fully characterize functional damage, owing to their reduced dynamic range (**Figure 6.6**). One factor that could explain this discrepancy is that Antwi-Boasiako et al.¹⁸ had access to histology-derived RGC counts in both healthy and glaucomatous eyes to calibrate their structural models, which would naturally improve accuracy. In contrast, we only relied on a limited histology data in healthy human subjects provided by Curcio and Allen³⁶. Additionally, it is unclear from their paper whether Antwi-Boasiako et al.¹⁸ accounted for RGC displacement by simply moving the centre of the 10-2 stimuli, as in Yoshioka et al.³³, or whether they applied the displacement to the edge of the stimulus (**Figure 6.1**). This is relevant because, despite yielding correct RGC counts in healthy eyes and in early damage, our method of displacement, by its nature, amplifies the floor-effect, since non-functional residual tissue is summed over a larger area, especially in the parafovea. Finally, the level of

damage in Antwi-Boasiako et al. was in general less advanced than in our dataset, with the lowest sensitivity values being approximately 10 dB. Indeed, restricting our analysis to locations with a sensitivity > 10 dB with a G-I stimulus resulted in a great improvement in the RMSE for structure-function estimates (**Table 6.3** and **Figure 6.7**). Nevertheless, our results find ample confirmation in previous literature^{37, 56, 57} documenting a structural floor-effect at around 10 dB of sensitivity loss in the macula and confirming that structurally derived estimates offer only a partial description of RGC loss and damage occurring in glaucoma. All these aspects, including the increased level of perimetric noise at more advanced damage, contributed to the poor RMSE in the structure-function predictions reported in **Table 6.3**. Our findings have important implications for the interpretation of macular perimetric damage in glaucoma. The first important aspect is that it confirms a change in the spatial scale of the response following RGC loss or damage, which corresponds to an enlargement of Ricco's area. As previously stated, the exact value of Ricco's area is irrelevant for testing our hypothesis and is not univocally defined for curves with a smooth transition from total to partial summation. However, Ricco's area is a useful concept to describe changes in spatial scaling, and here it is used as synonymous of *spatial scale*. One thing that should be noted is that previous work mostly focussed on the relationship between the number of RGC receptive fields covered by the stimulus and perimetric response. According to this view, the response of the visual system would scale to include a constant number of RGCs at Ricco's area^{17, 18}. Our interpretation differs slightly, because the total retinal input in our summation model would not differentiate between reduced input from RGC loss or dysfunction. Differentiating between these two contributions would require additional investigations. Adaptive optics OCT imaging has shown promising results allowing direct visualization of RGCs in healthy subjects¹ and glaucoma patients⁵⁸ and could be used to more precisely quantify the density of RGCs. Functional tests, such as high contrast grating stimuli, could be used for the same scope^{47, 59-62}.

The varying relationship between RGC damage and functional loss is especially important in the macular region because sensitivity to the widely used G-III, 200 ms stimulus would initially be determined by partial summation, making the relationship with retinal structure shallow. As RGCs are lost or damaged, the response would gradually transition into complete summation, where the relationship between sensitivity and retinal structure becomes steeper. This implies that, for the same percentage of RGC loss, changes in sensitivity would be much smaller early in the disease compared to more advanced damage. This might make the detection of early damage, and similarly early progression, more challenging^{7, 63}. Other strategies employing smaller targets or shorter durations for macular stimuli might make perimetric tests more efficient by testing always under complete summation conditions, although this might limit the dynamic range of the test. Some of these strategies have already been adopted in some home monitoring devices⁶⁴. Another approach would be to modulate the area or duration of the target instead of the luminance. This approach would take full advantage of the horizontal translation of the response profile observed in our data and in previous publications^{17, 63}, effectively testing the response at a fixed point of the summation curve. Such an approach has been shown to maximise signal-to-noise ratio in glaucoma and to reduce response variability compared to luminance modulation⁶³.

It should be noted that, while fitting a template and testing the spatial-scaling hypothesis did not require a link to RGC density, modelling the retinal input and the effect of RGC loss provides a linkage to an underlying biological substrate, offering a generalisable framework for interpreting the results. For example, using a computational model of an RGC mosaic

allowed us to provide a possible explanation for the edge effect for larger perimetric stimuli observed in the data (see **supplementary material**). Moreover, modelling changes in retinal input rather than simple translations of ‘healthy’ summation functions for each tested location highlighted how changes in spatial summation both across the healthy visual field and as a consequence of damage can arise in the context of different modifications to the same underlying biological substrate. It should be finally highlighted that, because of how the spatial summation template was calculated (i.e. using sensitivity values and estimated RGC counts in healthy subjects), the intrinsic linkage to the underlying retinal input is present in our calculations, regardless of whether it is made explicit or not in our interpretation of the results.

A better characterization of the relationship between RGC damage and perimetric sensitivity is also useful to improve the correspondence between perimetric changes and structural damage observed with imaging. As shown in this and previous work^{33, 37}, both measurements can be reported in a log-scale of RGC number. This could facilitate structure-function analyses for progression or enable seamless integration of structurally derived metrics into perimetric strategies⁶⁵. One limitation, however, is that structural metrics do not seem to have enough dynamic range, at least locally, to capture the full extent of functional damage measured by perimetry. Although such a discrepancy has been reduced by nonlinear estimates, such as with help of artificial intelligence⁶⁶⁻⁶⁸, structural tests are unlikely to replace perimetry. An efficient integration of the two sources of information seems, therefore, the most effective way of diagnosing and monitoring glaucoma.

A limitation of this work is that it was not possible to derive sensitivity estimates for all stimulus areas at all tested locations, especially among patients with intermediate or advanced glaucoma. This was expected given the technical limitations of the device (limited stimulus areas and fixed duration), and addressed with the use of a hierarchical model, which allowed for more robust estimates of RGC damage for locations where only limited data could be collected, and the use of censoring at 0 dB. However, the estimates for these locations are necessarily less precise and mostly reliant on the behaviour of the other locations within the same eye and on the general trend of the overall population. For the same reason, it was not possible for us to model the horizontal and vertical shift at the same time, because the fitting results would only be fully constrained for locations that span both partial and complete summation with the available stimulus diameters. For example, for locations exhibiting complete summation exclusively, the same fitting result can be achieved by either a vertical or a horizontal translation of the template. However, this would not affect the ability to compare our two alternative hypotheses. It is also important to note that previous work, especially by Gardiner et al.^{69, 70}, has shown poor correlation between accurate sensitivity estimates derived from frequency of seeing curves and clinical perimetry, especially for values < 20 dB. In our analysis, however, we assumed that low sensitivities would still provide useful information to test population-level hypotheses, especially in eyes with advanced glaucoma. We provide, as **supplementary**, additional analyses supporting this assumption. Importantly, we show that including sensitivity values < 15 dB reduced the prediction error for the fitted model for sensitivity > 15 dB. This indicates that, in our data, locations with advanced damage improved the precision of the model.

In our study, we could not control for the effect of optics on macular sensitivity. This could have been influenced by age-related changes to refractive media. We controlled for this limitation by comparing glaucoma with age similar controls. The effect of optics^{71, 72} and ageing⁷³ on spatial summation is still unclear. Redmond et al.⁷³ did not find any change in

the critical area with age. However, from our data, there does not seem to be any significant residual effect of ageing on explaining the change in sensitivity once the change in spatial summation is accounted for. However, our data does not allow us to test this hypothesis specifically and further, more targeted investigations, are needed.

6.5. Appendix

6.5.1. Computational model

The model, as previously explained²¹, predicts sensitivity as a function of the total retinal input, which is the product of the number of RGC receptive fields that underlie the stimulus, the duration of the stimulus presentation, and the cone-to-RGC convergence ratio at different eccentricities. This was derived by combining Curcio and Allen's data^{36, 74} and the RGC receptive field (RGC-RF) density obtained from the equations provided by Drasdo et al.^{35, 38}. In our previous analysis of spatial summation data in healthy subjects²¹, we showed that this weighted RGC-RF number, rather than the raw count of RGC-RFs covered by the stimulus, were able to equate the spatial summation curves at different eccentricities. The model uses a capacitor equation and continuous integration over the input. A Minkowski exponent is used in the integration, similar to the vector summation equation used by Pan and Swanson²⁰. The model has three parameters that can be fitted: α determines the vertical offset of the template (in \log_{10} scale); τ determines the transition from total to partial summation; κ determines the slope of the partial summation portion of the curve (slope = $1/\kappa$). The formula from Montesano et al.²¹, with small modifications, is

$$R = 10^\alpha \left(\int_0^T M^\kappa * d(st) \right)^{1/\kappa}. \quad (6.1)$$

Where R is the sensitivity in linear units ($10^{\text{dB}/10}$), M is the total retinal input filtered (convolved) with a capacitor equation in the form

$$RM = \exp(-st/\tau) \times S. \quad (6.2)$$

Where S is a step function of the retinal input and is equal to 1 over a segment of st (an arbitrary unit of spatiotemporal input) that indicates the extent of the total retinal input of the stimulus, i.e. it becomes longer when more RGCs are stimulated or the same RGCs are stimulated for a longer period of time. The symbol \times indicates the convolution operation.

6.5.2. Bayesian fitting

The fitting sought to find the optimal value of RGC density for each location that would give the best fit for the template. Changing RGC density corresponds to a horizontal shift of the template. RGC density at each location was modelled as a hierarchical random effect, nested within another random effect grouping locations from the same eye. A single global parameter also allowed a vertical offset of the template to achieve the optimal fit in the overall sample. This offset was however very small (-0.23 dB). The same procedure was adopted to fit vertical shifts of the template at each location (i.e. no change in Ricco's area), while a global parameter optimized the location of Ricco's area in the whole sample (this offset was also small, -0.05 \log_{10} -units). Note that the template was not allowed to move both horizontally and vertically at each eye/location because this would make the fitting

undetermined for all locations where sensitivity values showed no change in slope in the data, because the same fit could be obtained by infinite combinations of vertical and horizontal shifts.

VF sensitivity was assumed to have a Normal distribution of the residuals, censored at 0 dB. Fitting of the Bayesian model was achieved using JAGS (Just Another Gibbs Sampler⁷⁵) to run Markov Chain Monte Carlo (MCMC) simulations, within the R environment (R Foundation for Statistical Computing). Two parallel MCMCs were run for at least 5,000 iterations after 1,000 adaptation steps and 5,000 burn-in iterations. The MCMCs were stopped if the Gelman-Rubin diagnostic was < 1.2 for all the monitored parameters, indicating convergence⁷⁶. Prior distributions on the fixed effects were non-informative Normal distributions with a precision of 0.01 (Variance = 100).

6.6. Supplementary material

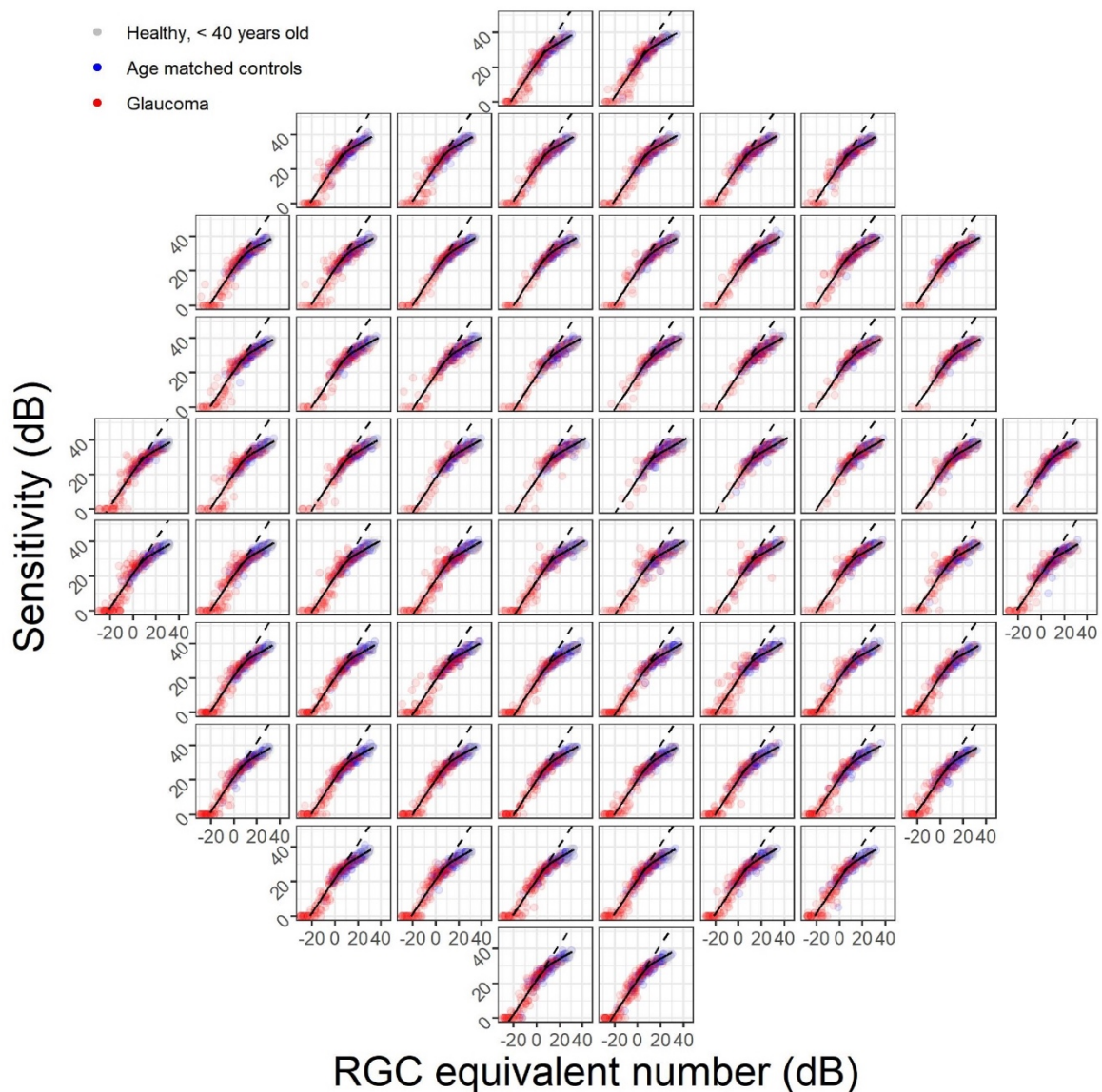


Figure 6.8. Template fit for each location of the 10-2 grid. The dashed lines indicate total summation. The horizontal axis reports the RGC equivalent count, i.e. the effective RGC contribution to the response as a combination of a RGC loss and dysfunction. This representation is possible because each location is plotted separately and the effect of Cone:RGC

convergence can be accounted for in each plot, leaving the RGC density as the only varying factor in each subplot. RGC = Retinal Ganglion Cells.

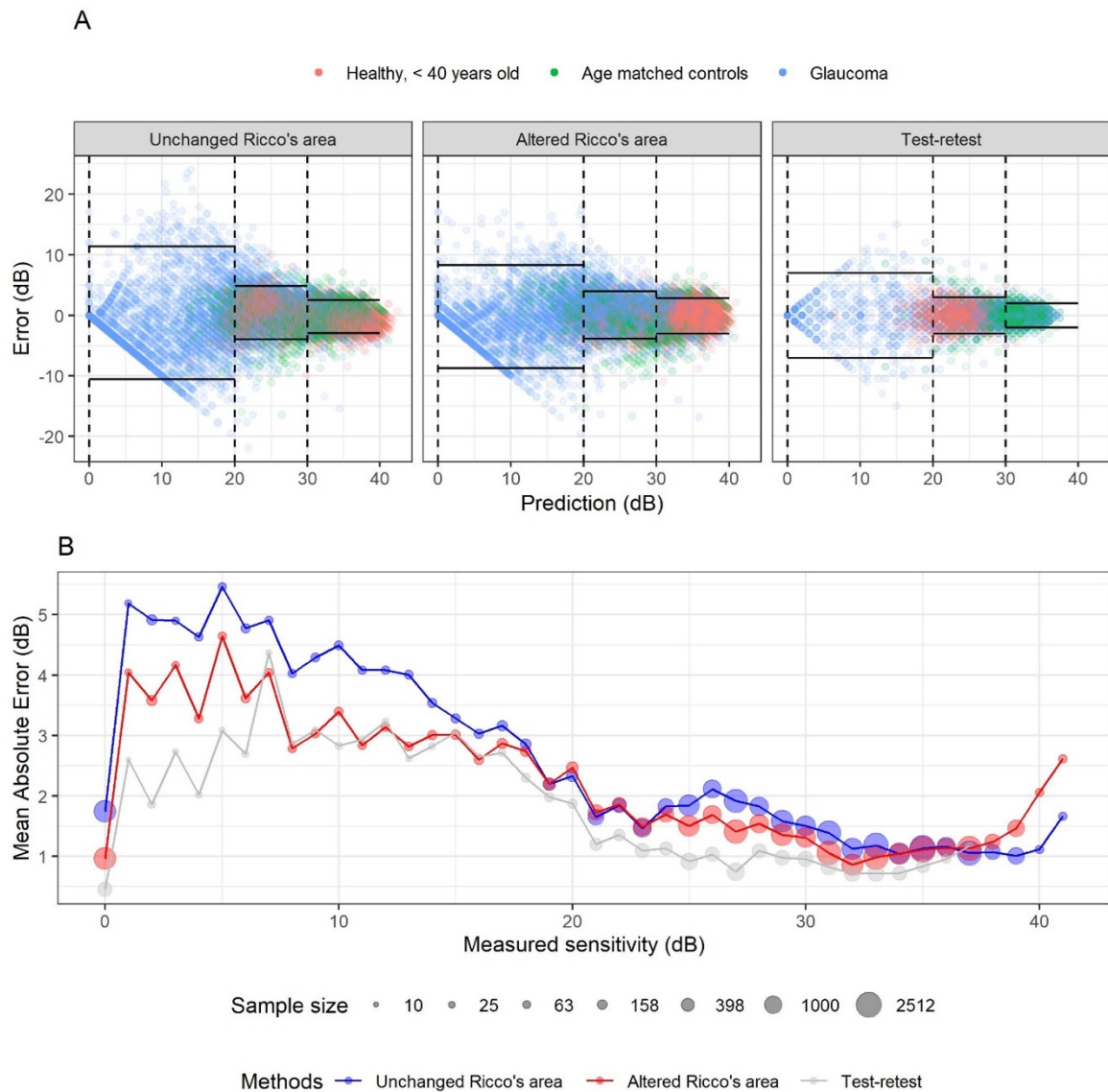


Figure 6.9. Prediction error and test-retest variability. **A)** Prediction against error plots for the two fitting procedures, i.e. horizontal shift (altered Ricco's area) and vertical shift (unchanged Ricco's area), compared to the test-retest variability. For test retest, the G-I stimulus was used for the healthy young cohort and the G-III stimulus was used for the glaucoma cohort and the age matched controls. The "prediction" for test-retest was calculated as the average between the two test repeats. The error was the difference of each repeat from their average. The solid lines represent the 95% limits of the error, calculated separately for three sensitivity levels. **B)** Absolute error stratified by measured sensitivity for the tests-retest and the prediction from the template. The best estimate of sensitivity used to calculate the error and to stratify the plot is the average of two tests repeats and the prediction from the template, respectively.

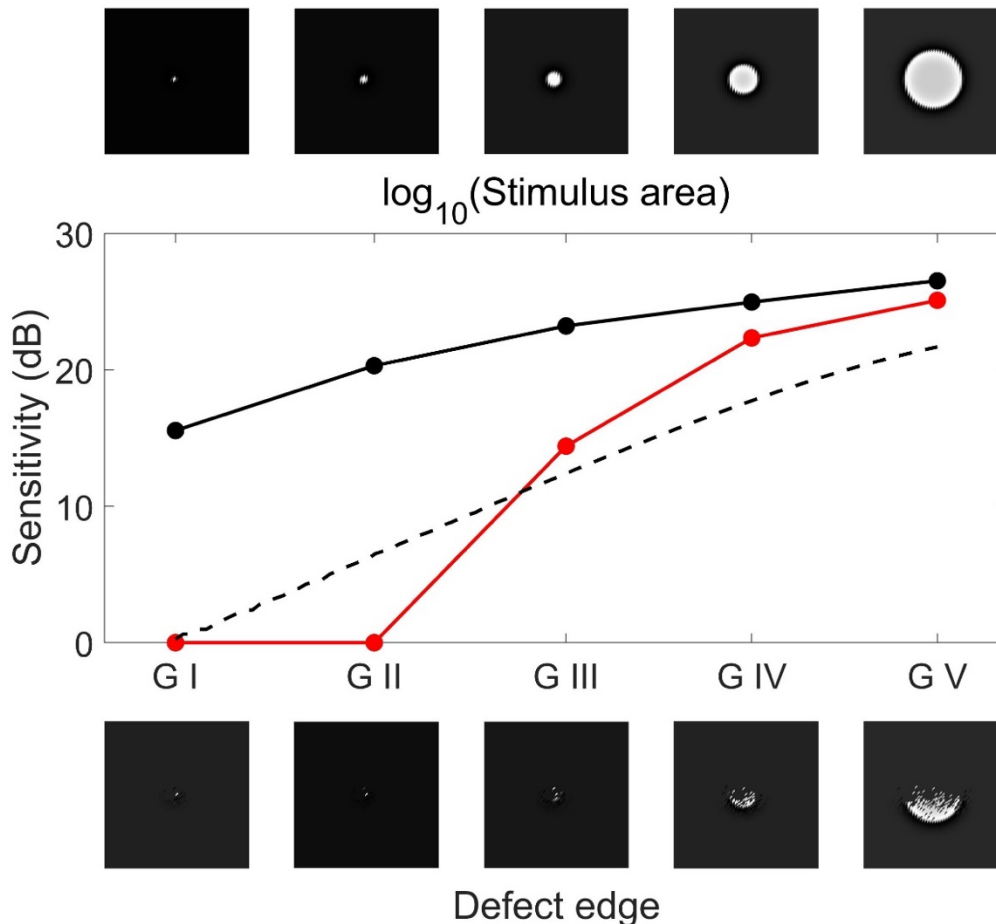


Figure 6.10. Simulation of sharp-edged defects. Example of how a sharp edge can produce the deviation from the model observed in the data. These responses are calculated from a full computation model simulating an RGC mosaic. The healthy mosaic is reported at the top (and the corresponding response is in black, solid line). The degraded mosaic with a sharp edge is reported at the bottom (and the corresponding response is in red). The dashed line represents the best fit of the template to the data generated from the degraded mosaic. Note how a sharp edge introduces deviations from the template, which assumes a homogeneous RGC density in the tested area. RGC = Retinal Ganglion Cell.

6.6.1. Influence of low perimetric accuracy for advanced damage

Gardiner et al.^{69, 70} showed that estimates of sensitivity obtained with SITA algorithms correlated poorly, for low sensitivity, with accurate estimates of the 50% threshold measured with frequency-of-seen curves, demonstrating a “floor effect”. The level of this floor is usually placed between 15 dB and 20 dB (note that the 10 dB floor for our analysis was chosen for comparison with Antwi-Boasiako et al.¹⁸). While this issue certainly affects estimates at the level of individual locations or eyes, we hypothesised that low sensitivity values would still provide useful information for population level estimates. We have performed two additional analyses, reported below, to confirm that this is the case.

We first tried to replicate, via simulations, the results that would be obtained from the full-threshold (FT) strategy implemented on the Humphrey Field Analyzer (HFA). While the specific details are not known, the Open Perimetry Interface (OPI)⁷⁷ offers an implementation

of the FT strategy based on the best available knowledge⁷⁸. We also tried to replicate the HFA ‘growth-pattern’ approach for a 10-2 grid based on what is known about the 24-2 grid⁷⁸. Briefly, the seed points were the locations at coordinates $\{\pm 3; \pm 3\}$. Each quadrant was treated independently. The testing sequence progressively extended to the periphery in three concentric clusters around the seed points. The FT 4-2 staircase started at the expected normative value for a G-III stimulus at the seed points and, for the other locations, at the average sensitivity of their nearest neighbours for which sensitivity had already been determined.

The ground-truth for the simulations were the thresholds predicted by the spatial summation functions fitted under H1 (changing Ricco’s area) on the original data. The objective was to see whether it was possible to retrieve the original ‘ground-truth’ RGC density by fitting the model under H1 to the simulated data. If the testing strategy introduced a floor effect, we would observe a proportional bias in our estimates. The responses were simulated using the formula provided by Henson et al.⁷⁹ for response variability, capping the standard deviation of the Gaussian psychometric function at 10 dB⁸⁰. The estimated and ground-truth RGC density values are reported in **Figure 6.11**. While there was a consistent offset, there was no proportional bias, indicating no floor effect from the testing strategy used for our study. Interestingly, the consistent offset was due to an underestimation of higher sensitivities (see **Figure 6.11**). However, these results can vary based on the starting values of the FT strategy. These were set to the normative G-III sensitivity for the four initial seeding points in our simulations, but we cannot be sure of what starting points are being used in the HFA for other stimulus sizes.

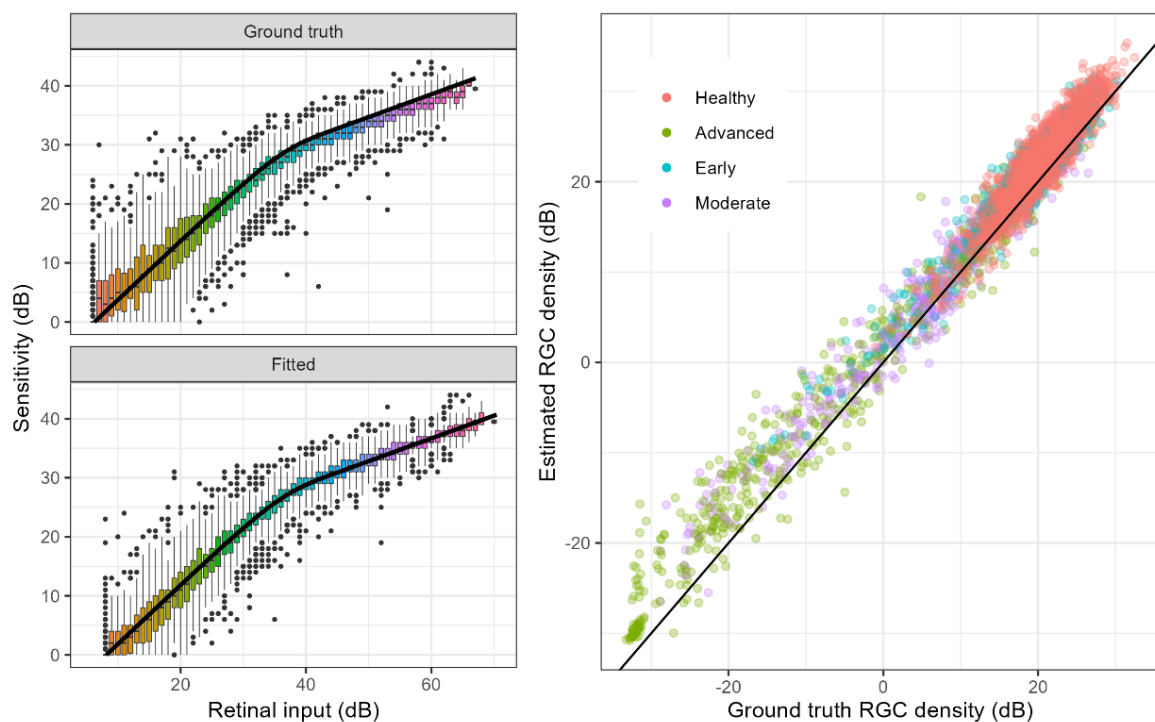


Figure 6.11. Template fitting on simulated full-threshold data. The left panels show a comparison of the summation model with the results of the simulations. The sensitivity values in the box-plots were grouped by ground-truth (top) or fitted (bottom) retinal input values, in rounded decibel units. Note how the results of the simulated full-threshold strategy for high sensitivity values are slightly lower than the ground-truth sensitivity, indicated

by the black line. The fitting procedure accounted for that by estimating a retinal ganglion cell density higher than the ground truth. This is shown in the right panel, where the diagonal indicates identity. This produced a better fit to the data (left bottom panel). Note that this is similar to shifting the model template (black line) down and to the left in the top left plot.

In our second analysis, we fitted the data under H1 censoring the sensitivity values at 15 dB instead of 0 dB (as in the original analysis). Note that the model would still retain the information that these values are smaller than 15 dB. We compared the Root Mean Squared Error (RMSE) and R^2 for the predictions obtained with the parameters fitted with the two levels of censoring ($RMSE_0$ and $RMSE_{15}$ respectively). Importantly, both the predictions and the data for this comparison were floored at 15 dB, regardless of the censoring level used for fitting. This ensured a fair comparison. Confidence intervals were calculated via bootstrap, as in the main analysis.

This analysis could have had three possible outcomes:

1. $RMSE_{15}$ was not different from $RMSE_0$: this result would indicate that sensitivity values below 15 dB provided no additional information to increase the prediction accuracy for sensitivities above 15 dB.
2. $RMSE_{15}$ was better (smaller) than $RMSE_0$: this would indicate the presence of spurious information in sensitivities 15 dB with a detrimental effect on the accuracy of the estimates. This would be the strongest indication of a floor effect biasing the estimates.
3. $RMSE_{15}$ was worse (larger) than $RMSE_0$: this would indicate that sensitivity values below 15 dB provided useful information to increase the accuracy of the estimates above 15 dB.

The results are reported in the **Table 6.4** below. $RMSE_0$ was significantly better than $RMSE_{15}$, a clear indication that locations with advanced damage can provide useful information for the accuracy of the estimates. Interestingly, the differences in RMSE were even more prominent in advanced cases.

Group	Estimate [95%-CIs]						
	Censored at 15 dB		Censored at 0 dB		Improvement (%)		
	R^2 (%)	RMSE (dB)	R^2 (%)	RMSE (dB)	R^2	RMSE	
All	91.0 [89.7-92.0]	2.04 [1.87-2.22]	93.5 [92.5-94.3]	1.74 [1.64-1.85]	2.7 [2.0-3.3]	14.9 [11.8-17.6]	
Healthy	90.8 [89.5-91.8]	1.59 [1.45-1.76]	91.4 [90.4-92.3]	1.53 [1.42-1.67]	0.7 [0.4-1.1]	3.6 [2.2-4.9]	
Glaucoma	Early	88.0 [85.6-89.7]	2.15 [1.84-2.49]	91.6 [89.8-93.0]	1.80 [1.57-2.06]	3.9 [2.7-5.2]	16.2 [11.6-20.6]
	Moderate	86.2 [80.7-90.6]	2.80 [2.30-3.20]	91.8 [89.5-93.9]	2.15 [1.88-2.39]	6.1 [3.1-10.1]	23.0 [16.3-28.8]
	Advanced	86.7 [81.5-90.0]	2.85 [2.52-3.21]	92.6 [90.0-94.3]	2.13 [1.89-2.37]	6.4 [4.5-9.6]	25.4 [23.0-27.5]

Table 6.4. Effect of censoring on fitting error. Prediction error from the same model (horizontal translation) fitted by censoring data at 0 dB (original) or at 15 dB. The prediction error for both was evaluated by capping the sensitivity values at 15 dB (i.e. all values smaller than this threshold were set to 15 dB both for the data and predictions). The 95%-Confidence Intervals were estimated via bootstrap. These statistics exclude the data from the young healthy cohort used for calibration. Improvement was calculated as percent increase in R^2 and percent reduction in RMSE. All improvements were significant ($p < 0.001$). RMSE = Root Mean Squared Error.

6.7. References

1. Liu Z, Kurokawa K, Zhang F, Lee JJ, Miller DT. Imaging and quantifying ganglion cells and other transparent neurons in the living human retina. *Proc Natl Acad Sci U S A* 2017;114:12803-12808.
2. Garway-Heath DF, Hitchings RA. Quantitative evaluation of the optic nerve head in early glaucoma. *Br J Ophthalmol* 1998;82:352-361.
3. Weinreb RN, Aung T, Medeiros FA. The pathophysiology and treatment of glaucoma: a review. *JAMA* 2014;311:1901-1911.
4. Harwerth RS, Carter-Dawson L, Shen F, Smith EL, 3rd, Crawford ML. Ganglion cell losses underlying visual field defects from experimental glaucoma. *Investigative ophthalmology & visual science* 1999;40:2242-2250.
5. Harwerth RS, Quigley HA. Visual field defects and retinal ganglion cell losses in patients with glaucoma. *Arch Ophthalmol* 2006;124:853-859.
6. Harwerth RS, Wheat JL, Fredette MJ, Anderson DR. Linking structure and function in glaucoma. *Prog Retin Eye Res* 2010;29:249-271.
7. Anderson RS. The psychophysics of glaucoma: improving the structure/function relationship. *Prog Retin Eye Res* 2006;25:79-97.
8. Riccò A. Relazione fra il minimo angolo visuale e l'intensità luminosa. *Memorie della Societa Degli Spettroscopisti Italiani* 1877;6:B29-B58.
9. Choi AY, Nivison-Smith L, Khuu SK, Kalloniatis M. Determining Spatial Summation and Its Effect on Contrast Sensitivity across the Central 20 Degrees of Visual Field. *PLoS One* 2016;11:e0158263.
10. Khuu SK, Kalloniatis M. Spatial summation across the central visual field: implications for visual field testing. *J Vis* 2015;15:15 11 16.
11. Khuu SK, Kalloniatis M. Standard Automated Perimetry: Determining Spatial Summation and Its Effect on Contrast Sensitivity Across the Visual Field. *Investigative ophthalmology & visual science* 2015;56:3565-3576.
12. Kwon M, Liu R. Linkage between retinal ganglion cell density and the nonuniform spatial integration across the visual field. *Proc Natl Acad Sci U S A* 2019;116:3827-3836.
13. Volbrecht VJ, Shrago EE, Scheffrin BE, Werner JS. Ricco's Areas for S- and L-Cone Mechanisms Across the Retina. *Color Res Appl* 2000;26:S32-S35.
14. Volbrecht VJ, Shrago EE, Scheffrin BE, Werner JS. Spatial summation in human cone mechanisms from 0 degrees to 20 degrees in the superior retina. *J Opt Soc Am A Opt Image Sci Vis* 2000;17:641-650.
15. Vassilev A, Ivanov I, Zlatkova MB, Anderson RS. Human S-cone vision: relationship between perceptive field and ganglion cell dendritic field. *J Vis* 2005;5:823-833.
16. Stapley V, Anderson RS, Saunders K, Mulholland PJ. Examining the concordance of retinal ganglion cell counts generated using measures of structure and function. *Ophthalmic Physiol Opt* 2022;42:1338-1352.
17. Redmond T, Garway-Heath DF, Zlatkova MB, Anderson RS. Sensitivity loss in early glaucoma can be mapped to an enlargement of the area of complete spatial summation. *Investigative ophthalmology & visual science* 2010;51:6540-6548.
18. Antwi-Boasiako K, Carter-Dawson L, Harwerth R, Gondo M, Patel N. The Relationship Between Macula Retinal Ganglion Cell Density and Visual Function in the Nonhuman Primate. *Investigative ophthalmology & visual science* 2021;62:5.
19. Swanson WH, Felius J, Pan F. Perimetric defects and ganglion cell damage: interpreting linear relations using a two-stage neural model. *Invest Ophthalmol Vis Sci* 2004;45:466-472.
20. Pan F, Swanson WH. A cortical pooling model of spatial summation for perimetric stimuli. *J Vis* 2006;6:1159-1171.
21. Montesano G, Mulholland PJ, Garway-Heath DF, Evans J, Ometto G, Crabb DP. Spatiotemporal summation of perimetric stimuli in healthy observers. *J Vis* 2023;23:2.
22. Swanson WH, Felius J, Pan F. Perimetric defects and ganglion cell damage: interpreting linear relations using a two-stage neural model. *Investigative ophthalmology & visual science* 2004;45:466-472.
23. Adams AJ, Heron G, Husted R. Clinical measures of central vision function in glaucoma and ocular hypertension. *Arch Ophthalmol* 1987;105:782-787.
24. Heijl A, Lundqvist L. The frequency distribution of earliest glaucomatous visual field defects documented by automatic perimetry. *Acta Ophthalmol (Copenh)* 1984;62:658-664.

25. De Moraes CG, Hood DC, Thenappan A, et al. 24-2 Visual Fields Miss Central Defects Shown on 10-2 Tests in Glaucoma Suspects, Ocular Hypertensives, and Early Glaucoma. *Ophthalmology* 2017;124:1449-1456.
26. Grillo LM, Wang DL, Ramachandran R, et al. The 24-2 Visual Field Test Misses Central Macular Damage Confirmed by the 10-2 Visual Field Test and Optical Coherence Tomography. *Translational vision science & technology* 2016;5:15.
27. Traynis I, De Moraes CG, Raza AS, Liebmann JM, Ritch R, Hood DC. Prevalence and nature of early glaucomatous defects in the central 10 degrees of the visual field. *JAMA ophthalmology* 2014;132:291-297.
28. West ME, Sharpe GP, Hutchison DM, et al. Utility of 10-2 Visual Field Testing in Glaucoma Patients with Early 24-2 Visual Field Loss. *Ophthalmology* 2020.
29. Montesano G, McKendrick AM, Turpin A, et al. Do Additional Testing Locations Improve the Detection of Macular Perimetric Defects in Glaucoma? *Ophthalmology* 2021;128:1722-1735.
30. Blumberg DM, De Moraes CG, Prager AJ, et al. Association Between Undetected 10-2 Visual Field Damage and Vision-Related Quality of Life in Patients With Glaucoma. *JAMA ophthalmology* 2017;135:742-747.
31. Montesano G, Gervasoni A, Ferri P, et al. Structure-function relationship in early diabetic retinopathy: a spatial correlation analysis with OCT and microperimetry. *Eye (Lond)* 2017;31:931-939.
32. Garway-Heath DF, Caprioli J, Fitzke FW, Hitchings RA. Scaling the hill of vision: the physiological relationship between light sensitivity and ganglion cell numbers. *Investigative ophthalmology & visual science* 2000;41:1774-1782.
33. Yoshioka N, Zangerl B, Phu J, et al. Consistency of Structure-Function Correlation Between Spatially Scaled Visual Field Stimuli and In Vivo OCT Ganglion Cell Counts. *Invest Ophthalmol Vis Sci* 2018;59:1693-1703.
34. Yohannan J, Wang J, Brown J, et al. Evidence-based Criteria for Assessment of Visual Field Reliability. *Ophthalmology* 2017;124:1612-1620.
35. Montesano G, Ometto G, Hogg RE, Rossetti LM, Garway-Heath DF, Crabb DP. Revisiting the Drasdo Model: Implications for Structure-Function Analysis of the Macular Region. *Translational vision science & technology* 2020;9:15.
36. Curcio CA, Allen KA. Topography of ganglion cells in human retina. *The Journal of comparative neurology* 1990;300:5-25.
37. Raza AS, Hood DC. Evaluation of the Structure-Function Relationship in Glaucoma Using a Novel Method for Estimating the Number of Retinal Ganglion Cells in the Human Retina. *Investigative ophthalmology & visual science* 2015;56:5548-5556.
38. Drasdo N, Millican CL, Katholi CR, Curcio CA. The length of Henle fibers in the human retina and a model of ganglion receptive field density in the visual field. *Vision research* 2007;47:2901-2911.
39. Tong J, Phu J, Alonso-Caneiro D, Khuu SK, Kalloniatis M. Clinical Evaluations of Macular Structure-Function Concordance With and Without Drasdo Displacement. *Translational vision science & technology* 2022;11:18.
40. Stapley V, Anderson RS, Saunders KJ, Mulholland PJ. Altered spatial summation optimizes visual function in axial myopia. *Sci Rep* 2020;10:12179.
41. Montesano G, Mulholland P, Garway-Heath DF, Evans J, Ometto G, Crabb DP. Spatio-temporal summation of perimetric stimuli in healthy observers. *bioRxiv* 2022;2022.2008.2010.503485.
42. Dacey DM. The mosaic of midget ganglion cells in the human retina. *J Neurosci* 1993;13:5334-5355.
43. Dacey DM, Petersen MR. Dendritic field size and morphology of midget and parasol ganglion cells of the human retina. *Proc Natl Acad Sci U S A* 1992;89:9666-9670.
44. Kaplan E, Lee BB, Shapley RM. Chapter 7 New views of primate retinal function. *Progress in Retinal Research* 1990;9:273-336.
45. Swanson WH, Sun H, Lee BB, Cao D. Responses of primate retinal ganglion cells to perimetric stimuli. *Investigative ophthalmology & visual science* 2011;52:764-771.
46. Kong AW, Della Santina L, Ou Y. Probing ON and OFF Retinal Pathways in Glaucoma Using Electroretinography. *Translational vision science & technology* 2020;9:14.
47. Demirel S. Psychophysical Evidence For RGC Dysfunction In Glaucoma. *Investigative ophthalmology & visual science* 2004;45:3303-3303.
48. Dannheim F, Drance SM. Psychovisual disturbances in glaucoma. A study of temporal and spatial summation. *Arch Ophthalmol* 1974;91:463-468.
49. Fellmann RL LJ, Starita RJ, Swanson WH. Clinical importance of spatial summation in glaucoma. In: A. H (ed), *VIII International Perimetric Society Meeting*. Amsterdam: Kugler & Ghedini; 1988:313-324.

50. Glezer VD. The receptive fields of the retina. *Vision research* 1965;5:497-525.
51. Barlow HB. Temporal and spatial summation in human vision at different background intensities. *J Physiol* 1958;141:337-350.
52. Lelkens AM, Zuidema P. Increment thresholds with various low background intensities at different locations in the peripheral retina. *J Opt Soc Am* 1983;73:1372-1378.
53. Mulholland PJ, Redmond T, Garway-Heath DF, Zlatkova MB, Anderson RS. Spatiotemporal Summation of Perimetric Stimuli in Early Glaucoma. *Investigative ophthalmology & visual science* 2015;56:6473-6482.
54. Owen WG. Spatio-temporal integration in the human peripheral retina. *Vision research* 1972;12:1011-1026.
55. Tong J, Phu J, Alonso-Caneiro D, Khuu SK, Kalloniatis M. Prediction of Retinal Ganglion Cell Counts Considering Various Displacement Methods From OCT-Derived Ganglion Cell-Inner Plexiform Layer Thickness. *Translational vision science & technology* 2022;11:13.
56. Hood DC, Kardon RH. A framework for comparing structural and functional measures of glaucomatous damage. *Prog Retin Eye Res* 2007;26:688-710.
57. Miraftebi A, Amini N, Morales E, et al. Macular SD-OCT Outcome Measures: Comparison of Local Structure-Function Relationships and Dynamic Range. *Investigative ophthalmology & visual science* 2016;57:4815-4823.
58. Liu Z, Saedi O, Zhang F, et al. Quantification of Retinal Ganglion Cell Morphology in Human Glaucomatous Eyes. *Investigative ophthalmology & visual science* 2021;62:34.
59. Lotmar W. Apparatus for the measurement of retinal visual acuity by moire fringes. *Investigative ophthalmology & visual science* 1980;19:393-400.
60. Williams DR. Visibility of interference fringes near the resolution limit. *J Opt Soc Am A* 1985;2:1087-1093.
61. Williams DR. Aliasing in human foveal vision. *Vision research* 1985;25:195-205.
62. Coletta NJ, Williams DR. Psychophysical estimate of extrafoveal cone spacing. *J Opt Soc Am A* 1987;4:1503-1513.
63. Rountree L, Mulholland PJ, Anderson RS, Garway-Heath DF, Morgan JE, Redmond T. Optimising the glaucoma signal/noise ratio by mapping changes in spatial summation with area-modulated perimetric stimuli. *Sci Rep* 2018;8:2172.
64. Bedggood P, Prea SM, Kong YXG, Vingrys AJ. Scaling the size of perimetric stimuli reduces variability and returns constant thresholds across the visual field. *J Vis* 2021;21:2.
65. Montesano G, Rossetti LM, Allegrini D, Romano MR, Crabb DP. Improving Visual Field Examination of the Macula Using Structural Information. *Translational vision science & technology* 2018;7:36.
66. Lazaridis G, Montesano G, Afgei SS, et al. Predicting Visual Fields From Optical Coherence Tomography via an Ensemble of Deep Representation Learners. *Am J Ophthalmol* 2022;238:52-65.
67. Kihara Y, Montesano G, Chen A, et al. Policy-Driven, Multimodal Deep Learning for Predicting Visual Fields from the Optic Disc and OCT Imaging. *Ophthalmology* 2022;129:781-791.
68. Hemelings R, Elen B, Barbosa-Breda J, et al. Pointwise Visual Field Estimation From Optical Coherence Tomography in Glaucoma Using Deep Learning. *Translational vision science & technology* 2022;11:22.
69. Gardiner SK, Swanson WH, Demirel S. The Effect of Limiting the Range of Perimetric Sensitivities on Pointwise Assessment of Visual Field Progression in Glaucoma. *Investigative ophthalmology & visual science* 2016;57:288-294.
70. Gardiner SK, Swanson WH, Goren D, Mansberger SL, Demirel S. Assessment of the reliability of standard automated perimetry in regions of glaucomatous damage. *Ophthalmology* 2014;121:1359-1369.
71. Davila KD, Geisler WS. The relative contributions of pre-neural and neural factors to areal summation in the fovea. *Vision research* 1991;31:1369-1380.
72. Dalimier E, Dainty C. Role of ocular aberrations in photopic spatial summation in the fovea. *Opt Lett* 2010;35:589-591.
73. Redmond T, Zlatkova MB, Garway-Heath DF, Anderson RS. The effect of age on the area of complete spatial summation for chromatic and achromatic stimuli. *Investigative ophthalmology & visual science* 2010;51:6533-6539.
74. Curcio CA, Sloan KR, Kalina RE, Hendrickson AE. Human photoreceptor topography. *The Journal of comparative neurology* 1990;292:497-523.
75. Plummer M. JAGS: A program for analysis of Bayesian graphical models using Gibbs sampling. 2003.
76. Andrew G, Donald BR. Inference from Iterative Simulation Using Multiple Sequences. *Statistical Science* 1992;7:457-472.

77. Turpin A, Artes PH, McKendrick AM. The Open Perimetry Interface: an enabling tool for clinical visual psychophysics. *J Vis* 2012;12.
78. Turpin A, McKendrick AM, Johnson CA, Vingrys AJ. Properties of perimetric threshold estimates from full threshold, ZEST, and SITA-like strategies, as determined by computer simulation. *Investigative ophthalmology & visual science* 2003;44:4787-4795.
79. Henson DB, Chaudry S, Artes PH, Faragher EB, Ansons A. Response variability in the visual field: comparison of optic neuritis, glaucoma, ocular hypertension, and normal eyes. *Investigative ophthalmology & visual science* 2000;41:417-421.
80. Gardiner SK, Swanson WH, Mansberger SL. Long- and Short-Term Variability of Perimetry in Glaucoma. *Translational vision science & technology* 2022;11:3.

7. Conclusions and future directions

The work presented in this thesis advances the understanding of structure-function relationship in the macula. One important aspect was the refinement and improvement of previous widely used methodology to report perimetric stimuli onto anatomical maps generated with imaging. This offered the chance to correct and revisit previously published results, especially in the field of macular damage from glaucoma^{1,2}.

Differently from many previous investigations focussing on empirical structure-function relationship, our modelling approach sought to relate results from functional tests, mostly clinical perimetry, to an underlying biological substrate through computational models of the retina and cortical integration. The model improved upon previous similar attempts³ by reproducing the interaction between stimulus size and duration. The model also predicted a change in spatial and temporal summation from changes in the number of photoreceptors converging onto the ganglion cells. This has potential for applications in outer retinal diseases, but the predictions from the model will need further confirmation, for example by studying spatial summation in patients with disease of the outer retina.

Other aspects will require further investigation, such as the contribution of optical factors. Different implementation of our computational model predicted two very different effect magnitudes, from negligible to very strong. Both are compatible with previous literature^{4,5}. Future work could employ adaptive optics to deliver stimuli unaffected by optical aberration, isolating the neural contribution to spatial summation. Adaptive optics could also be used to improve estimates of RGC densities at the tested locations by imaging individual ganglion cells^{6,7}, overcoming the need for indirect estimates from retinal thickness values.

Finally, the prediction from our computational model proved to be an effective description of the changes observed in glaucoma from damage to the RGC mosaic. While these results did not make a large improvement to the empirical structure-function relationship, mostly because of the floor effect in the structural measurements, they can be used to improve functional testing. For example, this model could be used to develop perimetric testing strategies that exploit the established relationship between perimetric sensitivity and stimulus characteristics by modulating contrast, size and duration. Such an approach could improve the reliability⁸ and speed of perimetric tests. Interestingly, we proved that a similar paradigm could be used to evaluate neural loss from diabetes. This is an indication of the potential generalisability of our findings beyond the applications to glaucoma.

Further investigations would also need to assess whether reactive changes occur in the visual cortex. Our model does not require any specific alterations to cortical processes in response to retinal damage. For example, our results in glaucoma suggest a consistent response of the visual system for healthy and diseased eyes, since the effect of RGCs loss from disease appeared identical to the effect of testing a healthy eye with smaller stimulus sizes. These results will need to be confirmed with more detailed investigations, for example with the use of functional magnetic resonance imaging, in patients with retinal and optic nerve diseases, such as glaucoma⁹⁻¹¹.

7.1. References

1. Miraftebi A, Amini N, Morales E, et al. Macular SD-OCT Outcome Measures: Comparison of Local Structure-Function Relationships and Dynamic Range. *Investigative ophthalmology & visual science* 2016;57:4815-4823.
2. Yoshioka N, Zangerl B, Phu J, et al. Consistency of Structure-Function Correlation Between Spatially Scaled Visual Field Stimuli and In Vivo OCT Ganglion Cell Counts. *Investigative ophthalmology & visual science* 2018;59:1693-1703.
3. Pan F, Swanson WH. A cortical pooling model of spatial summation for perimetric stimuli. *J Vis* 2006;6:1159-1171.
4. Dalimier E, Dainty C. Role of ocular aberrations in photopic spatial summation in the fovea. *Opt Lett* 2010;35:589-591.
5. Tuten WS, Cooper RF, Tiruveedhula P, et al. Spatial summation in the human fovea: Do normal optical aberrations and fixational eye movements have an effect? *J Vis* 2018;18:6.
6. Liu Z, Kurokawa K, Zhang F, Lee JJ, Miller DT. Imaging and quantifying ganglion cells and other transparent neurons in the living human retina. *Proc Natl Acad Sci U S A* 2017;114:12803-12808.
7. Liu Z, Saeedi O, Zhang F, et al. Quantification of Retinal Ganglion Cell Morphology in Human Glaucomatous Eyes. *Invest Ophthalmol Vis Sci* 2021;62:34.
8. Rountree L, Mulholland PJ, Anderson RS, Garway-Heath DF, Morgan JE, Redmond T. Optimising the glaucoma signal/noise ratio by mapping changes in spatial summation with area-modulated perimetric stimuli. *Sci Rep* 2018;8:2172.
9. Carvalho J, Invernizzi A, Martins J, Renken RJ, Cornelissen FW. Local neuroplasticity in adult glaucomatous visual cortex. *Sci Rep* 2022;12:21981.
10. Wang B, Yan T, Zhou J, et al. Altered fMRI-derived functional connectivity in patients with high-tension glaucoma. *J Neuroradiol* 2021;48:94-98.
11. Zhou W, Muir ER, Nagi KS, Chalfin S, Rodriguez P, Duong TQ. Retinotopic fMRI Reveals Visual Dysfunction and Functional Reorganization in the Visual Cortex of Mild to Moderate Glaucoma Patients. *J Glaucoma* 2017;26:430-437.